



UNIVERSITAT DE  
BARCELONA

## Integration of Micro Solid Oxide Fuel Cells in Power Generator Devices

Dolors Pla i Asesio

**ADVERTIMENT.** La consulta d'aquesta tesi queda condicionada a l'acceptació de les següents condicions d'ús: La difusió d'aquesta tesi per mitjà del servei TDX ([www.tdx.cat](http://www.tdx.cat)) i a través del Dipòsit Digital de la UB ([diposit.ub.edu](http://diposit.ub.edu)) ha estat autoritzada pels titulars dels drets de propietat intel·lectual únicament per a usos privats emmarcats en activitats d'investigació i docència. No s'autoritza la seva reproducció amb finalitats de lucre ni la seva difusió i posada a disposició des d'un lloc aliè al servei TDX ni al Dipòsit Digital de la UB. No s'autoritza la presentació del seu contingut en una finestra o marc aliè a TDX o al Dipòsit Digital de la UB (framing). Aquesta reserva de drets afecta tant al resum de presentació de la tesi com als seus continguts. En la utilització o cita de parts de la tesi és obligat indicar el nom de la persona autora.

**ADVERTENCIA.** La consulta de esta tesis queda condicionada a la aceptación de las siguientes condiciones de uso: La difusión de esta tesis por medio del servicio TDR ([www.tdx.cat](http://www.tdx.cat)) y a través del Repositorio Digital de la UB ([diposit.ub.edu](http://diposit.ub.edu)) ha sido autorizada por los titulares de los derechos de propiedad intelectual únicamente para usos privados enmarcados en actividades de investigación y docencia. No se autoriza su reproducción con finalidades de lucro ni su difusión y puesta a disposición desde un sitio ajeno al servicio TDR o al Repositorio Digital de la UB. No se autoriza la presentación de su contenido en una ventana o marco ajeno a TDR o al Repositorio Digital de la UB (framing). Esta reserva de derechos afecta tanto al resumen de presentación de la tesis como a sus contenidos. En la utilización o cita de partes de la tesis es obligado indicar el nombre de la persona autora.

**WARNING.** On having consulted this thesis you're accepting the following use conditions: Spreading this thesis by the TDX ([www.tdx.cat](http://www.tdx.cat)) service and by the UB Digital Repository ([diposit.ub.edu](http://diposit.ub.edu)) has been authorized by the titular of the intellectual property rights only for private uses placed in investigation and teaching activities. Reproduction with lucrative aims is not authorized nor its spreading and availability from a site foreign to the TDX service or to the UB Digital Repository. Introducing its content in a window or frame foreign to the TDX service or to the UB Digital Repository is not authorized (framing). Those rights affect to the presentation summary of the thesis as well as to its contents. In the using or citation of parts of the thesis it's obliged to indicate the name of the author.





# INTEGRATION OF MICRO SOLID OXIDE FUEL CELLS IN POWER GENERATOR DEVICES

Thesis submitted by **Dolors Pla i Asesio** to apply for the  
Degree of Doctor at the University of Barcelona,  
in the “Engineering and Advanced Technologies” Program.  
Departament d'Electrònica, Facultat de Física

Supervisors:

Dr. Albert Tarancón i Rubio

Dr. Marc Sallleras i Freixes

Tutor:

Dr. Joan Ramón Morante i Lleonart

June 2015





El Dr. Albert Tarancón i Rubio, investigador del Institut de Recerca en Energia de Catalunya (IREC) i el Dr. Marc Salleras i Freixes, investigador del Institut de Microelectrònica de Barcelona (IMB-CNM, CSIC), CERTIFIQUEN:

Que la memòria titulada *Integration of micro solid oxide fuel cells in power generator devices*, presentada per Dolors Pla i Asesio per optar al grau de Doctor en el Programa d'Enginyeria i Tecnologies Avançades que concedeix la Universitat de Barcelona, ha estat realitzada sota la seva direcció al Institut de Recerca en Energia de Catalunya (IREC).

Barcelona, maig de 2015,

Dr. Albert Tarancón i Rubio

Dr. Marc Salleras i Freixes



seieu al porxo,  
contempleu la dòcil  
cal·ligrafia dels estels.”

Francesc Garriga i Barata  
*La nit dels peixos, 2005*

**Allegro assai. Die Königin der Nacht. QUEEN OF NIGHT.**

Der Höl-le Ra - chekocht in mei-nem Her-zen,  
The pangs of hell are ra-ging in my bo - som.

Tod und Ver-zweiflung, Tod und Ver-zweif-lung flam -  
Death and des-truc-tion death and des-truc-tion wild -

- men um mich her! Führt nicht durch dich Sa - ra - stro To - des -  
ly flare a - round! Go forth, and bear my vengeance to Sa -

schmerzen, Sa - ra - stro To - des - schmerzen, so bist du mei - ne  
ras - tro, my vengeance to Sa - ra - stro. Se thou shalt be my

Toch - ter nim-mer-mehr, so bist du mein', meine Toch - ter nim-mer-  
daugh - ter nev - er more or thou shalt be be my daugh - ter ne - ver -

Die Hölle Rache kocht in meinem Herzen  
Die Zauberflöte, K.620, W.A. Mozart





## Acknowledgements/Agraïments

*(En un últim acte que el possible lector, si ho prefereix, es pot estalviar i que el director d'alguna futura representació de l'obra, al seu criteri, pot escurçar o suprimir).*

«Hem viscut uns anys intensos» li va dir. El capità no havia sentit les seves paraules i seguia amb els binocles entre les mans a la recerca de nous horitzons. L'admirava. Encara avui es pregunta com el va acceptar. Ell, poruc, que del mar només coneixia el blau i el salat. Però el capità era un tipus segur, que caminava amb pas ferm. El dia que es van conèixer, el va agafar per les espatlles i li va etzibar «Benvingut a bord de la nau SOC. Què te'n sembla?». El novell no badava boca. Estava aclaparat. «No pateixis vailet, el temps i la resta de tripulació t'ensenyaran». Va riure a pulmó una estona llarga. L'admirava al capità, un llop de mar amb anys d'experiència a l'esquena, una passió contagiosa per les misterioses profunditats i una calma serena que amansia tempestes.

Rere el pal llarg, el contramestre va treure el cap, es va espolsar els pantalons de mitja cama i li va allargar una mà. «Així que tu ets el nou aprenent». Tenia una expressió dolça, amable, un bon jan. I era un dels mariners més desitjats per la resta de flotes del Mediterrani. Teixia els caps i els nusos amb una destresa inigualable. I mantenia la coberta i el buc sempre a punt de marxa. Havia après un munt del contramestre i patia per no haver sabut agrair-li prou.

Al costat del contramestre, hi havia un mariner ceapat, d'espatlla ample i posat callat. «Mosso, acosta't!» havia cridat el capità. El mosso, a pas lent, va fer cap. «Aquest serà el teu nou ajudant, mostra-li els secrets de la SOC». I, ai pobre, quina creu li va tocar! El mosso es va armar de paciència per intentar treure quelcom de profit d'aquell novell. Li va explicar una i altra vegada les tècniques de navegació. Li va ensinistrar el nas; peix fresc, sardina i gambot vermell. La finesa i precisió amb què treballava el mosso l'entusiasmaven. Però el mosso volia conèixer món i els va deixar per provar fortuna lluny del mar, entre muntanyes nevades. L'enyora, feien un bon equip.

Unes setmanes més tard, es va fer inseparable d'uns nans bessons que s'havien enrolat d'imprevist a la nau. Malgrat que d'aspecte eren ben diferents, tots dos estaven obsessionats per la meteorologia i els números. Desenvolupaven models matemàtics per predir la temperatura, la calor, els vents i les corrents marines. Al principi, es va aferrar al nan que provenia de les espanyes fins que va tornar a casa. Després, a poc a poc, es va infiltrar al tarannà del nan amb

accent de tramuntana. Era de paraules sàvies i l'havia ajudat molt en aquest llarg viatge.

Va sospirar mentre clavava els ulls a l'horitzó. A coberta només quedaven els últims raigs de sol que es fonien lentament. Havien passat quatre anys. I seria injust si en aquest últim acte deixés de banda a la resta de companys que formaven part de la tripulació, així com altres mariners amb qui havia navegat. Havia recuperat antics amics d'escola, n'havia fet de nous, havia viatjat amb altres vaixells a illes estranyes i apassionants, s'havia fet més gran i més ric. Va aixecar la vista al cel. Fosquejava. I els va veure aparèixer. Els seus estels que l'havien recolzat, consolat i estimat. A l'aigua tranquil·la, ja s'hi reflectia la lluna que, com cada vespre, el va abraçar i la va dir «Aquest viatge s'acaba aquí, però demà continuarem el nostre».

*(Un focus blanc empetiteix l'escena fins a desaparèixer i s'abaixa el taló).*

Intèrprets:

**Albert Tarancón**, capità / **Àlex Morata**, contramestre / **Iñigo Garbayo**, mosso / **Alberto Sánchez**, nan de les espanyes / **Marc Salleras**, nan amb accent de tramuntana / **Bibiana, Laura, Roberto, Diana, Verónica, Gerard, Mónica, Marc T., Pepín, Marcus, Aitor, Paula, Hedda, Eulàlia, Elba, Francesco, Eleonora i Saranya**, tripulació SOC / **Doris, Raquel, Andres, Javi, Àlex C., Diouldé, Cristian, Fran, Mariano, Jorge, Marta G., Marta D., Raquel P., M<sup>a</sup> Ángeles, Carlos, Neus, Jordi, Núria, Albert**, altres mariners / **Els meus pares i el meu germà**, estels / **En Marc**, lluna.

A tots, moltes gràcies!

## Abstract

In the last decades, energy requirements of portable devices are exponentially increasing while the capacity of the current battery technology is not progressing accordingly. This energy gap claims for the development of new technologies beyond Li-ion. Novel miniaturized devices able to efficiently operate on the low power regime (1 – 20 W) in continuous mode by using a fuel are receiving increased attention. Due to their long lifetime, high power density and integrability, probably the most promising alternative is the development of micro fuel cells. Amongst them, micro Solid Oxide Fuel Cells ( $\mu$ SOFCs) present the highest values of specific energy densities (by unit mass and volume), mainly due to their higher operating temperature and their capability of operating directly on hydrocarbon fuels. One of the most promising approaches for the  $\mu$ SOFCs is based on the monolithic integration of functional free-standing electrolyte membranes in silicon technology. This approach ensures high reproducibility and reliability, cheap mass production and easy integration to mainstream technology.

This thesis encompasses the design, fabrication and test of the main components of a novel  $\mu$ SOFC power generator as a first step to develop a complete device in the near future. The adopted approach is based on the use of MEMS fabrication methods to miniaturize  $\mu$ SOFCs in silicon technology and high energy density hydrocarbons as fuels. The  $\mu$ SOFC power generator is designed to supply 1W of electrical energy in a small volume (10-20 cm<sup>3</sup>). The work developed is divided into six chapters. The first chapter introduces the basics and challenges of a  $\mu$ SOFC power generator. The second chapter focuses on the experimental procedures and characterization techniques used. In the third chapter, the thermal analysis of a new  $\mu$ SOFC power generator with finite-volume simulations is presented. The fourth chapter shows the fabrication and characterization of a fuel processing unit capable to produce hydrogen from ethanol steam reforming and methane dry reforming. The next chapter is related to a catalytic micro-machined combustor. Finally, chapter six presents the development of a full ceramic  $\mu$ SOFC.



## Resum

La demanda d'energia dels dispositius electrònics portàtils augmenta exponencialment any rere any, però la tecnologia actual amb les bateries d'ió liti no progressa suficientment. Aquesta divergència energètica és una oportunitat per poder desenvolupar noves tecnologies. En aquest sentit, micro dispositius que operin de forma contínua mitjançant l'ús d'un combustible i que proporcionin una potència compresa entre 1 i 20 W reben una especial atenció per part de la comunitat científica. Probablement, l'alternativa més prometedora són les micro piles de combustible, ja que tenen una llarga vida útil, una alta densitat de potència i són fàcils d'integrar. Dels diferents tipus, les piles de combustible d'òxid sòlid ( $\mu$ SOFCs) són les que tenen una major densitat específica d'energia (per unitat de massa i de volum). A més a més, treballen a una temperatura més alta i aquesta característica permet utilitzar hidrocarburs com a combustible. Una de les configuracions més esteses de les  $\mu$ SOFCs és la que es basa en membranes electrolítiques en suspensió, integrades amb la tecnologia de silici. Aquesta configuració permet una producció elevada, barata i fiable.

La present tesi té com a objectiu dissenyar, fabricar i validar experimentalment els principals components d'un nou dispositiu generador. El resultat obtingut és un primer pas per desenvolupar en un futur proper un dispositiu complet basat en l'ús de MEMS (sistemes micro electromecànics) i hidrocarburs d'alta densitat d'energia. El dispositiu  $\mu$ SOFC ha estat ideat per subministrar 1W de potència elèctrica i ocupar un volum entre 10 i 20 cm<sup>3</sup>. La tesi consta de sis capítols. En el primer es descriuen els conceptes generals relacionats amb un dispositiu  $\mu$ SOFC i els principals reptes associats que presenta el seu desenvolupament. El segon es centra en els procediments experimentals i les tècniques de caracterització utilitzades al llarg de la tesi. El tercer capítol presenta l'anàlisi tèrmica del sistema proposat mitjançant simulacions termofluídiques. El quart mostra la fabricació i caracterització d'una unitat de processament de combustible capaç de produir hidrogen a partir del reformat d'etanol i metà. El cinquè descriu una unitat catalítica de combustió. I l'últim capítol, es centra en les capes funcionals d'una pila de combustible  $\mu$ SOFC completament ceràmica.



# Table of contents

<b>I. Introduction.....</b>	<b>1</b>
<b>1.1. Motivation.....</b>	<b>5</b>
1.1.1. Remote devices and portable power technology.....	5
1.1.2. Limitations of batteries for new energy demands.....	6
1.1.3. Micro fuel cell systems as battery replacement.....	7
<b>1.2. Fuel cells fundamentals.....</b>	<b>9</b>
1.2.1. Basic principles.....	9
1.2.2. Types of fuel cell.....	10
1.2.3. Thermodynamics of a fuel cell .....	10
1.2.4. Overvoltage sources in a real SOFC fuel cell.....	11
<b>1.3. Micro SOFC power generator.....</b>	<b>13</b>
1.3.1. Micro SOFC power generation technology.....	14
1.3.2. Main requirements of a micro SOFC PG.....	14
<b>1.4. Objectives and approach.....</b>	<b>18</b>
<b>II. Experimental methods.....</b>	<b>25</b>
<b>2.1. Introduction.....</b>	<b>29</b>
<b>2.2. Microfabrication technology.....</b>	<b>31</b>
2.2.1. MEMS fabrication.....	31
2.2.2. Processes for micromachining.....	31
2.2.2.1. Lithography.....	32
2.2.2.2. Etching.....	33
2.2.2.3. Anodic bonding.....	37
2.2.2.4. Film growth/deposition.....	39
<b>2.3. Pulsed laser deposition.....</b>	<b>42</b>
2.3.1. Effect of main deposition conditions on PLD films.....	42
2.3.2. Wafer level integration: large area PLD.....	44
2.3.3. Special issues related to large area PLD films.....	46
<b>2.4. Catalyst synthesis routes.....</b>	<b>49</b>



2.4.1. Hydrocarbon reforming catalysts.....	49
2.4.2. Catalyst for hydrogen combustion.....	50
<b>2.5. Structural characterization.....</b>	<b>52</b>
2.5.1. Optical microscopy.....	52
2.5.2. Scanning electron microscopy.....	53
2.5.3. Transmission electron microscopy.....	54
2.5.4. X-ray fluorescence.....	54
2.5.5. Reflectometry.....	55
2.5.6. X-ray diffraction.....	56
2.5.7. Gas chromatography.....	57
2.5.8. Thermo gravimetric analysis.....	57
2.5.9. Differential scanning calorimetry.....	58
2.5.10. Mass spectroscopy.....	58
2.5.11. Impedance spectroscopy.....	59
2.5.12. Electrical characterization.....	61
<b>2.6. Functional characterization.....</b>	<b>63</b>
2.6.1. Hydrocarbon reforming reactions.....	63
2.6.2. Catalytic combustion of hydrogen.....	65
2.6.3. Electrochemical $\mu$ SOFC measurement.....	66
<b>2.7. Simulations and modeling.....</b>	<b>68</b>
<b>III. Thermal management.....</b>	<b>75</b>
<b>3.1. Introduction.....</b>	<b>79</b>
<b>3.2. Thermal management strategies for a specific <math>\mu</math>SOFC PG.....</b>	<b>83</b>
<b>3.3. Geometric model.....</b>	<b>85</b>
3.3.1. System architecture and fluidics.....	85
3.3.2. Components design and specifications.....	86
3.3.2.1. Fuel processing unit.....	87
3.3.2.2. Micro-SOFC stack.....	88
3.3.2.3. Post combustion unit.....	89
<b>3.4. Physical modeling.....</b>	<b>90</b>
3.4.1. Meshing.....	90

3.4.2. Materials and boundary conditions.....	91
3.4.3. Components modeling and initial conditions.....	93
<b>3.5. Results and discussion.....</b>	<b>96</b>
3.5.1. Case study I: steady-state operation mode.....	96
3.5.1.1. Simulation details.....	96
3.5.1.2. Results.....	96
3.5.2. Case study II: transient operation mode.....	100
3.5.2.1. Simulation details.....	100
3.5.2.2. Results.....	102
<b>3.6. Conclusions.....</b>	<b>108</b>
<b>IV. Fuel processing unit.....</b>	<b>111</b>
<b>4.1. Introduction.....</b>	<b>115</b>
<b>4.2. Design and fabrication of a bulk <math>\mu</math>reformer.....</b>	<b>119</b>
4.2.1. Design outline and concept approach.....	119
4.2.2. Microfabrication process.....	121
4.2.3. Thermal characterization of the micro-heater.....	123
<b>4.3. Activity measurements of the bulk <math>\mu</math>reformer.....</b>	<b>126</b>
4.3.1. Structural characterization of the Pd-Rh/CeO <sub>2</sub> catalyst system....	126
4.3.2. Catalytic activity of the bulk $\mu$ reformer.....	127
4.3.2.1. Influence of the operation temperature.....	127
4.3.2.2. Influence of the fuel loading.....	130
<b>4.4. Design and fabrication of a suspended <math>\mu</math>reformer.....</b>	<b>133</b>
4.4.1. Design outline and concept approach.....	133
4.4.2. Microfabrication process.....	135
4.4.3. Start-up of the suspended $\mu$ reformer.....	137
4.4.4. Glass cover fabrication and encapsulation.....	137
<b>4.5. Activity measurements of the suspended <math>\mu</math>reformer.....</b>	<b>139</b>
4.5.1. Wet impregnation method of the Pd-Rh/CeO <sub>2</sub> catalyst system....	139
4.5.2. Activity of the suspended $\mu$ reformer as a standalone device.....	139
<b>4.6. Conclusions.....</b>	<b>141</b>

<b>V. Post combustion unit.....</b>	<b>147</b>
<b>5.1. Introduction.....</b>	<b>151</b>
<b>5.2. Characterization of CuO-NiO/CGO catalyst.....</b>	<b>155</b>
<b>5.3. Synergic effect of multi-component metal oxides.....</b>	<b>158</b>
<b>5.4. Post combustor prototype for a <math>\mu</math>SOFC PG.....</b>	<b>162</b>
5.4.1. Microfabrication of the silicon $\mu$ combustor.....	162
5.4.2. Catalyst infiltration.....	163
5.4.3. Operation conditions.....	163
5.4.2. Reaction tests.....	164
<b>5.5. Conclusions.....</b>	<b>166</b>
<b>VI. Full ceramic-based micro solid oxide fuel cell.....</b>	<b>171</b>
<b>6.1. Introduction.....</b>	<b>175</b>
<b>6.2. Self-supported electrolyte.....</b>	<b>179</b>
6.2.1. Low thermal mass architecture.....	179
6.2.2. Structural and microstructural characterization.....	180
6.2.3. YSZ cross-plane conductivity.....	181
<b>6.3. Ceramic cathodes for <math>\mu</math>SOFC.....</b>	<b>183</b>
6.3.1. Thin film $\text{La}_{0.6}\text{Sr}_{0.4}\text{CoO}_{3-\delta}$ .....	183
6.3.1.1. Structural and microstructural characterization.....	183
6.3.1.2. Integration in self-suspended membranes of YSZ.....	185
6.3.1.3. Electrochemical characterization.....	186
6.3.2. Thin film $\text{La}_{0.8}\text{Sr}_{0.2}\text{MnO}_{3+\delta}$ .....	189
6.3.2.1. Structural and microstructural characterization.....	189
6.3.2.2. Oxygen mass transport properties of the dense LSM layer.....	191
6.3.2.3. Electrochemical characterization.....	195
<b>6.4. Ceramic anodes for <math>\mu</math>SOFC.....</b>	<b>198</b>
6.4.1. Thin film $\text{Ce}_{0.8}\text{Gd}_{0.2}\text{O}_{1.9-\delta}$ .....	198
6.4.1.1. Structural and microstructural characterization.....	198

6.4.1.2. Integration in self-suspended membranes of YSZ.....	199
6.4.1.3. Electrochemical characterization.....	200
6.4.2. Thin film $\text{Sr}_2\text{Fe}_{1.5}\text{Mn}_{0.5}\text{O}_{6-\delta}$ .....	202
6.4.2.1. Structural and microstructural characterization.....	202
6.4.2.2. Oxygen mass transport properties of the dense LSM layer.....	203
6.4.2.3. Electrochemical characterization.....	204
<b>6.5. Full ceramic-based <math>\mu\text{SOFC}</math>.....</b>	<b>206</b>
6.5.1. Structural and microstructural characterization.....	206
6.5.2. Electrochemical performance of the $\mu\text{SOFC}$ .....	207
<b>6.6. Conclusions.....</b>	<b>210</b>
<b>VII. Conclusions.....</b>	<b>219</b>
<b>Appendices.....</b>	<b>225</b>
<b>Scientific contributions.....</b>	<b>243</b>



# **I. INTRODUCTION**



<b>1.1. Motivation</b> .....	5
1.1.1. Remote devices and portable power technology.....	5
1.1.2. Limitations of batteries for new energy demands.....	6
1.1.3. Micro fuel cell systems as battery replacement.....	7
<b>1.2. Fuel cells fundamentals</b> .....	9
1.2.1. Basic principles.....	9
1.2.2. Types of fuel cell.....	10
1.2.3. Thermodynamics of a fuel cell .....	10
1.2.4. Overvoltage sources in a real SOFC fuel cell.....	11
<b>1.3. Micro SOFC power generator</b> .....	13
1.3.1. Micro SOFC power generation technology.....	13
1.3.2. Main requirements of a micro SOFC PG.....	14
<b>1.4. Objectives and approach</b> .....	18

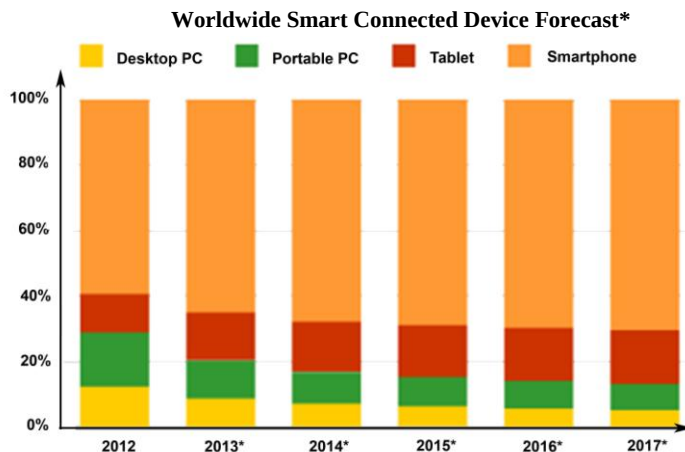




## 1.1. Motivation

### 1.1.1. Remote devices and portable power technology

Since the invention of the integrated circuit in the late 1950s, advances in processing and communications capabilities have driven a massive proliferation of portable devices and wireless sensor networks. Among these devices, consumer electronics such as mobile smartphones, laptops and other gadgets, e.g. e-books or media players, have annually increased in number of units since their introduction into the market. A recently published study from the International Data Corporation anticipates that the worldwide smart device market will accelerate until reaching 2 billion units by the end of 2015, i.e. a market value of \$735 billion [1]. **Figure 1.1** shows the distribution of sales by product category. PC's will drop from 28.7 % in 2013 to 13 % in 2017, tablets will increase from 11.8 % in 2013 to 16.5 % by 2017, and smartphones will increase from 59.5 % to 70.5 %.



**Figure 1.1:** Market share by product category, 2012-2017 from International Data Corporation study prediction; \* indicates forecasted values.

A classification of the most common portable devices, as a function of their operating power needs, is depicted in **Figure 1.2** [2]. Energy Harvesting (EH) and button batteries are the most common power supply systems used for the ultra-low power regime ( $< 1$  mW, see blue zone in the figure), e.g. electronic watches or calculators. Moreover, batteries are the most common option for powering devices in the low power regime (10 mW – 10 W, red zone in the figure) such as  $\mu$ P laptops,  $\mu$ P desktop or MP3.

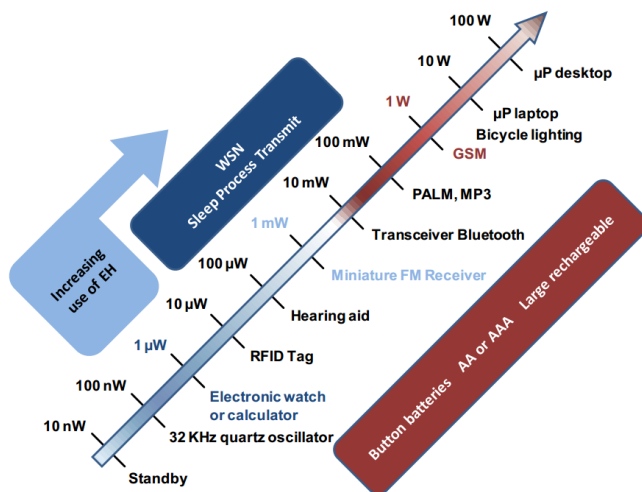
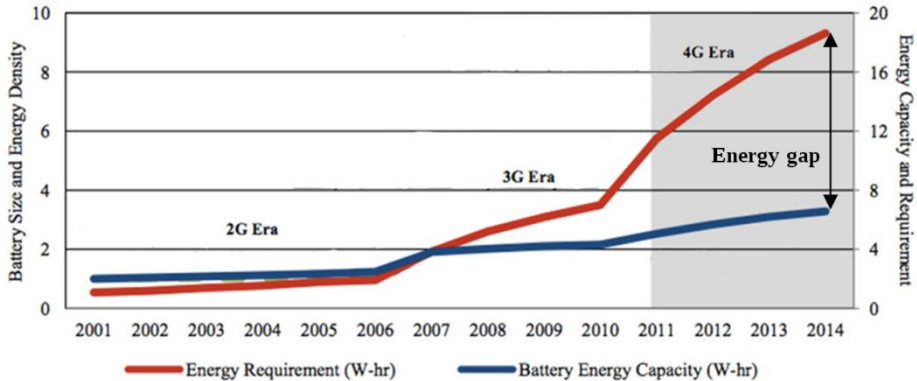


Figure 1.2: Power consumption of portable devices, extracted from [2]

### 1.1.2. Limitations of batteries for new energy demands

Up to now, batteries have served as primary source for storing and delivering power to portable electronic devices [3, 4]. Although in recent years batteries have improved in terms of energy density and rechargeability, these improvements in better battery performance are insufficient when compared with the consumer demand that has grown tenfold. **Figure 1.3** illustrates the evolution of energy requirements of the mobile phones with time, compared to the battery energy supply capacity (extracted from [5]). The figure clearly shows the large and growing energy demand gap appeared between device power needs (red line) and power supply capacities (blue line). According to this study, the already developed batteries would be reaching their energy density limit and no longer could be considered for powering reliably high-performance devices unless a disruptive improvement is provided. Therefore, this energy gap claims for the development of new energy storage technologies beyond batteries.



**Figure 1.3:** Evolution of the energy needs and capacities of different generations of mobile phones (adapted from [5]).

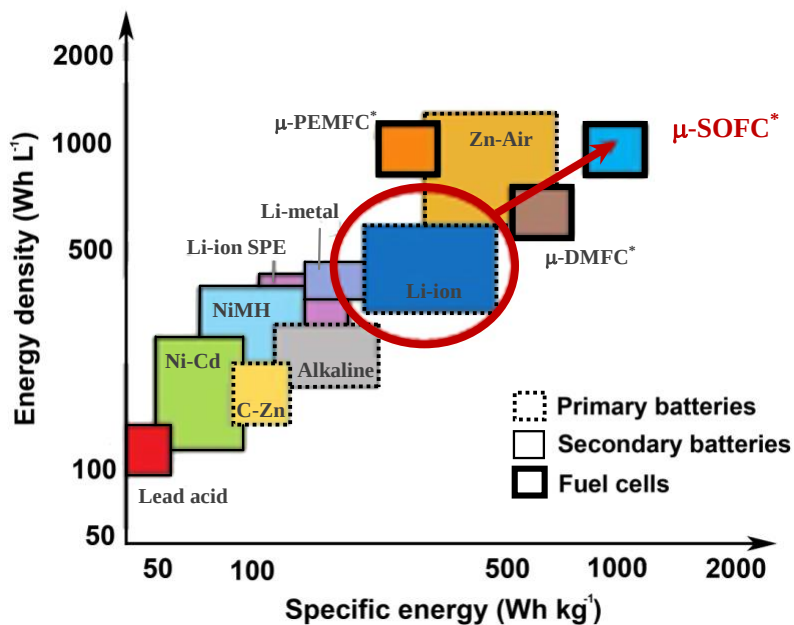
In general, portable devices require increasing amounts of energy for longer periods of time, while the existing portable power technologies fail to proportionally increase their storage capacity. This forces the search of new integrated power sources that could satisfy the requirements of high power density, high autonomy and low cost, while being small.

### 1.1.3. Micro fuel cell systems as battery replacement

According to this scenario, research efforts have been focused on developing new portable power generators such as micro-fuel cell systems, micro-engines and thermophotovoltaic systems. In particular, micro-fuel cells appear as one of the most promising alternatives due to:

- (a) Their high *specific energy*, which describes the net energy per unit weight, and *energy density*, which indicates the net energy per unit volume, are two orders of magnitude greater than those of their battery counterparts (see **Figure 1.4**)
- (b) Lack of movable parts.
- (c) Possibility of miniaturization.
- (d) Instant and cheap recharge (fuel refilling through cartridge replacement).

Although there are different types of fuel cells, only some of them are suitable for portable power applications. Polymer electrolyte membrane fuel cells ( $\mu$ PEMFCs), direct methanol fuel cells ( $\mu$ DMFCs), and solid oxide fuel cells ( $\mu$ SOFCs) have received attention for portable electronic applications [6].



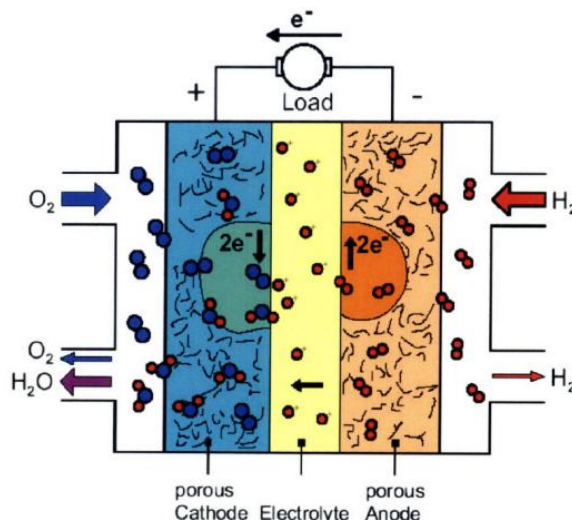
**Figure 1.4:** Comparison of specific energy and energy density of several portable energy sources, extracted from [3, 7]; \* indicates estimated values of systems still under development.

## 1.2. Fuel cells fundamentals

### 1.2.1. Basic principles

A fuel cell is an electrochemical device that directly converts a fuel into electrical energy via redox reactions. As an electrochemical converter, its efficiency is not limited by the Carnot's theorem such as in the case of heat engines. Therefore, efficiencies above 60 % can be expected for real devices

A basic structure of a hydrogen powered fuel cell is represented in **Figure 1.5**. While the manufacturing materials vary, the basic design is similar for all types of fuel cells: an ionic-conductor electrolyte is sandwiched between a porous anode and a porous cathode. The fuel,  $H_2$  in the case of **Figure 1.5**, passes through the porous anode and reacts catalytically at the anode-electrolyte interface. The electrolyte allows ions diffusing through it (positive or negative depending on the type of fuel cell) while preventing the conduction of electrons, which are forced to circulate outside the cell through an external load. Meanwhile, the oxidizer (usually  $O_2$  from air) diffuses through the porous cathode and reacts catalytically at the cathode-electrolyte interface. In the case of **Figure 1.5**, the oxidizer accepts the ions from the electrolyte and the free electrons from the external load, which closes the circuit. The by-products of the process leave the system [8, 9].



**Figure 1.5:** Schematic of hydrogen powered fuel cell operation, extracted from [9].

### 1.2.2. Types of fuel cell

While many types of fuel cells have been developed [10, 11], **Table 1.1** summarizes the main types of fuel cells that are identified as promising candidates for portable power generation: Proton Exchange Membrane Fuel Cell (PEMFC), Direct Methanol Fuel Cell (DMFC), and Solid Oxide Fuel Cell (SOFC).

**Table 1.1:** Fuel cell types suitable for portable applications. Their main features (electrolyte material, mobile ion, compatible fuels and typical operating temperature) are listed.

FC type	Electrolyte material	Mobile ion	Fuel compatibility	Operating temperature (°C)
PEMFC	Hydrated polymer	H <sup>+</sup>	H <sub>2</sub>	30-100
DMFC	Polymer	H <sup>+</sup>	CH <sub>3</sub> OH	50-120
SOFC	Ceramic	O <sup>2-</sup>	H <sub>2</sub> , C <sub>n</sub> H <sub>2n+2</sub>	600-1000

Among these three different FC types, the SOFC is chosen in this work for several reasons. First, SOFC shows higher electrical efficiency ( $\eta_{el}$  up to 65 %) compared to PEMFC and DMFC ( $\eta_{el} < 50$  %) [12]. Most importantly, due to high operation temperatures, SOFC can run using other fuels than hydrogen, such as hydrocarbons and alcohols, which are safe to handle and easy to storage [13]. When a fuel processing step is needed to convert hydrocarbon into hydrogen, carbon monoxide is produced. Carbon monoxide can be fed directly to a SOFC without poisoning the catalyst, while has dramatic effects on typical catalysts of PEMFC (noble metals). This feature allows removing the fuel purification step between the fuel processor and the SOFC [10]. Moreover, the solid oxide nature of the electrolyte makes SOFC more robust and mechanically stable than PEMFC or DMFC [14].

### 1.2.3. Thermodynamics of a fuel cell

The Nernst equation (1.1) defines the thermodynamic potential ( $E_r$ ) of the cell for the SOFC reaction (see **Table 1.2**) at a specific temperature ( $T$ ),

$$E_r = E_0 + \frac{RT}{2F} \ln \frac{p_{O_2}^{1/2} p_{H_2}}{p_{H_2O}} \quad (1.1)$$

where  $R$  is the ideal gas constant ( $8.31 \text{ J}\cdot\text{K}^{-1}\cdot\text{mol}^{-1}$ ),  $F$  is the Faraday constant ( $96485 \text{ C}\cdot\text{mol}^{-1}$ ),  $E_0$  is the standard cell potential,  $T$  is the temperature (K) and  $p$  is the partial pressure of reactants and products (Pa). This expression defines

the potential without current flowing through the device (Open Circuit Voltage, OCV).

**Table 1.2** shows the electrode and fuel cell reactions for SOFC. The corresponding electrode reduction potentials and subsequent cell potential at standard conditions are also included.

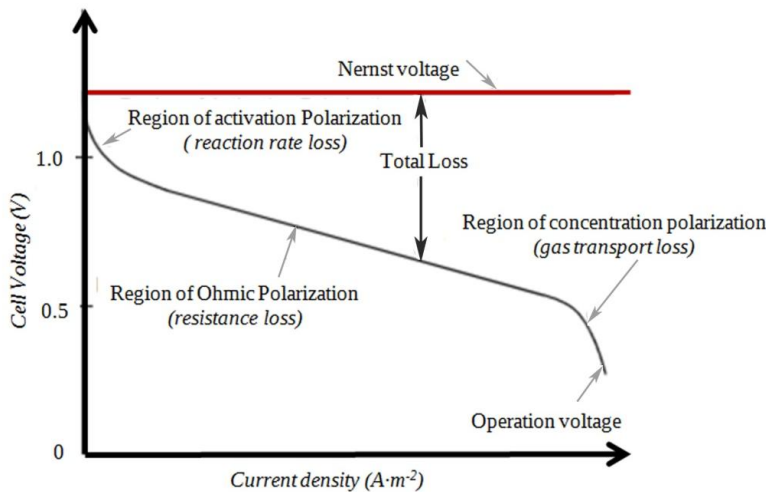
ELECTRODE	SEMI-REACTIONS		$E_0$ (V)
Anode	H <sub>2</sub> oxidation	$H_2(g) \leftrightarrow 2 H^+ + 2 e^-$	+0.00
Cathode	O <sub>2</sub> reduction	$\frac{1}{2} O_2(g) + 2 e^- \leftrightarrow O^{2-}$	+1.23
<b>CELL</b>	<b><math>\frac{1}{2} O_2(g) + H_2(g) \leftrightarrow H_2O(l)</math></b>		<b>+1.23</b>

The  $E_r$  can also be calculated from the specific half-cell potentials of each semi-reaction that take place in the electrodes, according to equation 1.2.

$$E_r = E_{reduction} - E_{oxidation} \quad (1.2)$$

#### 1.2.4. Overvoltage sources in a real SOFC

In practice, the real voltage (V) measured is lower than the standard cell potential due to several accumulative irreversible losses associated to different physico-chemical processes occurring under operation. As shown in **Figure 1.6**, three major losses can be described depending on the current flowing through the device, i.e. *activation losses*, *ohmic losses* and *concentration losses*.



**Figure 1.6:** Characteristic V-I curve of a fuel cell showing the ideal (Nernst) and real voltages, extracted from [8].



Therefore, the  $V$  seen by the load would be determined by equation 1.3,

$$V = E_r - \eta_{act} - \eta_{ohm} - \eta_{con} \quad (1.3)$$

where  $\eta_{act}$ ,  $\eta_{ohm}$  and  $\eta_{con}$  correspond to the *activation*, *ohmic* and *concentration losses* respectively.

- (a) *Activation losses* correspond to the activation energy of the electrochemical reactions at the electrodes. They result from complex surface electrochemical reaction steps; each of them has their own reaction rate and activation energy. They depend on the electro-catalyst material, the microstructure and current density.
- (b) *Ohmic losses* are caused by ionic resistance in the electrolyte and electrodes, electronic resistance in the electrodes, current collectors and electronic contact resistances. Ohmic losses increase linearly with the current density. They depend on materials, stack geometry and temperature.
- (c) *Concentration losses* are a result of mass transport limitation rates of the reactants and depend strongly on the current density, reactant activity, and electrode microstructure.

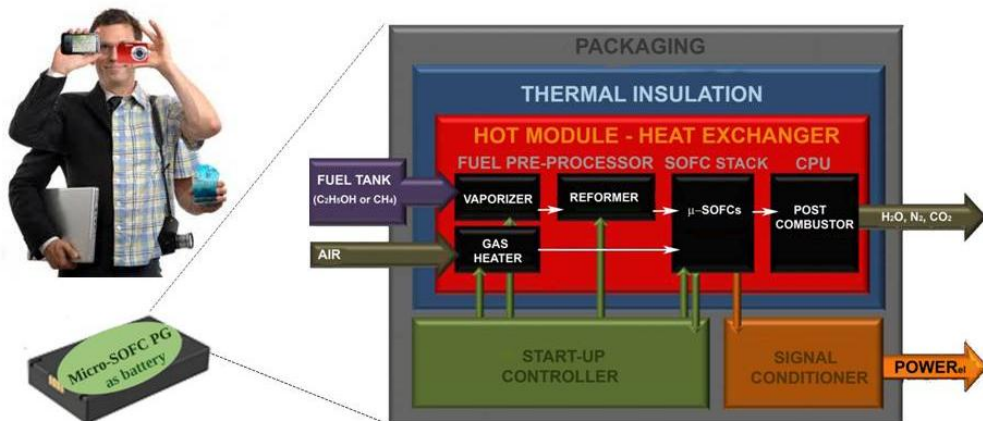
All these overvoltage sources represent the major losses of any fuel cell. Minimizing them is therefore fundamental for increasing the performance of the final device in terms of efficiency and power density generated.

### 1.3. Micro SOFC power generator

#### 1.3.1. Micro SOFC power generation technology

Although micro fuel cells represent a new field (starting only 25 years ago [15-17]), they have received increasing attention by the scientific and industrial communities [18-23]. In this sense, the first prototypes have been already commercialized based on polymeric membranes (e.g.  $\mu$ DMFC PG from Toshiba, Medis or Horizon). However, despite the promising future of  $\mu$ SOFC technology, the first miniaturized SOFC-based Power Generator ( $\mu$ SOFC PG) is not yet commercially available.  $\mu$ SOFCs present several challenges mostly associated with their high operation temperature (above 500 °C). To the best of our knowledge, only two initiatives have been devoted to the development of an entire  $\mu$ SOFC PG: the ONEBAT project led by ETH-Zurich on one hand [24], and the creation of Nectar Mobile Power <sup>TM</sup> (INTEL-MIT joint company) on the other hand [5].

The main components of a  $\mu$ SOFC PG are depicted in **Figure 1.8**: (a) a  $\mu$ SOFC stack for power generation; (b) a fuel pre-processor unit (FPU) for hydrogen production from a hydrocarbon fuel (if necessary); (c) a catalytic post-combustion unit (CPU) for exhaust gas processing; (d) a heat management unit consisting of a heat exchanger (HX) and a thermal insulation (INS) that defines a hot module (HM).



**Figure 1.8:** Sketch of a whole  $\mu$ SOFC PG including the main elements developed for this thesis.

The  $\mu$ SOFC PG operation is described as: fuel and air are fed separately into the FPU. The fuel is heated (and vaporized in the case of liquid fuels) in the  $\mu$ vaporizer. A first fraction of fuel is chemically converted into simpler molecules in the  $\mu$ reformer, i.e.  $H_2$ , CO and  $CO_2$ . In parallel, air is heated and provided to the cathode side of the  $\mu$ SOFCs. Hydrogen and air react in the fuel cell membrane, producing electrical power and heat. The unreacted fuel mixes with the remaining air in the CPU where is completely burned. Finally, clean exhaust leaves the device.

### 1.3.2. Main requirements of a micro SOFC PG

The major issues to overcome for developing a reliable and efficient  $\mu$ SOFC PG are:

#### ❖ Overall design to fulfill thermal management requirements

Thermal management of a  $\mu$ SOFC PG is critical. On one hand, in order to efficiently operate, the system must be thermally self-sustained in the steady state, i.e. the reforming/fuel cell zones have to remain at high temperatures (above 500 °C) while the outer surface should be kept closed to room temperature [5]. Given the enhanced heat transfer in micro systems (via conduction, convection and radiation), delivering those temperatures at low electrical power devices and in a small package requires an excellent insulation and a very compact integration of all the components.

On the other hand, the start-up process has to allow reaching the operation temperature of the reforming/fuel cell zones quickly and with minimum energy consumption, especially for portable applications [25]. In this sense, lower operating temperatures and/or reduced thermal masses improve the overall  $\mu$ SOFC PG efficiency due to a lower energy demand during the start-up process [26]. Usually, an auxiliary power source is used to cover the start-up step.

#### ❖ Fuel processing unit

Hydrogen is the best performance option amongst combustible fuels for  $\mu$ SOFC PGs, but unfortunately storing hydrogen on-board can be difficult, dangerous and inefficient. A number of strategies have been investigated including cryogenic storage, compression in high pressure vessels, adsorption within carbon nanostructures, and chemical binding in reversible and non-

reversible metal hydrides [27], but only metal hydride-based systems have been proven to efficiently supply on-board hydrogen [28].

As an alternative to hydrogen storage, direct processing of hydrocarbons in the fuel cell has also been studied. Direct methanol fuel cells generate power by directly converting liquid methanol into electricity. However, their efficiencies are behind those theoretically achievable in high-temperature SOFCs and even below existing batteries [8].

Another interesting approach is to chemically convert a hydrocarbon fuel into hydrogen via a fuel processing unit within the system. This chemical process is called **reforming**. Hydrocarbons are preferred because they are safe and easy to handle, and provide a high-energy density at low cost [29]. The energy characteristics of different hydrocarbon fuels are listed below (**Table 1.3**).

**Table 1.3:** Comparison of hydrogen to other hydrocarbon fuels.

Fuel	Mole mass (g/mole)	Density (kg/m <sup>3</sup> )	H <sub>2</sub> -content (mole H <sub>2</sub> /mole)	H <sub>2</sub> -density (kg H <sub>2</sub> /m <sup>3</sup> )	HHV (MJ/kg)	Energy per volume (MJ/m <sup>3</sup> )
Methanol (CH <sub>3</sub> OH)	32	792	0.125	99	22.7	1.78x10 <sup>3</sup>
Ethanol (C <sub>2</sub> H <sub>5</sub> OH)	46	789	0.130	103	29.7	2.34x10 <sup>3</sup>
Dimethylether (CH <sub>3</sub> OCH <sub>3</sub> )	46	666	0.130	87	31.7	2.11x10 <sup>3</sup>
Propane (C <sub>3</sub> H <sub>8</sub> )	44	1.88 <sup>(1)</sup>	0.182	0.34	50.2	94.38
Natural gas (CH <sub>4</sub> , alkanes, CO <sub>2</sub> )	19	0.90 <sup>(2)</sup>	0.211	0.19	52.23	47.00
Methane (CH <sub>4</sub> )	16	0.72 <sup>(2)</sup>	0.250	0.23	55.5	39.96
Hydrogen <sup>(3)</sup> (H <sub>2</sub> )	2	70	1.000	70	141.9	9.93

<sup>(1)</sup> NTP - Normal Temperature and Pressure - is defined as air at 20°C and 1 atm

<sup>(2)</sup> STP - Standard Temperature and Pressure - is defined as air at 0°C and 1 atm

<sup>(3)</sup> For comparison

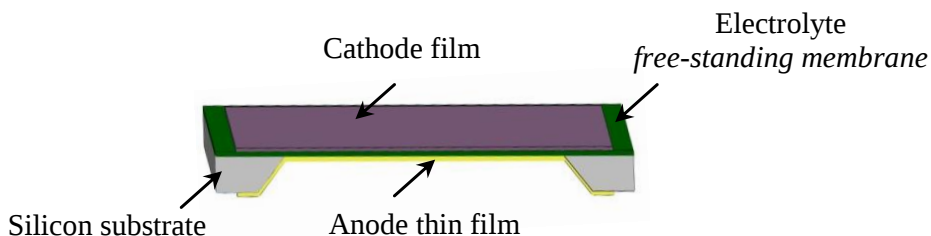
Any of these hydrocarbon fuels contains more energy per cubic meter (up to 235 times higher) than it is contained in the same volume of liquefied hydrogen. Liquid fuels present some advantages as energy carriers. They are liquid under normal temperature and pressure conditions, and are nontoxic and easy to synthesize. Furthermore, they have higher energy per unit volume

compared with gas fuels. Gas fuels such as propane, natural gas or methane have greater Higher Heating Values (HHV) and higher H<sub>2</sub>-content than liquid fuels. Moreover, they have been safely used over the last decades, e.g. in lighters, cooking, lighting, etc. These gas fuels are safe mainly due to their autoignition point at high temperatures (470 °C for C<sub>3</sub>H<sub>8</sub>, 580 °C for natural gas and 595 °C for CH<sub>4</sub>) [5].

As previously mentioned, the use of hydrogen in a portable device has important safety issues due to likely occurring leakages and low ignition energy. So, the unreacted hydrogen in the  $\mu$ SOFCs has to be eliminated to assure a safe operation at high temperatures. In addition, some hydrocarbon byproducts have harmful effects on environment and health. The most extended methodology to eliminate these undesirable gases is combustion by using a burner or a catalytic converter (flameless process). In both cases, the combustion minimizes the emissions of carbon monoxide (CO) and nitrogen oxides (NO<sub>x</sub>). Consequently, the fuel processing unit is usually subdivided into a pre-processor for hydrocarbon fuel reforming to produce hydrogen and a post-combustor for converting hydrogen and hydrocarbons from the exhaust into water and carbon dioxide.

### ❖ Low thermal mass $\mu$ SOFCs based on micro- and nanotechnology

The possibility of batch production is crucial for the scalability and low fabrication costs. If the fuel cell fabrication is integrated in silicon, a set of mature and well-known techniques and processes are available for fabricating hundreds of micro-devices in parallel with a high reproducibility and reliability [30]. As is represented in **Figure 1.7**, the most extended design for  $\mu$ SOFC devices is based on the fabrication of a thin free-standing membrane, an electrolyte thin film covered at each side by an anode and a cathode (electrodes), and supported on low thermal mass silicon platforms [6, 31-34].



**Figure 1.7:** Schematic view of a planar free-standing  $\mu$ SOFC.

Moreover, as previously mentioned,  $\mu$ SOFCs operate at high temperatures, thus the required thermal cycling raises the issue of materials compatibility and stability in order to minimize the thermal expansion stresses [12]. Furthermore, the most critical figure of merit for a fuel cell is the maximum power density. In order to improve this figure at any given temperature, different aspects need to be addressed like the electrode performance, which has to be improved by increasing the density of active electrode sites and/or by using more catalytically active materials [35], as well as, the electrolyte resistance, which must be minimized by either reducing the thickness and/or using more ionic conductor material [36].

#### ❖ **Auxiliary systems**

Several auxiliary components named as “Balance of Plant” (BoP) are needed to complete the top-level requirements of a  $\mu$ SOFC PG. The BoP should provide the Power Generator device with pumps to supply fuels which minimize the pressure drop within the system, valves to adjust the fuel flow, heaters for the start-up, closed-loop temperature controllers and power converters to maximize the electrical power output of the system. All of these operations should be managed by a controller which consumes electrical power, thus the  $\mu$ SOFC PG should produce “extra” power using additional fuel and generating additional heat.

### 1.4. Objectives and approach

The overall goal of this thesis was to design, fabricate and test the main components of a novel  $\mu$ SOFC power generator as a first step to develop a complete device in the near future. The adopted approach is based on employing MEMS fabrication methods to **miniaturize  $\mu$ SOFCs in silicon technology and high energy density hydrocarbons** as fuels. The  $\mu$ SOFC PG was designed to supply 1W of electrical energy in a small volume (10-20 cm<sup>3</sup>). Additional components like the fuel tank, fluidics and electrical connections are out of the scope of this thesis.

This work intends to cover some of the issues and requirements described in previous sections to advance in the final optimization of a  $\mu$ SOFC PG and it is expected that the results achieved during these four years may serve as a solid background for future generations of  $\mu$ SOFC PG of the *Nanoionics and Fuel Cells group* in the Advanced Materials Department at IREC. It is worth mentioning that this work has been carried out in collaboration with IMB-CNM (CSIC), INTE (UPC), Imperial College and University of Castilla-La Mancha.

This thesis is organized as described in the following list,

- **Chapter II** describes the fabrication, characterization and experimental techniques used during this thesis. *Section 2.2* is devoted to silicon micro-technology and MEMS fabrication techniques. Thin film fabrication by Pulsed Laser Deposition (PLD) is introduced in more detail in *Section 2.3*. The synthesis routes of the catalysts used in the fuel processing unit are described in *Section 2.4*. The different characterization techniques are also briefly described in *Section 2.5*. Finally, the experimental set-ups and the methodology for thermal modeling and simulating are briefly explained in *Section 2.6* and *Section 2.7*, respectively.
- Computational Fluid Dynamics (CFD) was used to study the thermal management strategies at system level and is presented in **Chapter III**. A new compact design of a vertically stacked device was analyzed by a 3D thermo-fluidic model and a finite-volume method as detailed in *Section 3.3* and *3.4*. The aim was to prove the feasibility of a thermally self-sustained regime (*Section 3.5.1*) and a rapid and low-power consuming start-up of the  $\mu$ SOFC PG (*Section 3.5.2*).

- Using the insight gained from the thermal management analysis in Chapter III, a micro-fuel processor was developed to efficiently perform high-temperature fuel-reforming reactions (**Chapter IV**). The design and fabrication process of a bulk  $\mu$ reformer are outlined in *Section 4.2*. Its catalytic activity was tested and discussed for Ethanol Steam Reforming (ESR) and Methane Dry Reforming (MDR) reactions (*Section 4.3*). A thermally optimized suspended  $\mu$ reformer was designed and fabricated (*Section 4.4*). The catalytic activity was tested as a standalone device for ESR in *Section 4.5*.
- **Chapter V** introduces the design and fabrication of a combustion unit. A  $\mu$ post combustor based on a bed micro-reactor was built, hermetically sealed with a glass cover and filled with a metal-mesoporous catalyst. The characterization of the mesoporous catalyst is described in *Section 5.2*. A synergic effect of multi-component metal oxides (nickel and copper oxides) impregnated in the mesoporous structures was studied in *Section 5.3*. The fabrication and experimental results of the  $\mu$ post combustor for the catalytic hydrogen/air reaction are presented in *Section 5.4*.
- **Chapter VI** focuses on the fabrication and characterization of ceramic thin films as functional layers integrated in silicon-based  $\mu$ SOFCs. As is described in *Section 6.2*, two electrolytes were studied, namely, 3 mol% and 8 mol% Ytria Stabilized Zirconia (3YSZ and 8YSZ, respectively). Pinhole-free electrolytic membranes were achieved in both cases. Moreover, ceramic thin films electrodes were fabricated and characterized, i.e. porous  $\text{La}_{0.6}\text{Sr}_{0.4}\text{CoO}_{3-\delta}$  (LSC) in *Section 6.3.1*, dense  $\text{La}_{0.8}\text{Sr}_{0.2}\text{MnO}_{3+\delta}$  (LSM) in *Section 6.3.2*,  $\text{Ce}_{0.8}\text{Gd}_{0.2}\text{O}_{1.9-\delta}$  (CGO) in *Section 6.4.1* and  $\text{Sr}_2\text{Fe}_{1.5}\text{Mo}_{0.5}\text{O}_{6-\delta}$  (SFM) in *Section 6.4.2*. The performance of a full ceramic  $\mu$ SOFC, consisting of LSC as a cathode, 8YSZ as an electrolyte and CGO as an anode is presented and discussed in *Section 6.5*.



Three additional appendices are included in this thesis. They represent preliminary studies carried out to complement the previously presented work:

- **Appendix A** describes the heat transfer analysis within the  $\mu$ SOFC in order to complete the thermal management study presented in **Chapter III**.
- **Appendix B** introduces the design and fabrication process of a  $\mu$ vaporizer.
- **Appendix C** shows the fabrication of porous metallic layers by means of dealloying technique as an alternative option for current collection in free-standing membranes.

## References

- [1] International Data Corporation, Worldwide smart connected device forecast: 2012–2017 (2014).
- [2] Harrop, P. & Das, R. Energy harvesting and storage for electronic devices 2009-2019, IDTechEx Technical Report (2009).
- [3] Pistoia, G. *Batter. Portable Devices*, (2005).
- [4] Tarascon, J.M. & Armand, M. Issues and challenges facing rechargeable lithium batteries. *Nature* **414**, 359–367 (2001).
- [5] Schaevitz, S. B. Powering the wireless world with MEMS. *Proc. SPIE* **8248**, 824802–824815 (2012).
- [6] International Electrotechnical Commission, Fuel cell technologies – Part 6: Micro fuel cell power systems, (IEC 62282-6-100, 2010).
- [7] Evans, A., Bieberle-Hütter, A., Rupp, J. L. M. & Gauckler, L. J. Review on microfabricated micro-solid oxide fuel cell membranes. *J. Power Sources* **194**, 119–129 (2009).
- [8] E.G.G. Services, Fuel cell handbook, 7th ed., (U.S. Dept. of Energy, 2004).
- [9] Carrette, L., Friedrich, K. A. & Stimming, U. Fuel Cells – Fundamentals and Applications. *Fuel Cells* **1**, 5–39 (2001).
- [10] Steele, B. C. H. & Heinzel, A. Materials for fuel-cell technologies. *Nature* **414**, 345–352 (2001).
- [11] Kirubakaran, A., Jain, S. & Nema, R. K. A review on fuel cell technologies and power electronic interface. *Renew. Sustain. Energy Rev.* **13**, 2430–2440 (2009).
- [12] Huang, K. & Goodenough, J. B. in *Solid Oxide Fuel Cell Technol.* (eds. Huang, K. & Goodenough, J. B.) 1–9 (Woodhead Publishing, 2009).
- [13] Singhal, S., Singhal, S. C. & Kendall, K. *High-temperature Solid Oxide Fuel Cells: Fundamentals, Design and Applications: Fundamentals, Design and Applications.* (Elsevier Science, 2003).
- [14] Huijsmans, J. P. P. Ceramics in solid oxide fuel cells. *Curr. Opin. Solid State Mater. Sci.* **5**, 317–323 (2001).
- [15] Tsai, T. & Barnett, S. A. Effect of LSM-YSZ cathode on thin-electrolyte solid oxide fuel cell performance. *Solid State Ionics* **93**, 207–217 (1997).
- [16] Dyer, C. K. Replacing the battery in portable electronics. *Sci. Am.* **281**, 88–93 (1999).
- [17] Will, J., Mitterdorfer, A., Kleinlogel, C., Perednis, D. & Gauckler, L. J. Fabrication of thin electrolytes for second-generation solid oxide fuel cells. *Solid State Ionics* **131**, 79–96 (2000).

- [18] Xie, C., Pavio, J., Hallmark, J., Bostaph, J. & Fisher, A. Key requirements of micro fuel cell system for portable electronics. *Energy Convers. Eng. Conf. 2002. IECEC '02. 2002 37th Intersoc.* 603–606 (2002).
- [19] Bieberle-Hütter, A. *et al.* A micro-solid oxide fuel cell system as battery replacement. *J. Power Sources* **177**, 123–130 (2008).
- [20] Flipsen, S. F. J. Power sources compared: The ultimate truth? *J. Power Sources* **162**, 927–934 (2006).
- [21] Kundu, A. *et al.* Micro-fuel cells—Current development and applications. *J. Power Sources* **170**, 67–78 (2007).
- [22] Morse, J. D. Micro-fuel cell power sources. *Int. J. Energy Res.* **31**, 576–602 (2007).
- [23] La O' G. J., In, H. J., Crumlin, E., Barbastathis, G. & Shao-Horn, Y. Recent advances in microdevices for electrochemical energy conversion and storage. *Int. J. Energy Res.* **31**, 548–575 (2007).
- [24] Evans, A. *et al.* Micro-solid oxide fuel cells: status, challenges, and chances. *Monatshefte für Chemie - Chem. Mon.* **140**, 975–983 (2009).
- [25] Brett, D. J. L., Atkinson, A., Brandon, N. P. & Skinner, S. J. Intermediate temperature solid oxide fuel cells. *Chem. Soc. Rev.* **37**, 1568–1578 (2008).
- [26] Goodenough, J. B., Oxide-ion Electrolytes. *Annu. Rev. Mater. Res.* **33**, 91–128 (2003).
- [27] Su, P.C., Chao, C.C., Shim, J. H., Fasching, R. & Prinz, F. B. Solid oxide fuel cell with corrugated thin film electrolyte. *Nano Lett.* **8**, 2289–2292 (2008).
- [28] Garbayo, I., Pla, D., Morata, A., Fonseca, L., Sabaté, N. & Tarancón, A. Full ceramic micro solid oxide fuel cells: Towards more reliable MEMS power generators operating at high temperatures. *Energy Environ. Sci.* **7**, 3617–3629 (2014)
- [29] Kerman, K., Lai, B. K. & Ramanathan, S. Nanoscale Compositionally Graded Thin-Film Electrolyte Membranes for Low-Temperature Solid Oxide Fuel Cells (Adv. Energy Mater. 6/2012). *Adv. Energy Mater.* **2**, 655 (2012).
- [30] Stutz, M. J., Grass, R. N., Loher, S., Stark, W. J. & Poulidakos, D. Fast and exergy efficient start-up of micro-solid oxide fuel cell systems by using the reformer or the post-combustor for start-up heating. *J. Power Sources* **182**, 558–564 (2008).
- [31] Tarancón, A. Strategies for Lowering Solid Oxide Fuel Cells Operating Temperature. *Energies* **2**, 1130–1150 (2009).
- [32] Schlapbach, L. & Züttel, A. Hydrogen-storage materials for mobile applications. *Nature* **414**, 353–358 (2001).

[33] Fakioglu, E., Yürüm, Y. & Veziroglu, T.N. A review of hydrogen storage systems based on boron and its compounds. *Int. J. Hydrogen Energy* **29**, 1371 (2004).

[34] Brown, L. F. A comparative study of fuels for on-board hydrogen production for fuel-cell-powered automobiles. *Int. J. Hydrogen Energy* **26**, 381–397 (2001).

[35] Madou, M.J., *Fundamentals of microfabrication*, (CRC Press, 1997)

[36] Fleig, J., Tuller, H. L. & Maier, J. Electrodes and electrolytes in micro-SOFCs: a discussion of geometrical constraints. *Solid State Ionics* **174**, 261–270 (2004).



## **II. EXPERIMENTAL METHODS**



<b>2.1. Introduction.....</b>	<b>29</b>
<b>2.2. Microfabrication technology.....</b>	<b>31</b>
2.2.1. MEMS fabrication.....	31
2.2.2. Processes for micromachining.....	31
2.2.2.1. Lithography.....	32
2.2.2.2. Etching.....	33
2.2.2.3. Anodic bonding.....	37
2.2.2.4. Film growth/deposition.....	39
<b>2.3. Pulsed laser deposition.....</b>	<b>42</b>
2.3.1. Effect of main deposition conditions on PLD films.....	42
2.3.2. Wafer level integration: large area PLD.....	44
2.3.3. Special issues related to large area PLD films.....	46
<b>2.4. Catalyst synthesis routes.....</b>	<b>49</b>
2.4.1. Hydrocarbon reforming catalysts.....	49
2.4.2. Catalyst for hydrogen combustion.....	50
<b>2.5. Structural characterization.....</b>	<b>52</b>
2.5.1. Optical microscopy.....	52
2.5.2. Scanning electron microscopy.....	53
2.5.3. Transmission electron microscopy.....	54
2.5.4. X-ray fluorescence.....	54
2.5.5. Reflectometry.....	55
2.5.6. X-ray diffraction.....	56
2.5.7. Gas chromatography.....	57
2.5.8. Thermo gravimetric analysis.....	57
2.5.9. Differential scanning calorimetry.....	58
2.5.10. Mass spectroscopy.....	58
2.5.11. Impedance spectroscopy.....	59
2.5.12. Electrical characterization.....	61
<b>2.6. Functional characterization.....</b>	<b>63</b>
2.6.1. Hydrocarbon reforming reactions.....	63
2.6.2. Catalytic combustion of hydrogen.....	65
2.6.3. Electrochemical $\mu$ SOFC measurement.....	66
<b>2.7. Simulations and modeling.....</b>	<b>68</b>





## 2.1. Introduction

The development of a  $\mu$ SOFC PG requires making compatible the micro fabrication technologies and SOFC technologies. The configuration of the  $\mu$ SOFC PG presented in **Chapter I** was based on several components that have to be integrated and enable specific functions into the system (e.g. the  $\mu$ SOFC stack, the FPU and the catalytic CPU). Thus, one of the most important challenges in this thesis was to ensure the compatibility between the functional layers of  $\mu$ SOFCs, the catalytic materials used in the FPU and CPU, and the needed micro fabricating processes to obtain each one of the components.

**The aim of this chapter** is to present the experimental methods and techniques used in this work for both fabrication and characterization of the main  $\mu$ SOFC PG components. For portable electronic applications, semiconducting substrates such as silicon are preferred, since they enable easy handling of the micro device through several fabrication steps and easy implementation in the integrated circuit industry [1]. So, the  $\mu$ SOFC PG components developed in this thesis were based on silicon. A general view of the silicon micro technology and its related techniques used are presented in *Section 2.2*.

*Section 2.3* is specifically devoted to the Pulsed Laser Deposition (PLD) technique used to deposit the functional layers of the  $\mu$ SOFCs, i.e. the electrolyte and the electrodes in thin film form. This technique has been successfully used to deposit a large amount of complex polycrystalline oxides since it allows excellent stoichiometric transferability from a bulk material (target) to the thin film [2]. Classical SOFC materials were chosen, i.e. YSZ as electrolyte [3-6], and CGO [7-9] and LSC [10] as ceramic electrodes. Furthermore, the applicability of SFM as a novel electrode material for symmetrical  $\mu$ SOFCs [11, 12] was proven by using PLD.

*Section 2.4* details the synthesis routes followed to prepare the catalysts used in the FPU and CPU. A brief explanation of the multi-step procedures, from the precursors to the final catalysts, is introduced. According to prior knowledge acquired in the catalysis field by Llorca and co-workers from INTE-UPC [13, 14], the Pd-Rh/CeO<sub>2</sub> catalyst system was chosen to study the Ethanol Steam Reforming (ESR) and Methane Dry Reforming (MDR) reactions. Moreover, a mesoporous backbone structure infiltrated with metal oxides was chosen as catalyst for the CPU. These new materials have recently

## **CHAPTER II. Experimental methods**

---

proven that they enhance catalytic activity and are stable at high temperature [15, 16]. In particular, nickel and copper oxides impregnated in CGO mesoporous were synthesized.

Overall concepts related to the structural characterization techniques are introduced in *Section 2.5.*; for example, optical microscopy to study the microstructure of the fabricated silicon-based components, x-ray diffraction to determine the crystallization temperature of the CeO<sub>2</sub>-based catalyst, or scanning electron microscopy to characterize the thin film functional layers of the  $\mu$ SOFCs.

The experimental setups to prove the functionality of the fabricated devices are outlined in *Section 2.6.* A first setup was developed to study the ESR and MDR in a bulk  $\mu$ reformer depending on the temperature and fuel loading. A second setup was used to test the  $\mu$ reformer as a standalone device. Another setup was developed to study the catalytic activity of CuO-NiO/CGO mesoporous catalyst system in the CPU. Finally, the electrochemical measurements of the  $\mu$ SOFCs were carried out in a ProboStat™ station.

Finally, in the *Section 2.7* there is a brief description of Computational Fluidic Dynamics (CFD) analysis. A specific design of the  $\mu$ SOFC PG was defined and its thermo-fluidic behavior was studied by developing a Finite Volume Model (FVM). For this purpose, computer-aided design and multiphysics software (Solidworks and ANSYS v.13, respectively) were used.

## 2.2. Microfabrication technology

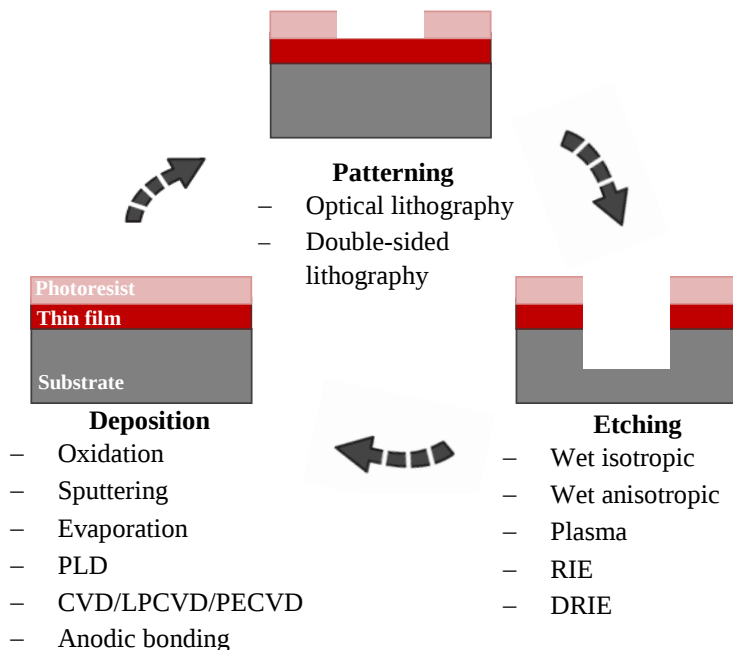
One of the most promising approaches for the miniaturization of SOFC-based power devices is focused on the monolithic integration of functional components in silicon technology. This approach ensures a high reproducibility and reliability, economical mass production and easy integration in the semiconductor integrated circuit industry.

### 2.2.1. MEMS fabrication

Micro-Electro-Mechanical Systems (MEMS) can be defined as the set of miniaturized devices and structures that combine electrical and mechanical elements and are developed using the techniques of microfabrication. Two main objectives are pursued on MEMS fabrication: miniaturization and multiplicity. By miniaturizing, new compact and quick-response devices are manufactured offering to the customer easy-handling products; while multiplicity refers to batch fabrication, where thousands of devices are fabricated in parallel at wafer level (i.e. 4'' or 100 mm silicon substrates) by standard processes.

### 2.2.2. Processes for micromachining

The objective of this section is to describe the silicon processes used in the microfabrication of components that integrate the  $\mu$ SOFC PG. As shown in **Figure 2.1**, silicon micromachining is based on a broad portfolio of fabrication processes grouped in three major categories: (a) *film deposition or growth*, where a new material is added on top of a surface; (b) *patterning*, where a pattern is transferred from a master to a resin covering a substrate, via a lithography process; and (c) *etching*, where an amount of material is removed, usually using a mask and following a pattern defined by a previous lithography step [17]. The process flow was repeated until completion of the microstructures.



**Figure 2.1:** Illustration of the basic processes found in silicon micromachining used in this work, adapted from [17]

### 2.2.2.1. Lithography

Lithography is a method to accurately transfer a pattern to a substrate. One of the most extended lithographic techniques is the photolithography, which is based on three sequential steps:

(a) *Spin-coating of a resin*, where a photoresist is applied by spin-coating on a wafer resulting in a thin and homogeneous film (thickness vary between 0.5  $\mu\text{m}$  and 10  $\mu\text{m}$ ).

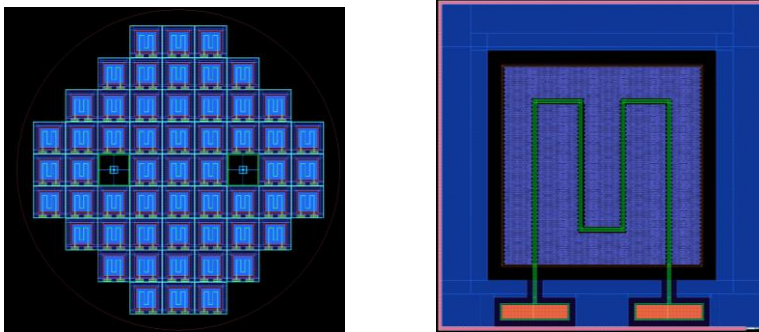
(b) *Optical exposure*, where the coated wafer is irradiated by UV light through a mask to transfer a pattern onto the resin.

(c) *Development*, where the resin is removed on the desired zones by dissolving it in a proper solvent, i.e. developer. Then the patterned design is rendered visible on the resin and can be used as a mask for the next process.

There are two different types of resins depending on its polarity: positive and negative. If the resin is positive, the illuminated zones are eliminated; on the contrary if the resin is negative the unexposed zones are removed. A sensitizer agent prevents the dissolution of the exposed (or

unexposed) zones. Moreover, two kinds of masks can be also distinguished, i.e. light field masks where the pattern to be transferred appears opaque over a transparent glass substrate, and dark field masks where the pattern is transparent on a dark substrate (the glass substrate is completely covered with a metal film, usually chromium).

❖ *In this work*, contact photolithography was employed using HIPR6512 positive photoresist. The masks were fabricated using soda-lime glass as substrate and chromium as metal film. Both types of masks, i.e. dark and light field, were used for the several microfabrication process flows. As an example, **Figure 2.2** shows the design of a mask used in the fabrication of the suspended  $\mu$ reformer.



**Figure 2.2:** Design of the photolithographic masks for the suspended  $\mu$ reformer, (a) wafer-level view and (b) single device.

#### 2.2.2.2. Etching

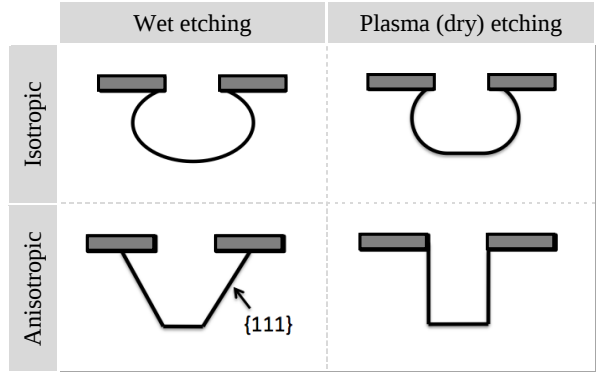
After a photolithographic step, the pattern defined on the resin can be selectively transferred to the substrate mainly by two ways: adding any material on top of it, or removing part of the bulk material from the exposed zones. Etching refers to this second option, where the pattern is transferred by either chemical or physical removal of material from the layer underneath.

Four different types of etch methods exist depending on the resulting profiles. Further, these four methods can be classified in two groups, as is depicted in **Figure 2.3**. The first group is divided in function of the etch medium:

- (a) *Wet etching* uses etchants in aqueous solutions
- (b) *Dry etching* involves reactant gases in low pressure plasma.

On the other hand, the second group is split up in:

- (c) *Isotropic etching* which uniformly eliminates material in all directions, resulting in rounded cross-sectional features.
- (d) *Anisotropic etching* that etches in one crystallographic direction preferentially over other directions. This process is used to produce trenches and cavities aligned with crystallographic planes.



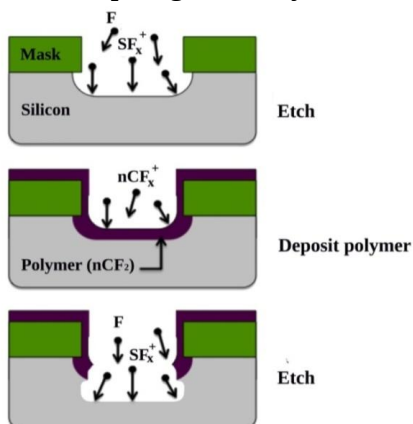
**Figure 2.3:** Cross-sectional profiles resulting from four different types of etch methods; adapted from [17].

The selection of a suitable etching method depends on the final shape desired and also on the selectivity of the process (etch rate ratio between the mask and the substrate to be etched).

Dry etching techniques

On a plasma (or dry) etching, the material is etched by a gas phase, either physically by inert ion bombardment, chemically by a chemical reaction, or both. The process involves the generation of chemically reactive neutral atoms (e.g., F, Cl) and energetic ions (e.g., SF<sub>x</sub><sup>+</sup>) that are accelerated under the effect of an electric field. The reactive species are formed by the collision of molecules in the reactant gas (e.g., SF<sub>6</sub>, CF<sub>4</sub>, Cl<sub>2</sub>, CClF<sub>3</sub>) with a cloud of energetic electrons excited by an electric field. When the etch process is purely chemical, powered by the spontaneous reaction of neutrals with target material, it is referred to as plasma etching. But if the ion bombardment to the material surface plays a synergistic role, the process is referred to as Reactive Ion Etching (RIE). Due to the vertical delivery of reactive ions, RIE in general produces anisotropic etch profiles, but some types of RIE system, e.g. Inductively Coupled Plasma (ICP) RIE, generate high plasma densities by a magnetic field and the etch profiles tend to be more isotropic.

Deep Reactive Ion Etching (DRIE) is a highly anisotropic etch process patented by Robert Bosch GmbH capable of vertically etching high-aspect-ratio trenches at rates substantially larger than the typical values of traditional plasma and RIE etchers ( $0.1\text{-}0.5\ \mu\text{m}\cdot\text{min}^{-1}$ ). The method combines etch and deposition steps sequentially. The etch step uses  $\text{SF}_6$  which supplies fluorine radicals to etch silicon (see **Figure 2.4**). In the deposition step, a fluorocarbon polymer made of a chain of  $\text{CF}_2$  groups about 10 nm thick is plasma-deposited using  $\text{C}_4\text{F}_8$  as precursor gas. In the following etch step, the ions ( $\text{SF}_x^+$ ) enhance the effect of fluorine radicals removing the protective polymer at the bottom of the trench, while the film remains relatively intact along the sidewalls. The repetitive alternation of etch and passivation steps results in a very directional etch at rates from 1 to over  $15\ \mu\text{m}\cdot\text{min}^{-1}$ , depending on the recipe and machine. A limitation of DRIE process is the dependence of the etch rates on the aspect ratio (ratio of height to width  $\leq 20$ ) of the trench. Furthermore, the etch rate is limited by the flux reactants and drops significantly for narrow trenches.



**Figure 2.4:** The process cycles of DRIE between an etch step using  $\text{SF}_6$  gas and a polymer deposition step using  $\text{C}_4\text{F}_8$ .

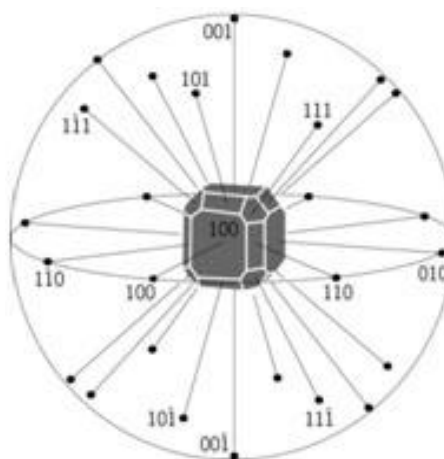
❖ *In this work*, RIE and DRIE etching techniques were used in several fabrication flows; e.g., RIE was used for releasing the electrolyte free-standing membranes of  $\mu\text{SOFCs}$  by etching the silicon nitride and silicon oxide sacrificial layers (see details in **Chapter VI**). In this case, 21 sccm  $\text{CHF}_3$  plus 6 sccm  $\text{O}_2$  as species etchants, RF power of 150 W and low chamber pressure (50 mTorr) were used by a RIE Oxford 80Plus equipment placed at the Clean Room of the Autonomous University of Barcelona (UAB). Also RIE Alcatel AMS equipment placed at IMB-CNM's Clean Room was used to eliminate the dielectric layers in specific zones of the  $\mu\text{reformer}$ . On the other hand, DRIE



process (Alcatel 601 equipment located at IMB-CNM's Clean Room) was used to define the vaporizer's micro pillars (details in **Appendix B**) and the vertical channels in the  $\mu$ reformer (details in **Chapter IV**). The etch step of DRIE typically takes about 7 seconds and the deposition step 3 seconds.

### Wet etching techniques

Wet etching is based on the immersion of the substrate on a chemical solution to etch it by dissolving the target material. Compared to dry etching techniques, wet chemical etching provides higher selectivity being often faster. The high selectivity is enhanced if a proper mask is used for a specific etchant. The main requirement to be a good mask is a good resistance and stability during the wet etching process, being its etch rate lower than the material to be etched. Typical masks for wet etching processes of silicon are photoresists,  $\text{SiO}_2$  and  $\text{Si}_3\text{N}_4$ . Depending on the etchant, silicon wet etching can be orientation dependent (anisotropic) or independent (isotropic). The most common isotropic wet etchants for silicon is named HNA, a mixture of Hydrofluoric acid (HF), Nitric acid ( $\text{HNO}_3$ ) and Acetic acid ( $\text{CH}_3\text{COOH}$ ), although water may replace the acetic acid. In the chemical reaction, the nitric acid oxidizes silicon, which is then etched by the hydrofluoric acid. The etch rate of silicon in HNA can vary from  $0.1$  to  $100 \mu\text{m}\cdot\text{min}^{-1}$  depending on the proportions used in the mixture. Due to the particular and well-known silicon crystal structure, i.e. a diamond type cubic structure (see **Figure 2.5**), silicon anisotropic wet etchants are also widely used for micromachining silicon substrates because their etch rates depend on the crystallographic orientation.



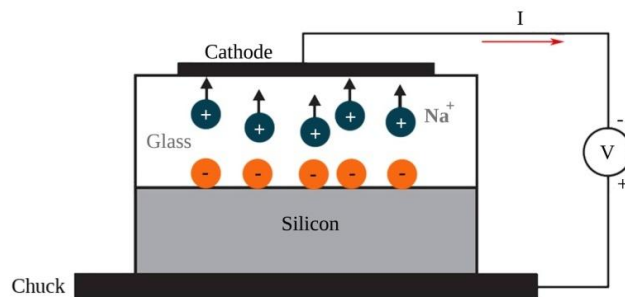
**Figure 2.5:** Spherical projection of normals to silicon crystal planes.

The most common anisotropic etchant is potassium hydroxide (KOH). Etch rates using KOH are typically given for the [100] direction. The (110) planes are etched twice as rapidly as (100) planes, while (111) planes are etched at a rate 100 times slower, being their etch rate negligible compared to the other planes. This KOH etching behavior in silicon allows predicting the angle generated on a specific feature being etched (e.g. the (100) -oriented silicon, the one used in this work, generates sidewalls leaning  $54^\circ$  from the vertical; see **Figure 2.3**).

❖ *In this work*, silicon wet etching was made using 40 % KOH at  $80^\circ\text{C}$  to remove bulk material in several fabrication flows; e.g., to release the  $\mu\text{SOFC}$  membranes or to define the bed-reactor cavity of the post-combustor. Also wet etching of glass was carried out by 49 % HF at room temperature to fabricate the cover that encapsulates the components as standalone devices.

### 2.2.2.3. Anodic bonding

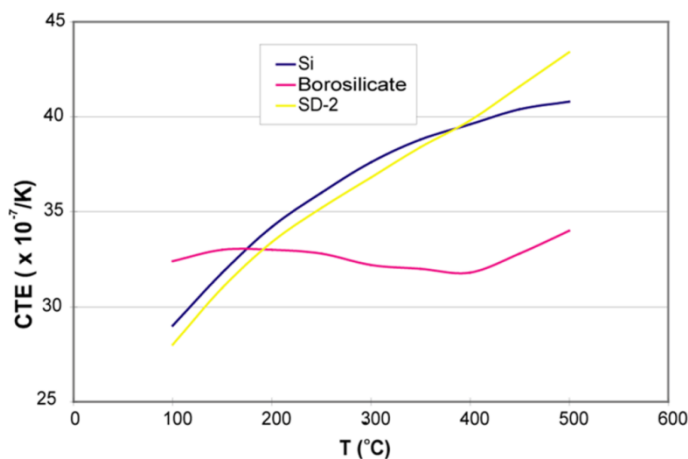
Anodic bonding is a process to bond together a silicon wafer and a sodium-containing glass substrate. The bonding is performed at a temperature between  $200$  and  $500^\circ\text{C}$  in vacuum, air, or an inert gas. The application of  $500$  to  $1500\text{ V}$  across the two substrates, with the glass held at the negative potential, causes mobile positive ions (mostly  $\text{Na}^+$ ) in the glass to migrate away from the silicon-glass interface toward the cathode, leaving fixed negative charges at the interface (see **Figure 2.6**). The bonding is complete when the ion current vanishes, indicating that all mobile ions have reached the cathode. The electrostatic attraction between the fixed negative charge in the glass and positive charge induced in the silicon holds the two substrates together and facilitates the chemical bonding of glass to silicon. Silicon dioxide on the silicon surface should be removed before bonding, as a thin ( $\sim 100\text{ nm}$ ) layer is sufficient to disturb the current flow and the bond.



**Figure 2.6:** Illustration of anodic bonding fundamentals between glass and silicon.

Sputtered, evaporated, or spin-on glass films containing sodium can also be used to anodically bond two silicon substrates. In this case, the required voltage to initiate the bond process decreases to less than 100V due to the thin glass layer.

Borosilicate glasses (e.g. Corning Pyrex® 7740, Schott 8330, etc.) have been widely used as a bonding material to silicon. Ideally, the Coefficient of Thermal Expansion (CTE) of these glass substrates should match to that of silicon in order to minimize thermal stresses (silicon coefficient is  $2.6 \cdot 10^{-6} \text{ }^\circ\text{C}^{-1}$  at room temperature, rising to  $3.8 \cdot 10^{-6} \text{ }^\circ\text{C}^{-1}$  at 300 °C); but in fact, the CTE curves of a borosilicate glass and silicon generally cross at about 170 °C (see **Figure 2.7**). So, when anodic bonding is performed at high temperature, the different CTEs create important residual stresses in the silicon causing cracks or even fractures. In order to solve this drawback, the SD-2 substrate from HOYA OPTICS is specially designed with a CTE curve which closely matches that of silicon in a wide range of temperatures (100 - 400 °C), minimizing the stress caused by the thermal mismatch between these two materials. Therefore, this material was chosen to encapsulate the silicon devices.



**Figure 2.7:** comparison of CTE curves of silicon, borosilicate and SD-2 glass versus temperature, extracted from HOYA OPTICS©.

❖ *In this work*, PLASMOS equipment located at IMB-CNM's Clean Room was used to hermetically bond a silicon device with a SD-2 HOYA glass cover. A temperature of 450 °C and a voltage of 1000 V were applied for 30 minutes to reach a complete bonding.

#### **2.2.2.4. Film growth/deposition**

Thin film deposition of metallic, insulating, conductive and dielectric materials plays an important role on the micro fabrication. This process comprises all the techniques in which the substrate surface is modified, basically, by depositing a new material on it (film deposition) or by a chemical change, i.e. no addition of any new material (film growth). Depending on the application, thicknesses of the deposited/grown films can range between a few tens to hundreds of nanometers.

##### Film growth

The most common growing process used in silicon technology is the thermal oxidation of silicon. Thermal SiO<sub>2</sub> is widely used due to their excellent electrical and thermal insulating properties. It is also used as mask or as sacrificial layer because it can be preferentially etched in HF acid with high selectivity. The oxidation of silicon takes place when heating the wafer to elevated temperatures. Depending on the chosen temperature (usually ranging between 600 and 1250 °C) and the chamber atmosphere (air, or O<sub>2</sub>/N<sub>2</sub> mixtures), SiO<sub>2</sub> film properties can be slightly tuned. Nevertheless, thermal SiO<sub>2</sub> films have compressive stress. For this reason, thermal SiO<sub>2</sub> layers are usually combined with tensile Si<sub>3</sub>N<sub>4</sub> layers that together form a stress compensated multilayer. The bilayer Si<sub>3</sub>N<sub>4</sub>/SiO<sub>2</sub> is thermo-mechanically stable and acts as an excellent electronic and ionic barrier.

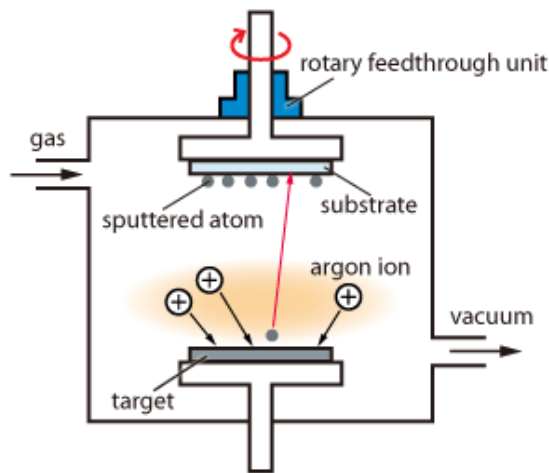
❖ *In this work*, thermal SiO<sub>2</sub> layers were grown on both sides of the silicon wafers and were used as insulation layers, together with Si<sub>3</sub>N<sub>4</sub> layers that were deposited on top of the oxide. 100 nm thick SiO<sub>2</sub> layers were grown on the Si by heating the wafers at 1100 °C for 20 min on a wet oxidant atmosphere.

##### Film deposition

Multiple film deposition techniques are available for micro fabrication applications. Basically, they can be grouped into two major categories: Physical Vapor Deposition (PVD) and Chemical Vapor Deposition (CVD) techniques. On one hand, in a PVD process no reaction takes place during deposition but only a material is vaporized and transferred directly to the substrate. On the other hand, a CVD process is based on a surface chemical reaction in a controlled atmosphere. In any case, either PVD or CVD process, the chosen deposition parameters will be crucial for the final film properties. They will affect on the purity of the film (as a general rule, the higher vacuum,

the purer the film), crystalline phase (depending on the specific phase diagram of the material being deposited), type of growth (either epitaxial or polycrystalline), stress on the film (that will depend on the deposition temperature, and also on the substrate and thin film material themselves) and any possible shadow effect (depending on the conformal properties of the deposit).

Among the different PVD techniques, apart from PLD (used for growing the functional layers of the  $\mu$ SOFCs and described on next *Section 2.3*), sputtering was also widely used in this work. As depicted in **Figure 2.8**, in sputter deposition, a target material is physically bombarded by a flux of inert-gas ions (usually  $\text{Ar}^+$ ) in a vacuum chamber at a pressure of 0.1-10 Pa. The target material, placed in the cathode plate, is then etched and ejected away to the substrate which is placed on the opposite plate of the deposition chamber (anode).



**Figure 2.8:** scheme of the sputtering process. Atoms are ejected from a solid target material due to bombardment of the target by energetic particles.

There are also different types of CVD techniques depending on the specific conditions used during the process, mainly categorized as Atmospheric-Pressure (APCVD), or Low Pressure (LPCVD), or Plasma-Enhanced (PECVD). APCVD and LPCVD processes operate at rather elevated temperatures (400-800 °C). In PECVD, the substrate temperature is typically near 300 °C since plasma is used to deliver additional energy to the reaction.

❖ *In this work*, sputtering was the technique chosen for depositing metallic films used as current collectors on the fabricated  $\mu$ SOFCs. Platinum films were deposited on Alcatel A610 equipment over thin film functional layers. Dense Pt films of 150 nm thickness were obtained by using an argon pressure of 1 Pa, 100 W of power and a RF velocity of 13.6 MHz. Also metal alloy films (Ag 25 % - Al 75 % and Cu 30 % - 70 % Mn) were sputtered as alternative current collectors (described on **Appendix C** of this thesis). Moreover, LPCVD and PECVD processes were used for depositing thin films. Insulating  $\text{Si}_3\text{N}_4$  films were deposited by LPCVD at 800 °C and a pressure of 25 Pa on previously oxidized silicon wafers, using dichlorosilane ( $\text{SiCl}_2\text{H}_2$ ) and ammoniac ( $\text{NH}_3$ ) as chemical precursors. Polysilicon films as a hard mask in the glass cover fabrication flow (described on **Chapter IV**, *Section 4.4*) were deposited at 615 °C and a pressure of 666 Pa by reacting silane ( $\text{SiH}_4$ ) in a CVD located at IREC (see **Figure 2.9**). A PECVD process was used to deposit  $\text{SiO}_2$  as a passivation layer of the tungsten heaters embedded in the  $\mu$ reformer and  $\mu$ vaporizer, at low temperature (380 °C) by reacting  $\text{SiH}_4$ , nitrous oxide ( $\text{N}_2\text{O}$ ) and oxygen ( $\text{O}_2$ ).



**Figure 2.9:** Nano EasyTube® 3000 equipment used in this work for depositing polysilicon films (located at IREC)

### **2.3. Pulsed laser deposition**

Pulsed Laser Deposition (PLD) is a versatile thin-film processing technique based on the laser ablation of a target material, often in vacuum conditions, and its deposition on a substrate. The PLD system comprises a laser, a set of optical components used to focus the laser beam onto the target surface, and an Ultra High Vacuum (UHV) chamber where the target and substrate are located facing each other. One of the major benefits of the PLD technique is the decoupling of the UHV chamber and the evaporation power source (the laser), enabling to choose the ambient background gas and pressure during deposition [2]. A relevant example is the introduction of oxygen into the UHV chamber during deposition of YSZ, to assure sufficient oxygen in the micro structures [18].

The technique relies on a focused laser beam that ablates a small amount of material creating a plasma plume. This plume containing the evaporated material is ejected perpendicular to the target surface toward the substrate placed just on top of it, allowing the deposition by condensation [19]. The nonequilibrium nature of the PLD ablation process, due to absorption of high laser energy densities by a small volume of material on the target, allows growing films with similar stoichiometry than the one of the target material [2]. It is then possible to grow crystalline films at temperatures much lower than the typical crystallization temperatures required for most complex oxides (usually higher than 1000 °C). Therefore, there is no need of thermal post-treatment at these high temperatures to crystallize the deposited materials, which makes this technique very practical for silicon-based  $\mu$ SOFCs.

The most common excimer lasers provide reliable average powers ranging from 6 W up to 300 W at 248 nm (KrF) (the laser utilized in this work) or 308 nm [XeCl].

#### **2.3.1. Effect of main deposition conditions on PLD films**

The deposition of complex oxides usually implies the control of several parameters, such as substrate temperature, gas pressure, working distance and laser fluence, affecting the as-deposited film-properties such as thickness, density, homogeneity and microstructure.

*a) Substrate temperature*

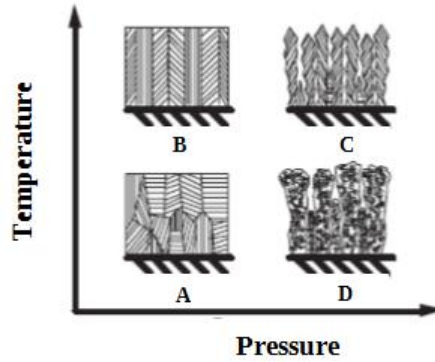
The substrate temperature is critical for thin-film microstructure due to the dependency of surface and bulk diffusion on temperature. Structure zone models have been developed to systematically categorize the influence of deposition temperature on film microstructure for PVD techniques such as PLD [20]. In each of these models, multiple zones with distinct microstructures were found to be roughly defined by the ratio of the reduced temperature ( $T_r$ ), defined as  $T_r = T_s/T_m$ , with  $T_s$  the substrate temperature and  $T_m$  the melting temperature of the target material [9]. Various zones were defined by Thornton in 1974 as following [9, 21]:

- $T_r < 0.3$ , the low substrate temperature does not allow sufficient surface diffusion and columns preserve a random orientation leading to extensive porosity.
- $0.3 < T_r < 0.5$ , significant surface diffusion leads to a polycrystalline, smooth and dense columnar microstructures.
- $T_r > 0.5$ , bulk diffusion and enhancement of crystallization and grain growth is favored.

*b) Gas pressure*

The background pressure allows tuning the film density since it influences the plume dynamics. During the deposition, the background pressure is maintained constant by introducing a small flux of a certain gas (typically  $O_2$  if growing oxides). These gas molecules collide with the ejected particles in the plume, so they scatter and thermalize by reducing their kinetic energy. This phenomenon promotes the phase formation by providing  $O^{2-}$  to the film growth. In consequence, the spatial distribution, deposition rate and kinetic energy of the ablated species decrease with increasing pressure [18]. **Figure 2.10** shows the resulting ceramic oxide thin-film microstructures depending on the combined effect of temperature and pressure in the  $T_r < 0.5$  range. In case A, a low pressure and a moderate temperature yield a dense, polycrystalline structure due to significant surface diffusion. In case B, higher temperatures yields even more significant surface diffusion and strongly ordered grains form a dense structure. In case C, at high pressure and temperature conditions, columnar grains spanning the whole film thickness are formed due to moderate surface diffusion, but shadowing effects prevent full density. In case D, at low temperatures and high pressures, an accumulation of loosely packed clusters of atoms form in a columnar and porous structure [18].





**Figure 2.10:** Combined effect of temperature and pressure in the ceramic oxide thin-film microstructure growth by PLD.

*c) Working distance*

The target-substrate distance has also a clear effect on the growing rate. The optimum distance depends on the plume size which is determined by the energy of the incoming particles (the substrate is usually maintained at least as separated as the size of the plume) [18]. The further the substrate from the target, the lower the growing rate because less material arrive with enough energy for film growth.

*d) Laser fluence*

The laser fluence, defined as the laser energy per unit area ( $\text{mJ}\cdot\text{cm}^{-2}$ ), mainly affects the deposition rate. The plasma plume diameter depends on the spot size of the laser beam. The spot size increases with increasing laser fluence as a larger volume of material is evaporated and ablated. The laser fluence also influences the kinetic and thermal energy of the ablated species.

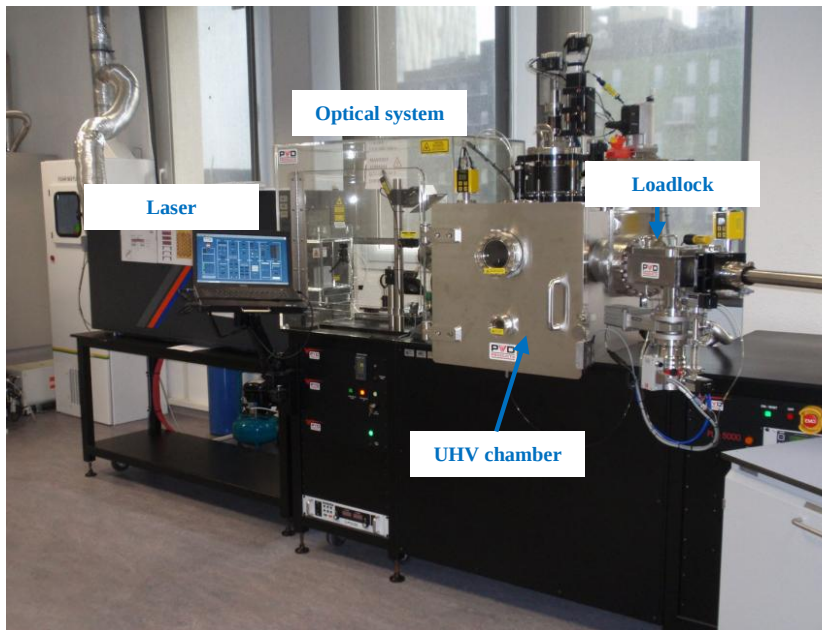
There are other deposition parameters that influence the ablation rate and the film microstructure such as the laser photon energy (must be higher than the target material bandgap), the laser pulse frequency, the total number of pulses and the wavelength of the laser. The typical growing rate ranges from 0.001 to 1 Å per pulse (a single shot corresponds to a submonolayer growth).

**2.3.2. Wafer level integration: large area PLD**

Large area PLD is needed for an up-scaling of the PLD process and integrating it on a MEMS fabrication flow. The principle of actuation consists of manipulating the relative plume-substrate position. Therefore instead of having

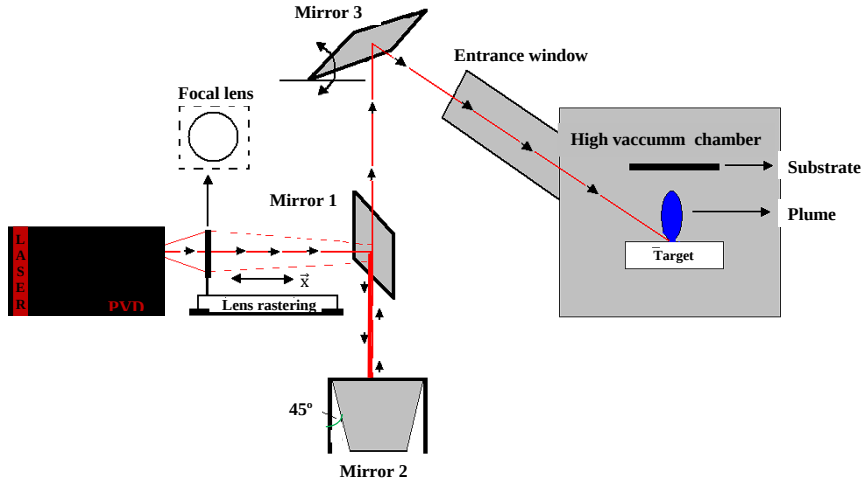
a plume fixed on a single position, as in the case of deposition at chip level, the laser beam sweeps the whole area of the target through a programmable raster mirror.

The large-area PLD equipment utilized in this work was a PLD5000 from PVD ®, located at IREC facilities, which allowed depositing functional layers on substrates as large as 4” diameter. An image of the equipment is presented in **Figure 2.11**, with a KrF excimer laser (Lambda Physik COMPex PRO 205), UHV-chamber, optical system and loadlock indicated.



**Figure 2.11:** General view of the large area PLD 5000.

The optical system is based on a focal lens and high reflecting mirrors, where the last mirror in the laser path is dynamic. The path of the laser beam for the large area PLD used in this thesis is depicted in **Figure 2.12**. The focal lens is mounted on a support that allows movement in the  $\vec{x}$  direction. The focal lens and the dynamic mirror (mirror 3 in the figure) are linearly correlated, so that the distance from the focal lens to the target surface is constant, maintaining a fixed laser spot size, and thus, a fixed laser fluence during deposition.

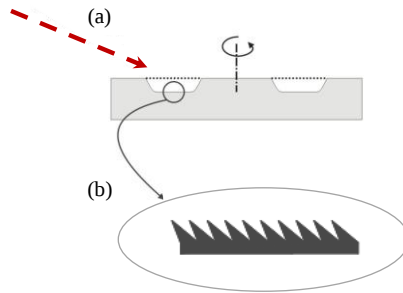


**Figure 2.12:** Path of the laser beam in large area PLD deposition.

### 2.3.3. Special issues related to large area PLD films

Large area thin film depositions add some additional issues to the PLD process, mainly concerning the targets. This PLD configuration requires bigger targets to be effective, usually the same size or slightly smaller than the substrate to cover the whole wafer. Moreover, higher laser powers are needed to achieve an acceptable growing rate. This can generate problems on ceramic targets due to their low thermal conductivity, because laser can cause a localized heating and then cracking of the target. This effect can be minimized by moving the laser spot at higher velocity over the target area, avoiding nonuniform thermal expansion.

As depicted in **Figure 2.13**, the erosion of the target due to laser ablation can produce two main morphological effects, namely *gross deformation* and *cone formation* [19]. The first effect is macroscopic and appears if mirror raster scanning is not properly defined. In consequence, the plume is tilted affecting the film homogeneity and growing rate. The second effect is formed by micro changes on the target surface due to repeated melting, cooling and recrystallization of material, causing lower deposition rates and an increment of particle ejection. Both these effects can be partially solved by raster scanning the laser through the whole target area and carefully maintaining the target polished.



**Figure 2.13:** (a) Macroscopic trenches formed by the incident laser when using a not proper rastering (*gross deformation*) and (b) microscopic cones formed by the laser interaction with the substrate surface (*cone formation*).

The ejection of particles from the target is another significant problem for  $\mu$ SOFCs fabrication by PLD [22]. There are four major causes:

- a) *Exfoliation* occurs when high pressurized gas expands and breaks loose solid fragments of the target.
- b) *Stress-induced target breakdown*, as previously mentioned, is a consequence of the repeated heating and cooling of the material, inducing mechanical stresses due to the expansion and contraction of the ceramic target.
- c) *Explosive boiling* is the ejection of molten material when the laser fluence is above a threshold value, where material ablated is in the liquid state and directly ejected towards the substrate, yielding spherical droplets in the micrometer range [23].
- d) *Nanoclusters* are formed by influence of ambient gas pressure on the plume dynamics. The gas limits the plume expansion and increases the probability of collision between the ablated species, as the plume becomes more and more saturated with particles at higher pressures. The saturation facilitates the nucleation and growth of nano-sized clusters in the plume. These clusters reach the substrate surface with a given energy (thermal and kinetic energy) and if this value is below a threshold value, they maintain their shape and size, while above the threshold value, they dissociate [9].

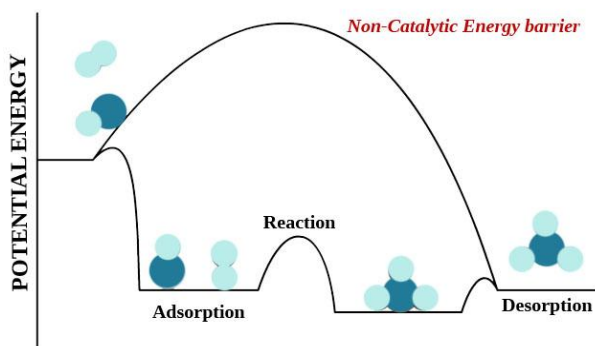
A common characteristic for all these ejected particles is that they can induce surface defects, cracks and pinholes. To avoid *exfoliation* and *stress-induced target breakdown*, a target material with small grain size and optimized mechanical properties can be used. To avoid *nanoclusters* and *explosive boiling*, the gas pressure and laser fluence during deposition must be tuned.

❖ *In this work* functional layers were deposited by the use of PLD 5000. Dense 3YSZ thin films were obtained using a background pressure of 2.67 Pa by flowing 10 sccm of O<sub>2</sub> and a work distance of 110 mm; while dense 8YSZ thin films were obtained using the same gas pressure and gas flow rate, but a work distance of 90 mm. The substrate temperature was fixed in both cases at 600 °C. The laser energies used were 240 mJ and 200 mJ for 3YSZ and 8YSZ, respectively. The microstructure and growth rate of both thin film electrolytes were known from a previous work [19, 22, 24]. Therefore, deposition at wafer level was the next step. Thin film electrolyte layers were deposited on 4" wafers with a Si/SiO<sub>2</sub>/Si<sub>3</sub>N<sub>4</sub> structure. The wafer was mounted on a sample holder provided by PVD Products. During the deposition process, the target and the wafer substrate were rotated with a velocity of 15 rpm and 6 rpm, respectively. A mirror rastering program was defined to move the laser spot over the entire surface of both target materials, so the plume could cover the whole substrate area.

All ceramic  $\mu$ SOFCs were obtained by deposition of porous electrodes. Two  $\mu$ SOFCs configurations were developed: one based on CGO as anode and LSC as cathode, and another based on symmetrical SFM electrodes. A background pressure of 13.33 Pa, a temperature of 100 °C and a work distance of 90 mm were used in CGO and LSC depositions, whereas a temperature of 600 °C was used in the case of SFM. Target rastering was adjusted for each case, depending on the target dimensions.

## 2.4. Catalyst synthesis routes

The ability of solid surfaces to make and break molecular bonds is the basis for the phenomenon of heterogeneous catalysis. The presence of a catalyst provides an alternative sequence of elementary steps to accomplish a desired chemical reaction. If the energy barriers of the catalytic path are much lower than the barriers of the non-catalytic path, significant enhancements in the reaction rate can be achieved by the use of a catalyst. Typical heterogeneous catalysts are inorganic solids such as metals, oxides and metal salts, but they may also be organic materials such as hydroperoxides, ion exchangers and enzymes. As depicted in **Figure 2.14**, the mechanism of a catalyzed reaction can be described by the sequence of elementary reaction steps, including adsorption, surface diffusion, chemical transformations of adsorbed species, and desorption.



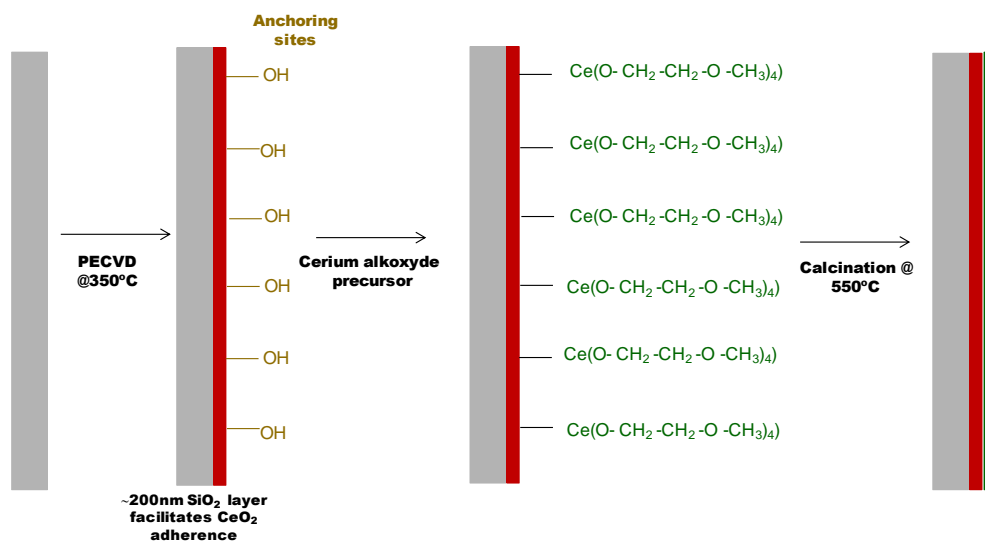
**Figure 2.14:** The general route by which heterogeneous catalysts work.

❖ *In this work*, heterogeneous catalysis was used for hydrogen production by hydrocarbon reforming reactions that take place in the  $\mu$ reformer and for the catalytic combustion of hydrogen through a complete oxidation into the  $\mu$ post combustor.

### 2.4.1. Hydrocarbon reforming catalysts

Noble metals like Pt, Rh, Ru or Pd on different support materials like  $\text{SiO}_2$ ,  $\text{ZrO}_2$ ,  $\text{CeO}_2$  or  $\text{Al}_2\text{O}_3$  have been widely described in the literature as suitable catalytic systems for hydrocarbon reforming reactions [13, 25-29]. Among different options, Pd-Rh/ $\text{CeO}_2$  catalyst system was chosen to study the Ethanol Steam Reforming (ESR) and Methane Dry Reforming (MDR) as possible reactions to generate hydrogen fuel in the  $\mu$ SOFC PG.

A scheme of the synthesis route is described in **Figure 2.15**. A thin layer of SiO<sub>2</sub> was first deposited by PECVD covering the microchannels walls of the reformer, where the catalyst was going to be placed afterwards. On a first step, the CeO<sub>2</sub> support was deposited on the walls from a cerium methoxyethoxide solution by ionic exchange with the surface hydroxyl groups of the SiO<sub>2</sub> layer. A homogenous distribution of the cerium precursor across the microchannels walls was achieved by using a polyamide membrane filter (NL 16, Whatman®) and applying a pressure gradient between both sides of the silicon chip. Then, the microreactor was heated up to 500 °C in air for 3 h (5 °C·min<sup>-1</sup>) to decompose the ceria precursor and to form a CeO<sub>2</sub> layer. Noble metals with nominal content fixed at 1 %wt were grafted onto the CeO<sub>2</sub> support by free impregnation. The chloride precursors (PdCl<sub>2</sub> and RhCl<sub>3</sub>) were used for this goal. The catalytic system was calcined at 300 °C for 6 h using a heating ramp of 2 °C·min<sup>-1</sup>. Finally, the catalyst was activated prior to the experiments under reducing atmosphere (5 % H<sub>2</sub>- 95 % Ar) at 300 °C for 1 h.



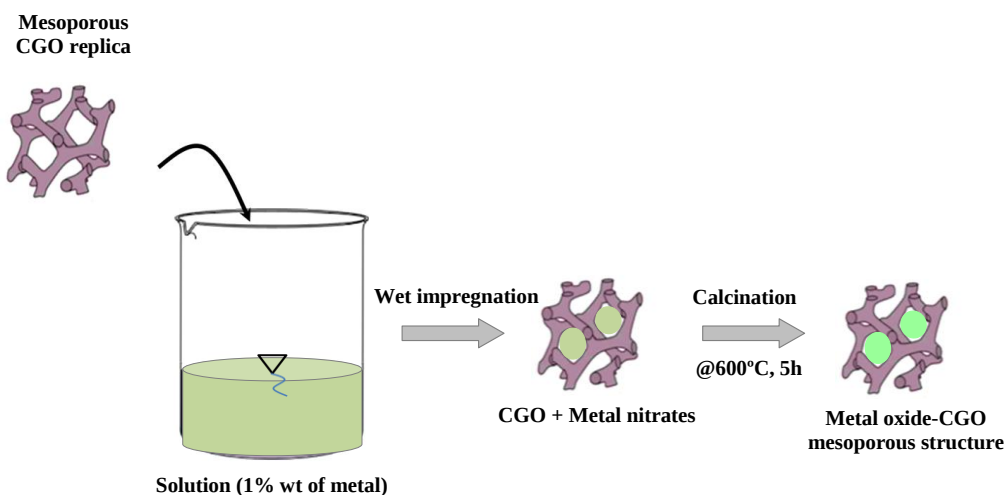
**Figure 2.15:** Scheme of the Pd-Rh/CeO<sub>2</sub> synthesis route used in this work for the hydrocarbon reforming reactions.

## 2.4.2. Catalyst for hydrogen combustion

A mesoporous nanostructure was chosen as catalytic support for hydrogen combustion. Regarding the metallic component of the catalyst, multi-component metal oxides were selected in order to study a possible synergy between them. In particular, nickel and copper oxides impregnated in ceria

doped gadolinium mesoporous structures ( $\text{Ce}_{0.8}\text{Gd}_{0.2}\text{O}_{1.9}$ , named as CGO mesoporous) were studied for the catalytic oxidation of hydrogen.

The mesoporous catalyst was synthesized by consecutive wet impregnation steps, as detailed in **Figure 2.16**. First, the CGO mesoporous replica was synthesized by nanocasting method using the silica template KIT-6 (3D cubic structure) as extensively described in refs [17, 18]. Then, the CGO mesoporous structure was impregnated with a stoichiometric amount of metal nitrates (1 %wt of metal) in ethanol solution, stirred for 1 h and calcined at 600 °C for 5 h, thus forming the corresponding metal oxide-CGO mesoporous structure.



**Figure 2.16:** Scheme of the synthesis route used in this work for the hydrogen combustion catalyst, CuO-NiO/mesoporous CGO.



## **2.5. Structural characterization**

### **2.5.1. Optical microscopy**

Optical Microscopy (OM) is used to magnify 2D images of small samples. Two basic acquisitions can be made depending on the position of the light source with respect to the sample, i.e. transmission and reflection images. The corresponding image comes from the transmitted light through the sample or the reflected light when illuminating it.

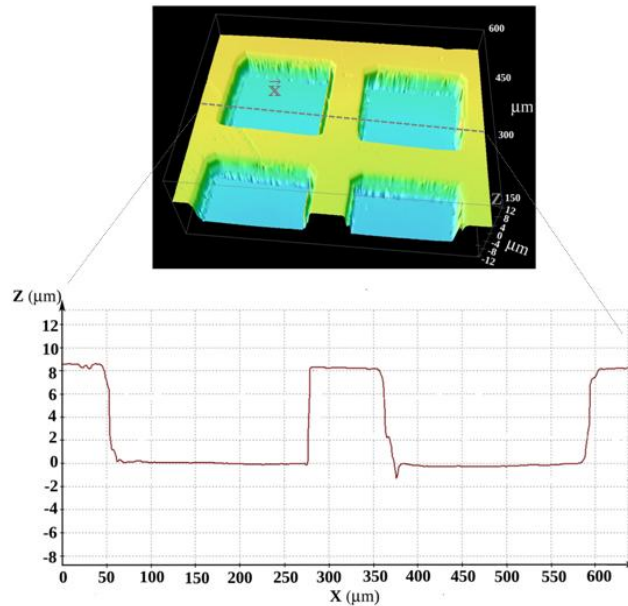
Moreover, there are few techniques that provide a 3D surface representation from a microscope image, including (a) *the confocal microscopy* and (b) *the interferometry*.

(a) In *Confocal Scanning Optical Microscopy (CSOM)*, the sample to check is moved vertically in small steps such that each point on the surface passes through focus. A very small aperture placed between specimen and detector is used to select information from a single focal plane, named as confocal, producing a sharply focused optical slice through the specimen. It is this ability to block the light out-of-focus by spatial filters that makes CSOM so well suited for generating 3D images by scanning planes in Z.

(b) *Interferometry* takes advantage of the light properties to analyze surface characteristics, in particular surface height variations. For evaluation of surface topography, this technique separates source light so that it follows two different paths, one of them includes a reference surface while the other includes the target surface. The separated light beams then recombine and are measured by a digital camera that gives the resultant light intensity over the whole image. The intensity of the recombined light exhibits high sensitivity to the differences in path lengths, effectively comparing the object surface with the reference surface with nanometric resolution.

❖ *In this work*, OM (3D PLu Neox Optical from SensoScan) was regularly used to check the microstructure of different components after each fabrication step. It is also helpful to study the particles ejected after PLD depositions. Furthermore, pinholes on the membrane could be easily distinguished by using transmission light through a reflective film (such as thin platinum). Confocal and interferometry techniques were useful for analyzing

surface topographies, e.g. studying the wet etching of SD-2 HOYA glass, as depicted in **Figure 2.17**.



**Figure 2.17:** Typical 3D image and Z profile obtained by confocal microscopy.

### 2.5.2. Scanning electron microscopy

A Scanning Electron Microscope (SEM) uses a focused high-energy beam of electrons to generate a surface image of a sample. Accelerated electrons carry a significant amount of kinetic energy, which is dissipated by electron-sample interactions. These interactions generate: secondary electrons (used to produce SEM images), backscattered electrons (used to contrast areas with different chemical composition), diffracted backscattered electrons (used to determine crystal structures), photons (used to determine the elemental composition, named as Energy-Dispersive X-ray spectroscopy, EDX), visible light, and heat.

❖ *In this work*, SEM images were taken to observe the results of different processes, e.g. the catalyst deposition on microchannels of the  $\mu$ reformer or the microstructure of functional thin films after PLD depositions. Also EDX analyses were carried out to identify the elements present on the catalysts and thin films.

### 2.5.3. Transmission electron microscopy

Transmission Electron Microscopy (TEM) uses the electrons transmitted through a specimen when it is illuminated with a focused beam of high-energy electrons (accelerated in high voltages, usually 200-300 kV) to form an image. This image is magnified and focused either onto a fluorescent screen or onto a detector.

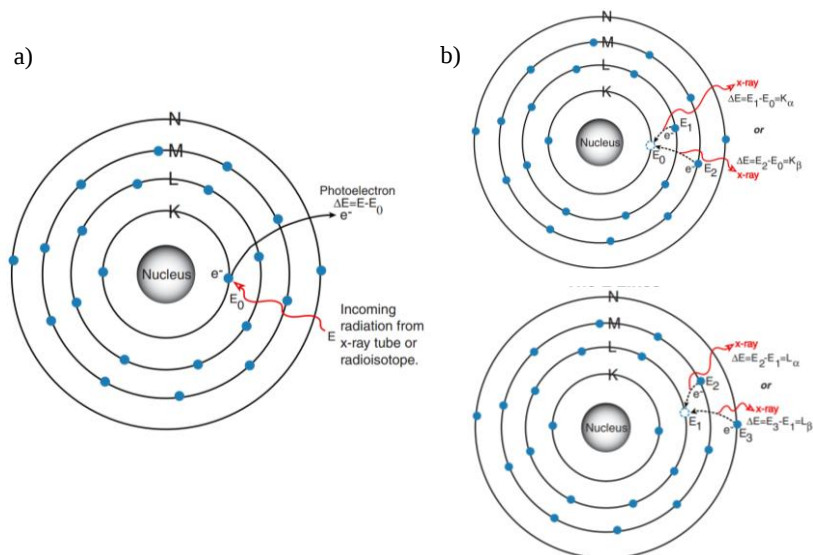
A crystalline material interacts with the electron beam mostly by diffraction rather than absorption, although the intensity of the transmitted beam is affected by the volume and density of the material through which it passes. Two different types of imaging are then possible, depending on which electrons are collected. On one side, *bright field* images are obtained when looking only at unscattered electrons. The diffracted electrons are blocked by deflecting them away from the optical axis of the microscope, obtaining high contrast images. This is made by placing an aperture that only allows unscattered electrons to go through it. On the other side, the observation of those diffracted electrons results on a *dark field* image. This second type of imaging is acquired by either moving the aperture or tilting the electron beam, in such way that the diffracted electrons can pass through it while the unscattered ones are blocked. The two types of imaging are complementary, and are used depending on the information required.

❖ *In this work*, TEM was used to characterize the mesoporous structure of the CGO. The porous size and the matrix distribution were examined by using a Zeiss Libra 120 microscope operating at 120 kV, located at IREC.

### 2.5.4. X-ray fluorescence

X-Ray Fluorescence (XRF) is a non-destructive analytical technique that consists of the emission of characteristic secondary (or fluorescent) X-rays from a material when it is excited by bombarding it with high-energy X-rays (or gamma-rays). If the primary energy of X-rays is equal to or larger than the binding energy of an inner shell electron, then the primary source is absorbed by an atom of the material and excites the electron which is ejected, creating a vacancy (**Figure 2.18a**). Outer shell electrons then fill the vacancy, emitting photons with energy equal to the energy difference between the two states (**Figure 2.18b**). Since each element has a unique set of atomic energy levels, it emits a unique set of X-rays (fluorescence spectrum) which are characteristic of this element.

❖ *In this work*, XRF was used to quantify the metal content (Ni and Cu) impregnated in the mesoporous catalyst by using a Fischerscope X-Ray XDV equipment located in IREC. The operating conditions used were 50kW, 0.25 mm of collimator diameter and 120 s of acquisition time.



**Figure 2.18:** (a) An electron in the K shell is ejected from the atom by an external primary excitation x-ray, creating a vacancy and (b) an electron from the L or M shell fills the vacancy. In the process, it emits a characteristic x-ray unique to this element and in turn, produces a vacancy in the L or M shell.

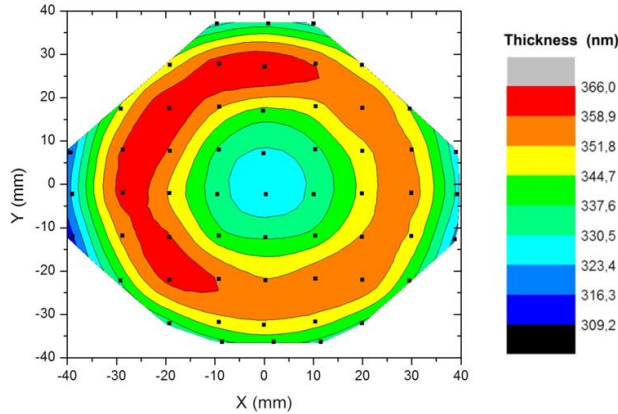
### 2.5.5. Reflectometry

Reflectometry consists of the measurement of the amount of light reflected from a thin film, at a certain range of wavelengths, with the incident light normal to the sample surface. This optical technique is very attractive for the characterization of thin film thicknesses and optical constants because of its high accuracy and the fact of being nondestructive.

The measurement is based on the study of the fraction of light reflected at each interface between two films, which is determined by the discontinuity in their optical constants: refractive index ( $\eta$ ) and extinction coefficient ( $\kappa$ ). When having multiple interfaces, the total amount of reflected light is the sum of all the individual reflections. Reflections may then add together either constructively or destructively, depending on their phase relationship, which is again determined by the optical constants, but also by the thickness of the film and the incident wavelength. The resultant spectra can be fitted by using

mathematical models to obtain either the thickness of the film, if knowing the optical constants, or vice versa.

❖ *In this work*, reflectometry was used to measure the thickness of YSZ thin films. The reflected light on a wavelength range from 400 to 700 nm was acquired on Plu 2300 Neox Optical Profiler equipment, placed at IREC. Film thicknesses of  $\mu$ SOFCs were then calculated at wafer level using  $\eta$  and  $\kappa$  values for YSZ from the literature (see **Figure 2.19**).



**Figure 2.19:** Mapping of the 8YSZ thickness after PLD deposition in a whole 4'' silicon wafer which contains 57  $\mu$ SOFC devices.

### 2.5.6. X-ray diffraction

X-Ray Diffraction (XRD) is a nondestructive technique used in crystallography for compositional analysis and phase identification of crystalline materials. The exposition of the sample to X-rays produces a specific pattern that is recorded and analyzed. If the X-rays wavelength has the same order of magnitude than the interatomic distances of the sample atoms, the X-rays diffracted have specific directions and intensities depending on the crystalline structure and a characteristic diffraction pattern is generated.

❖ *In this work*, XRD Bruker-D8 Advance equipment, located in IREC, was used to identify the crystalline phases obtained in functional thin films of  $\mu$ SOFCs. The experiments were carried out at room temperature in a flat plate  $\theta/2\theta$  geometry. Moreover, in-situ temperature XRD experiments were also used to study the crystallography changes of the  $\text{CeO}_2$  support catalyst. This technique is based on a heating stage mounted on an Anton PAAR XRK 900 chamber coupled in the Bruker-D8 equipment. A silicon substrate was impregnated with the catalyst and loaded onto the sample holder. A XRD

pattern evolution with temperature, ranging from room temperature up to 650 °C, was analyzed in order to observe the crystallization of CeO<sub>2</sub> and then establish the specific temperature needed for its synthesis.

### **2.5.7. Gas chromatography**

Chromatography is a separation process that is achieved by distributing different components of a mixture between two phases, a stationary phase and a mobile phase. Those components held preferentially in the stationary phase are retained longer in the system than those that are distributed selectively in the mobile phase. In consequence, solutes are eluted from the system as local concentrations in the mobile phase that are detected continuously in the detector. In particular, for Gas Chromatography (GC), the mobile phase is a gas and the stationary phase can be a solid or a liquid.

❖ *In this work*, different GC equipments were used, located at IREC and INTE-UPC, both from Agilent Technologies and equipped with specific columns for short chain hydrocarbon analysis (MolSieve 5Å columns).

### **2.5.8. Thermo gravimetric analysis**

Thermo Gravimetric Analysis (TGA) is an analytical technique used to determine the thermal stability of materials by monitoring the weight change due to the fraction of volatile components released when it is heated. The measurement is normally carried out in air or inert atmospheres, and the weight is recorded as a function of temperature.

❖ *In this work*, this technique coupled with differential scanning calorimetry and mass spectrometry (see the following sections) was used to study the activity of CGO mesoporous catalysts in the H<sub>2</sub> combustion reaction, where the catalysts lose weight due to the reduction of metal oxide into metal. TGA was also used to detect coke deposition on the catalyst infiltrated (Pd-Rh/CeO<sub>2</sub>) in the channels of  $\mu$ reformer after performing the reforming reactions.

### **2.5.9. Differential scanning calorimetry**

Differential Scanning Calorimetry (DSC) measures the temperatures and heat flows associated with transitions in materials as a function of time and temperature in a controlled atmosphere. These measurements provide quantitative and qualitative information about physical and chemical changes

that involve endothermic or exothermic processes or changes in heat capacity. In a DSC the difference in heat flow to the sample and a reference is recorded as a function of temperature. The reference is an inert material such as alumina. The temperature of both, the sample and reference, are increased at a constant rate. Since the DSC is at constant pressure, heat flow is equivalent to enthalpy changes, according equation 2.1,

$$\left(\frac{dq}{dt}\right)_p = \frac{dH}{dt} = m \cdot C_p \cdot \frac{dT}{dt} \quad (2.1)$$

where  $\frac{dq}{dt}$  is the heat flow rate ( $\text{cal}\cdot\text{s}^{-1}$ ),  $\frac{dH}{dt}$  is the rate of enthalpy change ( $\text{cal}\cdot\text{s}^{-1}$ ),  $m$  is the mass (g),  $C_p$  is the specific heat ( $\text{cal}\cdot\text{g}^{-1}\cdot\text{K}^{-1}$ ) and  $\frac{dT}{dt}$  is the rate of temperature change ( $\text{K}\cdot\text{s}^{-1}$ ).

❖ ***In this work***, the activity of CGO mesoporous catalysts to initiate  $\text{H}_2$  combustion was investigated by means of Sensys Evo TG-DSC equipment from Setaram. Four temperature steps in the range from 100 to 250 °C were carried out by flowing 20  $\text{ml}\cdot\text{min}^{-1}$  of 5 %  $\text{H}_2/\text{Ar}$  and 100  $\text{ml}\cdot\text{min}^{-1}$  synthetic air (21 %  $\text{O}_2$  and 79 %  $\text{N}_2$ ). During the heating ramp only argon flows.

As previously mentioned, this technique was also used to detect coke deposition on the catalyst infiltrated in the channels of  $\mu$ reformer after performing reforming reactions by flowing 10  $\text{ml}\cdot\text{min}^{-1}$  of synthetic air.

### 2.5.10. Mass spectroscopy

Mass Spectroscopy (MS) is an analytical technique in which ions, produced from a sample, are separated by an electric or magnetic field according to their ratios of charge to mass. A record is produced (mass spectrum) of the different types of ion present and their relative amounts. Since ions are very reactive and short-lived, their formation and manipulation must be conducted in vacuum.

❖ ***In this work***, a MS from Pfeiffer was coupled to a Sensys Evo TG-DSC system in order to detect the species derived from coke deposition on metal-catalyst after performing reforming reactions, in particular to monitor the carbon dioxide ( $\text{CO}_2$ ) and carbon monoxide (CO) formation. Since  $\text{CO}_2$  and CO are composed of only a few atoms (1 atom of  $^{12}\text{C}$  and 2 or 1 atoms of  $^{16}\text{O}$ ), their mass spectrum is based on a specific peak mass-to-charge ratio ( $m/z$ ) in 44 a.m.u and in 28 a.m.u, respectively.

### 2.5.11. Impedance spectroscopy

Electrochemical Impedance Spectroscopy (EIS) is one of the most common methods for analyzing the electrical properties of materials in solid state ionic systems [30]. This method has the ability of separating the resistance related to each phenomenon that take place in a  $\mu$ SOFC from its total resistance (e.g. ionic conductivity through the electrolyte, charge transfer and mass transport on the electrode, gas diffusion, etc.), since each process has associated a characteristic time. Thus, applying an AC excitation on the system, different impedances are measured at different frequencies.

Mathematically, the voltage applied can be expressed by equation 2.3,

$$E(t) = E_0 \cdot e^{i\omega t} \quad (2.3)$$

where  $E_0$  is the amplitude,  $t$  is the time and  $\omega$  is the angular frequency. Similarly, the generated current can be defined in the same way, as equation 2.4,

$$I(t) = I_0 \cdot e^{i(\omega t + \theta)} \quad (2.4)$$

being  $\theta$  the phase difference between the voltage and the current. So, impedance can be defined as the voltage to current ratio for a single complex exponential at a particular frequency ( $\omega$ ), corresponding to equation 2.5.

$$Z(\omega) = \frac{E(t)}{I(t)} = |Z| \cdot e^{-i\theta} \quad (2.5)$$

Using the Euler relation (equation 2.6),

$$e^{i\theta} = \cos\theta + i \cdot \sin\theta \quad (2.6)$$

this complex impedance number can also be expressed in terms of a real and an imaginary component (equation 2.7),

$$Z(\omega) = |Z| \cdot (\cos\theta - i \cdot \sin\theta) = Z'(\omega) - i \cdot Z''(\omega) \quad (2.7)$$

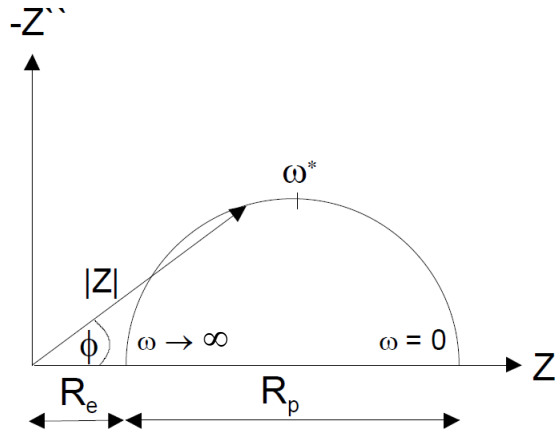
where  $Z'(\omega)$  is the real part and  $Z''(\omega)$  is the imaginary part.

An impedance spectra can be plotted in several ways, but the most common representation to study the experimental data is the Nyquist plot where the negative imaginary part of the impedance ( $Z''$ ) is plotted vs. the real part of the impedance ( $Z'$ ) (see **Figure 2.20**). The following characteristic parameters are obtained from the impedance data,

- the polarization resistance ( $R_p$ ), which is related to the purely ohmic part of the electrode resistance,

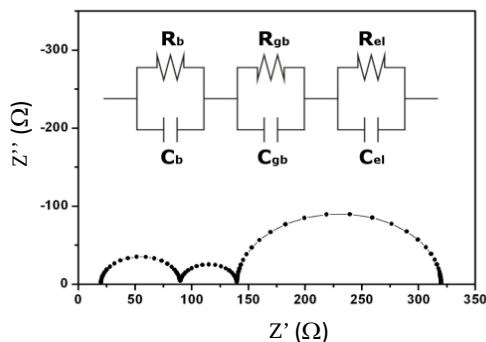


- the so-called electrolyte resistance ( $R_e$ ). It can be determined from the high frequency part of the Nyquist plot at the intersection of the impedance data with the real axis,
- the relaxation frequency ( $\omega^*$ ), which is defined as the frequency at the maximum imaginary impedance value. In the case of several relaxation processes, there exist several relaxation frequencies which can be identified as a local maximum in the Nyquist plot.



**Figure 2.20:** Schematic representation of the Nyquist plot.

In a complex system such as a multilayer  $\mu$ SOFC, different semicircles appear on the Nyquist plot, due to the different phenomena that take place. The semicircles are separated from each other depending on its characteristic time constant ( $\tau$ ). Most of the semicircles appear overlapped, happening when the values of time constant are less than two orders of magnitude apart. The characteristic time constant of a process is defined as  $\tau = 1/(R \cdot C)$ , so it is not only dependent on the resistance, but also on the capacitance associated to the process. In consequence, electrochemical impedance spectra are usually analyzed by fitting the data to an equivalent electrical circuit consisting of resistances, capacitances, and inductances. The main difficulty with this method is related to the physical and chemical meaning of the equivalent circuit elements. Each semicircle appeared on the Nyquist plot can be associated to a (RC) sub-circuit, and the whole process can then be related to an equivalent electrical circuit. **Figure 2.21** shows a Nyquist plot that would correspond to a simple fuel cell system, with the associated equivalent circuit also depicted. The different mechanisms involved are reflected as multiple semicircles in the graph, each one corresponding to a RC pair on the equivalent circuit.



**Figure 2.21:** Nyquist plot of an EIS for a simple electrolyte cell and its equivalent electric circuit; where  $R_b$  and  $R_{gb}$  are the ohmic resistances ( $\Omega$ ) related to the electrolyte (i.e. the bulk and grain boundary resistances, respectively) and  $R_{el}$  is the polarization resistance of electrode ( $\Omega$ ), while  $C_b$ ,  $C_{gb}$  and  $C_{el}$  are their associated capacitances ( $F \cdot cm^2$ )

❖ **In this work**, EIS measurements of the electrochemical cells, i.e. LSC/8YSZ/LSC, LSM/8YSZ, CGO/8YSC/CGO, SFM/3YSZ/SFM and LSC/8YSZ/CGO, were carried out on a Probostat™ system, using Novocontrol equipment (Alpha-A High performance frequency analyzer). In general, a frequency range from 3MHz to 0.01 Hz and a small AC voltage signal of 50 mV were used. In all cases, EIS data was analyzed by using the Z-view analysis software [31].

### 2.5.12. Electrical characterization

A metal heater was patterned in the components that require active heating, i.e. the  $\mu$ vaporizer and  $\mu$ reformer, both included in the FPU. Prior to test these components, the Temperature Coefficient of Resistance (TCR) of metal heater was measured.

Tungsten (W) was chosen because is CMOS compatible, represents a mainstream technology and can operate reliably at high temperatures [32]. Three metallic configurations were designed and studied. The first, was based on a 500 nm layer of W. The second configuration consisted of a 50 nm layer of titanium tungsten (TiW, with 10 % of Ti content) as adhesion layer between the dielectric layers and the metal layer, a 450 nm thick layer of W and 20 nm thick layer of gold (Au) in order to prevent W oxidation. The last configuration was based on a 30 nm layer of TiW, a 250 nm layer of W and a 20 nm thick layer of Au on the top.

## **CHAPTER II. Experimental methods**

---

A thermal calibration of the tungsten heaters was performed by measuring the TCR according the following expression (equation 2.2),

$$R = R_0(1 + \alpha \cdot \Delta T) \quad (2.2)$$

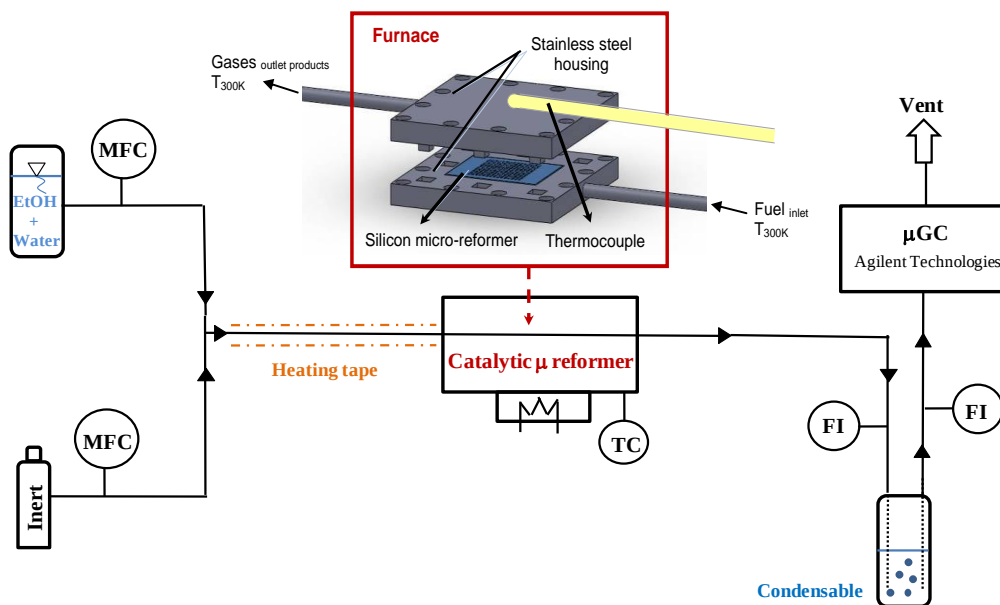
where,  $\alpha$  is the TCR ( $^{\circ}\text{C}^{-1}$ ),  $R_0$  is the nominal resistance at  $T_0=0$   $^{\circ}\text{C}$  ( $\Omega$ ) and  $\Delta T$  is the change in temperature,  $(T - T_0)$ , ( $^{\circ}\text{C}$ ).

The resistances of metal thin films were measured from  $T= 25$  to  $500$   $^{\circ}\text{C}$  with steps of  $20$   $^{\circ}\text{C}$  by using a Linkam station with a heating plate (HFS91 PB4), a Keithley multimeter, and a reference temperature sensor. The Linkam station was closed with a cover to minimize thermal convection. Successive resistance measurements were performed to determin both the TCR and  $R_0$  in each of the heater configurations.

## 2.6. Functional characterization

### 2.6.1. Hydrocarbon reforming reactions

The performance of ESR and MDR was accomplished in an experimental setup as represented in **Figure 2.22**. Several reforming tests were performed for both fuels (ethanol and methane) in an external furnace at atmospheric pressure. The  $\mu$ reformer was placed in a gas-tight homemade stainless steel housing sealed with a ceramic sealant (Ceramabond®). In the ESR experiments, the liquid mixture (water/ethanol) was injected directly from a storage tank by using a pump (Knauer Smartline) and heating tapes were used for feed evaporation and overheating sections before the furnace. In the MDR experiments, the gas mixture feed was supplied by mass flow controllers (Bronkhorst).



**Figure 2.22:** Schematic representation of the experimental setup for ethanol steam reforming, where *MFC* indicates a mass flow controller, *TC* a thermocouple and *FI* a flow indicator.

The influence of the temperature and fuel loading was studied for both ESR and MDR. The temperature range chosen for testing was between 600 °C and 800 °C, i.e. a range of temperatures suitable for ensuring a good performance of  $\mu$ SOFCs. The fuel loads under study were fixed after thermodynamic calculations detailed in *Section 3.4* of **Chapter III**. For the ESR experiments, a fuel loading, ranged from  $1 \cdot 10^{-2}$  to  $3 \cdot 10^{-2}$  ml $\cdot$ min $^{-1}$ , of a liquid steam/ethanol

mixture with S/E= 4 (molar) was injected by HPLC pump. This water content appears appropriate to balance the energetic cost related to its evaporation and overheating, and a suitable thermal management within the  $\mu$ SOFC PG, as shown in the results achieved in **Chapter III**. In the MDR experiments, a gas mixture feed from 18 to 36 ml·min<sup>-1</sup> was supplied by mass flow controllers. This range was used considering a CO<sub>2</sub>/CH<sub>4</sub> ratio equal 2, which appears to minimize coke poisoning according to the thermodynamic analysis described in [28]. In both reforming tests, ESR and MDR, 8 ml·min<sup>-1</sup> of argon was used as gas carrier. The products of the effluent gas stream were quantitatively evaluated in terms of volumetric total flow rate (bubble soap meter) and composition by an online automated microGC at steady state, whereas outlet flow rates of ethanol and water (and acetaldehyde, if present) were evaluated by closing mass balances. The carbon mass balance values were always higher than 95%.

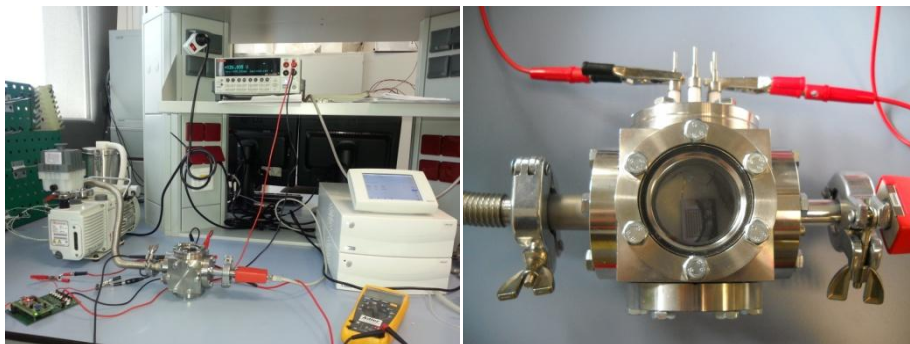
The reforming performances were measured in terms of fuel conversion ( $\chi_i$ , %), hydrogen selectivity on a dry basis ( $S_{H_2}$ , %), volumetric hydrogen production rate ( $\dot{V}_{H_2}$ , ml·min<sup>-1</sup>) and hydrogen yields ( $\psi_{H_2}$ ) of the outlet gas stream, as presented in the next equations,

<i>Ethanol steam reforming (ESR)</i>	<i>Methane dry reforming (MDR)</i>
$\chi_{C_2H_5OH} = \frac{\dot{n}_{C_2H_5OH,in} - \dot{n}_{C_2H_5OH,out}}{\dot{n}_{C_2H_5OH,in}} \times 100$	$\chi_{CH_4} = \frac{\dot{n}_{CH_4,in} - \dot{n}_{CH_4,out}}{\dot{n}_{CH_4,in}} \times 100$
$S_{H_2} = \frac{\dot{n}_{H_2,out}}{\dot{n}_{H_2,out} + \dot{n}_{CH_4,out} + \dot{n}_{CO_2,out} + \dot{n}_{CO,out}} \times 100$	$S_{H_2} = \frac{\dot{n}_{H_2,out}}{\dot{n}_{H_2,out} + \dot{n}_{CO,out}} \times 100$
$\dot{V}_{H_2} = \dot{V}_{gas,out} \times S_{H_2}$	$\dot{V}_{H_2} = \dot{V}_{gas,out} \times S_{H_2}$
$\psi_{H_2} = \frac{\dot{n}_{H_2,out}}{6 \times \dot{n}_{C_2H_5OH,in}}$	$\psi_{H_2} = \frac{\dot{n}_{H_2,out}}{2 \times \dot{n}_{CH_4,in}}$

where  $\dot{n}_i$  are the molar flow rates (mol·min<sup>-1</sup>) of each specie and  $\dot{V}_{gas,out}$  is the total volumetric flow rate (ml·min<sup>-1</sup>); *in* and *out* labels were used for inlet and outlet flows, respectively.

Moreover, a vacuum chamber with electrical and fluidic connections was designed and fabricated, as shown in **Figure 2.23**. On the one hand, this station was used to investigate the start-up process of the two  $\mu$ reformers (bulk and suspended) by analyzing the energy consumption and the time required to achieve the suitable operating temperatures when a vacuum of *ca.* 1 Pa and an electrical power of 5 W were applied. On the other hand, the station allowed

studying the ESR in a suspended  $\mu$ reformer encapsulated as a standalone device by using the integrated heater to reach the operation temperature autonomously.



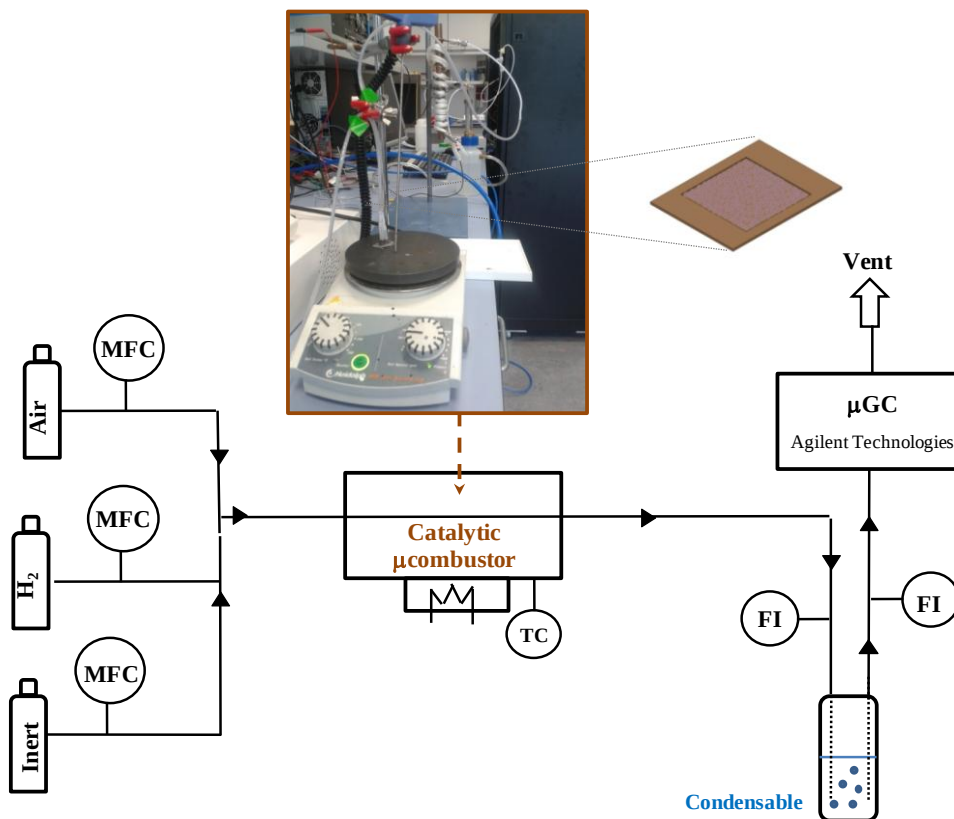
**Figure 2.23:** Vacuum station fabricated with detail of electrical connections.

### 2.6.2. Catalytic combustion of hydrogen

A  $\mu$ combustor encapsulated by a SD-2 glass cover with two micro holes was filled with a mesoporous catalyst by an infiltration process induced by a pressure gradient. The fluidic connectors were bonded using a high-temperature cement (Nural 30®). The reaction performance was accomplished in a lab scale setup, as shown in **Figure 2.24**.

The influence of reaction temperature and air flow rate was assessed separately. The gas feed mixture was provided by mass flow controllers (Bronkhorst). A hotplate (Heidolph) was used for heating the  $\mu$ combustor and a thermocouple was placed on the hot zone as temperature controller. The temperature range chosen for testing was from 120 to 200 °C (minimum values to get hydrogen combustion in agreement with [33]). Furthermore, the influence of air flow rate was studied at 150 °C, i.e. 60 ml·min<sup>-1</sup>, 100 ml·min<sup>-1</sup> and 120 ml·min<sup>-1</sup>. This range was selected considering the thermodynamic calculations from **Chapter III** and the air density at this operating temperature. The volumetric flow rate of pure hydrogen was fixed at 12.5 ml·min<sup>-1</sup>. According also to the thermodynamic calculations detailed in **Chapter III**, this value corresponds to the maximum amount of hydrogen that the  $\mu$ combustor has to oxidize. This occurs during the start-up process when the  $\mu$ reformer works properly but not yet the  $\mu$ SOFCs, so all the hydrogen generated by the  $\mu$ reformer has to be oxidized in the  $\mu$ combustor.

All measurements were carried out under steady-state flow conditions. After collecting the condensable water from the reactor, an online automated microGC (Agilent Technologies) was used to measure the gas effluent composition. Outlet molar flow rates of the non-condensable components ( $H_2$ ,  $O_2$ ) were calculated from the measured composition (by GC) and total volumetric flow rate of the gaseous outlet stream (bubble soap meter), whereas outlet flow rate of water was evaluated by closing element balances.

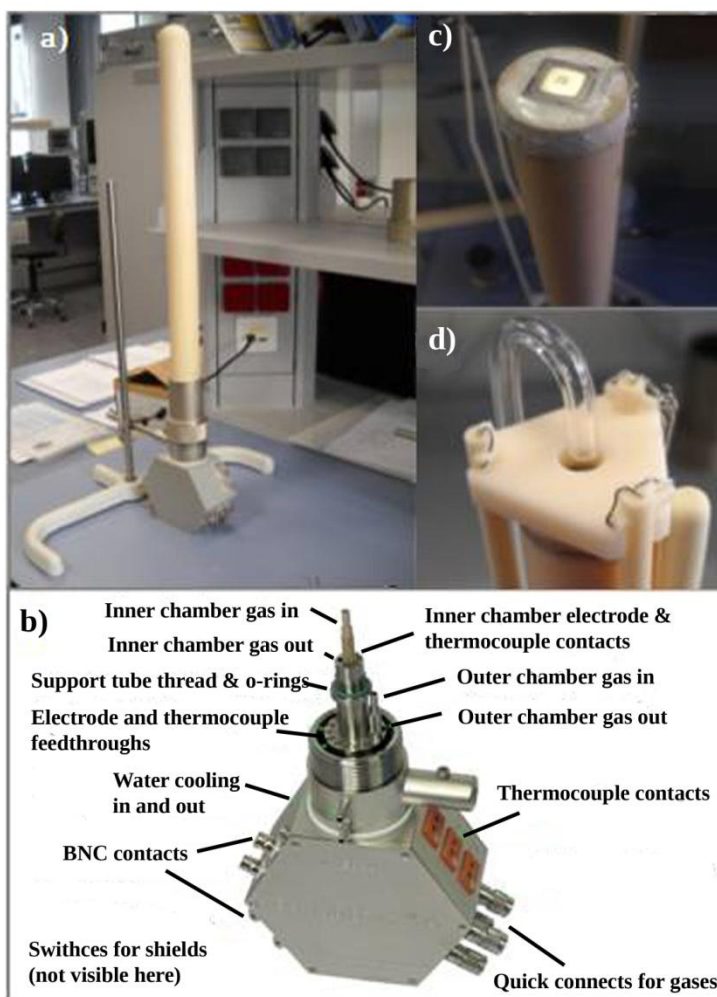


**Figure 2.24:** Schematic representation of the experimental setup for catalytic combustion of  $H_2$ , where *MFC* indicates a mass flow controller, *TC* a thermocouple and *FI* a flow indicator.

### 2.6.3. Electrochemical $\mu$ SOFC measurement

The experimental setup to electrochemically characterize the  $\mu$ SOFCs was composed by (a) a ProboStat™ NorECs system, (b) a tubular furnace and a temperature controller, (c) gas flow meters and a humidifier, (d) an impedance analyzer, and (e) a potentiostat / galvanostat. Images of the ProboStat™ system and the base unit with its feedthroughs are shown in **Figure 2.25a** and **b**,

respectively. The special design of the Probostat™ allows the separation of the oxidizing and reducing atmospheres at high temperatures (up to 900 °C) through a hermetic sealing. The sample was placed on top of the alumina tube and sealed by a silver ring and Ceramabond™ (see **Figure 2.25c**). Three springs provided the needed pressure for a proper sealing as depicted in **Figure 2.25d**. The collection of current was made by placing Pt meshes on top and back sides of the sample, avoiding direct contact with the membrane to prevent breaking it.



**Figure 2.25:** Scheme of the Probostat™ system (a) general view and (b) detail of the elements included, (c) image of one sample sealed on top of the alumina tube and (d) detail of the top side of the alumina tube.



## 2.7 Simulations and modeling

Computational Fluid Dynamics (CFD) is related to the analysis of systems involving fluid flow, heat transfer and associated phenomena, such as chemical reactions, by means of computer-based simulations.

CFD approach is based on the conservation laws of physics and heat transfer, i.e. conservation of mass, which is expressed in the form of the continuity equation (equation 2.8), Newton’s law of motion that implies the conservation of momentum described using Navier-Stokes equations (equation 2.9) and the conservation of energy from the first law of thermodynamics (equation 2.10).

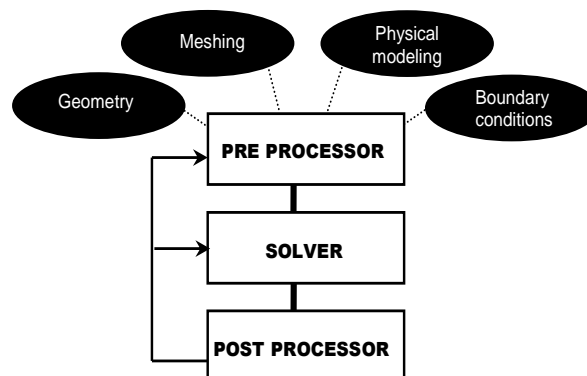
$$\text{mass continuity: } \frac{\partial \rho}{\partial t} + \nabla \cdot (\rho \vec{v}) = 0 \quad (2.8)$$

$$\text{momentum: } \rho \left( \frac{\partial \vec{v}}{\partial t} + \vec{v} \cdot \nabla \vec{v} \right) = -\nabla P + \nabla \cdot \tau + F \quad (2.9)$$

$$\text{energy: } \frac{\partial E}{\partial t} + \nabla \cdot (\vec{v}(E + P)) = 0 \quad (2.10)$$

Where  $\rho$  is the mass density,  $\vec{v}$  is the flow velocity,  $P$  is the pressure and  $\tau$  is the stress tensor (both correspond to the internal forces related to the velocity field),  $F$  is the external of body forces (e.g. gravity) and  $E$  is the energy.

In order to provide easy access to their solving power, all commercial CFD packages include sophisticated user interfaces to input the problem parameters and examine the results. As depicted in **Figure 2.24**, all codes contain three main elements: (a) a *pre-processor*, (b) a *solver* and (c) a *post-processor*.



**Figure 2.24:** Schematic procedure of CFD analysis.

*(a) Pre-processor*

The pre-processor consists of the input of a problem to a CFD program by means of a user-friendly interface and the subsequent transformation of this input into a form suitable by the solver. The main steps involved at the pre-processing stage are,

- definition of the geometry,
- grid generation by the sub-division of the geometry into smaller non-overlapping sub-domains, i.e. a mesh composed of discrete elements,
- selection of the physical and chemical phenomena that need to be modeled,
- definition of fluid and solid properties, and specification of appropriate boundary conditions.

*(b) Solver*

There are different numerical solution methods for representing and evaluating the partial differential equations, e.g. Finite Difference Method (FDM), Finite Element Method (FEM) or Finite Volume Method (FVM). The analysis of the numerical algorithm consists of the following steps,

- integration of the governing equations of fluid flow over all the discrete elements of the computational domain,
- conversion of the resulting integral equations into a set of algebraic equations (named as discretization process),
- solution of the algebraic equations by an iterative method.

*(c) Post processor*

The post processor allows easy visualization and quantitative analysis of the results, for example by generating images and graphics or defining locations for quantitative calculations.

❖ ***In this work***, the general CFD procedure was followed to investigate the thermal management of the  $\mu$ SOFC PG proposed, i.e. the steady state and start-up processes. The  $\mu$ SOFC PG geometry was created by CAD software (SolidWorks). A structured mesh was defined to divide the geometric domain into discrete elements. Cut-cell Cartesian method, based on the use of a large fraction of small hexahedron cells, was chosen for meshing. Global and local mesh settings were selected to keep the mesh metrics within suitable values avoiding large and poorly shaped mesh elements and ensuring a good mesh

## **CHAPTER II. Experimental methods**

---

quality (cell skewness greater than 0.95 and minimum orthogonal quality at least more than 0.1). After meshing, the physical model was defined. All the governing equations were solved in ANSYS (version 13.0) by FVM, using a pressure-based FLUENT solver. First Order Up-Wind Discretization scheme was selected for calculating the convection terms of each governing equation. Semi-Implicit Method for Pressure-Linked Equations solution method (SIMPLE) was selected for iterative calculation of pressure and velocity. The evaluation of gradient simulations was computed according to Least Squares Cell-Based method. The First Order Implicit formulation was employed for transient simulations and the Fixed Time Stepping method is used to obtain the transient solution.

## References

- [1] Kilby, J. S. Invention of the Integrated Circuit, *IEEE Trans. Electronic Devices* **23**, 648–654 (1976).
- [2] Eason, R. Pulsed Laser Deposition of Thin Films: Applications-Led Growth of Functional Materials, Wiley (2007).
- [3] Caricato, A. P. *et al.* Excimer pulsed laser deposition and annealing of YSZ nanometric films on Si substrates. *Appl. Surf. Sci.* **248**, 270–275 (2005).
- [4] Heiroth, S. *et al.* Yttria-stabilized zirconia thin films by pulsed laser deposition: Microstructural and compositional control. *J. Eur. Ceram. Soc.* **30**, 489–495 (2010).
- [5] Hobein, B., Tietz, F., Stöver, D. & Kreutz, E. W. Pulsed laser deposition of yttria stabilized zirconia for solid oxide fuel cell applications. *J. Power Sources* **105**, 239–242 (2002).
- [6] Joo, J. H. & Choi, G. M. Electrical conductivity of YSZ film grown by pulsed laser deposition. *Solid State Ionics* **177**, 1053–1057 (2006).
- [7] Rupp, J. L. M., Infortuna, A. & Gauckler, L. J. Microstrain and self-limited grain growth in nanocrystalline ceria ceramics. *Acta Mater.* **54**, 1721–1730 (2006).
- [8] Jung, W., Dereux, J.O., Chueh, W.C., Hao, Y. & Haile, S.M. High electrode activity of nanostructured, columnar ceria films for solid oxide fuel cells, *Energy Environ. Sci.* **5**, 8682–8689 (2012).
- [9] Infortuna, A., Harvey, A. S. & Gauckler, L. J. Microstructures of CGO and YSZ Thin Films by Pulsed Laser Deposition. *Adv. Funct. Mater.* **18**, 127–135 (2008).
- [10] Januschewsky, J., Ahrens, M., Opitz, A., Kubel, F. & Fleig, J. Optimized  $\text{La}_{0.6}\text{Sr}_{0.4}\text{CoO}_{3-\delta}$  Thin-Film Electrodes with Extremely Fast Oxygen-Reduction Kinetics. *Adv. Funct. Mater.* **19**, 3151–3156 (2009).
- [11] Liu, Q., Dong, X., Xiao, G., Zhao, F. & Chen, F. A Novel Electrode Material for Symmetrical SOFCs. *Adv. Mater.* **22**, 5478–5482 (2010).
- [12] Liu, Q. *et al.*  $\text{Sr}_2\text{Fe}_{1.5}\text{Mo}_{0.5}\text{O}_{6-\delta}$  as a regenerative anode for solid oxide fuel cells. *J. Power Sources* **196**, 9148–9153 (2011).
- [13] Llorca, J., Casanovas, A., Trifonov, T., Rodríguez, A. & Alcubilla, R. First use of macroporous silicon loaded with catalyst film for a chemical reaction: A microreformer for producing hydrogen from ethanol steam reforming. *J. Catal.* **255**, 228–233 (2008).
- [14] López, E. *et al.* Ethanol steam reforming for hydrogen generation over structured catalysts. *Int. J. Hydrogen Energy* **38**, 4418–4428 (2013).

- [15] Almar, L. *et al.* High-temperature long-term stable ordered mesoporous Ni-CGO as an anode for solid oxide fuel cells. *J. Mater. Chem. A* **1**, 4531–4538 (2013).
- [16] Almar, L. *et al.* High-surface-area ordered mesoporous oxides for continuous operation in high temperature energy applications. *J. Mater. Chem. A* **2**, 3134–3141 (2014).
- [17] Maluf, N. An Introduction to Microelectromechanical Systems Engineering. *Artech House, Inc.* (2000).
- [18] Krebs, H.U. *et al.* Pulsed laser deposition (PLD) - a versatile thin film technique. *Adv. Solid State Phys.* **43**, 505–517 (2003).
- [19] Nordby, H. Deposition of Thin Film Electrolyte by Pulsed Laser Deposition (PLD) for micro-SOFC Development. Master's thesis, Norwegian University of Science and Technology (2012).
- [20] Petrov, I., Barna, P. B., Hultman, L. & Greene, J. E. Microstructural evolution during film growth. *J. Vac. Sci. Technol. A* **21**, (2003).
- [21] Mazor, A., Srolovitz, D. J., Hagan, P. S., Bukiet & G., B. Columnar growth in thin films. *Phys. Rev. Lett.* **60**, 424–427 (1988).
- [22] Garbayo, I. *et al.* Pinhole-free YSZ self-supported membranes for micro solid oxide fuel cell applications. *Solid State Ionics* **216**, 64–68 (2012).
- [23] Ashfold, M. N. R., Claeysens, F., Fuge, G. M. & Henley, S. J. Pulsed laser ablation and deposition of thin films. *Chem. Soc. Rev.* **33**, 23–31 (2004).
- [24] Garbayo, I. *et al.* Electrical characterization of thermomechanically stable YSZ membranes for micro solid oxide fuel cells applications. *Solid State Ionics* **181**, 322–331 (2010).
- [25] Divins, N. J., López, E., Rodríguez, Á., Vega, D. & Llorca, J. Bio-ethanol steam reforming and autothermal reforming in 3- $\mu\text{m}$  channels coated with RhPd/CeO<sub>2</sub> for hydrogen generation. *Chem. Eng. Process. Process Intensif.* **64**, 31–37 (2013).
- [26] Serrano-Lotina, A. & Daza, L. Influence of the operating parameters over dry reforming of methane to syngas. *Int. J. Hydrogen Energy* **39**, 4089–4094 (2014).
- [27] Santis-Alvarez, A. J., Büchel, R., Hild, N., Stark, W. J. & Poulidakos, D. Comparison of flame-made rhodium on Al<sub>2</sub>O<sub>3</sub> or Ce<sub>0.5</sub>Zr<sub>0.5</sub>O<sub>2</sub> supports for the partial oxidation of methane. *Appl. Catal. A Gen.* **469**, 275–283 (2014).
- [28] Pakhare, D. & Spivey, J. A review of dry (CO<sub>2</sub>) reforming of methane over noble metal catalysts. *Chem. Soc. Rev.* **43**, 7813–7817 (2014).

- [29] Bitter, J. H., Seshan, K. & Lercher, J. A. Mono and Bifunctional Pathways of CO<sub>2</sub>/CH<sub>4</sub> Reforming over Pt and Rh Based Catalysts. *J. Catal.* **176**, 93–101 (1998).
- [30] MacDonald, J.R. Impedance spectroscopy: emphasizing solid materials and systems. *John Wiley & Sons Australia, Limited* (1987).
- [31] Johnson, D. Zplot, Zview Electrochemical Impedance Software, version 2.3b. *Scribner Associates, Inc.* (2000).
- [32] Ali, S. Z. *et al.* High Temperature SQI CMOS Tungsten Micro-Heaters. *Sensors, 2006. 5th IEEE Conf.* 847–850 (2006).
- [33] Haruta, M. & Sano, H. Catalytic combustion of hydrogen I—Its role in hydrogen utilization system and screening of catalyst materials. *Int. J. Hydrogen Energy* **6**, 601–608 (1981).



## **III. THERMAL MANAGEMENT**





<b>3.1. Introduction.....</b>	<b>79</b>
<b>3.2. Thermal management strategies for a specific <math>\mu</math>SOFC PG.....</b>	<b>83</b>
<b>3.3. Geometric model.....</b>	<b>85</b>
3.3.1. System architecture and fluidics.....	85
3.3.2. Components design and specifications.....	86
3.3.2.1. Fuel processing unit.....	87
3.3.2.2. Micro-SOFC stack.....	88
3.3.2.3. Post combustion unit.....	89
<b>3.4. Physical modeling.....</b>	<b>90</b>
3.4.1. Meshing.....	90
3.4.2. Materials and boundary conditions.....	91
3.4.3. Components modeling and initial conditions.....	93
<b>3.5. Results and discussion.....</b>	<b>96</b>
3.5.1. Case study I: steady-state operation mode.....	96
3.5.1.1. Simulation details.....	96
3.5.1.2. Results.....	96
3.5.2. Case study II: transient operation mode.....	100
3.5.2.1. Simulation details.....	100
3.5.2.2. Results.....	102
<b>3.6. Conclusions.....</b>	<b>108</b>



### 3.1. Introduction

Micro fuel cell power generators compare favorably with batteries since they are small, lightweight, and efficient. However, the generation of 1 electric watt by a SOFC-based portable power device with efficiencies of 40-60 % [1] involves heat losses that can be as large as 1.5 thermal watts. Therefore, the **thermal management** is an important challenge for a  $\mu$ SOFC PG that operates at high temperatures (873-1073 K<sup>1</sup>). These temperatures are required for (i) the use of hydrocarbons as fuel, since reforming reactions are endothermic and take place at temperatures above 773 K, and (ii) the use of  $\mu$ SOFCs as fuel cells, since high temperatures are necessary to achieve a high-enough O<sup>2-</sup> ion diffusion through the electrolyte [2]. In order to be feasible, the  $\mu$ SOFC PG has to be thermally self-sustained in the steady state, i.e. well-insulated from the environment by designing a hot module which does not increase significantly its overall size. Apart from reducing thermal heat losses in steady state mode, the thermal management of a  $\mu$ SOFC PG for portable applications must enable a fast start-up process with minimum energy consumption.

The fundamental modes of heat transfer in a general system are **conduction**, **convection** and **radiation** [3].

(a) **Conduction** is described by Fourier's Law (equation 3.1),

$$\dot{q}_{cd} = -\kappa \cdot A \cdot \nabla T \quad 3.1$$

where  $\dot{q}_{cd}$  is the heat flow (W),  $\kappa$  is the thermal conductivity (W·K<sup>-1</sup>·m<sup>-1</sup>),  $A$  is the cross-sectional area normal to the direction of the thermal gradient (m<sup>2</sup>), and  $\nabla T$  is the thermal gradient (K·m<sup>-1</sup>).

(b) **Convection** follows the Newton's Law of Cooling (equation 3.2),

$$\dot{q}_{cv} = h \cdot A \cdot \Delta T \quad 3.2$$

where  $\dot{q}_{cv}$  is the heat flow (W),  $h$  is the convective heat transfer coefficient (W·K<sup>-1</sup>·m<sup>-2</sup>),  $A$  is the external surface area (m<sup>2</sup>) and  $T$  is the temperature (K).

(c) Finally, the amount of heat transfer due to **radiation** is characterized by its emissivity and can be calculated as equation 3.3,

$$\dot{q}_r = \varepsilon \cdot \sigma \cdot A \cdot T^4 \quad 3.3$$

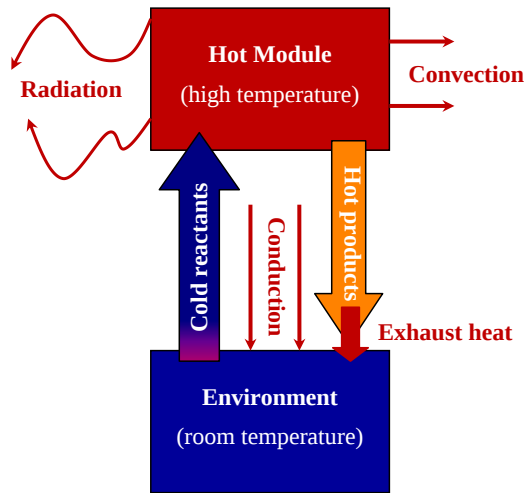
where  $\dot{q}_r$  is the heat flow (W),  $\varepsilon$  is the emissivity of the emitter,  $\sigma$  is the Stefan-

---

<sup>1</sup>In this Chapter III, the temperature unit is Kelvin in order to be coherent with thermal parameters used in the FVM simulations.

Boltzmann constant ( $5.7 \times 10^{-8} \text{ W} \cdot \text{m}^{-2} \cdot \text{K}^{-4}$ ),  $A$  is the external surface area of the emitter ( $\text{m}^2$ ) and  $T$  is the temperature of the emitter (K).

As depicted in **Figure 3.1**, the thermal losses from the hot module of a  $\mu\text{SOFC}$  PG can take place through the insulator via conduction, through the external faces via convection and radiation, and through the hot exhaust gases via convection.



**Figure 3.1:** Sketch of the different heat-loss pathways occurring in the hot module of a  $\mu\text{SOFC}$  PG.

Mathematical models can help elucidating the heat-transfer phenomena within a general  $\mu\text{SOFC}$  PG. In this sense, several models have been recently proposed to investigate the thermal management of SOFC-based micro-power plants. An exergy analysis reported by Hotz et al. yielded a maximum efficiency of 21.9 % by adjusting the SOFC inlet temperature to 900 K, a cell voltage to 0.78 V and air/fuel ratio to 1.2 [4]. By using thermal-flow finite element simulations, Bieberle-Hütter and co-workers investigated the steady-state regime of different system configurations [5]. A range of electrical power outputs, heat transfer through the insulation and system volumes were analyzed assuming a single operating temperature inside the whole micro system. The results of this work showed that for systems with smaller electrical power outputs, it is more difficult to find an insulation material with a low enough thermal conductivity; whereas systems with lower heat transfer towards the surroundings lead to larger volumes. Meier et al. extended this approach providing an analytical method for a particular layout of a  $\mu\text{SOFC}$  PG [6]. Considering overall electrical efficiencies between 20 and 40% and the wide

range of possible heat-loss-to-power ratios, the study concludes that no universally applicable thermal design configuration is found for 2.5 to 20 W systems and a suited configuration must be elaborated for a specific application. In the case of  $\mu$ SOFC systems with a power output of up to 10 W, the study suggests that a vacuum packaged thermal insulation is desirable in order to obtain a high volumetric power density.

As previously mentioned, the start-up (transient regime) of a  $\mu$ SOFC PG is crucial for the final feasibility of the device, since it has to be fast, but also consume as low energy as possible. The energy required for the start-up process can be supplied by an electrical or chemical source, i.e. using the heat released from an electric heater by Joule's effect or by converting the chemical energy of a fuel into heat by combustion. Only few works have been published regarding the start-up. Krummenacher et al. [7] showed a start-up via homogeneous combustion of hydrocarbons, i.e. n-decane and n-hexadecane. The process was initiated by an ignition spark in a separate chamber close to the device that needs to be heated up. However, this method can generate very high temperatures unsuitable for  $\mu$ SOFC applications. Jung et al. [8] presented a start-up method where a metallic monolith was electrically heated up to the operation temperature for partial oxidation of methane. In this case, the entire energy was provided by an electrical source. Another interesting start-up method reported is based on use the catalytic activity of  $H_2$  on platinum at room temperature to start-up a fuel cell system [9]. The hydrogen needed comes from a hydrogen buffer, which is refilled in normal operation by a fuel reformer. The drawback of this system is that requires a complicated purification process of the reformat gas and the difficulty of hydrogen storage. Poulidakos et al. [10, 11] have proposed a hybrid post-combustor in which a heater embedded inside a catalytic bed reactor allowed to achieve the ignition temperature of butane. Then, the fuel was catalytically oxidized until the system reached the steady-state. This method was proven to be faster and energetically more efficient than electrical heating alone, achieving a time reduction of two minutes by a 10x higher electrical energy input.

Although all the existing works represent an excellent first approach to understand the complexity of a SOFC-based micro system, an explicit design of the whole  $\mu$ SOFC PG, including the geometry and experimental data from the individual elements, is required to advance in the optimization of the stacking configuration and the heat management strategy.

**This chapter** presents the thermal analysis of a new  $\mu$ SOFC PG by using FVM simulations. The methodology used is described in *Section 2.7* of **Chapter II**. The thermal modeling aims to understand the  $\mu$ SOFC PG's steady-state and transient regimes, by defining a geometric model (*Section 3.3*), a proper mesh (*Section 3.4.1*), and the boundary and initial conditions (*Section 3.4.2* and *Section 3.4.3*, respectively). Different thermal insulation configurations were analyzed to ensure a thermally self-sustained  $\mu$ SOFC regime and a proper temperature distribution in the fuel processor unit and fuel cell stack. Moreover, a hybrid start-up sequence was also optimized in order to demonstrate a rapid transition from the standby to the steady-state regimes. By a combination of several micro heaters, which selectively heat the main components ( $\mu$ reformer and fuel cell membranes), and the use of heat released during the oxidation reactions in fuel cells and CPU, a reasonable energy and time consumption were achieved for the start-up process.

### 3.2. Thermal management strategies for a specific $\mu$ SOFC PG

The  $\mu$ SOFC PG based on 1 electric watt output and fuelled with ethanol was developed following several thermal management strategies to reduce the thermal losses, homogenize the temperature within the system in steady-state and optimize its start-up. The main approaches to achieve this goal are:

*(a) Very low  $k$  insulating materials were selected.*

In large-scale, conductive heat losses can be reduced via the addition of thermal insulation layers, but the  $\mu$ SOFC PG device volume cannot increase disproportionately since specific power per unit volume is a key feature for portable applications. So, in order to avoid adding several centimeters of insulation, a very low  $\kappa$  insulating material should be selected. The best insulation is vacuum, but this choice requires the development of thermally-stable and vacuum-tight sealing materials. Another attractive choice is the use of aerogels, due to its extremely low density and low  $\kappa$ . Several thermal insulation configurations were analyzed as presented in *Section 3.5.1* taking into account reasonable insulator thicknesses and the typical  $\kappa$  values of state of the art of insulators.

*(b) Low-emissivity materials were employed.*

By including reflective shields or using low-emissivity materials, the radiative heat losses are minimized [3]. Some materials have emissivities of 0.1 or less and can operate at high temperatures, such as aluminum foils or aerogels.

*(c) Design features in the  $\mu$ SOFCs and  $\mu$ reformers to enhance heat transfer.*

Microstructures with low thermal mass inertia, as well as thermally isolated contribute to a rapid start-up process. Since the FPU and  $\mu$ SOFCs operating temperatures are critical for a proper operation of the whole device, specific features were included in our design. In particular,  $\mu$ SOFC design was based on a large-area free-standing membrane supported on a silicon structure to achieve a rapid start-up. The membrane also included a grid of doped-silicon slabs. On one hand, these doped-silicon slabs were the support for the integration of a micro heater which allows directly heating the active part of the cell and further accelerating the start-up process. On the other hand, the silicon grid acts as a heat spreader in the steady-state allowing a proper heat release from the membrane and its thermal homogenization. Moreover, the

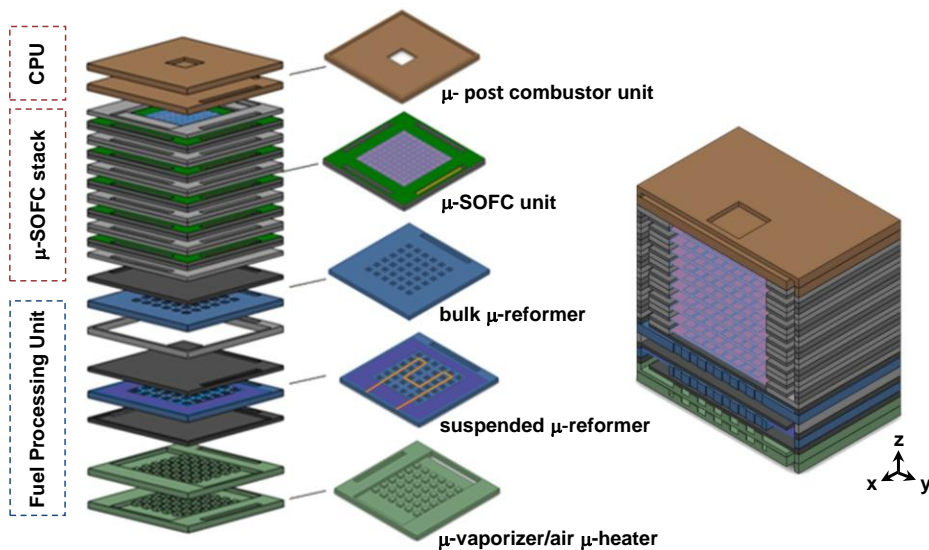


suspended  $\mu$ reformer design was based on a silicon platform with an active area formed by an array of vertical micro channels and suspended on a thermally insulating silicon nitride membrane. The active part also included a micro heater. This thermally isolated microstructure allows a quick start-up process. The suitability of these features was evaluated by simulations (see *Section 3.6.1.1* and *Section 3.6.2*, respectively).

### 3.3. Geometric model

#### 3.3.1. System architecture and fluidics

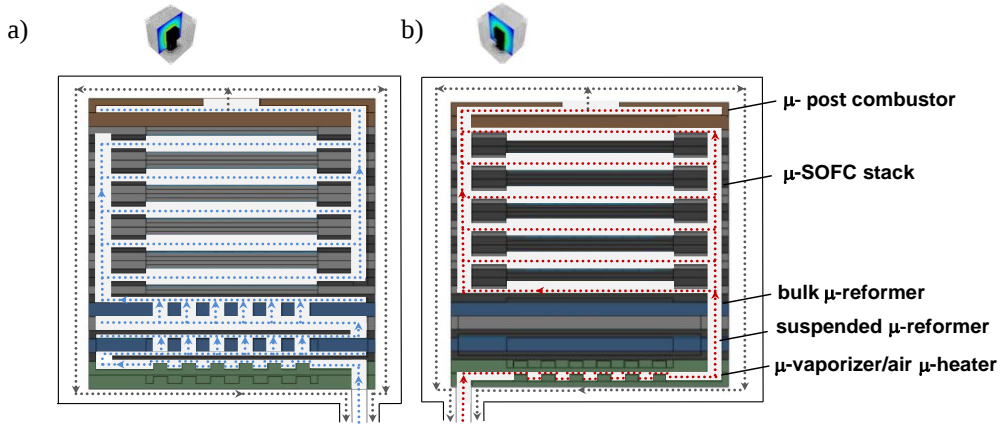
A layout of the  $\mu$ SOFC PG proposed in this work is depicted in **Figure 3.1**. The system was based on vertically stacked silicon chips ( $10 \times 10 \text{ mm}^2$ ) covered by a thermal insulation enclosing the hot module (not depicted in the figure for the sake of clarity). The  $\mu$ SOFC stack was sandwiched between the FPU and the CPU. The  $\mu$ SOFC stack was composed by ten individual fuel cells and their corresponding spacers to allow a proper fuel distribution. Due to the use of ethanol as fuel, the FPU consisted of an evaporator for the change phase of liquid fuel and two  $\mu$ reformers where the ethanol steam reforming taken place. The CPU was based on a bed-reactor placed after the  $\mu$ SOFC stack. As previously mentioned, additional components like the fuel tank or the power management unit were not considered in the present work.



**Figure 3.1:** Layout of the different elements vertically stacked and detail of the main components of the  $\mu$ SOFC PG, namely, a  $\mu$ vaporizer and air  $\mu$ heater, two types of  $\mu$ reformer, a  $\mu$ SOFC stack composed by ten  $\mu$ SOFC units and separators (in grey) and a  $\mu$ post combustor.

Two orthogonal cross-sections of the system are represented in **Figure 3.2**. Fuel and air flow pathways are detailed in **Figure 3.2a** and **Figure 3.2b**, respectively. Due to the proposed configuration, a cross-flow configuration was achieved by lateral openings in  $\mu$ SOFC and  $\mu$ reformer units.

The ethanol-water mixture was vaporized inside the  $\mu$ vaporizer before reaching the first  $\mu$ reformer. A first fraction of ethanol was reformed there, generating a product mainly containing  $H_2$ ,  $CO$  and  $CO_2$ . The remaining ethanol was consumed in the second reformer, generating extra amounts of hydrogen and carbon oxides. In parallel, the air flowed through perpendicular channels after being heated inside the air  $\mu$ heater. Reformed fuel and air flowed, respectively, towards the anode and cathode sides of the consecutive  $\mu$ SOFC stacked cells. Due to the electrochemical reactions taken place at the fuel cells, electrical power and heat were produced. The unreacted fuel and air were mixed in the catalytic  $\mu$ post combustor placed at the end of the circuit. Released heat from the  $\mu$ SOFC stack and the CPU was used to keep the  $\mu$ reformers at the proper operation temperature. The exhaust gas finally went out concentrically to the hot module also giving heat to the system.



**Figure 3.2:** Orthogonal cross-section schemes of the  $\mu$ SOFC PG system showing the flow pathways of (a) the fuel and (b) air. The different components of the vertical stack are labelled.

### 3.3.2. Components design and specifications<sup>2</sup>

As previously mentioned, the hot module of the system includes all the required components. This hot module was defined by an insulation shell of a variable thickness. The geometry of each component included in the hot module was determined to account for specific thermal requirements desired for the  $\mu$ SOFC PG, namely:

---

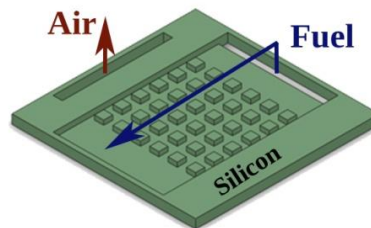
<sup>2</sup> Simplified structures with the essential features were simulated in order to achieve a reasonable mesh and reduce the calculation time.

- (a) Operating temperatures inside the hot module between 873 K and 1073 K to ensure a correct operation of the fuel cells and the  $\mu$ reformers.
- (b) A homogeneous distribution of these temperatures to avoid thermo-mechanical stresses, especially in the fuel cell membranes.
- (c) A moderate temperature (below 323 K) in the external surface of the insulating material.
- (d) A rapid and efficient transition to the steady-state.

The next sections are devoted to present and shortly discuss the chosen geometry for each component according to these criteria.

### 3.3.2.1. Fuel processing unit

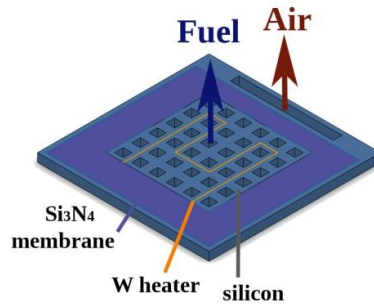
The architecture of the  $\mu$ vaporizer and air  $\mu$ heater was based on a set of micro pillars distributed along a 300  $\mu$ m thick bed defined on a 500  $\mu$ m thick silicon substrate as shown in **Figure 3.3**. The micro pillars were chosen to maximize the contact area of solid and fluid, thus enhancing the heat transfer, as suggested in [12, 13]. The projected area was 6x6 mm<sup>2</sup>, but presented a total active area of 54 mm<sup>2</sup> that was achieved by a square micro pillar array (36 micro pillars with 500  $\mu$ m diameter, 250  $\mu$ m height and 1 mm edge-to-edge distance in the x and y directions). This approach, considered for a reasonable mesh, could be extended by reducing the size of  $\mu$ pillars e.g. to 100  $\mu$ m diameter, thus increasing the total active area two orders of magnitude ( $\sim$ 3.5 cm<sup>2</sup>). In the case of the vaporizer, the micro pillars avoid bubble formation in the fluid during the evaporation of the liquid fuel [12, 13]. A tungsten micro heater was placed on the backside of the vaporizer that allowed an independent heating of this element.



**Figure 3.3:**  $\mu$ vaporizer based on a set of micro pillars distributed along a cavity defined on a silicon chip.

Two different  $\mu$ reformers in series were required in the FPU to generate enough hydrogen to fuel the 1We-SOFC stack according to the experimental results presented in **Chapter IV**. This double reformer approach allowed fulfilling the necessities of two different operating conditions, i.e. transient and

steady regimes. The active area of both  $\mu$ reformers consisted of an array of vertical micro channels crossing a 500  $\mu\text{m}$  thick silicon chip, where the catalyst was deposited on their walls. The high surface-to-volume ratio of the micro channels, coated with the catalytic system, led to higher performance of the fuel steam reforming reaction. The transient regime requires fast heating and low heat loss; therefore a first  $\mu$ reformer in which the active area was suspended on a thermally insulating silicon nitride membrane and heated up by an integrated heater (2.75  $\text{mm}^2$  of area and 300 nm in thickness) were proposed (see **Figure 3.4**). On the other hand, a bulk  $\mu$ reformer thermally connected to the silicon substrate was exclusively operated during the steady regime, i.e. when heated up to 823 K by using excess heat produced on  $\mu\text{SOFC}$  stack and CPU under operation.



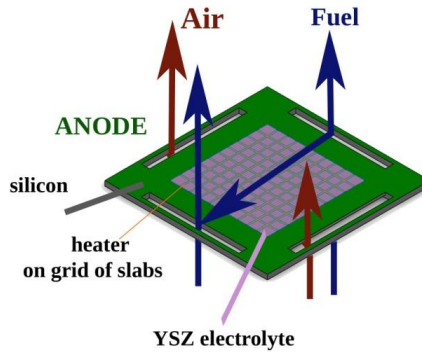
**Figure 3.4:** suspended  $\mu$ reformer including an insulating silicon nitride membrane and an integrated tungsten heater.

Between the two reformers, a 500  $\mu\text{m}$  thick glass spacer was incorporated in order to reduce the start-up time of the  $\mu\text{SOFC}$  PG by insulating the FPU which required heat from an auxiliary power source. A special glass of HOYA OPTICS with minimum thermal mismatch with silicon (i.e. similar thermal expansion coefficient) was selected to separate the endothermic and exothermic parts and helping to accelerate the start-up process.

### 3.3.2.2. Micro-SOFC stack

The  $\mu\text{SOFC}$  stack consisted of ten single  $\mu\text{SOFC}$  cells vertically stacked and connected electrically in series and fluidically in parallel. The  $\mu\text{SOFC}$  cells were mounted by pairs, always facing two consecutive anodes and/or cathodes (i.e. cathode/electrolyte/anode-anode/electrolyte/cathode). This configuration reduced to half the number of spacers and, also, the mass of  $\mu\text{SOFC}$  stack.

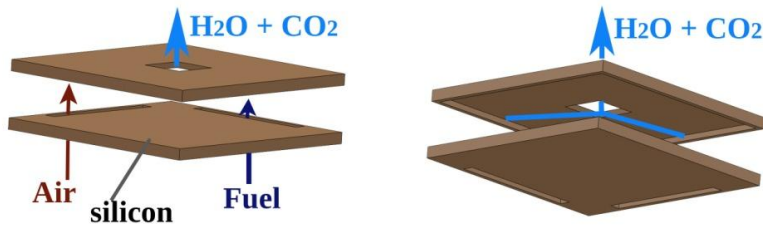
The  $\mu$ SOFC design was based on a large-area free-standing membrane ( $6 \times 6 \text{ mm}^2$ ) supported on  $300 \text{ }\mu\text{m}$  thick silicon structure. The membranes also included an integrated tungsten micro heater ( $0.81 \text{ mm}^2$  of area and  $300 \text{ nm}$  in thickness) for directly heating up the active part of the device and facilitating the start-up process. Moreover, an alternative design that includes a grid of doped-silicon slabs ( $45 \text{ }\mu\text{m}$  wide and  $500 \text{ nm}$  in thickness), as depicted in **Figure 3.5**, was also evaluated [14-16].



**Figure 3.5:**  $\mu$ SOFC anode design including the free-standing membrane as electrolyte and the heater embedded on the grid of silicon slabs.

### 3.3.2.3. Post combustion unit

The CPU design was based on a  $500 \text{ }\mu\text{m}$  thick silicon substrate with a cavity ( $200 \text{ }\mu\text{m}$  depth) filled by a mesoporous catalyst with a large contact area of  $\sim 6 \text{ m}^2$ , leading to high hydrogen fuel conversions (see details in **Chapter V**). As represented in **Figure 3.6**, remaining fuel after the SOFC stack entered into the cavity and was mixed with air forming either water (with hydrogen) or carbon oxides (with ethanol). The exhaust gas went out through a micro channel between the hot module and the insulator defined by a heat exchange (made of stainless steel) where flowed vertically downwards to the outlet and concentrically to the hot module, therefore allowing partial heat recovery (see **Figure 3.2**).



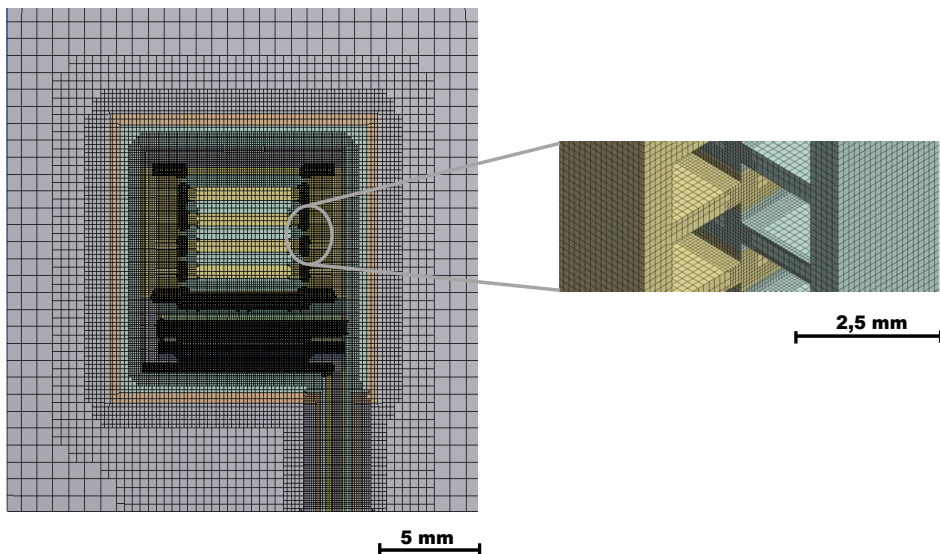
**Figure 3.6:**  $\mu$ post combustor unit design based on a cavity filled by a mesoporous catalyst.

## 3.4. Physical modeling

### 3.4.1. Meshing

The quality of the mesh has a significant impact on the accuracy, convergence and speed of the computational solutions. The complex 3D geometry presented required a structured meshing without independent subdivisions that fits perfectly the domains and reduces the number of inaccuracies that could propagate through them. Since the model geometry did not have curves or sloping surfaces, the Cut-cell Cartesian method, based on the use of a large fraction of small hexahedron cells, was chosen.

Global and local mesh settings were selected to keep the mesh metrics within proper values, avoiding large and poorly shaped mesh elements and ensuring a good mesh quality (cell skewness greater than 0.95 and minimum orthogonal quality at least more than 0.1). In order to manage the radically different dimension scales present along the geometry, e.g.  $\mu$ SOFC membrane thickness was 3-4 orders of magnitude smaller than the spacers; different elements (membranes, heaters and supporting silicon slabs) had been defined as surfaces. **Figure 3.7** shows the final refined and smooth mesh used for the simulation of the complete  $\mu$ SOFC PG by FVM. More than  $7 \times 10^6$  cells were obtained considering a minimum of three cells in narrowing paths.



**Figure 3.7:** Cross-section of the mesh solution for the  $\mu$ SOFC PG and detail of the refined meshing at the flow channels.

### 3.4.2. Materials and boundary conditions

The components of the simulated  $\mu$ SOFC PG were made of different materials, namely, (a) silicon for the substrates; (b) tungsten for the heaters; (c) silicon nitride ( $\text{Si}_3\text{N}_4$ ) for the thermal insulating membrane of the suspended  $\mu$ reformer; (d) Yttria-Stabilized Zirconia (YSZ) for the fuel cell membranes; (e) commercial HOYA OPTICS glass for the FPU spacer; (f) 316 stainless steel for the heat exchanger and (g) commercial Spacetherm<sup>®</sup> aerogel for the thermal insulation. Only carrier gases (air and water) were simulated in order to optimize the computational time while maintaining the relevant information concerning the thermal management of the system (i.e. heat and sink sources as defined in next *Section* 3.4.3). Therefore, ethanol and hydrogen were not taken into account because thermal dynamics was mostly controlled by water. Thermal characteristics of fluid and solid materials are summarized in **Table 3.1**. Properties for minority solid materials were constant, but silicon and stainless-steel were expressed as piecewise continuous functions of temperature. Fluid properties were calculated by using the Chapman-Enskog kinetic theory and Lennard-Jones parameters [20]. The gas phase was treated as a continuum and the ideal gas law was always applied. Dominating incompressible-laminar flows were assumed due to the small length scale and small velocity and pressure gradients (e.g. the Reynolds number of air was approximately 0.05). Gravitational effects were negligible.

The thermal boundary conditions employed for the simulations are also included in **Table 3.1**. In order to reproduce realistic operation conditions, the calculations considered radiation and natural convection through a heat exchange coefficient ( $h$ ) at the external surface at 300 K (without external heating or cooling). A surface emissivity ( $\varepsilon$ ) of 0.15 was considered based on values achievable by using current technological solutions like shield radiant barriers [18].



**Table 3.1:** Thermal properties of fluids and solids included in the  $\mu$ SOFC PG and its corresponding thermal boundary conditions

COMPONENT		THERMAL CHARACTERISTICS									
HM	Fluid	H2O, air	$\rho \Rightarrow$ incompressible ideal gas law ( $\text{kg}\cdot\text{m}^{-3}$ ) $C_p$ ( $\text{J}\cdot\text{kg}^{-1}\cdot\text{K}^{-1}$ ) $\kappa$ ( $\text{W}\cdot\text{m}^{-1}\cdot\text{K}^{-1}$ ) $\eta$ ( $\text{kg}\cdot\text{s}^{-1}\cdot\text{K}^{-1}$ ) <table style="display: inline-table; vertical-align: middle;"> <tr> <td rowspan="2">} Kinetic theory Lennard-Jones parameters:</td> <td><u>L-J length (<math>\text{\AA}</math>)</u></td> <td><u>Energy parameter (K)</u></td> </tr> <tr> <td><math>\sigma_{\text{H}_2\text{O}} = 2.6</math></td> <td><math>\epsilon/k_{\beta \text{H}_2\text{O}} = 572.4</math></td> </tr> <tr> <td></td> <td><math>\sigma_{\text{air}} = 3.6</math></td> <td><math>\epsilon/k_{\beta \text{air}} = 78.6</math></td> </tr> </table>	} Kinetic theory Lennard-Jones parameters:	<u>L-J length (<math>\text{\AA}</math>)</u>	<u>Energy parameter (K)</u>	$\sigma_{\text{H}_2\text{O}} = 2.6$	$\epsilon/k_{\beta \text{H}_2\text{O}} = 572.4$		$\sigma_{\text{air}} = 3.6$	$\epsilon/k_{\beta \text{air}} = 78.6$
	} Kinetic theory Lennard-Jones parameters:	<u>L-J length (<math>\text{\AA}</math>)</u>	<u>Energy parameter (K)</u>								
		$\sigma_{\text{H}_2\text{O}} = 2.6$	$\epsilon/k_{\beta \text{H}_2\text{O}} = 572.4$								
		$\sigma_{\text{air}} = 3.6$	$\epsilon/k_{\beta \text{air}} = 78.6$								
Solid	Si (*)	$\rho = 2309 - 2.19\cdot 10^{-5}\cdot T \text{ kg}\cdot\text{m}^{-3}$ $C_p = 821 + 1.09\cdot 10^{-1}\cdot T - 1.04\cdot 10^{-5}\cdot T^2 \text{ J}\cdot\text{kg}^{-1}\cdot\text{K}^{-1}$ $\kappa = 593.09 - 2.58\cdot T + 4.90\cdot 10^{-3}\cdot T^2 - 4\cdot 10^{-6}\cdot T^3 + 1\cdot 10^{-9}\cdot T^4 \text{ W}\cdot\text{m}^{-1}\cdot\text{K}^{-1}$									
	glass	$\rho = 2230 \text{ kg}\cdot\text{m}^{-3}$ $C_p = 736.8 \text{ J}\cdot\text{kg}^{-1}\cdot\text{K}^{-1}$ $\kappa = 1.09 \text{ W}\cdot\text{m}^{-1}\cdot\text{K}^{-1}$									
Surface	YSZ	$\rho = 6000 \text{ kg}\cdot\text{m}^{-3}$ $C_p = 400 \text{ J}\cdot\text{kg}^{-1}\cdot\text{K}^{-1}$ $\kappa = 2.70 \text{ W}\cdot\text{m}^{-1}\cdot\text{K}^{-1}$									
	W	$\rho = 19250 \text{ kg}\cdot\text{m}^{-3}$ $C_p = 132.02 \text{ J}\cdot\text{kg}^{-1}\cdot\text{K}^{-1}$ $\kappa = 173 \text{ W}\cdot\text{m}^{-1}\cdot\text{K}^{-1}$									
	Si <sub>3</sub> N <sub>4</sub>	$\rho = 3440 \text{ kg}\cdot\text{m}^{-3}$ $C_p = 712 \text{ J}\cdot\text{kg}^{-1}\cdot\text{K}^{-1}$ $\kappa = 30 \text{ W}\cdot\text{m}^{-1}\cdot\text{K}^{-1}$									
HX	Solid	Stainless Steel 316 (**)	$\rho = 7962.7 - 0.421\cdot T \text{ kg}\cdot\text{m}^{-3}$ $C_p = 539.55 - 0.14\cdot T + 2\cdot 10^{-4}\cdot T^2 \text{ J}\cdot\text{kg}^{-1}\cdot\text{K}^{-1}$ $\kappa = 12.76 + 1.45\cdot 10^{-2}\cdot T \text{ W}\cdot\text{m}^{-1}\cdot\text{K}^{-1}$ $\epsilon = 0.57$ $t = 0.5 \text{ mm}$								
INS	Solid	Aerogel (***)	$\rho_{\text{INS}} = 50 \text{ kg}\cdot\text{m}^{-3}$ $C_{p \text{ INS}} = 840 \text{ J}\cdot\text{kg}^{-1}\cdot\text{K}^{-1}$ $\kappa_{\text{INS}} = 0.014 \text{ W}\cdot\text{m}^{-1}\cdot\text{K}^{-1}$ $t = 10 \text{ mm}$ $\epsilon = 0.15$ $h = 10 \text{ W}\cdot\text{m}^{-2}\cdot\text{K}^{-1}$ $T_{\text{environment}} = 300 \text{ K}$								

(\*) from ref [37]

(\*\*) Based on the reference data presented in BS EN 10088-1

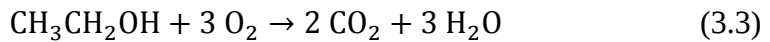
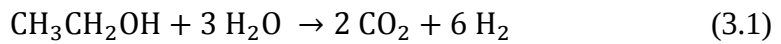
(\*\*\*) Data from the commercial product Spacetherm ®

### 3.4.3. Components modeling and initial conditions

In order to quantify the mass and heat exchange associated to each component of the  $\mu$ SOFC PG, the corresponding mass and energy balances were carried out by thermodynamic calculations and existing experimental data. A schematic representation of these balances for the whole  $\mu$ SOFC PG assuming an operation at the target temperature  $T_{HM} = 973$  K is detailed in **Figure 3.8**. This temperature was chosen as adequate for both efficient fuel reforming on the  $\mu$ reformers and proper fuel cell operation [13].

The mass balance was carried out by assuming molar flow rates of fuel and air calculated for  $\mu$ SOFCs continuously operating with 40 % of electric efficiency ( $\eta_{el}$ ) [1] and supplying a power density of  $100 \text{ mW/cm}^2$  (in concordance with results presented in **Chapter VI**). The fuel utilization ( $U_f$ ) was assumed to be 68 % [20] and a reasonable value of air-to-fuel ratio ( $\lambda$ ) was approximated to 2 [5].

The molar flow rates of each species were determined from the stoichiometric reactions (3.1) and (3.2)-(3.3) that took place in the  $\mu$ reformers and CPU, respectively. The efficiency of the ethanol steam reforming was considered to be 82 % at temperatures higher than 823 K [21, 22]. A liquid water/ethanol mixture with molar ratio equal 4 was selected according results reported in **Chapter IV**. Combustion of unreacted fuels was assumed to be complete at temperatures higher than 423 K for hydrogen [23] and higher than 523 K for ethanol [24].



The energy balance was carried out including all the chemical reactions that took place in the  $\mu$ SOFC PG, namely, (a) the fuel conversion to hydrogen through steam reforming and (b) the complete oxidation of the fuel at the CPU. Given a constant pressure, the heat flux associated to any of these reactions was calculated according to equation 3.4 and considering the molar rates calculated as described above.

$$\dot{Q}_{r,T} = \sum_{\text{prod.}} \dot{n} \times C_p \times \Delta T - \sum_{\text{react}} \dot{n} \times C_p \times \Delta T \quad (3.4)$$

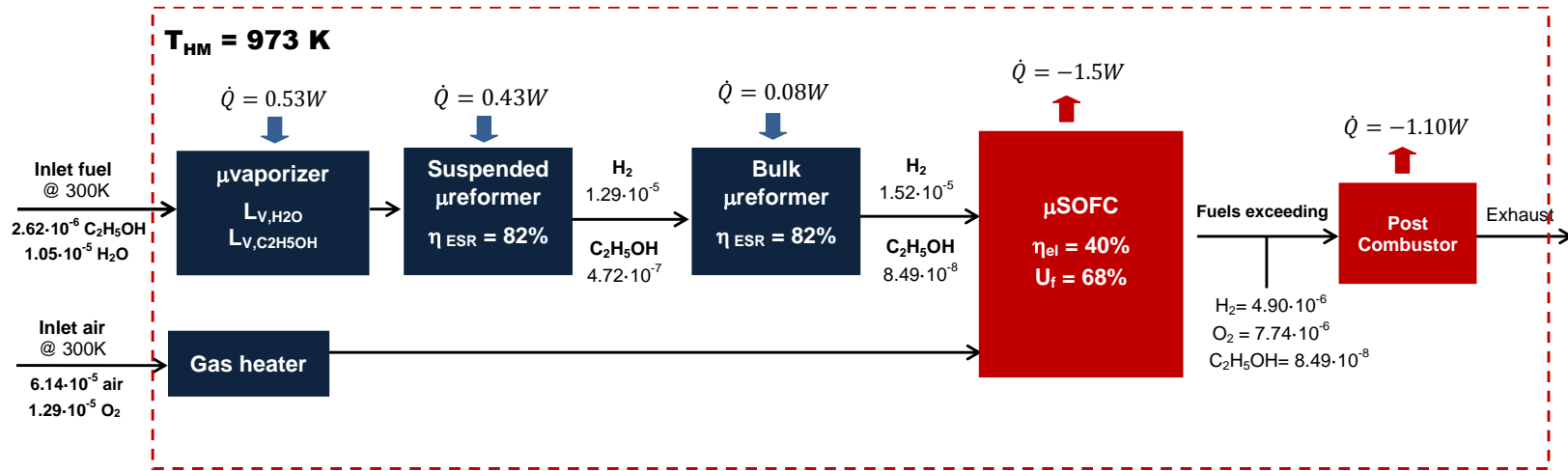
where  $\dot{Q}_{r,T}$  is the heat flux of reaction (W),  $\dot{n}$  is the molar rates of products and reactants, respectively ( $\text{mol}\cdot\text{s}^{-1}$ ), and  $C_p$  is its specific heat capacity ( $\text{J}\cdot\text{mol}^{-1}\cdot\text{K}^{-1}$ ).

For the particular case of the heat associated to the phase change of the water and ethanol from liquid to gas in the  $\mu$ vaporizer, the corresponding latent heat of evaporation was considered. Furthermore, the heat released by the  $\mu$ SOFC membranes due to the electrochemical reactions was calculated considering the previously assumed electrical efficiency ( $\eta_{el} = 40\%$ ) and equation 3.5 [6].

$$\dot{Q}_{SOFC} = P_{el} \left( \frac{1}{\eta_{el}} - 1 \right) \quad (3.5)$$

where  $\dot{Q}_{SOFC}$  is the heat flux (W),  $P_{el}$  is the electric power generated (W) and  $\eta_{el}$  is the electrical efficiency of  $\mu$ SOFC stack.

It is noteworthy that the model proposed was valid for a minimum efficiency operation of the  $\mu$ reformers and  $\mu$ SOFCs, as described above. However, other operation efficiencies of these critical components could lead to other optimizations of the  $\mu$ SOFC PG system.



**Figure 3.8:** Scheme of molar and energy balance for the individual components of the  $\mu$ SOFC PG by fixing an operation temperature inside the hot module of  $T_{HM} = 973 \text{ K}$ .

### 3.5. Results and discussion

The study is carried out for (i) the steady state, where all micro heaters were switched off and (ii) the transient state, where micro heaters were used to reach the steady-state.

#### 3.5.1. Case study I: steady-state operation mode

##### 3.5.1.1. Simulation details

The thermal losses in the  $\mu$ SOFC PG were mainly controlled by the thermal insulation of the hot module. Its thermal conductivity ( $\kappa$ ) and thickness ( $t$ ) were identified as the most relevant parameters determining the temperature map in the steady-state. For this work, (a) thermal conductivities between 1 and 14  $\text{mW}\cdot\text{m}^{-1}\cdot\text{K}^{-1}$  were used, according to the typical values of thermal conductivities of state of the art highly insulating materials (commercial aerogels present  $\kappa$  values of 14-30  $\text{mW}\cdot\text{m}^{-1}\cdot\text{K}^{-1}$  [25] and vacuum encapsulated of 1-5  $\text{mW}\cdot\text{m}^{-1}\cdot\text{K}^{-1}$ ), and (b) thickness of the insulation between 5 and 25 mm were evaluated. **Table 3.2** summarizes the different case studies considered (labelled in the next as case A, B, C, D and E).

**Table 3.2:** Thermal insulation specifications analysed in the steady-state.

	A	B	C	D	E
$\kappa$ ( $\text{mW}\cdot\text{m}^{-1}\cdot\text{K}^{-1}$ )	1	5	14	5	5
$t$ (mm)	10	10	10	25	5

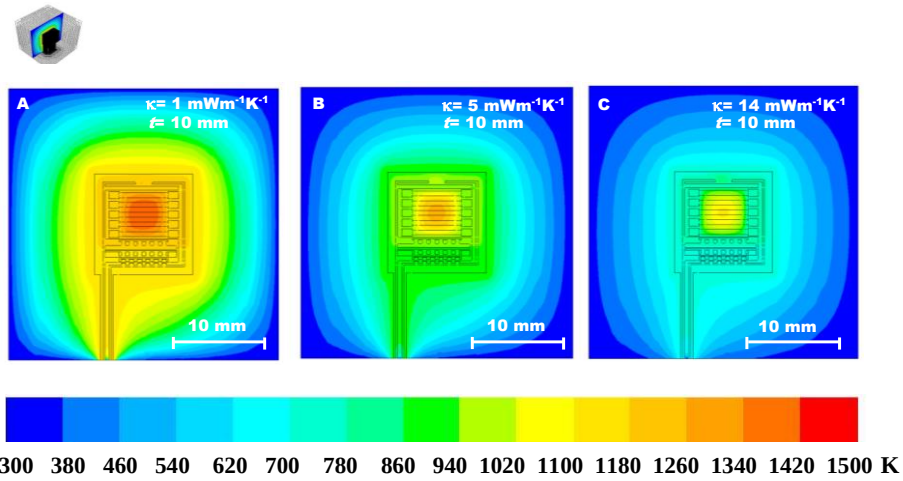
##### 3.5.1.2. Results

###### ❖ *Insulating material choice*

The temperature distribution across the hot module of the  $\mu$ SOFC PG for different thermal insulations with a fixed thickness of 10 mm is presented in **Figure 3.9**. A dramatic drop in temperature was observed along the insulation,  $\Delta T = 60\text{-}90 \text{ K}\cdot\text{mm}^{-1}$ , in all cases. Inside the vertical stack, average temperatures between 815 K and 1120 K were obtained, depending on the configuration. The highest temperature was always achieved at the thin film membranes of the  $\mu$ SOFC stack while the coldest parts of the system were the  $\mu$ reformers that involve the main endothermic reactions.

**Table 3.3** lists the average temperature of each component of the  $\mu$ SOFC PG for the different insulation architectures. According to this table,

low thermal conductivities (case A) led to extreme temperatures in the  $\mu$ SOFC cells ( $>1173$  K) while thermal conductivities of  $\kappa=14$   $\text{mW}\cdot\text{m}^{-1}\cdot\text{K}^{-1}$  (case C) limited the temperature at both  $\mu$ reformers below 740 K, which was clearly below the one required for an efficient and selective fuel conversion into hydrogen ( $T >823$  K). By employing the insulation with  $\kappa=5$   $\text{mW}\cdot\text{m}^{-1}\cdot\text{K}^{-1}$  (case B), the different components of the  $\mu$ SOFC PG achieved the target temperatures. Temperatures below 313 K in the open domain and above 873 K and 1000 K in the  $\mu$ reformers and the  $\mu$ SOFCs, respectively, fulfilled the requirements of the real device.



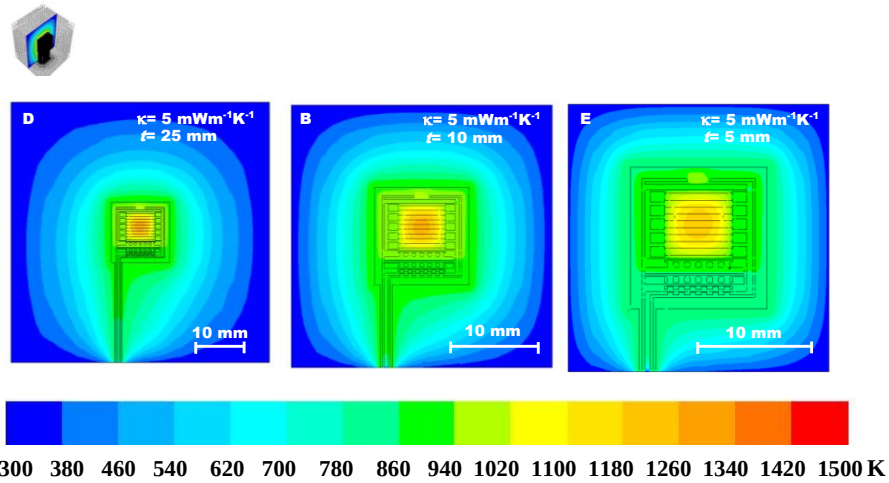
**Figure 3.9:** Cross-section temperature maps of the hot module of the  $\mu$ SOFC PG operating in a steady-state for a thermal insulation configuration with variable thermal conductivity and constant thickness.

**Table 3.3:** Average temperatures of critical components of the  $\mu$ SOFC PG as a function of the thermal conductivity ( $\kappa$ ).

Case	A	B	C
$T_{\text{suspended } \mu\text{-reformer}}$ (K)	988	884	696
$T_{\text{block } \mu\text{-reformer}}$ (K)	1029	926	740
$T_{\text{fuel cell membranes}}$ (K)	1177	1085	920
$T_{\text{outer surface}}$ (K)	303	311	317

❖ *Minimum thickness of the insulating layer*

Since specific power per unit volume is a key feature for portable applications, different thicknesses were analyzed for the insulation with  $\kappa=5 \text{ mW}\cdot\text{m}^{-1}\cdot\text{K}^{-1}$ . **Figure 3.10** shows temperature maps for simulations carried out considering an insulation thickness of 5, 10 and 25mm. From the figure, it is clear that this parameter had a second-order effect on the temperature distribution. As illustrated in **Table 3.4**, a reduction below  $t=5 \text{ mm}$  led to a higher temperature outside the system, certainly in the limit of an acceptable value (324 K), while increasing thickness up to  $t=25 \text{ mm}$  did not reflect a relevant improvement on the temperature distribution. Due to this and previously discussed advantages, in the following, this work was limited to systems with a 10 mm-thick insulation and  $5 \text{ mW}\cdot\text{m}^{-1}\cdot\text{K}^{-1}$  thermal conductivity, as referred case B.



**Figure 3.10:** Cross-section temperature maps of the hot module of the  $\mu\text{SOFC}$  PG operating in a steady-state for a thermal insulation configuration with variable thickness and constant thermal conductivity.

**Table 3.4:** Average temperatures of critical components of the  $\mu\text{SOFC}$  PG as a function of the thickness ( $t$ ).

Case	B	D	E
$T_{\text{suspended } \mu\text{-reformer}}$ (K)	884	888	826
$T_{\text{block } \mu\text{-reformer}}$ (K)	926	928	866
$T_{\text{fuel cell membranes}}$ (K)	1085	1086	1031
$T_{\text{outer surface}}$ (K)	311	304	324

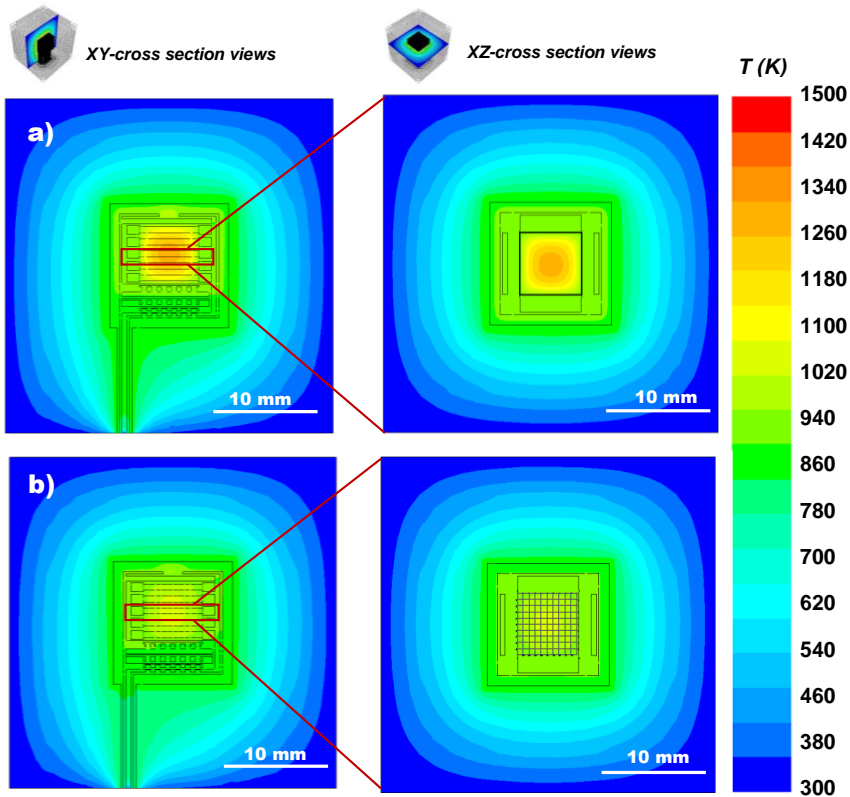
*❖ Homogenization of the temperature in  $\mu$ SOFCs*

A detail of the temperature distribution inside one of the  $\mu$ SOFC membranes, that form the stack, is represented in **Figure 3.11a**. A non-homogeneous distribution of the temperature with a gradient from the hottest central part to the coldest frame was clearly observed. This effect is inherent to a high thermal resistance of YSZ in thin film form that prevents a proper evacuation of the heat produced by the  $\mu$ SOFC. In order to minimize this gradient, thin film membranes supported on a grid of silicon slabs were proposed to analysis. These silicon slabs act as heat spreaders allowing a proper heat release from the membrane towards the bulk substrate and improving the temperature homogeneity across the functional membrane area.

**Figure 3.11b** shows the temperature map obtained for the modified  $\mu$ SOFC chip after simulation in the same conditions. As predicted, the grid of silicon slabs had a clear influence on the temperature distribution inside the  $\mu$ SOFC die. While for the plane membrane a maximum temperature of 1350 K and a gradient of  $39 \text{ K}\cdot\text{mm}^{-1}$  were calculated, the modified membrane presented values of 1020 K and  $12 \text{ K}\cdot\text{mm}^{-1}$ . In this way, the probability of formation of failure inducers, e.g. hotspots, was drastically reduced, thus improving the thermo-mechanical stability and reliability of the thin film membranes. This type of membrane configuration had been employed to obtain the results presented in the following sections.

It is noteworthy that the system proposed was robust to external temperature and  $\mu$ SOFC electrical efficiency changes. Simulations had been performed for external temperature as low as 273 K and for 40-60 % electrical efficiency regime. In all cases, the system continued to fulfill the thermal requirements and it was self-sustained. Moreover, several auxiliary components and control strategies must be used to ensure a high efficiency of  $\mu$ SOFCs ( $\eta_{el} \geq 40\%$ ) and therefore, guarantee the device reliability. For example, the auxiliary source used in the start-up process (see next section) can serve as energy buffer that counterbalance eventual power demand variations.





**Figure 3.11:** Distribution of temperature for a cross-section of the whole  $\mu$ SOFC PG on the left column and top view images of the  $\mu$ SOFC chips on the right column for membranes configuration (a) without and (b) with silicon slabs.

### 3.5.2. Case study II: transient operation mode

#### 3.5.2.1. Simulation details

After defining the insulation configuration, the transient was studied in order to minimize the start-up time and reduce the energy consumption. A hybrid start-up was employed for an efficient activation of the device. It combined an auxiliary power source for powering the different micro heaters (at the  $\mu$ SOFC stack,  $\mu$ vaporizer and suspended  $\mu$ reformer) with the use of heat released at the CPU. The optimization of the start-up process was thus related to: the mass flow rates of fuels ( $\dot{m}$ ), the power supplied to the heaters ( $P$ ), the heat released due to complete combustion of unreacted fuels ( $\dot{Q}$ ) and the target temperatures of each component.

After an iterative process (not presented here for the sake of clarity), a sequence of five steps was finally defined for this work. The five steps corresponded to: (a) switch on all the integrated micro heaters to reach the minimum operation temperature of the  $\mu$ vaporizer, suspended  $\mu$ reformer and CPU; (b) introduce a certain amount of fuel and air to release heat at the CPU and increase the temperature of the whole system (the heater of the vaporizer was switched off); (c) and (d) gradually increase the amount of fuel and air to the final values for full activation of the  $\mu$ SOFC stack; (e) gradually switch off the micro heaters until the steady-state was reached. **Table 3.3** lists all the parameters used in this sequence.

**Table 3.5:** Input parameters for a five-step hybrid start-up sequence.

	1	2	3	4	5	Steady State
<b>Mass flow rate, <math>\dot{m}</math> (kg·s<sup>-1</sup>)</b>						
$\dot{m}_{fuel}$	-	$1.0 \times 10^{-7}$	$2.1 \times 10^{-7}$	$3.1 \times 10^{-7}$	$3.1 \times 10^{-7}$	$3.1 \times 10^{-7}$
$\dot{m}_{air}$	-	$5.9 \times 10^{-7}$	$1.2 \times 10^{-6}$	$1.8 \times 10^{-6}$	$1.8 \times 10^{-6}$	$1.8 \times 10^{-6}$
<b>Power supply, P (W)</b>						
Heater on $\mu$ -vaporizer	0.5	-	-	-	-	-
Heater on suspended $\mu$ -reformer	5	5	5	5	From 5 to 0	-
Heater on fuel cell membranes	4.5	5	5	5	From 5 to 0	-
<b>Target temperatures (K)</b>						
$\mu$ -vaporizer	< 373	> 373	> 373	> 373	> 373	> 373
Suspended $\mu$ -reformer	< 823	> 823	> 823	> 823	> 823	> 823
Bulk $\mu$ -reformer	-	-	-	-	-	> 823
$\mu$ -SOFC cells	-	-	-	773	> 773	> 773
CPU	> 423	> 523	> 523	> 523	> 523	> 523
<b>Heat from chemical reactions, Q (W)</b>						
$\mu$ -vaporizer	-	0.18	0.35	0.53	0.53	0.53
Suspended $\mu$ -reformer	-	0.14	0.29	0.43	0.43	0.43
Bulk $\mu$ -reformer	-	-	-	-	-	0.08
$\mu$ -SOFC cells	-	-	-	-	-1.50	-1.50
CPU	-	-0.87	-1.82	-3.18	-1.10	-1.10

It is worth mentioning that the fuel was not supplied into the system until the suspended  $\mu$ reformer had reached the target temperature (823 K), minimizing fluctuations of temperature due to the kinetics of the reforming reaction. After that moment and for the rest of the start-up process, an efficiency of 82% was considered for this element. In the case of  $\mu$ SOFCs, the efficiency was assumed to be 40% right after the activation of the membrane components at 773 K [1].

### 3.5.2.2. Results

❖ *From the initial to the start-up time*

**Figure 3.12** shows the evolution of the temperature map of the  $\mu$ SOFC PG during the transient regime. In the last frame, the start-up was reached. Snapshots for each step of the sequence described above in **Table 3.5** are presented.

- **First 35 s**

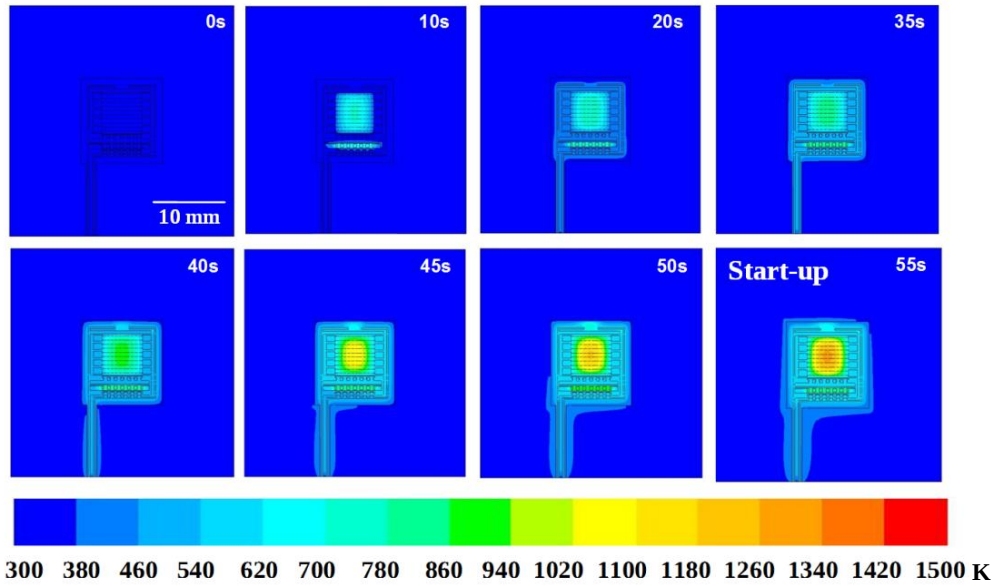
As depicted in the four frames of the first row, the first step of the start-up process sequences was achieved after 35 s, i.e. the  $\mu$ vaporizer reached a temperature high enough to vaporize the liquid fuel ( $T > 373$  K), the suspended  $\mu$ reformer achieved the minimum temperature for the fuel conversion into hydrogen ( $T > 823$  K) and the CPU reached the temperature required to start the fuel oxidation ( $T > 423$  K).

- **From 35 to 50 s**

Then, a certain amount of fuel and air was introduced gradually according to second, third and fourth steps (see 40 s, 45 s and 50 s frames respectively). As a consequence, heat was released at the CPU and the temperature of the hot module was raised from 490 K to 545 K (ca.  $5.5 \text{ K}\cdot\text{s}^{-1}$ ) achieving the activation of the  $\mu$ SOFC membranes.

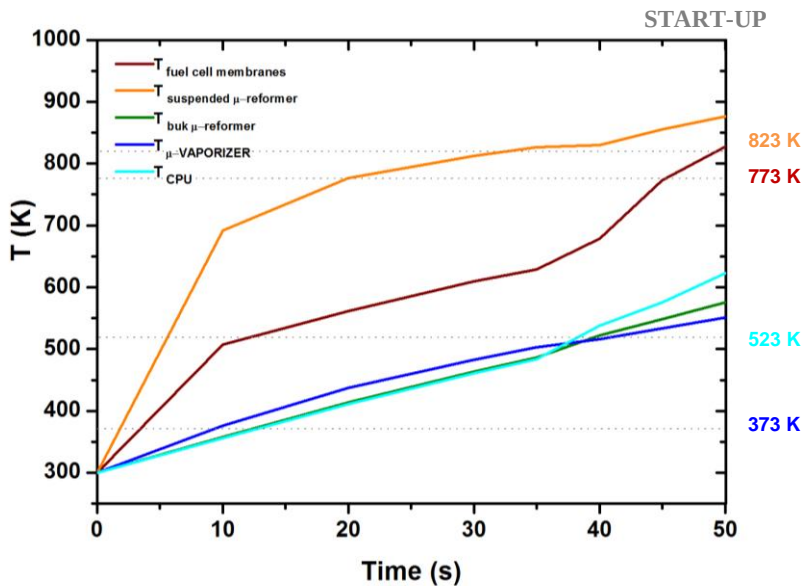
- **Start-up**

From this moment, as is illustrated in the frame 55 s, the  $\mu$ SOFC PG was fully operative (in agreement with the fifth step).



**Figure 3.12:** Evolution with time of the temperature map of the  $\mu$ SOFC PG from initial to the start-up.

A detail of the start-up process, i.e. the period after which all the components are fully operative is presented in **Figure 3.13**. The target temperatures for each component are highlighted in the right axes, which allow determining the time at which different units become operative.



**Figure 3.13:** Evolution with time of the temperature associated specifically to the elements until the start-up.

According to the **Figure 3.13**, only 10 seconds were required to reach the vaporizing temperature of the fuel mixture ( $> 373$  K). Therefore, the  $\mu$ vaporizer became the first operative unit and provided gas to the  $\mu$ reformers and the CPU. Once the liquid fuel was vaporized, the reforming step started as long as the temperature in the micro channels of the  $\mu$ reformers was higher than 823 K. This occurs for the suspended  $\mu$ reformer after 35 s mainly due to heat released by the integrated heater and the CPU. The shortest start-up time of the suspended  $\mu$ reformer was on the basis of the here proposed double  $\mu$ reformer design. This rapid response of the suspended  $\mu$ reformer allowed fuelling the system with hydrogen from the very beginning.

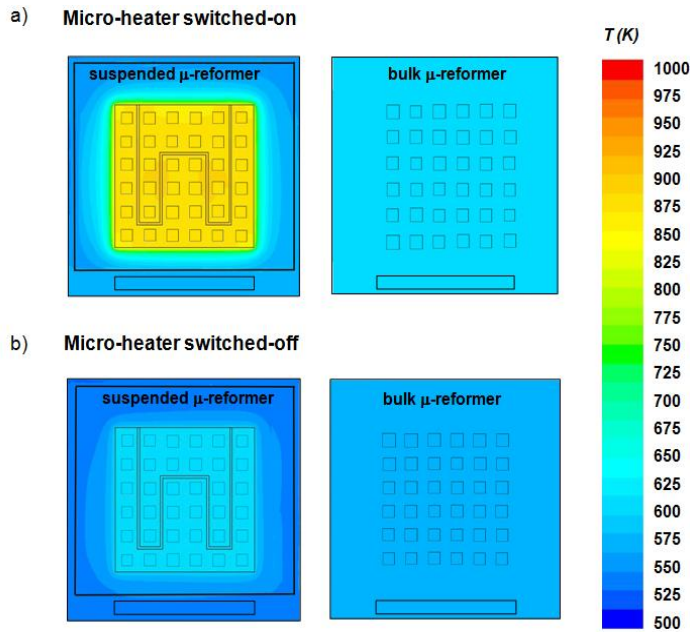
However, until the fuel cell membranes reached the minimum operating temperature, set to 773 K, they were unable to convert the hydrogen coming from the reformers into electrical power. This fuel went directly to the  $\mu$ post combustor where it oxidized to water. The minimum temperature needed for promoting the hydrogen oxidation process is 423 K, and was reached also at  $t=30$  s. The total oxidation of unreacted fuels led to a faster heating up of the  $\mu$ SOFC stack. This effect can be observed as a change in the slope of the temperature evolution in the SOFC membranes, after  $t= 35$  s. Until that time, the fuel cells were linearly heated up by the effect of the micro heaters integrated on the membranes (external power source). Finally, the fuel cell membranes achieved the required 773 K to start operating properly at  $t=45$  s. We can then consider that the start-up time of the whole system was less than one minute.

### ❖ *From the start-up to the steady-state*

Although a rapid start-up of 50 s was achieved, the transition process was not completed until the steady-state. Despite the outstanding contribution of the suspended  $\mu$ reformer to accomplish a quick start-up, a counterpart effect existed when trying to stabilize its temperature for reaching the steady-state. **Figure 3.14** shows this effect by comparing the suspended  $\mu$ reformer and the bulk  $\mu$ reformer when the micro heater was switched-on during 50 s and then it was switched-off for 10 s.

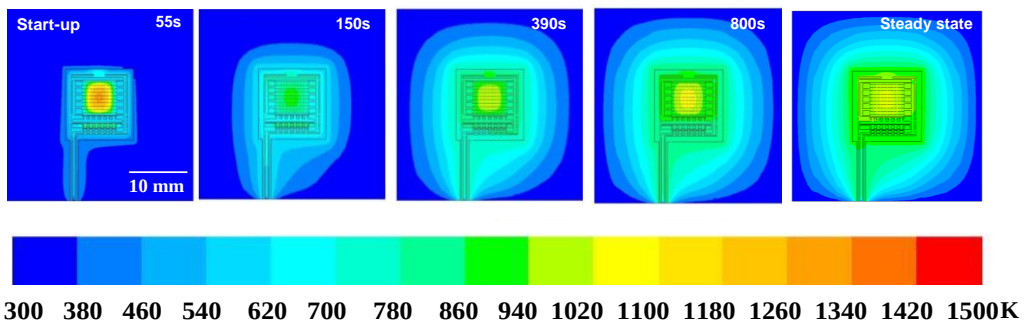
Due to the previously mentioned excellent thermal insulation of the suspended  $\mu$ reformer, this component heated up very quickly when the integrated micro heater was switched on (a gradient of c.a. 300 K is observed in **Figure 3.14a**), but it also cooled down fast when the micro heater was

switched off (see **Figure 3.14b**). In contrast, the bulk  $\mu$ reformer in both cases remains at the same temperature ( $\sim 615$  K) because of its high thermal inertia.



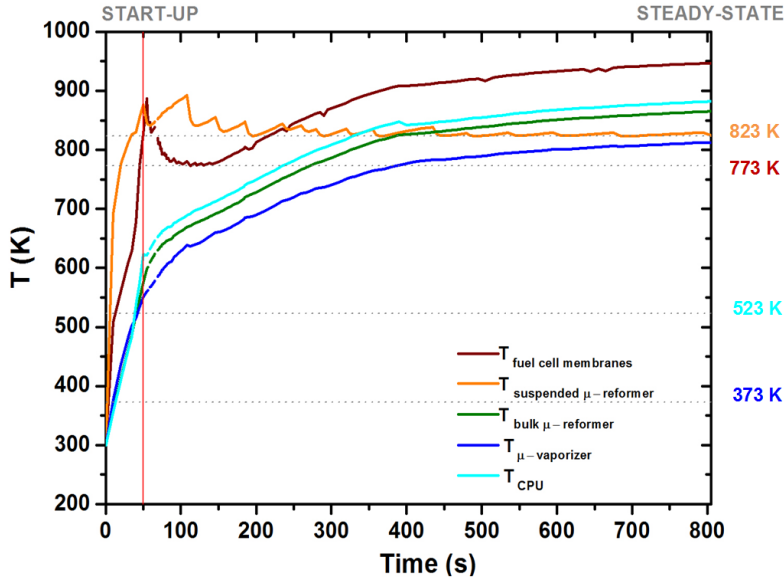
**Figure 3.14:** (a) Temperature effects on each  $\mu$ reformer with the micro heater switched on for 50 s and (b) 10 s after switching it off.

For this reason, a closed control loop to gradually reduce the heat dissipated in the suspended  $\mu$ reformer was required with the consequent effect on achieving the final steady system that can be delayed several minutes. **Figure 3.15** shows the snapshots related to this last step of the transient process in which the micro heaters were progressively switched-off until attaining the steady-state of the whole system.



**Figure 3.15:** Evolution with time of the temperature map of the  $\mu$ SOFC PG from the starting point to the steady-state.

A detail of the whole transient process is presented in **Figure 3.16**. The target temperatures for each component are highlighted in the right axes. It is worth mentioning that the bulk  $\mu$ reformer did not reach the target temperature until  $t=390$  s.

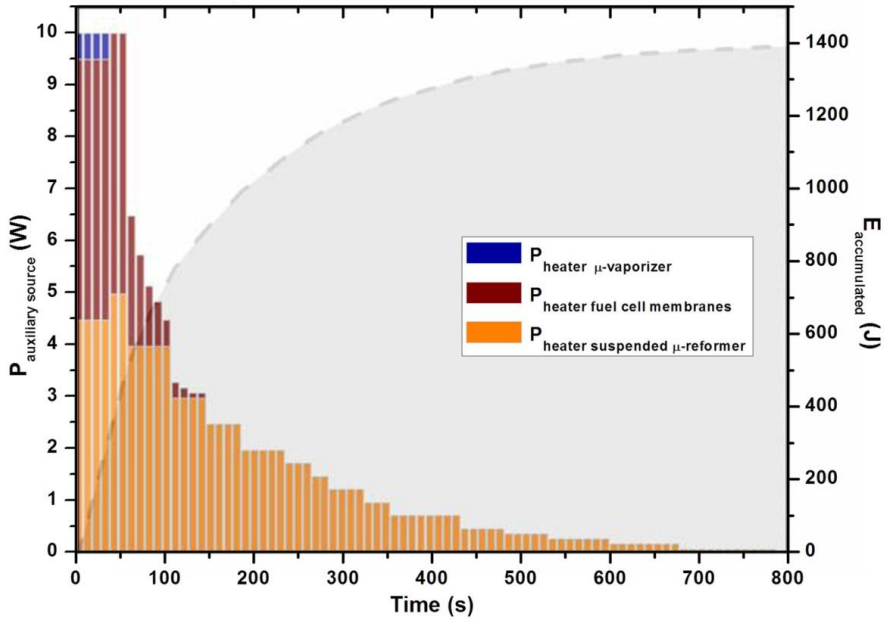


**Figure 3.16:** Evolution with time of the temperature for the different units that form part of the  $\mu$ SOFC PG during the whole transient process.

The evolution with time of the power supplied to the different heaters (left axis) and the accumulated energy (right axis) for the whole transient step is outlined in **Figure 3.17**. A maximum power of 10 W was fixed in order to limit the auxiliary power unit to a reasonable size. The most energy consuming units were the SOFC stack and the suspended  $\mu$ reformer requiring 250 J and 232 J, respectively, to be fully operative. The  $\mu$ vaporizer was activated with less than 20 J provided in the first 35 s. Therefore, the total energy accumulated for the start-up period ( $t=50$  s) was approximately 500 J. This amount of energy (and power) can be obtained from commercial ultra capacitors or small batteries.

However, the amount of heat required to increase the temperature of all the components included in the hot module up to 773K, by using a conventional start-up method based on electrical heating would involve an amount of energy consumption one order of magnitude higher (approximately 5000 J). Therefore, apart from a longer start-up time (estimated in 8 min), the

pure electrical solution would yield to unpractical auxiliary power units. On Moreover, a system purely based on catalytic oxidation, will not allow controlling the sequential activation of the different elements, significantly increasing the start-up time of the whole system. Finally, removing integrated heaters would limit the control of the individual elements (they can be used as temperature sensors) and will not allow employing liquid fuels at an atmospheric pressure.



**Figure 3.12:** Evolution with time of the power supplied to the different heaters (left axis) and the accumulated energy (right axis) for the whole transient step.



### **3.6. Conclusions**

The thermal management feasibility of a one-watt  $\mu$ SOFC PG fully integrated in silicon and fuelled with ethanol has been presented in this chapter. An innovative system design consisting of a vertical stack of a  $\mu$ vaporizer, a double  $\mu$ reformer, a  $\mu$ SOFC stack and a  $\mu$ post combustor unit was proposed. Finite volume analysis of this particular geometry and design was carried out for the steady and transient regimes. The parameterization of each component was based on experimental results from this work and other studies found in the literature.

The system showed a self-sustained regime of operation at 950 K for an insulation configuration based on materials with a thermal conductivity of  $5 \text{ mW}\cdot\text{m}^{-1}\cdot\text{K}^{-1}$  and a thickness of 10 mm. Observed inhomogeneities of the temperature distribution inside the  $\mu$ SOFC cells were solved by proposing a membrane supported in a grid of silicon slabs. A quick transient regime from room temperature was proven by employing a hybrid electrical-chemical start-up. Start-up times fairly below 1 minute with energy consumptions of 500 J showed the feasibility of this system for portable applications, therefore anticipating a new family of mobile and uninterrupted power generators fuelled with hydrocarbons.

## References

- [1] Singhal, S., Singhal, S. C. & Kendall, K. *High-temperature Solid Oxide Fuel Cells: Fundamentals, Design and Applications: Fundamentals, Design and Applications*. (Elsevier Science, 2003).
- [2] Tarascon, J.M. & Armand, M. Issues and challenges facing rechargeable lithium batteries. *Nature* **414**, 359–367 (2001).
- [3] Bejan, A. & Kraus, A. D. *Heat Transfer Handbook*. (Wiley, 2003).
- [4] Hotz, N., Senn, S. M. & Poulikakos, D. Exergy analysis of a solid oxide fuel cell micropowerplant. *J. Power Sources* **158**, 333–347 (2006).
- [5] Bieberle-Hütter, A. *et al.* A micro-solid oxide fuel cell system as battery replacement. *J. Power Sources* **177**, 123–130 (2008).
- [6] Meier, C., Hocker, T., Bieberle-Hütter, A. & Gauckler, L. J. Analyzing a micro-solid oxide fuel cell system by global energy balances. *Int. J. Hydrogen Energy* **37**, 10318–10327 (2012).
- [7] Krummenacher, J. J., West, K. N. & Schmidt, L. D. Catalytic partial oxidation of higher hydrocarbons at millisecond contact times: decane, hexadecane, and diesel fuel. *J. Catal.* **215**, 332–343 (2003).
- [8] Jung, H. *et al.* Fast start-up reactor for partial oxidation of methane with electrically-heated metallic monolith catalyst. *J. Power Sources* **124**, 76–80 (2003).
- [9] Ryi, S. K., Park, J. S., Cho, S. H. & Kim, S. H. Fast start-up of microchannel fuel processor integrated with an igniter for hydrogen combustion. *J. Power Sources* **161**, 1234–1240 (2006).
- [10] Stutz, M. J., Grass, R. N., Loher, S., Stark, W. J. & Poulikakos, D. Fast and exergy efficient start-up of micro-solid oxide fuel cell systems by using the reformer or the post-combustor for start-up heating. *J. Power Sources* **182**, 558–564 (2008).
- [11] Santis-Alvarez, A. J., Nabavi, M., Hild, N., Poulikakos, D. & Stark, W. J. A fast hybrid start-up process for thermally self-sustained catalytic-butane reforming in micro-SOFC power plants. *Energy Environ. Sci.* **4**, 3041–3050 (2011).
- [12] Mihailovic, M., Rops, C., Cremer, J. F. & Sarro, P. M. MEMS silicon-based micro-evaporator with diamond-shaped fins. *Procedia Eng.* **5**, 969–972 (2010).
- [13] Kuang-Han, C. M.Sc. Thesis, Massachusetts Institute of Technology (2013).
- [14] Garbayo, I. Ph.D. Thesis, University of Barcelona (2013).

- [15] Garbayo, I. *et al.* Porous  $\text{La}_{0.6}\text{Sr}_{0.4}\text{CoO}_{3-\delta}$  thin film cathodes for large area micro solid oxide fuel cell power generators. *J. Power Sources* **248**, 1042–1049 (2014).
- [16] Garbayo, I., Pla, D., Morata, A., Fonseca, L., Sabaté, N. & Tarancón. A. Full ceramic micro solid oxide fuel cells: Towards more reliable MEMS power generators operating at high temperatures. *Energy Environ. Sci.* **7**, 3617-3629 (2014).
- [17] Sergent, J. & Krum, A. *Thermal Management Handbook for Electronic Assemblies*. (McGraw-Hill Education, 1998).
- [18] Matsch, L.C. US3139206 A (1961).
- [19] Glassbrenner, C. J. & Slack, G. A. Thermal Conductivity of Silicon and Germanium from 3 K to the Melting Point. *Phys. Rev.* **134**, A1058–A1069 (1964).
- [20] Ivers-Tiffée, E., Weber, A. & Herbstritt, D. Materials and technologies for SOFC-components. *J. Eur. Ceram. Soc.* **21**, 1805–1811 (2001).
- [21] Vaidya, P. D. & Rodrigues, A. E. Insight into steam reforming of ethanol to produce hydrogen for fuel cells. *Chem. Eng. J.* **117**, 39–49 (2006).
- [22] Haryanto, A., Fernando, S., Murali, N. & Adhikari, S. Current Status of Hydrogen Production Techniques by Steam Reforming of Ethanol: A Review. *Energy & Fuels* **19**, 2098–2106 (2005).
- [23] Haruta, M. & Sano, H. Catalytic combustion of hydrogen I—Its role in hydrogen utilization system and screening of catalyst materials. *Int. J. Hydrogen Energy* **6**, 601–608 (1981).
- [24] Rajesh, H. & Ozkan, U. S. Complete oxidation of ethanol, acetaldehyde and ethanol/methanol mixtures over copper oxide and copper-chromium oxide catalysts. *Ind. Eng. Chem. Res.* **32**, 1622–1630 (1993).
- [25] Cohen, E. *Thermal Properties of Advanced Aerogel Insulation*. (Massachusetts Institute of Technology, Department of Mechanical Engineering, 2011).

## **IV. FUEL PROCESSING UNIT**



<b>4.1. Introduction.....</b>	<b>115</b>
<b>4.2. Design and fabrication of a bulk <math>\mu</math>reformer.....</b>	<b>119</b>
4.2.1. Design outline and concept approach.....	119
4.2.2. Microfabrication process.....	121
4.2.3. Thermal characterization of the micro heater.....	123
<b>4.3. Activity measurements of the bulk <math>\mu</math>reformer.....</b>	<b>126</b>
4.3.1. Structural characterization of the Pd-Rh/CeO <sub>2</sub> catalyst system....	126
4.3.2. Catalytic activity of the bulk $\mu$ reformer.....	127
4.3.2.1. Influence of the operation temperature.....	127
4.3.2.2. Influence of the fuel loading.....	130
<b>4.4. Design and fabrication of a suspended <math>\mu</math>reformer.....</b>	<b>133</b>
4.4.1. Design outline and concept approach.....	133
4.4.2. Microfabrication process.....	135
4.4.3. Start-up of the suspended $\mu$ reformer.....	137
4.4.4. Glass cover fabrication and encapsulation.....	137
<b>4.5. Activity measurements of the suspended <math>\mu</math>reformer.....</b>	<b>139</b>
4.5.1. Wet impregnation method of the Pd-Rh/CeO <sub>2</sub> catalyst system....	139
4.5.2. Activity of the suspended $\mu$ reformer as a standalone device...139	
<b>4.6. Conclusions.....</b>	<b>141</b>



## 4.1. Introduction

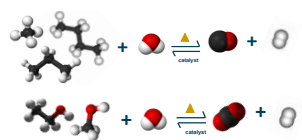
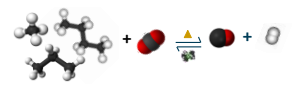
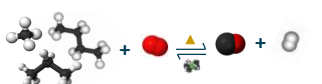
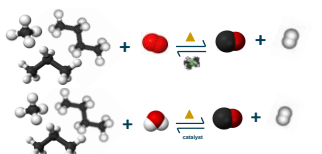
In an ideal scenario, the  $\mu$ SOFC PG would be directly fed with pure hydrogen, but storing hydrogen on-board can be difficult, dangerous and inefficient. Short-chain hydrocarbons are widely used as a fuel to produce hydrogen because they are safe and easy to handle, offer the possibility of fuel-refilling in small cartridges and provide high energy density at low cost [1]. Among them, methane ( $\text{CH}_4$ ) and ethanol ( $\text{C}_2\text{H}_5\text{OH}$ ) are probably the most interesting since both present a clear regulation, can be produced from renewable sources (biogas and bio-ethanol) and, particularly the ethanol, yield high hydrogen content on a molar basis [2].

Reforming of hydrocarbons is a well-established technology, currently employed by most SOFC developers to avoid typical problems that appear when using other methods like hydrocarbon cracking [3]. Hydrocarbons are used as fuel by converting them into hydrogen, either by internal [4, 5] or external reforming [6-9]. In internal reforming, the gas is reformed directly inside the SOFC stack, in particular in the anode side. The main advantage of this option is its simple implementation in the fuel cell system. However, this type of reforming leads to inhomogeneous temperature distributions which can result in mechanical failure due to thermally induced stresses [10] and progressive inhibition of the anode catalyst by coke deposition, which reduces the cell performance and durability [11]. Moreover, the external reforming takes place in a different unit with controlled temperature separately from the SOFC stack, thus avoiding temperature gradients and minimizing carbon deposition. However this reforming requires a more complex engineering involving higher volumes and efficient heat transfer [12].

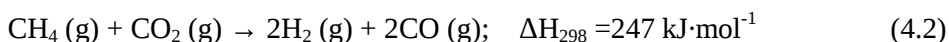
The four major catalytic reforming reactions of hydrocarbons, according to the type of oxidants used, are: Steam Reforming (SR), Dry Reforming (DR), Partial OXidation reforming (POX) and Auto-Thermal Reforming (ATR). The main characteristics of each type are described in **Table 4.1**.



**Table 4.1:** Main characteristics of the four major catalytic reforming reactions of hydrocarbons.

	<b>Advantages for SOFCs</b>	<b>Drawbacks for SOFCs</b>
<p style="text-align: center;"><b>Steam reforming</b></p> $C_n H_{2n+2} + n H_2 O \rightarrow n CO + (2n + 1) H_2$ $C_n H_{2n+1} OH + (2n - 1) H_2 O \rightarrow n CO_2 + 3n H_2$ 	<p>Generally higher hydrogen yield than 50 % at T &gt; 600 °C.</p> <p>Heat of SOFCs can be used to drive SR reaction with overall higher system efficiency.</p>	<p>Several side reactions may occur. The most common is the Water Gas Shift (WGS).</p> $CO + H_2 O \leftrightarrow CO_2 + H_2$ <p>Endothermic reaction; so an external power for starting-up the reaction and an efficient heat transfer are required.</p>
<p style="text-align: center;"><b>Dry reforming</b></p> $C_n H_{2n+2} + n CO_2 \rightarrow n CO + (2n + 1) H_2$ 	<p>CO2 is much easier to handle than steam.</p> <p>Heat of SOFCs can be used to drive DR reaction with overall higher system efficiency.</p>	<p>An excess of CO2 can promote carbonaceous material.</p> <p>Highly endothermic reaction.</p>
<p style="text-align: center;"><b>Partial Oxidation reforming</b></p> $C_n H_{2n+2} + \frac{1}{2} n O_2 \rightarrow n CO + (n + 1) H_2$ 	<p>Exothermic reaction, so no external heat is required and start-up is fast.</p> <p>The POX unit is more compact than a steam or dry reformer.</p>	<p>Lower hydrogen yield than SR and DR</p> <p>If fuel conversion is not complete, unreacted air remains in anode side causing fuel depletion</p>
<p style="text-align: center;"><b>Auto-thermal reforming</b></p> $C_n H_{2n+2} + \frac{1}{2} n O_2 \rightarrow n CO + (n + 1) H_2$ $C_n H_{2n+2} + n H_2 O \rightarrow n CO + (2n + 1) H_2$ 	<p>Integrates steam reforming with partial oxidation.</p> <p>No energy demanding in steady-state operating mode.</p>	<p>Lower hydrogen yield than SR and DR</p> <p>May need start-up heat and a control system to switch between lean fuel oxidation and SR regime.</p>

Since methane is a gas and ethanol is a liquid (at atmospheric temperature and pressure), Methane Dry Reforming (MDR) and Ethanol Steam Reforming (ESR) (equation 4.1 and 4.2) were the reforming reactions preferred for supplying hydrogen to the  $\mu$ SOFC PG proposed in this thesis. It is worth mentioning that partial oxidation reforming of hydrocarbons like butane has been recently proposed as an alternative conversion pathway at lower temperatures (*ca.* 500 °C) [13-15]. However, this approach still presents several limitations for SOFC applications, mainly due to the species content of the final outlet gas that could affect the fuel cell performance (anode oxidation and fuel depletion) [15].



MDR and ESR reactions are mainly endothermic and require high operation temperatures to achieve suitable conversions (>85%) and high selectivity rates (T= 550-800°C) [16]. In this sense, great efforts have been focused on the development of efficient and stable metal catalysts at such high temperatures, minimizing their deactivation by deposition of inactive carbon, metal oxidation or metal sintering. Among the active materials for both reforming reactions, noble metals like Pt, Rh, Ru and Pd exhibit the lower carbon formation rates [17-23]. In particular, Rh exhibits the lowest rate because of its capacity to dissociate C-C bond successfully [24]. On the contrary, its H-H recombination capacity is relatively weak [24]. The presence of a second metal with efficient H-H bond formation seems to be necessary to maintain high catalytic activity. In this sense, Pd shows efficient H-H bond formation with adsorption of considerable amounts of hydrogen that favour the hydrogenation [24].

In addition, it is well known that reforming reactions are bi-functional, i.e. the reaction mechanism not only depends on the metal components, but also on the support which can play an important role in the catalytic process by providing new active sites or/and affecting the properties of the metal [24, 25]. For example, in the ESR reaction, acidic supports such as  $\text{Al}_2\text{O}_3$  are prone to ethylene formation, which can decompose forming coke deposition [26]. For dry reforming reactions, inert supports such as  $\text{SiO}_2$  have relatively weak metal support interaction and are less stable and less active compared to acidic or basic support [21]. Amongst basic supports,  $\text{CeO}_2$  and  $\text{ZrO}_2$  are commonly

used due to their high Oxygen Store Capacity (OSC), which avoid carbon deposition through the oxidation of the carbon surfaces through oxy-carbonates, and their high thermal stability [23].

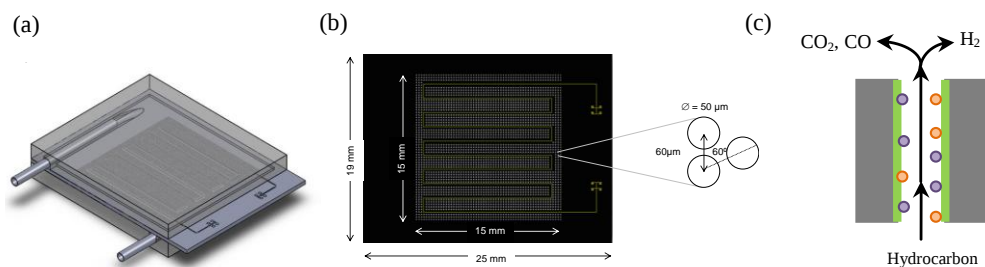
Apart from an efficient and stable metal catalyst, a reformer unit for the  $\mu$ SOFC PG has to fulfill several design and fabrication requirements to ensure a high performance of MDR and ESR reactions. First, similar to the catalytic system, its operating temperature has to be compatible with the one of the  $\mu$ SOFC PG. Second, since reforming reactions are strongly endothermic, the  $\mu$ reformer has to facilitate the heat exchange with the exothermic part of the system, i.e. the fuel cells and the  $\mu$ post combustor. Finally, it has to be fully compatible with mainstream MEMS technology and offer the possibility of easy integration into the full power generator system. Due to this complexity, only few MEMS-based  $\mu$ reformers have been reported up to now [27-31]. Most of them are based on a bed reactor with long in-plane micro channels and external heating to meet the energy demand of the fuel reforming. This micro channel configuration has several problems associated to high pressure drop, non-modularity, high energy consumption and long start-up times. Llorca *et al.* recently proposed a novel micro reactor design based on a vertical micro channel configuration that solves some of these major issues, but still requires non-conventional micro-fabrication routes for its fabrication [17-18, 32-33].

**This chapter** presents the fabrication and characterization of a fully integrated silicon-based  $\mu$ reformer capable to produce hydrogen from ESR and MDR. The architecture and fabrication process of a bulk  $\mu$ reformer are presented in *Section 4.2*. The design was based on thousands of vertical micro channels crossing a silicon platform with an embedded tungsten heater integrated for heating up to the temperature required for the reforming reactions. The fuel flexibility and suitability of the bulk  $\mu$ reformer was tested and discussed for ESR and MDR reactions using Pd-Rh/CeO<sub>2</sub> as catalyst system (*Section 4.3*). Once the main concept and materials were validated, a new low-thermal mass suspended  $\mu$ reformer was designed, fabricated and encapsulated as detailed in *Section 4.4*. The suspended  $\mu$ reformer was tested as a standalone device. The proof of concept of this thermally optimized  $\mu$ reformer is presented in *Section 4.5*.

## 4.2. Design and fabrication of a bulk $\mu$ reformer

### 4.2.1. Design outline and concept approach

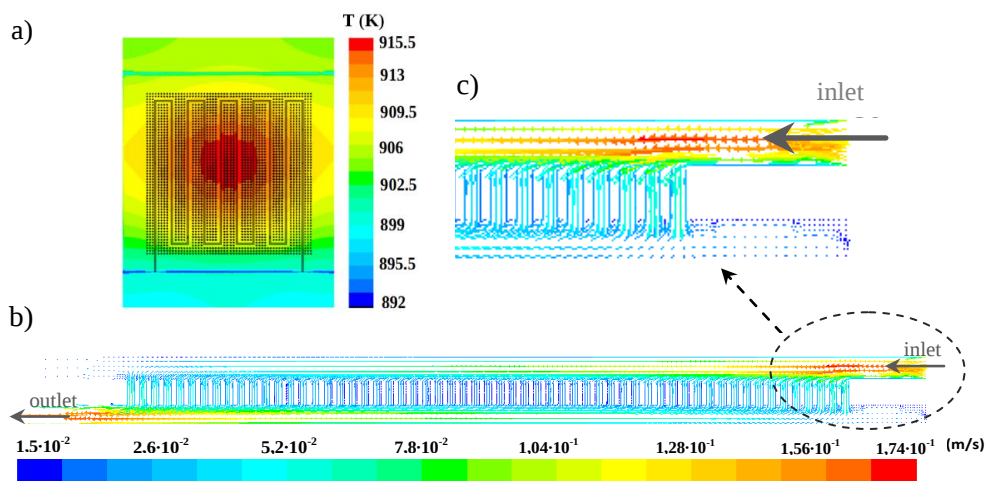
A schematic of the design proposed is provided in **Figure 4.1**. The  $\mu$ reformer is a silicon chip of 500  $\mu\text{m}$  in thickness with dimensions of 19x25  $\text{mm}^2$ . The reaction area has 15x15  $\text{mm}^2$  and contains a highly dense array of through-silicon micro channels with 50  $\mu\text{m}$  in diameter. The catalyst was deposited on the walls of the micro channels and the fuel flowed along them. An integrated heater on top of the silicon chip was also designed for locally heating up the active area of the  $\mu$ reformer. The geometry of the micro heater was based on a metal serpentine with dimensions of *ca.* 150  $\mu\text{m}$  long, 100  $\mu\text{m}$  wide and thickness varying from 250 to 500 nm. Tungsten (W) was chosen as metal for the heater because is CMOS compatible, represents a mainstream technology and can operate reliably at high temperatures [34].



**Figure 4.1:** (a) 3D representation of the  $\mu$ reformer design encapsulated, (b) top view and (c) cross section schematic layouts.

An electro-thermal analysis of the micro heater was carried out by FVM simulations in steady state. **Figure 4.2a** shows the temperature distribution map obtained in the  $\mu$ reformer when a current density of  $1 \cdot 10^9 \text{ A} \cdot \text{m}^{-2}$  was applied to the micro heater (250 nm thick) and fuel was crossing through the micro channels (the fuel mass flow rate was fixed to  $3.1 \cdot 10^{-7} \text{ kg} \cdot \text{s}^{-1}$  in agreement with the thermodynamic calculations presented in **Chapter III**). Notice here, that the maximum current density in metal thin films for avoiding electro-migration effects is typically  $1 \cdot 10^{10} \text{ A} \cdot \text{m}^{-2}$  [35]. The dissipated power in the heater ( $\sim 5 \text{ W}$ ) was enough for achieving a uniform temperature in the whole area of the  $\mu$ reformer. This temperature was higher than the minimum one required to take place the reforming reactions ( $T > 823 \text{ K}$ ). The maximum gradient from the hottest central part to the coldest part of the active area was  $1.9 \text{ K} \cdot \text{mm}^{-1}$ . Moreover, the fuel distribution within

the micro channels was obtained from the thermo-fluidic simulations. The cross section of the micro channels and the velocity vectors of the fuel in steady-state are shown in **Figure 4.2b**. The fuel flowed through the micro channels homogenously with a velocity comprised from  $2.6 \cdot 10^{-2} \text{ m}\cdot\text{s}^{-1}$ , in the central part, to  $5.2 \cdot 10^{-2} \text{ m}\cdot\text{s}^{-1}$  at the perimeter of the active area, which correspond to a residence time of 0.08 s and 0.04 s, respectively. Therefore, the simulations confirmed that the fuel will be in contact with the whole catalytic reactive area during the reforming reactions.

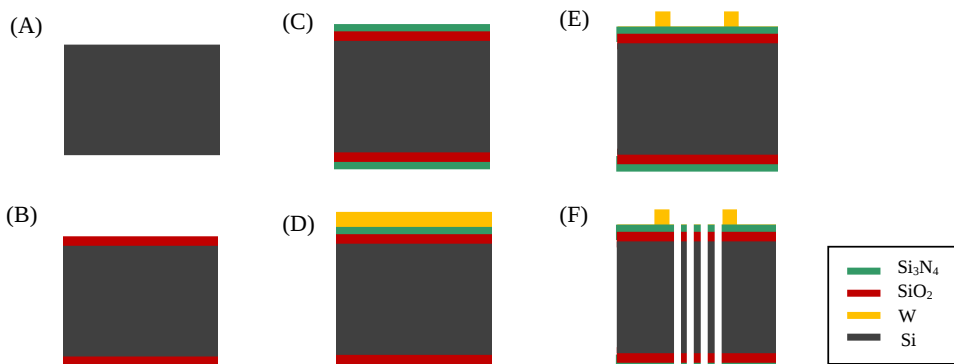


**Figure 4.2:** (a) Distribution of temperature in steady-state when a current density of  $1 \cdot 10^9 \text{ A}\cdot\text{m}^{-2}$  was applied to the micro heater (250nm in thick), (b) cross section of micro channels and velocity vectors of the fuel in steady-state and (c) a magnification of the inlet part of the cross section.

This vertical configuration coupled with a heater presented several advantages compared with other more conventional designs. On one side, it was possible to manage heat in a more compact configuration, thus minimizing thermal losses and improving the heat transfer in the active area of the  $\mu$ reformer (more details in **Chapter III**). On the other side, it allowed reducing (virtually to zero) the pressure drop, i.e. the pressure required for the fuels to flow through the micro channels. Finally, the high surface-to-volume ratio of the micro channels, loaded with catalytic material, was expected to lead to higher performance of fuel reforming reactions, since a large specific contact area and a short diffusion length were developed in the device.

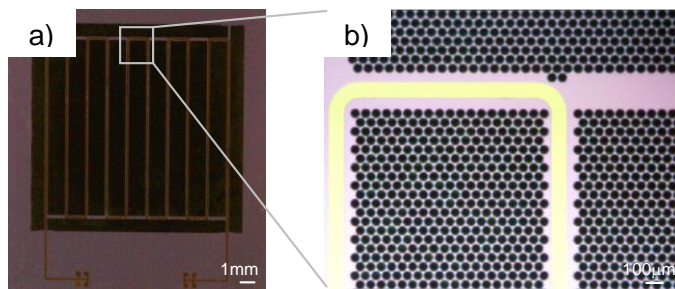
### 4.2.2. Microfabrication process

**Figure 4.3** illustrates the major steps involved in the fabrication of the  $\mu$ reformer chips. Single crystal (100)-oriented p-type silicon wafers of 100 mm diameter and 500  $\mu\text{m}$  thick were thermally oxidized at 1100  $^{\circ}\text{C}$  to obtain a 100 nm thick  $\text{SiO}_2$  layer (Figure 4.3A-B). Then, a Low-Pressure Chemical Vapor Deposition (LPCVD) process was used to deposit 300 nm thick layers of  $\text{Si}_3\text{N}_4$  on both sides (Figure 4.3C). A metallic multilayer was deposited by sputtering on the front side of wafer: 30 nm of TiW as an adhesion layer, 250 nm of W and, finally, 20 nm of Au to avoid W oxidation (Figure 4.3D). After that, a photolithographic step was used to define the heater shape and pads. The exposed areas were removed by wet etching in 40%wt  $\text{H}_2\text{O}_2$  at 80  $^{\circ}\text{C}$  (Figure 4.3E). A second photolithographic step was used to define the micro channels area on the top side and a Reactive Ion Etching (RIE) process was carried out to eliminate dielectric layers. Then, a 1  $\mu\text{m}$  thick aluminum/cooper hard mask was deposited by sputtering on the back side. A final double-sided photolithography step defined the micro channels on the back of the wafer. At that point, a back side DRIE – Bosch process was carried out to form the through-silicon holes with the wafer front side protected with a 2  $\mu\text{m}$  thick resin. Finally, the exposed copper-aluminum mask was chemically removed (Figure 4.3F).



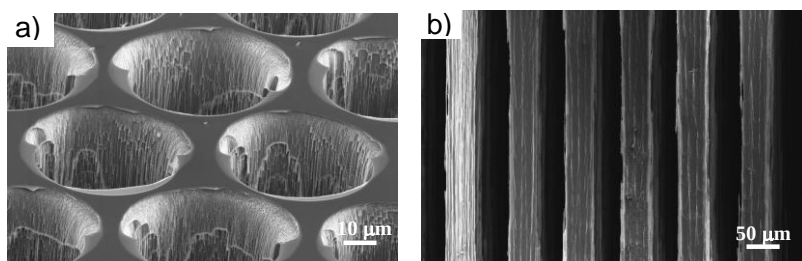
**Figure 4.3:** Fabrication flow of the bulk  $\mu$ reformer. Silicon wafers were thermally oxidized to obtain a 100 nm thick  $\text{SiO}_2$  layer (Figure 4.3A-B). Then, a LPCVD process was used to deposit 300 nm thick layers of  $\text{Si}_3\text{N}_4$  on both sides (Figure 4.3C). A metallic multilayer was deposited by sputtering on the front side of wafer (Figure 4.3D). After that, a photolithographic step defined the heater. The exposed areas were removed by wet etching (Figure 4.3E). A second photolithographic step defined the micro channels on the back side and the dielectric layers were eliminated by RIE. Finally, a back side DRIE – Bosch process was carried out to form the through-silicon holes (Figure 4.3F).

Optical images of the microfabricated reformer are shown in **Figure 4.4**. The projected area of 2.25 cm<sup>2</sup> was composed by approximately 4.6·10<sup>4</sup> micro channels leading to an active area of more than 36 cm<sup>2</sup>, i.e. the active surface per projected area and the surface-to-volume ratio of the micro channels were 16 cm<sup>2</sup>/cm<sup>2</sup> and 8·10<sup>4</sup> m<sup>2</sup>/m<sup>3</sup>, respectively. This great enhancement of the contact area between the fuel and the catalyst is expected to significantly reduce the residence times, diffusion distances and force a laminar flow pattern due to a low Reynolds number<sup>1</sup>.



**Figure 4.4:** (a) General view of the bulk reformer and (b) detail of the micro channels array and tungsten metallic micro-heater pad (yellow strip).

**Figure 4.5** shows SEM images of a series of micro channels. Figure 4.5a shows that inter-channel walls as thin as 10 µm were fabricated without mechanical failure of the structure. Moreover, there was no significant tapering effect along the 500 µm channels, thus avoiding undesirable pressure drop associated to bottlenecks (see Figure 4.5b).



**Figure 4.5:** (a) Top view and (b) cross-section SEM images of micro channels of the bulk reformer.

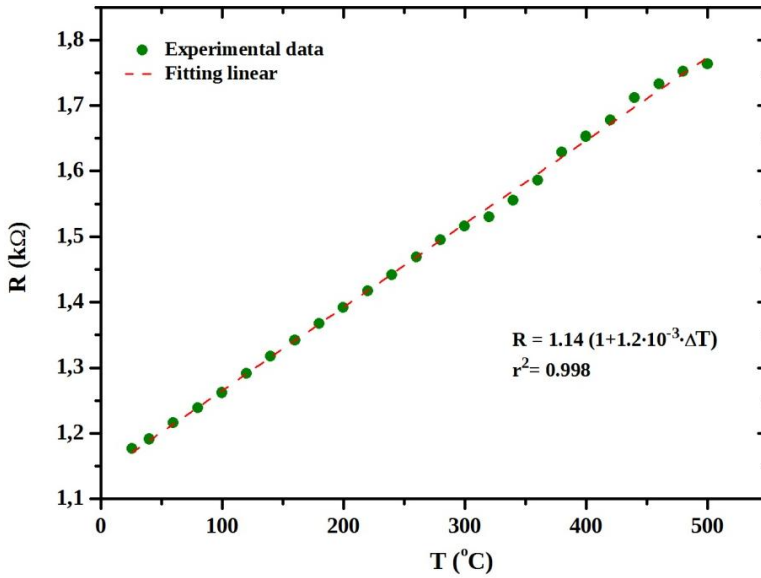
<sup>1</sup> Reynolds number is calculated according the following equation 4.3,

$$Re = \frac{\rho \cdot v_s \cdot D}{\mu} < 2300; \text{Laminar flow} \quad (4.3)$$

where  $\rho$  is the fluid density (e.g. 0.26 kg·m<sup>-3</sup> of steam water at 550 °C),  $v_s$  is the velocity of the fluid (e.g. 0.04 m·s<sup>-1</sup> was the fuel mixture velocity crossing the micro channels in steady-state according thermal simulations),  $D$  is the diameter of micro channel and  $\mu$  is the dynamic viscosity of the fluid (e.g. 3.1·10<sup>-5</sup> Pa·s of steam water at 550 °C).

### 4.2.3. Thermal characterization of the micro heater

Three metal configurations were fabricated and studied, namely, (a) 500 nm of W, (b) 50 nm of TiW as adhesion layer + 450 nm thick of W + 20 nm thick of Au and (c) 30 nm of TiW + 250 nm of W + 20 nm thick of Au + 1  $\mu\text{m}$  of  $\text{SiO}_2$  passivation. A thermal calibration was performed on the three configurations by measuring the Thermal Coefficient of Resistance (TCR), as described in Section 2.6.1 in Chapter II. As an example, Figure 4.6 shows the TCR results obtained for the first heater configuration.


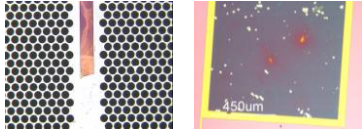


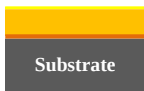
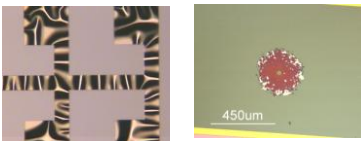



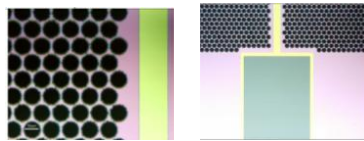




**Figure 4.6:** Resistance versus temperature plot for the thermal calibration of the first heater configuration (500 nm of W).

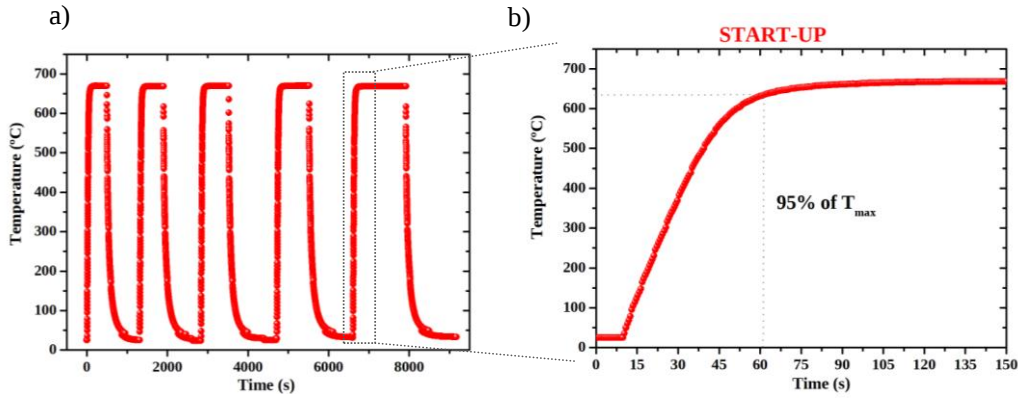
Moreover, the  $\mu$ reformer chips were thermally annealed up to 600  $^{\circ}\text{C}$  to validate the thermo-mechanical stability of the metal heaters under temperature operating conditions. Table 4.2 shows the results obtained for each configuration. Metal track detachment problems were observed in configuration (a) due to a bad adherence with the dielectric layers and, further, the tungsten was oxidized. A corrugated metal layer was observed in configuration (b), likely due to thermal stress, causing punctual problems of adherence and metal oxidation. On the contrary, in configuration (c), no degradation, delamination or oxidation was observed in the heater after the thermal treatment. Therefore, this heater configuration was chosen for the final  $\mu$ reformer device and used to obtain the results presented in the following sections.



**Table 4.2:** Thermal calibration and thermo-mechanical stability of the different micro heater configurations studied.

Configuration	TCR ( $^{\circ}\text{C}^{-1}$ )	$R_0$ ( $\Omega$ )	Heater stability
 Substrate 500 nm W	$1.2 \cdot 10^{-3}$	1140	  Delamination  Metal oxidation
 Substrate 450 nm W +50 nm TiW + 20nm Au	$1.5 \cdot 10^{-3}$	535.9	  Poor adherence  Metal oxidation
 Substrate 1 $\mu\text{m}$ $\text{SiO}_2$ + 20nm Au +250 nm W +30 nm TiW	$1.4 \cdot 10^{-3}$	827.9	  

The transient response of the bulk  $\mu$ reformer was studied under vacuum conditions ( $\sim 1$  Pa), without any fuel, and by applying a constant electrical power of 5 W to the heater to achieve the steady temperature of *ca.* 700  $^{\circ}\text{C}$ . As presented in **Figure 4.7a**, several thermal cycles were performed ensuring the reliability of the micro heater. A detail of the measured start-up time of the  $\mu$ reformer is shown in **Figure 4.7b**. The start-up was achieved after 62 s and the maximum temperature reached was 670  $^{\circ}\text{C}$ . This means that 310 J of electrical input energy was required. Although these values were in agreement with other electric heating results reported in literature [36], the energetic cost was unacceptable for a final  $\mu\text{SOFC}$  PG device (see more details in **Chapter III**). Consequently, a second  $\mu$ reformer especially optimized from the thermal point of view was developed (see *Section 4.4*).



**Figure 4.7:** (a) Transient response of the micro heater in several thermal cycles and (b) detail of the measured start-up time of bulk  $\mu$ reformer.

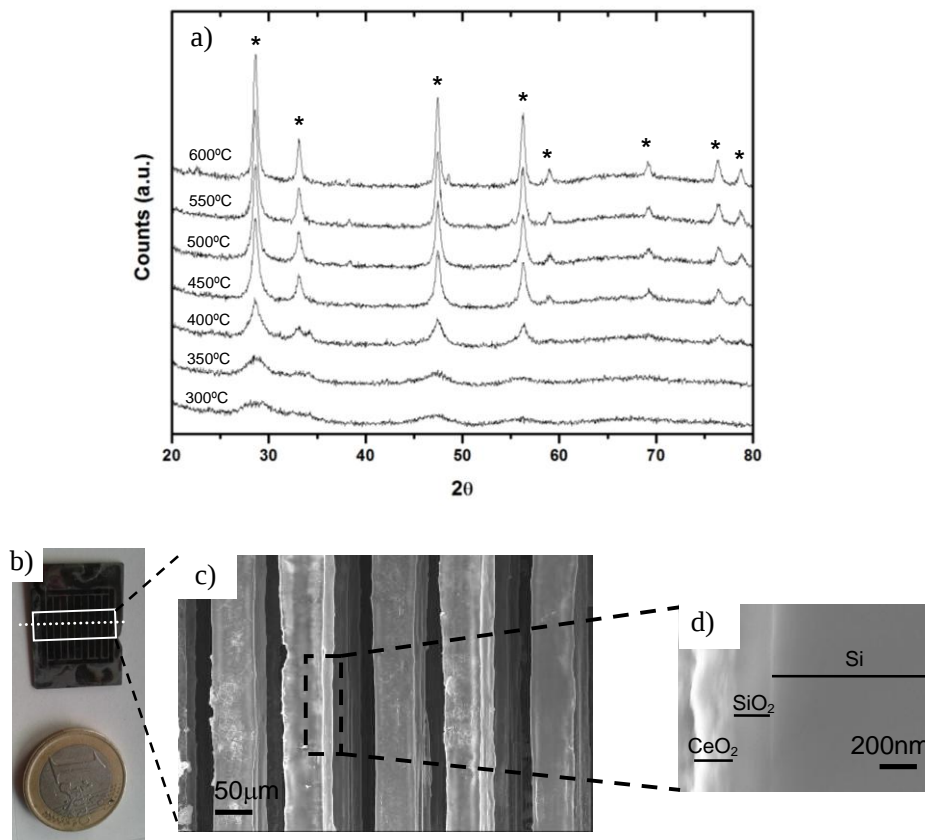
### 4.3. Activity measurements of the bulk $\mu$ reformer

In this work, Pd-Rh/CeO<sub>2</sub> catalyst system was used to study the activity of the bulk  $\mu$ reformer towards ESR and MDR reactions. The synthesis route of the catalyst is described in *Section 2.4.1* of **Chapter II**.

#### 4.3.1. Structural characterization of the Pd-Rh/CeO<sub>2</sub> catalyst system

A structural characterization of the Pd-Rh/CeO<sub>2</sub> catalyst system was carried out by SEM and XRD. First, cross section SEM images of the  $\mu$ reformer were obtained to verify by EDX that the internal surface area of the micro channels was fully covered with SiO<sub>2</sub>. Second, in order to make compatible the decomposition of the cerium precursor to CeO<sub>2</sub> with the thermo-mechanical stability of the micro heater, the evolution with temperature of the cerium methoxyethoxide precursor deposited on the SiO<sub>2</sub>/Si substrate was studied by *in situ* XRD.

As presented in **Figure 4.8a**, no diffraction peaks were observed for the as-deposited cerium precursor on the substrate indicating its amorphous nature. The formation of the nanocrystalline CeO<sub>2</sub> catalyst support took place between 450 °C and 500 °C as clearly shown by the appearance of the diffraction peaks corresponding to the typical fluorite  $Fm\bar{3}m$  structure of the cubic ceria. Cross section images of the  $\mu$ reformer were acquired to verify the homogeneity of the micro channel infiltration process with the Pd-Rh/CeO<sub>2</sub> catalyst. As shown in **Figure 4.8b-c**, the wet impregnation method used for catalyst deposition covered very homogeneously the walls of the micro channels. As a result, the coverage per unit mass of catalyst took values up to  $6.1 \times 10^3 \text{ cm}^2 \cdot \text{g}^{-1}$ . A detail of the cross section of one micro channel is presented in **Figure 4.8c**. The silicon substrate is clearly covered by a uniform SiO<sub>2</sub> layer *ca.* 200 nm thick and a homogeneous layer of CeO<sub>2</sub> of about 200 nm in thickness.



**Figure 4.8:** (a) XRD patterns of the evolution of the cerium precursor deposited on a SiO<sub>2</sub>/Si substrate obtained by *in situ* measurements from 300 °C to 600 °C. The main peaks of a crystalline CeO<sub>2</sub> pattern are labeled with stars and appeared between 450 °C and 500 °C. (b)-(c) bulk μreformer image and representative SEM image of the cross section of several micro channels after catalyst impregnation and thermal treatment and (d) detail of a micro channel wall showing the CeO<sub>2</sub> and SiO<sub>2</sub> layers deposited on the Si substrate.

## 4.3.2. Catalytic activity of the bulk μreformer

### 4.3.2.1. Influence of the operation temperature

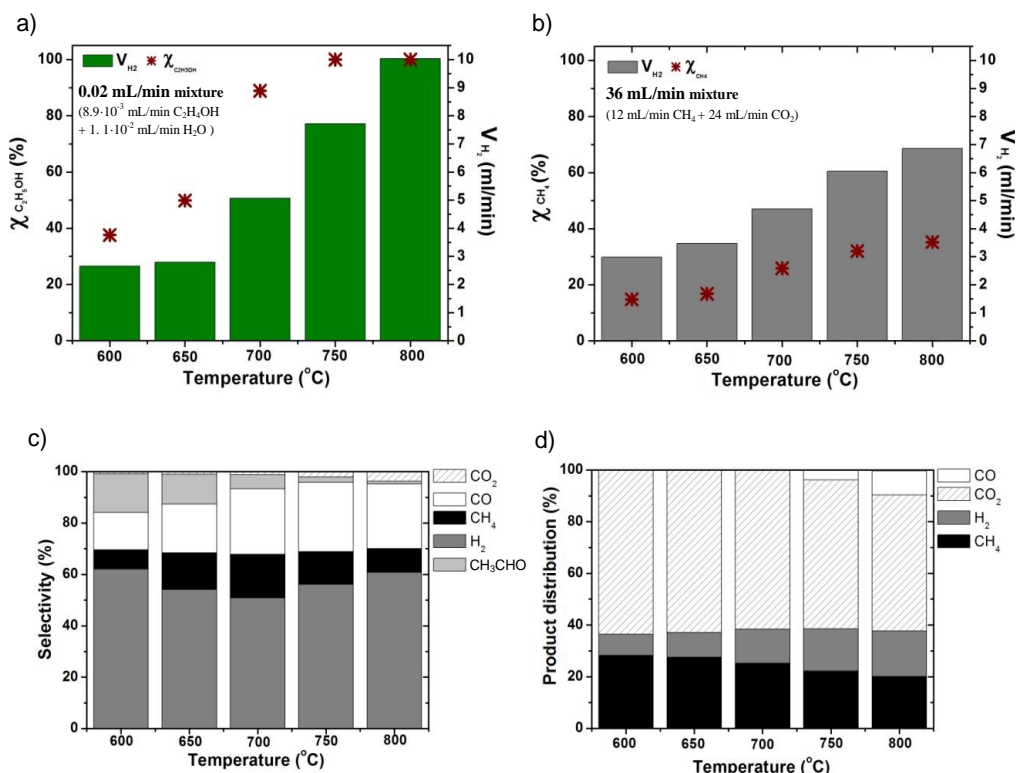
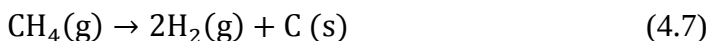
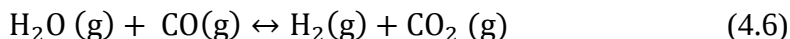
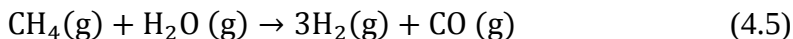
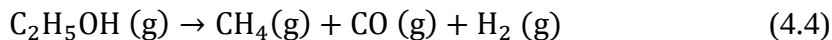
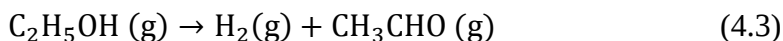
**Figure 4.9** shows the fuel conversion and volumetric hydrogen production obtained over the bulk μreformer for the ESR (Figure 4.9a) and MDR (Figure 4.9b) reactions depending on the operation temperature. The selectivity towards ESR and MDR products are shown in Figure 4.9c and Figure 4.9d, respectively.

As observed in Figure 4.9a and Figure 4.9b, the conversion rate of both fuels increased with temperature, as expected from thermodynamics, but the production of hydrogen was not significant until 700 °C (5.1 ml·min<sup>-1</sup> for ESR and 4.7 ml·min<sup>-1</sup> for MDR). Ethanol was completely converted at 750 °C yielding higher amounts of hydrogen (7.7 ml·min<sup>-1</sup> at 750 °C and 10 ml·min<sup>-1</sup> at 800 °C), whereas the maximum methane conversion achieved was *ca.* 35% at 800 °C leading to a hydrogen production of 6.9 ml·min<sup>-1</sup>.

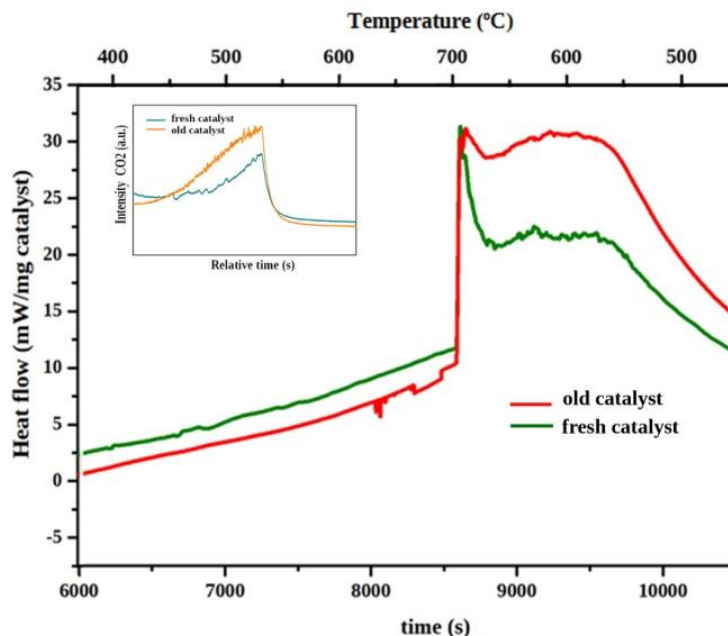
As presented in Figure 4.9c and Figure 4.9d, the reforming rates had no significant extent at lower temperatures compared to decomposition of fuels. In the case of ESR (Figure 4.9c), the dehydrogenation of ethanol to acetaldehyde and ethanol decomposition to methane, carbon monoxide and hydrogen appeared as dominant reactions (equation 4.3 and 4.4). Only at high temperatures (from 700 °C onwards) methane was reformed to a high extent and the amount of hydrogen produced increased notably (equation 4.5). Furthermore, the selectivity towards acetaldehyde was drastically reduced, while selectivity towards carbon monoxide was increased due to the Reverse Water Gas Shift reaction (RWGS) (equation 4.6). These results are in agreement with the reaction mechanism of ESR for Pd-Rh/CeO<sub>2</sub> catalyst proposed in Ref. [18]. Similarly, methane decomposition (equation 4.7) is the main reaction producing hydrogen at lower temperatures (from 600 to 700 °C), since no detectable amounts of carbon monoxide were measured and the CO<sub>2</sub>/CH<sub>4</sub> ratio was higher than 2. Methane dry reforming appears from 750 °C, leading to higher syngas productions and carbon dioxide consumption. RWGS also occurs in a similar extent than ESR, since a small amount of water in the outlet stream was detected.

In order to confirm the methane decomposition to coke and hydrogen at low temperatures, a DSC analysis - coupled to MS and TGA - was performed after the MDR tests. The analysis was carried out under synthetic air flow (10 ml·min<sup>-1</sup>) up to 700 °C (heating ramp of ~8 °C·min<sup>-1</sup>). The carbon content of the used catalyst (i.e. used  $\mu$ reformer) was compared to the carbon content of a fresh catalyst. As shown in **Figure 4.10**, a higher heat flow was measured in the old catalyst likely due to a higher extent of the reaction of carbon oxidation. A higher CO<sub>2</sub> production was also observed in the mass spectra (depicted in the inset). No significant amounts of CO were detected. An increment of 0.09 mg and 0.14 mg in mass was detected for the old and fresh catalyst, respectively. These weight changes were a superposition of the

weight loss due to the oxidation of carbon into CO<sub>2</sub> and/or the weight gain due to the oxidation of metal catalyst into metal oxides.



**Figure 4.9:** Performance of methane and ethanol reforming reactions for different temperatures and a fuel loading of 36 ml·min<sup>-1</sup> and 0.02 ml·min<sup>-1</sup>, respectively; (a) ethanol conversion and hydrogen production for ESR, (b) methane conversion and hydrogen production for MDR, (c) selectivity towards ESR products and (d) outlet gas composition of MDR.

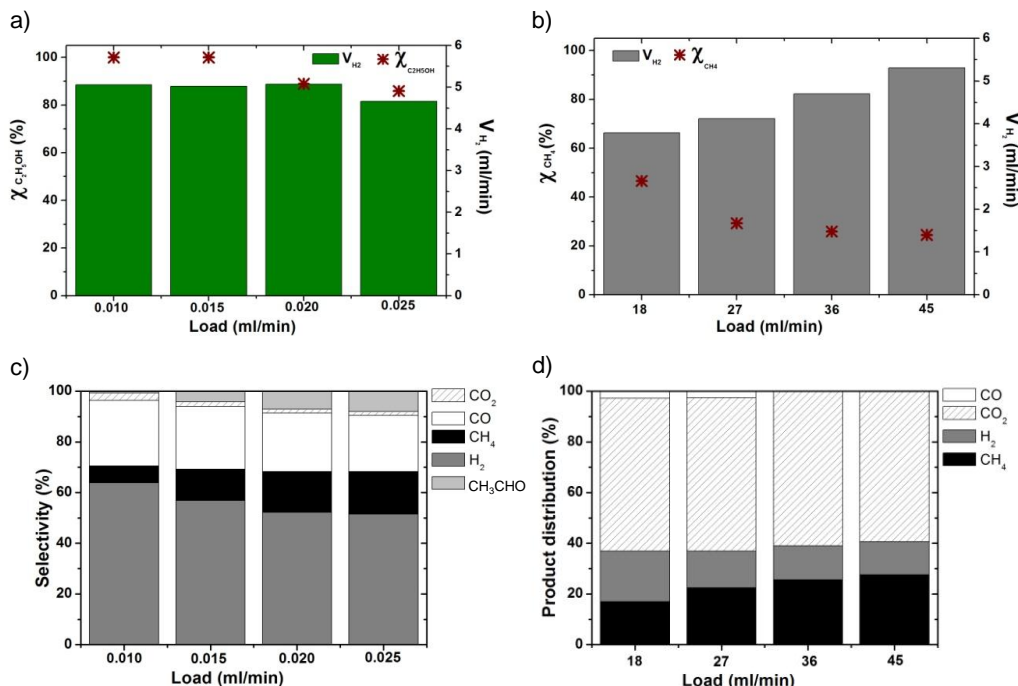


**Figure 4.10:** DSC analysis to compare the carbon content on a fresh and an used catalyst. The inset shows the corresponding CO<sub>2</sub> mass spectra.

#### 4.3.2.2. Influence of the fuel loading

**Figure 4.11a-b** depicts the fuel conversion and volumetric hydrogen production conversion obtained for both ESR and MDR reactions depending on the fuel loading. The selectivity towards ESR and MDR products are shown in Figure 4.11c and Figure 4.11d, respectively. As observed in Figure 4.11a and Figure 4.11b, the conversion rate of both fuels slightly decreased with fuel loading, but the production of hydrogen remained almost constant for ESR and increased for MDR. In particular, as represented in Figure 4.11a, ethanol conversion kept almost constant for the first two fuel loads, leading to residence times of 0.16 s and 0.13 s, and then decreased gradually as the fuel load increased, due to reduced residence times of 0.11 s and 0.09 s respectively. In contrast, as observed in Figure 4.11b, methane conversion showed a notable drop due to shorter contact times between fuel and catalyst compared to ESR (from 0.10 s for 18ml/min to 0.05 s for 45ml/min). The hydrogen production did not suffer from big variation in the case of ESR because the extent of reactions at 700 °C was maintained approximately constant. Higher fuel load rates led to higher production of hydrogen in the case of MDR due to methane decomposition which dominates at this temperature. Figure 4.11c shows the selectivity towards products of ESR.

Particularly, selectivity towards hydrogen decreased progressively as increased the fuel load due to a lower ethanol conversion, as well as a lower extension of methane reforming and WGS reactions. In addition, higher production of acetaldehyde was measured, confirming that the dehydrogenation reaction of ethanol was extended when residence time is reduced. The MDR followed a similar trend as depicted in Figure 4.11d. There was selectivity towards syngas at low fuel loading, but no CO was detected at high fuel loading due to shorter contact time between methane and catalyst.



**Figure 4.11:** Performance of methane and ethanol reforming reactions at 700 °C for different fuel mixture loads; (a) ethanol conversion and hydrogen production for ESR, (b) methane conversion and hydrogen production for MDR, (c) selectivity towards ESR and (d) outlet gas composition of MDR.



**Table 4.3** summarizes the catalytic activity of the bulk  $\mu$ reformer for ESR and MDR reactions under different conditions of temperature and fuel loading. Although results of methane conversion achieved in MDR reaction were lower than reported in literature [21], the selectivity towards hydrogen (64%) and hydrogen yield (0.28) at 800 °C (temperature at which the methane decomposition was minimized) were within the range of previous works suggesting that the operation flow rate required for a real  $\mu$ SOFC system is too high if a ratio of  $\text{CO}_2:\text{CH}_4$  equal 2 was applied. In contrast, the results obtained at 750 °C for ESR yielded complete ethanol conversion, hydrogen selectivity of 52.7% and hydrogen yield of 0.36, which were in good agreement with the results reported for the same catalyst system Pd-Rh/CeO<sub>2</sub> in previous works [18]. The main goal of producing significant volume rates of hydrogen to supply the  $\mu$ SOFC PG was achieved in both reforming reactions (7 ml·min<sup>-1</sup> at 800 °C for MDR and 8 ml·min<sup>-1</sup> at 750 °C for ESR). However, due to the better performance and catalytic activity of Pd-Rh/CeO<sub>2</sub> towards ESR, ethanol was the fuel selected for the following sections devoted to the suspended  $\mu$ reformer device.

**Table 4.3:** Catalytic activity of the bulk  $\mu$ reformer.

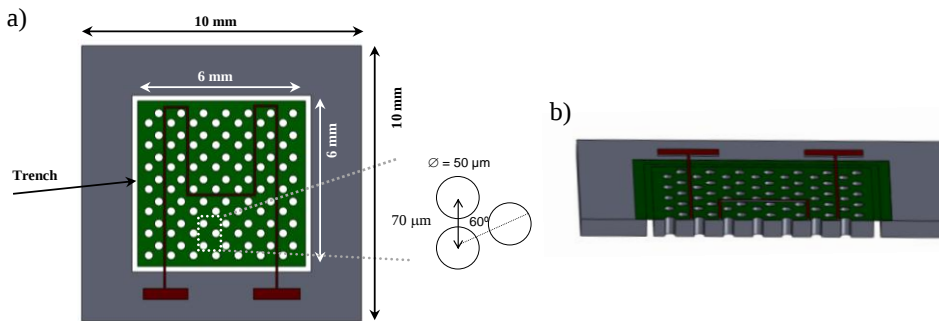
		Ethanol Steam Reforming (ESR)				Methane Dry Reforming (MDR)				
		$\chi_{\text{CH}_3\text{CH}_2\text{OH}}$ (%)	$S_{\text{H}_2}$ (ml·min <sup>-1</sup> )	$\dot{V}_{\text{H}_2}$ (ml·min <sup>-1</sup> )	$\Psi_{\text{H}_2}$	$\chi_{\text{CH}_4}$ (%)	$S_{\text{H}_2}$ (ml·min <sup>-1</sup> )	$\dot{V}_{\text{H}_2}$ (ml·min <sup>-1</sup> )	$\Psi_{\text{H}_2}$	
Temperature (°C)	600	36.9	57	2.6	0.12	600	15	100	3	0.12
	650	49	49.1	2.8	0.13	650	17	100	3.5	0.14
	700	87.2	44.8	5.1	0.24	700	26	100	4.7	0.19
	750	98.1	52.7	7.7	0.36	750	32	81	6.1	0.25
	800	100	58	10	0.47	800	35	64	6.9	0.28
Fuel Loading (ml·min <sup>-1</sup> )	0.01	100	54.4	5.1	0.48	18	46.6	85.1	3.79	0.32
	0.015	98.7	49.7	5.0	0.32	27	29.3	87.7	4.12	0.23
	0.02	89	46.4	4.6	0.22	36	25.9	100	4.70	0.19
	0.025	75.4	46	4.7	0.18	45	25.1	100	5.31	0.18

## 4.4. Design and fabrication of a suspended $\mu$ reformer

A suspended  $\mu$ reformer thermally optimized was designed on the basis of a low thermal mass architecture in order to achieve a rapid start-up, while keeping the catalytic activity towards ESR as in the bulk  $\mu$ reformer.

### 4.4.1. Design outline and concept approach

A schematic of the proposed design is depicted in **Figure 4.12**. The suspended  $\mu$ reformer was also based on a silicon platform (500  $\mu\text{m}$  thick) and a vertical micro channel configuration. However, the active area was suspended on a thermally insulating silicon nitride membrane, i.e. there was a trench between the active area and the rest of the silicon substrate. The  $\mu$ reformer had dimensions of 10x10 mm<sup>2</sup> and presented a reaction zone of 6x6 mm<sup>2</sup>. This active area consisted of a highly dense array of through-silicon micro channels with 50  $\mu\text{m}$  in diameter. More than  $7 \cdot 10^3$  channels resulted in a total active area of 5.75 cm<sup>2</sup> to be covered with the Pd-Rh/CeO<sub>2</sub> catalytic system. A serpentine-like heater with dimensions of *ca.* 2.4 cm long and 100  $\mu\text{m}$  wide was integrated in the suspended mass. The heater was fabricated in the form of a multilayer consisting of 30 nm of TiW + 250 nm of W + 20 nm thick of Au (see *Section 4.2.3*).



**Figure 4.12:** (a) Schematic view and (b) cross section layout of the suspended  $\mu$ reformer design. Micro channels are not to scale.

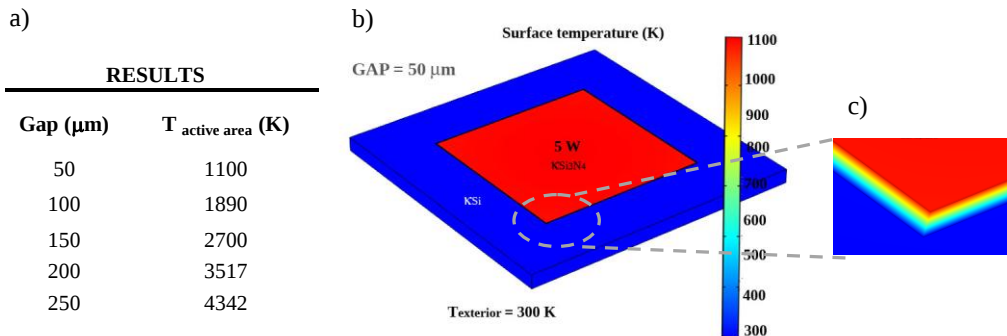
The thermal effect of the silicon nitride membrane was analysed by FVM simulations. **Table 4.3** summarizes the materials properties and boundary conditions used. Different gap distances were simulated while a heat source of 5 W was applied in the active area (in agreement with the maximum electric power supplied in the embedded heater during the start-up, *Section 3.5.2 Chapter III*). Furthermore, as the  $\mu$ reformer should be stacked with

other components within the hot module of the  $\mu$ SOFC PG (see Section 3.3.1 of Chapter III) only the heat loss pathway by thermal conductivity was considered.

**Table 4.3:** Materials properties and boundary conditions applied in the simulations.

Materials		
	Si	Si <sub>3</sub> N <sub>4</sub>
Heat capacity (at constant pressure)	700	712 J/(kg·K)
Density	2309	3440 kg/m <sup>3</sup>
Thermal conductivity	130	30 W/(m·K)
Boundary conditions		
External temperature	300	K
Heat source	5	W

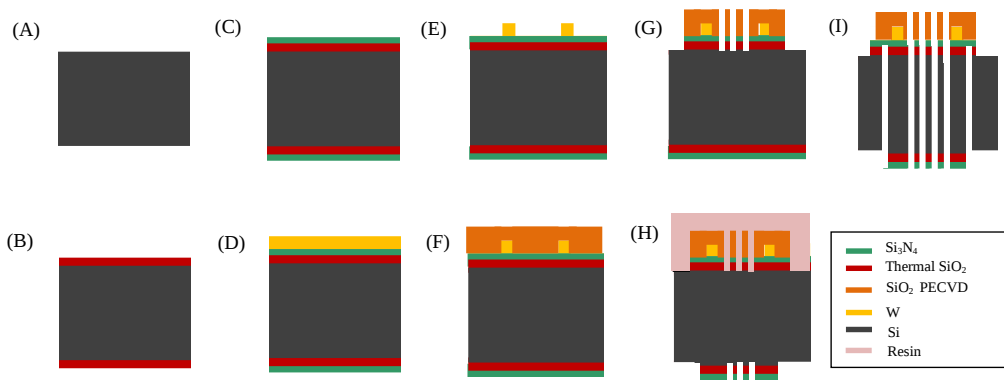
**Figure 4.13** shows the temperatures obtained as a function of the gap between the bulk frame and the suspended active mass. For all gap distances, thermal gradients greater than 800 K were attained. Thus, this new design allowed the suspended active area to be thermally insulated from the rest of the silicon substrate due to the Si<sub>3</sub>N<sub>4</sub> membrane (300 nm thick). After validating the thermal behaviour of the membrane, the basics of the  $\mu$ reformer fabrication process were considered for the selection of the gap distance. Taking into consideration that a suitable aspect ratio of DRIE in silicon is 20 and the etch rate is limited by the gas diffusion in the material targeted of being eliminated, the gap distance most appropriate to achieve in a single step an uniform trench and uniform micro channels was 50  $\mu$ m.



**Figure 4.13:** (a) Temperatures obtained by FVM simulations as a function of the gap distance, (b) temperature profiles for a gap of 50  $\mu$ m and (c) detail of the thermal gradient across the Si<sub>3</sub>N<sub>4</sub> membrane (300 nm thick).

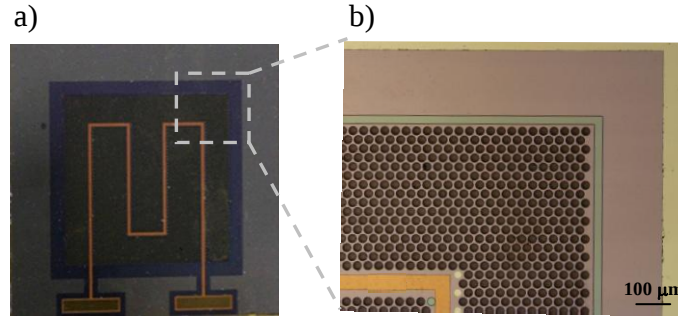
#### 4.4.2. Microfabrication process

The major steps involved in the fabrication of the suspended  $\mu$ reformer were similar to those of the bulk  $\mu$ reformer. Single crystal (100)-oriented p-type silicon wafers of 100 mm diameter and 500  $\mu$ m thick were passivated with a stress-free combination of 100 nm  $\text{SiO}_2$  and 300 nm  $\text{Si}_3\text{N}_4$  layers (Figure 4.14A-C). A metallic multilayer was deposited by sputtering on the front side of wafer: 30 nm of TiW, 250 nm of W and 20 nm of Au (Figure 4.14D). After that, a photolithographic step was used to define the heater shape and pads. The exposed areas were removed by wet etching in 40% wt  $\text{H}_2\text{O}_2$  (Figure 4.14E). Then, the active area was passivated with a 1  $\mu$ m thick  $\text{SiO}_2$  PECVD layer (Figure 4.14F). A second photolithographic step defined the micro channels and the bulk frame, which was used to encapsulate later, on the top side. A RIE process was carried out to eliminate the dielectric layers (Figure 4.14G). After that, a double-sided alignment photolithographic step defined the micro channels, the bulk frame and the trench on the back side of the wafer. A RIE process eliminated the dielectric layers (Figure 4.14H). Then, a photolithographic step was used to define only the micro channels and the trench on the back side and a 1  $\mu$ m thick aluminum/cooper hard mask was deposited by sputtering. At that point, a DRIE – Bosch process was carried out to form the through-silicon holes and the trench, while the wafer top side was protected with a 2  $\mu$ m thick resin. The exposed copper-aluminum mask was chemically removed (Figure 4.14H-I).



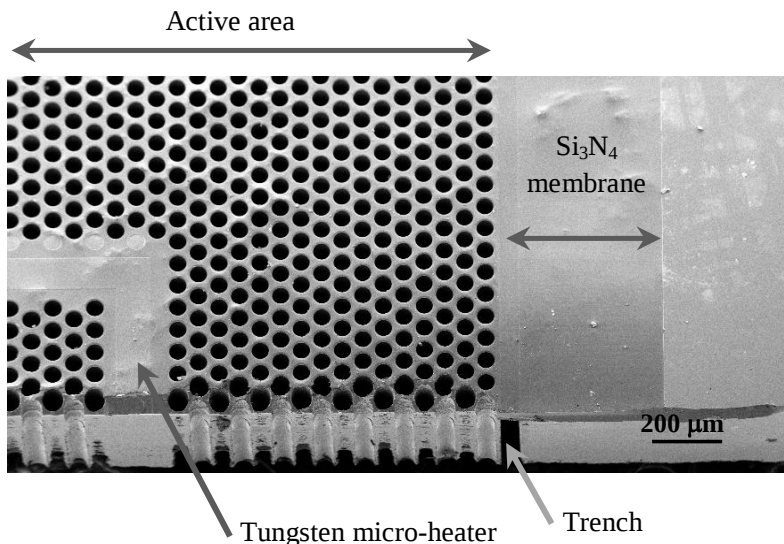
**Figure 4.14:** Scheme of the fabrication flow of the suspended  $\mu$ reformer. Silicon wafers were passivated with  $\text{SiO}_2$  and  $\text{Si}_3\text{N}_4$  layers (Figure 4.3A-C). A metallic multilayer was defined on the front side (Figure 4.3D-F). A photolithographic steps followed by a RIE process defined the micro channels and the bulk frame on both sides. Finally, a DRIE – Bosch process was carried out to form the through silicon micro channels and the trench (Figure 4.3F).

Optical images of the microfabricated reformer are shown in **Figure 4.15**. The projected area obtained was  $0.36 \text{ cm}^2$ , while the reactive area represented more than  $5.75 \text{ cm}^2$ , i.e. the active surface per projected area was  $16 \text{ cm}^2/\text{cm}^2$ .



**Figure 4.15:** (a) General view of the fabricated suspended reformer and (b) detail of the micro channels array, the trench (in green) and tungsten metallic micro heater pad (yellow strip).

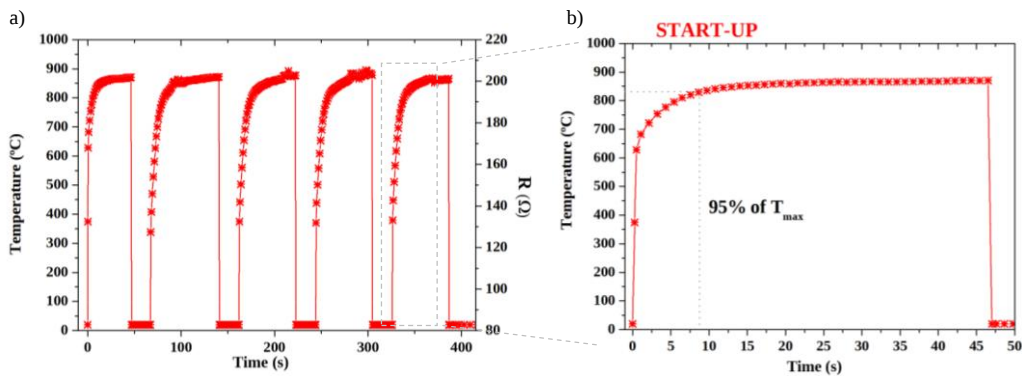
The suspended reformer was fabricated without mechanical failure of the structure. **Figure 4.16** shows a SEM image where the active area suspended on the  $\text{Si}_3\text{N}_4$  membrane, the micro heater and the micro channels through the silicon platform are detailed. As in the bulk reformer, there was no significant tapering effect along the  $500 \text{ }\mu\text{m}$  channels, thus avoiding undesirable pressure drop due to bottlenecks.



**Figure 4.16:** SEM image where the active area suspended on the  $\text{Si}_3\text{N}_4$  membrane, the micro heater and the micro channels through the silicon platform were detailed.

### 4.4.3. Start-up of the suspended $\mu$ reformer

Following the same experimental protocol presented for the bulk  $\mu$ reformer, the transient response of the suspended  $\mu$ reformer was studied under vacuum conditions ( $\sim 1$  Pa), without any fuel, and by applying 5 W to the heater ( $R_0 = 91.4 \Omega$ ). As shown in **Figure 4.17a**, several thermal cycles were performed ensuring the reliability of the micro heater. A detail of the measured start-up time of the suspended  $\mu$ reformer is shown in **Figure 4.17b**. The start-up was achieved after 8.75 s and the maximum temperature reached was 870 °C. The energy consumption was 43.75 J. Thus, a lower thermal mass structure with the active area thermally isolated allowed reducing the start-up time and the energy consumption *ca.*  $\sim 86\%$  compared to bulk  $\mu$ reformer.

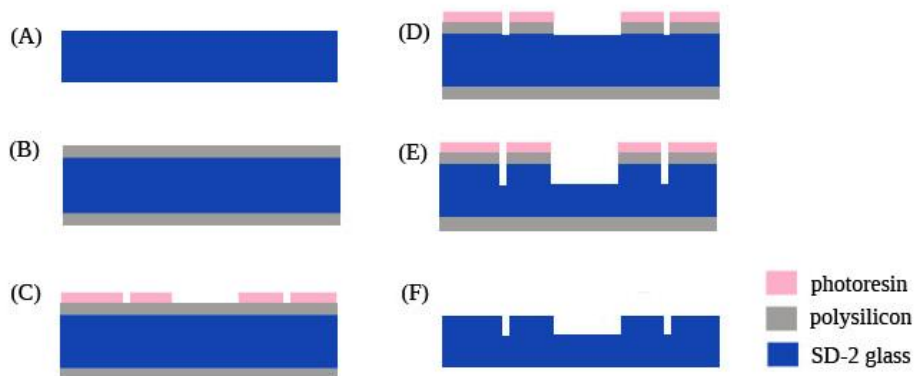


**Figure 4.17:** (a) Thermal cycles of the suspended  $\mu$ reformer under vacuum conditions ( $\sim 1$  Pa), without any fuel, and by applying 5 W to the heater ( $R_0 = 91.4 \Omega$ ), and (b) detail of the measured start-up time.

### 4.4.4. Glass cover fabrication and encapsulation

Once the suspended  $\mu$ reformer was fabricated and characterized, a glass cover and an encapsulation process was required to test its catalytic activity as a standalone device. **Figure 4.18** shows the fabrication process of the glass covers (SD-2 from HOYA OPTICS) at wafer level. Glass wafers of 100 mm diameter and 1 mm thick were covered with polysilicon at 630 °C to obtain a 350 nm thick hard mask (Figure 4.18a-b). Then, a photolithographic step was used to define two cavities, one for the active area where the fuel will flow and the other for the outlet path of the heater (Figure 4.18c). The polysilicon exposed areas were removed by wet etching in 3:2:60 HF:HNO<sub>3</sub>:H<sub>2</sub>O (Figure 4.18d). After that, the glass exposed was partially removed by wet etching in 49% HF during 2 minutes which correspond to 40  $\mu$ m of depth (Figure 4.18e).

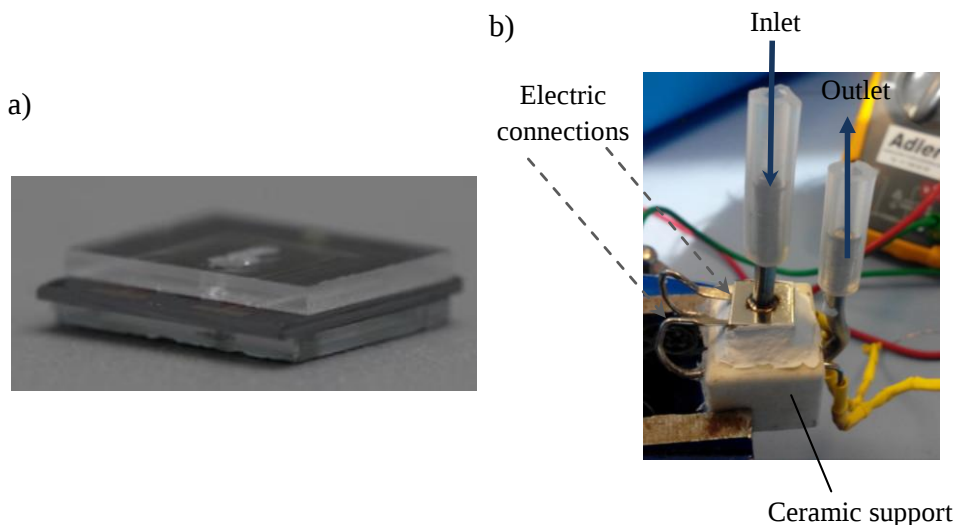
As it is an isotropic process there was some lateral etch. Finally the photoresist was removed in acetone and the polysilicon mask in 3:2:60 HF:HNO<sub>3</sub>:H<sub>2</sub>O (Figure 4.18f).



**Figure 4.18:** Scheme of the fabrication flow of the glass covers.

After the glass cover fabrication, a micro hole (1 mm in diameter) was drilled with a Dremel® tool.

The encapsulation was done using an anodic bonding process as described in **Chapter II**, *Section 2.2.2.3*. **Figure 4.19** shows an image of the suspended  $\mu$ reformer encapsulated without (Figure 4.19a) and with the fluidic connections (sealed using Ceramabond ®) and electric connections (Figure 4.19b).

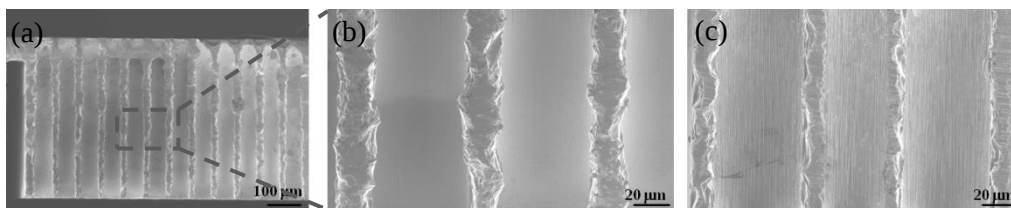


**Figure 4.19:** Encapsulated  $\mu$ reformer as a standalone device (a) without and (b) with the fluidic and electric connections.

## 4.5. Activity measurements of the suspended $\mu$ reformer

### 4.5.1. Wet impregnation method of the Pd-Rh/CeO<sub>2</sub> catalyst system

Since the suspended  $\mu$ reformer was already encapsulated (to allow a proper anodic bonding), a modified synthesis route was used for the wet impregnation of the Pd-Rh/CeO<sub>2</sub> catalyst system by using the micro holes. First, a piranha solution (4:1 H<sub>2</sub>SO<sub>4</sub>:H<sub>2</sub>O<sub>2</sub>) was flowed through the micro channels to oxidize the walls. Then, the cerium precursor solution was introduced by applying a pressure gradient in the micro holes and was calcined at 500 °C forming the CeO<sub>2</sub> support. As shown in **Figure 4.20**, this method allowed covering very homogeneously the walls of the micro channels with a CeO<sub>2</sub> layer (~200 nm in thickness). As a result, the coverage per unit mass of catalyst took values up to  $18 \cdot 10^3 \text{ cm}^2 \cdot \text{g}^{-1}$ .



**Figure 4.20:** (a) SEM image of the cross section of several micro channels after catalyst impregnation and thermal treatment, (b) magnification of the homogenous CeO<sub>2</sub> layer on micro channels and (c) silicon walls without CeO<sub>2</sub> layer for comparison.

### 4.5.2. Activity of the suspended $\mu$ reformer as a standalone device

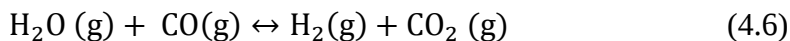
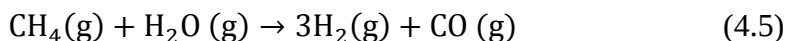
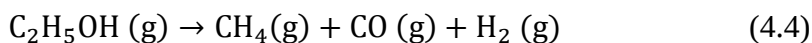
The activity of the suspended  $\mu$ reformer was tested for ESR inside a vacuum chamber (see *Section 2.6.1* in **Chapter II**) and using its embedded micro heater. The temperature reached in the active area was approximately 750 °C while a fuel load of  $0.02 \text{ ml} \cdot \text{min}^{-1}$  was supplied.

The volumetric flow rate at the outlet was  $6 \text{ ml} \cdot \text{min}^{-1}$ , a much lower value than the expected one due to the important leakages from the system to the chamber (probably more accentuated in the electrical contacts). In consequence, the micro GC analysis was not quantitative. Despite that, as shown in **Table 4.4**, the product distribution obtained was in agreement with the results previously reported for the bulk  $\mu$ reformer at the same temperature.



The conversion of the ethanol was almost complete. Furthermore, the reforming of methane was observed after ethanol decomposition since the ratio CH<sub>4</sub>:CO:H<sub>2</sub> was not 1 (equations 4.4 and 4.5). In particular, a 7.74% of CH<sub>4</sub>, 15.52% of CO and a 65.56% of H<sub>2</sub> were detected. The WGSR reaction (equation 4.6) occurred in series with ethanol decomposition and methane reforming but in less extent, likely due to a reduced residence time (~ 0.02 s). The dehydrogenation of ethanol to acetaldehyde was scarce (0.1% of CH<sub>3</sub>CHO). Furthermore, although ethylene (0.96 % CH<sub>2</sub>=CH<sub>2</sub>) and ethane (0.27% C<sub>2</sub>H<sub>6</sub>) were detected in the gas outlet, the ethanol dehydration and the ethylene hydrogenation reactions were not significant.

Therefore, the proof of concept of the suspended  $\mu$ reformer was proved as a standalone device. However, further work should be focused on quantitative analysis without leakages and by extending the punctual measurements to specific long-term tests.



**Table 4.4:** Product distribution obtained in the suspended  $\mu$ reformer as a standalone device.

PRODUCT DISTRIBUTION (%)							
CH <sub>3</sub> CH <sub>2</sub> OH	CH <sub>4</sub>	CO	H <sub>2</sub>	CO <sub>2</sub>	CH <sub>3</sub> CHO	C <sub>2</sub> H <sub>4</sub>	C <sub>2</sub> H <sub>6</sub>
5.45	7.74	15.52	65.56	4.39	0.10	0.96	0.27

## 4.6. Conclusions

Silicon-based  $\mu$ reformers with a novel design were fabricated using robust and reproducible MEMS mainstream technology.

The bulk  $\mu$ reformer presented more than 20000 through-silicon vertically aligned micro-channels per  $\text{cm}^2$  with a diameter of 50  $\mu\text{m}$  and a length of 500  $\mu\text{m}$ . This microstructure yields a total active surface per projected area of  $16 \text{ cm}^2/\text{cm}^2$  and per total volume of  $320 \text{ cm}^2/\text{cm}^3$ . Moreover, an embedded metal micro heater was integrated for locally heating the active area. The micro heater based on 30 nm of TiW, 250 nm of W and 20 nm of Au was tested by performing several thermal cycles. The maximum temperature reached in the active area was 670  $^\circ\text{C}$  in 82.5 s, leading to an energy consumption of 412.5 J. A catalytic system based on Pd-Rh/CeO<sub>2</sub> was deposited successfully over the micro-channel walls. The suitability of the catalytic device for methane dry reforming and ethanol steam reforming was proved under operating conditions compatible with the  $\mu$ SOFC PG. Hydrogen yields of 0.36 and 0.28 and hydrogen selectivities of 58% and 64% were obtained for ESR (T=750  $^\circ\text{C}$ ) and MDR (T=800  $^\circ\text{C}$ ), respectively.

A second  $\mu$ reformer based on a low thermal mass architecture suspended on a silicon nitride membrane was fabricated in order to achieve a rapid start-up, while keeping the catalytic activity as efficient as in the bulk  $\mu$ reformer. The  $6 \times 6 \text{ mm}^2$  active area was composed by a highly dense array of more than  $7 \cdot 10^3$  micro channels, which resulted in a total active area of  $5.75 \text{ cm}^2$ . A micro heater based on 30 nm of TiW, 250 nm of W and 20 nm of Au was integrated in the suspended mass. The total active surface per projected area and per total volume were maintained constant with respect to the bulk  $\mu$ reformer, i.e.  $16 \text{ cm}^2/\text{cm}^2$  and  $320 \text{ cm}^2/\text{cm}^3$ , respectively. The mass with the catalytic active area was suspended on a Si<sub>3</sub>N<sub>4</sub> membrane and was isolated from the rest of the micro reactor by a trench of 50  $\mu\text{m}$  without yielding any mechanical failure. Using the same heater configuration as in the bulk, the start-up was achieved after 8.75 s reaching a maximum temperature of 870  $^\circ\text{C}$  and consuming 44 J. Thus, this thermally optimized suspended  $\mu$ reformer allowed reducing the start-up time and the energy consumption in *ca.* 86%. The device was first encapsulated and, afterwards, the Pd-Rh/CeO<sub>2</sub> catalytic system was introduced covering homogeneously the walls of micro channels. Its catalytic activity for ethanol steam reforming was also

qualitatively proved under operating conditions compatible with the  $\mu$ SOFC PG.

## References

- [1] Brown, L. F. A comparative study of fuels for on-board hydrogen production for fuel-cell-powered automobiles. *Int. J. Hydrogen Energy* **26**, 381–397 (2001).
- [2] Llorca, J., Casanovas, A., Trifonov, T., Rodríguez, A. & Alcubilla, R. First use of macroporous silicon loaded with catalyst film for a chemical reaction: A microreformer for producing hydrogen from ethanol steam reforming. *J. Catal.* **255**, 228–233 (2008).
- [3] Mogensen, M. & Kammer, K. Conversion of hydrocarbons in solid oxide fuel cells. *Annu. Rev. Mater. Res.* **33**, 321–331 (2003).
- [4] Park, S., Vohs, J. M. & Gorte, R. J. Direct oxidation of hydrocarbons in a solid-oxide fuel cell. *Nature* **404**, 265–267 (2000).
- [5] Takagi, Y., Kerman, K., Ko, C. & Ramanathan, S. Operational characteristics of thin film solid oxide fuel cells with ruthenium anode in natural gas. *J. Power Sources* **243**, 1–9 (2013).
- [6] Compact integrated manifold/reformer for SOFC systems. *Fuel Cells Bull.* **2002**, 16 (2002).
- [7] Finnerty, C., Tompsett, G. A., Kendall, K. & Ormerod, R. M. SOFC system with integrated catalytic fuel processing. *J. Power Sources* **86**, 459–463 (2000).
- [8] Stutz, M. J., Grass, R. N., Loher, S., Stark, W. J. & Poulikakos, D. Fast and exergy efficient start-up of micro-solid oxide fuel cell systems by using the reformer or the post-combustor for start-up heating. *J. Power Sources* **182**, 558–564 (2008).
- [9] Scherrer, B. *et al.* A thermally self-sustained micro-power plant with integrated micro-solid oxide fuel cells, micro-reformer and functional micro-fluidic carrier. *J. Power Sources* **258**, 434–440 (2014).
- [10] Lehnert, W., Meusinger, J. & Thom, F. Modelling of gas transport phenomena in SOFC anodes. *J. Power Sources* **87**, 57–63 (2000).
- [11] Singhal, S., Singhal, S. C. & Kendall, K. *High-temperature Solid Oxide Fuel Cells: Fundamentals, Design and Applications: Fundamentals, Design and Applications.* (Elsevier Science, 2003).
- [12] Cimenti, M. & Hill, J. M. Direct Utilization of Liquid Fuels in SOFC for Portable Applications: Challenges for the Selection of Alternative Anodes. *Energies* **2**, 377–410 (2009).
- [13] Bieberle-Hütter, A. *et al.* Syngas generation from n-butane with an integrated MEMS assembly for gas processing in micro-solid oxide fuel cell systems. *Lab Chip* **12**, 4894–902 (2012).

- [14] Santis-Alvarez, A. J. *et al.* A nanoparticle bed micro-reactor with high syngas yield for moderate temperature micro-scale SOFC power plants. *Chem. Eng. Sci.* **84**, 469–478 (2012).
- [15] Scherrer, B. *et al.* A thermally self-sustained micro-power plant with integrated micro-solid oxide fuel cells, micro-reformer and functional micro-fluidic carrier. *J. Power Sources* **258**, 434–440 (2014).
- [16] Schaevitz, S. B. Powering the wireless world with MEMS. *Proc. SPIE* **8248**, 824802–824815 (2012).
- [17] Llorca, J., Casanovas, A., Trifonov, T., Rodríguez, A. & Alcobilla, R. First use of macroporous silicon loaded with catalyst film for a chemical reaction: A microreformer for producing hydrogen from ethanol steam reforming. *J. Catal.* **255**, 228–233 (2008).
- [18] Divins, N. J., López, E., Rodríguez, Á., Vega, D. & Llorca, J. Bio-ethanol steam reforming and autothermal reforming in 3  $\mu\text{m}$  channels coated with RhPd/CeO<sub>2</sub> for hydrogen generation. *Chem. Eng. Process. Process Intensif.* **64**, 31–37 (2013).
- [19] Serrano-Lotina, A. & Daza, L. Influence of the operating parameters over dry reforming of methane to syngas. *Int. J. Hydrogen Energy* **39**, 4089–4094 (2014).
- [20] Santis-Alvarez, A. J., Büchel, R., Hild, N., Stark, W. J. & Poulikakos, D. Comparison of flame-made rhodium on Al<sub>2</sub>O<sub>3</sub> or Ce<sub>0.5</sub>Zr<sub>0.5</sub>O<sub>2</sub> supports for the partial oxidation of methane. *Appl. Catal. A Gen.* **469**, 275–283 (2014).
- [21] Pakhare, D. & Spivey, J. A review of dry (CO<sub>2</sub>) reforming of methane over noble metal catalysts. *Chem. Soc. Rev.* **43**, 7813–7837 (2014).
- [22] Costilla, I. O., Sánchez, M. D. & Gigola, C. E. Palladium nanoparticle's surface structure and morphology effect on the catalytic activity for dry reforming of methane. *Appl. Catal. A Gen.* **478**, 38–44 (2014).
- [23] Bitter, J. H., Seshan, K. & Lercher, J. A. Mono and Bifunctional Pathways of CO<sub>2</sub>/CH<sub>4</sub> Reforming over Pt and Rh Based Catalysts. *J. Catal.* **176**, 93–101 (1998).
- [24] Idriss, H. *et al.* A Phenomenological Study of the Metal–Oxide Interface: The Role of Catalysis in Hydrogen Production from Renewable Resources. *ChemSusChem* **1**, 905–910 (2008).
- [25] Divins, N. J., Angurell, I., Escudero, C., Pérez-Dieste, V. & Llorca, J. Influence of the support on surface rearrangements of bimetallic nanoparticles in real catalysts. *Sci.* **346**, 620–623 (2014).

- [26] Fajardo, H. V. & Probst, L. F. D. Production of hydrogen by steam reforming of ethanol over Ni/Al<sub>2</sub>O<sub>3</sub> spherical catalysts. *Appl. Catal. A Gen.* **306**, 134–141 (2006).
- [27] Cai, W. *et al.* Hydrogen production from ethanol steam reforming in a micro-channel reactor. *Int. J. Hydrogen Energy* **35**, 1152–1159 (2010).
- [28] Men, Y., Kolb, G., Zapf, R., Hessel, V. & Löwe, H. Ethanol Steam Reforming in a Microchannel Reactor. *Process Saf. Environ. Prot.* **85**, 413–418 (2007).
- [29] Casanovas, A., Saint-Gerons, M., Griffon, F. & Llorca, J. Autothermal generation of hydrogen from ethanol in a microreactor. *Int. J. Hydrogen Energy* **33**, 1827–1833 (2008).
- [30] Cheun, K. M.Sc. Thesis, Massachusetts Institute of Technology (2005).
- [31] Blackwell, B. S., M.Sc. Thesis, Massachusetts Institute of Technology (2008).
- [32] López, E. *et al.* Ethanol steam reforming for hydrogen generation over structured catalysts. *Int. J. Hydrogen Energy* **38**, 4418–4428 (2013).
- [33] López, E., Irigoyen, A., Trifonov, T., Rodríguez, A. & Llorca, J. A million-channel reformer on a fingertip: Moving down the scale in hydrogen production. *Int. J. Hydrogen Energy* **35**, 3472–3479 (2010).
- [34] Ali, S. Z. *et al.* High Temperature SQI CMOS Tungsten Micro-Heaters. *Sensors, 2006. 5th IEEE Conf.* 847–850 (2006).
- [35] Tu, K. N. *Electronic Thin-Film Reliability*. (Cambridge University Press, 2010).
- [36] Santis-Alvarez, A. J., Nabavi, M., Hild, N., Poulikakos, D. & Stark, W. J. A fast hybrid start-up process for thermally self-sustained catalyticn-butane reforming in micro-SOFC power plants. *Energy Environ. Sci.* **4**, 3041–3050 (2011).



## **V. POST COMBUSTION UNIT**



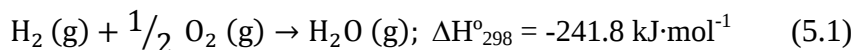


<b>5.1. Introduction.....</b>	<b>151</b>
<b>5.2. Characterization of CuO-NiO/CGO catalyst.....</b>	<b>155</b>
<b>5.3. Synergic effect of multi-component metal oxides.....</b>	<b>158</b>
<b>5.4. Post combustor prototype for a <math>\mu</math>SOFC PG.....</b>	<b>162</b>
5.4.1. Microfabrication of the silicon $\mu$ combustor.....	162
5.4.2. Catalyst infiltration.....	163
5.4.3. Operation conditions.....	163
5.4.2. Reaction tests.....	164
<b>5.5. Conclusions.....</b>	<b>166</b>



## 5.1. Introduction

There is a mixture of fuels that still remains unreacted after passing through the  $\mu$ SOFC stack (like unreacted  $H_2$ ,  $CO$ ,  $C_nH_{2n+2}$  or  $C_nH_{2n+1}OH$ ). Some of these exhaust gases are harmful and detrimental to environment and health:  $CO$  is toxic,  $H_2$  is explosive and  $CH_4$  is a greenhouse gas 20 times more efficient than  $CO_2$  [1]. Consequently, for safety and efficiency reasons, the  $\mu$ SOFC PG includes a Catalytic Post combustion Unit (CPU) placed after the  $\mu$ SOFC stack to convert the exhaust gases. The CPU has to fulfill several requirements, namely, a feasible design for an easy integration with the rest of components and a catalyst system able to efficiently convert  $H_2$  and short-chain hydrocarbons at a wide range of temperatures (from 150 °C to 700 °C, related to start-up and steady state, respectively). This **Chapter V** is devoted to develop the CPU and is focused on the  $H_2$  combustion (equation 5.1) at low temperatures, as the ones required during the hybrid start-up process (*Section 3.5.2 Chapter III*).



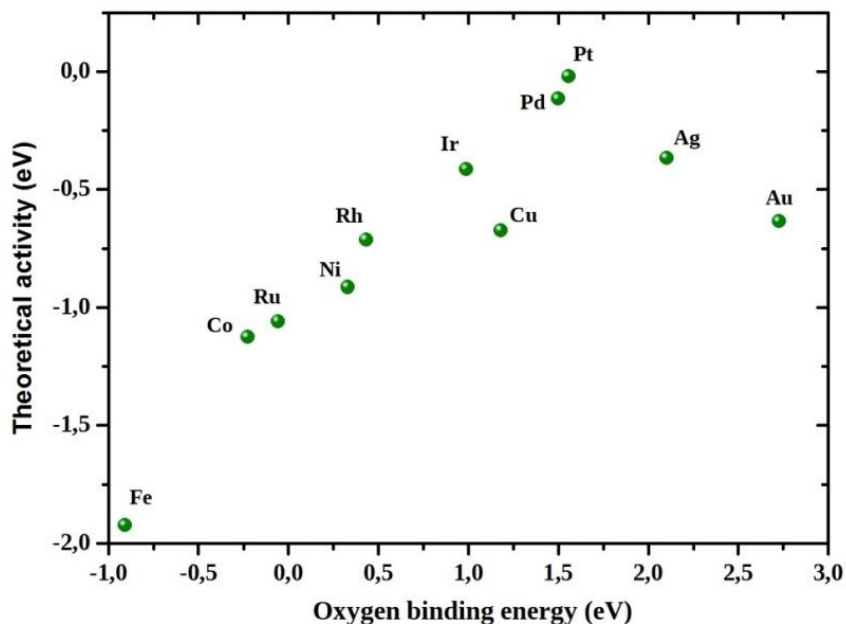
Three methods for  $H_2$  combustion are known, namely, conventional flame-type, low-temperature catalytic and hybrid combustion. As summarized in **Table 5.1**, conventional flame-type combustion requires high-temperatures and produces large amounts of nitrogen oxides ( $NO_x$ ), while suffering from backflashes [2]. Low-temperature catalytic combustion involves a catalyst that allows combustion outside the flammability limits and maintains a stable combustion of lean fuel/air mixtures [3]. The hybrid method, otherwise called catalytically supported thermal combustion, is effective in providing a large heat output with a minimum  $NO_x$  emission.

**Table 5.1:** Comparison of characteristic features of different hydrogen combustion methods, extracted from [2].

Combustion type	Temperature (°C)	Heat power released ( $W\cdot cm^{-2}$ )	Advantages	Drawbacks
Flame combustion	1200-2100	ca 1162.2	large heat output	high $NO_x$ emission danger of backflash
<b>Catalytic combustion</b>				
Hybrid	500-1200	119.7-1162.2	low $NO_x$ emission	fire
Low-temperature	room temp. - 500	0.035-1.16	no $NO_x$ emission safety from fire	small heat output

Low-temperature flameless combustion over a catalyst with a large surface-to-volume ratio appears as a suitable solution for converting the exhaust gases of the  $\mu$ SOFC PG. It allows using a lean hydrogen mixture as a fuel, which is the composition of the gases leaving the  $\mu$ SOFC stack. Furthermore, as the combustion starts at low temperature, a fraction of the heat released can be used early in the start-up process. Finally, the combustion takes place outside the flammability limit without  $\text{NO}_x$  formation, so it ensures a safe handling of the device and emissions within the limits of the current regulation.

The catalysts used for the  $\text{H}_2$  low-temperature flameless combustion require a high efficiency and uniform temperature distribution over the catalyst surface. Several metals have shown catalytic activity for this reaction, which mainly depends on the interaction between the reactants and the catalyst metal. For example, metals which form strong bonds with  $\text{O}_2$  oxidize quickly and thus generate inert surfaces. Moreover, metals that do not interact strongly enough with  $\text{O}_2$  lead to short adsorption lifetimes, so the surface reaction cannot take place. Noble metals, such as Pt and Pd which form weak oxides, have an appropriate balance, allowing for effective adsorption of  $\text{O}_2$ , as well as desorption of the products. This balance is shown in the Volcano plot depicted in **Figure 5.1** [4].



**Figure 5.1:** Volcano plot for the oxygen reduction reaction on the surface of various transition metals [4].

Most catalyst systems, instead of using a high content of noble metal, are based on metal dispersion at low concentration onto a support with high specific surface area (e.g. porous ceramics, zeolites or amorphous silicas). Several catalytic noble metal-support configurations have been reported in the literature for H<sub>2</sub> combustion [5-10]. However, the high cost of noble metals has increased the use of metal oxides based on transition metals [11-14]. The high activity of metal oxides for oxidation reactions is associated to the transition metal, which can assume more than one valence state, so they are charge carriers favoring a highly mobile chemisorbed surface oxygen [15].

In the last decades, the development of nanomaterials has emerged as a new approach on applied catalysis due to its exceptional properties. As the particle dimensions reduce towards the nanoscale, the surface-to-volume ratio proportionally increases and the small size effects associated with nanoparticles become more pronounced, like catalytic activity [16]. However, one of the main drawbacks for the usage of nanomaterials is that tend to sinter at high temperatures, such as the one needed for a proper operation inside a  $\mu$ SOFC PG.

The knowledge gained over years in H<sub>2</sub> catalytic combustion and the promising properties of nanomaterials appear as an excellent opportunity for developing new catalysts. In this chapter, a 3D-ordered mesoporous nanostructure impregnated with metal oxides is proposed as a catalyst system. High ordered Ce<sub>0.8</sub>Gd<sub>0.2</sub>O<sub>1.9</sub> mesoporous (CGO-mesoporous) was selected as the host support for the metallic component, because it shows large specific surface area, high thermal stability (up to 1000 °C), compatibility with humidity and high Oxygen Storage Capacity (OSC) [17-18]. Regarding the metallic component, oxides of inexpensive transition metals such as Co, Ni, Mn and Cu have been proven to be active for H<sub>2</sub> combustion from temperatures as low as 100 °C [13]. Among them, NiO and CuO were chosen due to their ability for oxidizing also CH<sub>4</sub> and CO, respectively, as reported elsewhere [19-22].

Specific works related to silicon based micro combustors that could be integrated onto a  $\mu$ SOFC PG are sparse. Kaisare and co-workers numerically investigated catalytic micro burners [23, 24]. Specchia *et al.* studied the combustion of CH<sub>4</sub>/H<sub>2</sub>/HC mixtures on SiC monoliths via in situ solution combustion synthesis [25]. The Massachusetts Institute of Technology has been involved on the development of a hydrocarbon-fuelled catalytic micro combustion system, as a part of a micro gas turbine engine [26, 27].

**In this chapter**, three configurations for the catalytic system were synthesized and characterized, i.e. CuO/CGO, NiO/CGO and CuO-NiO/CGO. The specific characterization of the CuO-NiO/CGO-mesoporous catalyst is presented in detail in *Section 5.2* as an example. The activity of binary-component metal oxides (i.e. both CuO and NiO impregnated in the CGO-mesoporous support) was compared to their respective mono-component metal oxides by DSC coupled to TGA and MS in *Section 5.3*. Finally, a silicon micro machined combustor filled with the CuO-NiO/CGO-mesoporous catalyst was fabricated and experimentally tested as a standalone device by applying realistic operation conditions for the  $\mu$ SOFC PG, as described in *Section 5.4*

## 5.2. Characterization of CuO-NiO/CGO catalyst

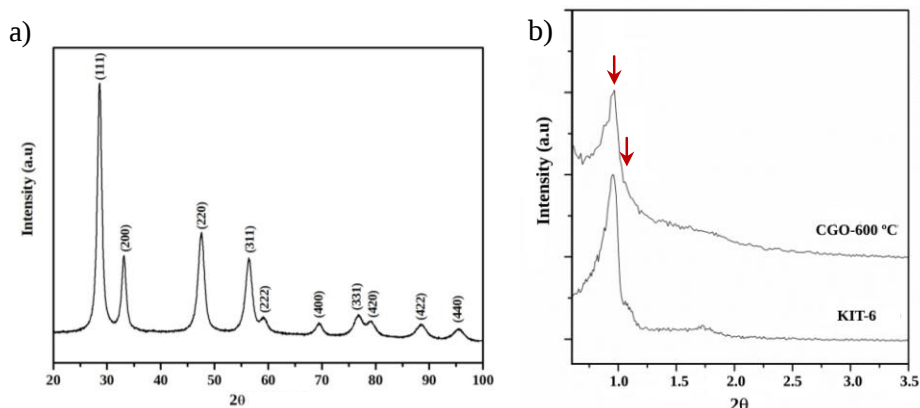
The  $\text{Ce}_{0.8}\text{Gd}_{0.2}\text{O}_{1.9}$  mesoporous material was previously developed and well-characterized as SOFC anode by Almar [28], thus a complementary characterization is presented in this section for the new applicability of this material in a CPU.

The structural parameters of the mesoporous CGO synthesized at 600 °C, like the specific surface area, the pore volume and area analysed using nitrogen adsorption-desorption data, are listed in **Table 5.2**. A high specific surface area of  $115 \text{ m}^2\cdot\text{g}^{-1}$  and a total pore volume of  $0.275 \text{ cm}^3\cdot\text{g}^{-1}$  were obtained, similar to other oxides synthesized by the same hard-template route [29].

**Table 5.2:** Structural parameters of CGO-mesoporous synthesized at 600 °C (extracted from [28]).

Specific surface area ( $\text{m}^2\cdot\text{g}^{-1}$ )	Pore volume ( $\text{cm}^3\cdot\text{g}^{-1}$ )	Pore area ( $\text{m}^2\cdot\text{g}^{-1}$ )
115	0.275	38.37

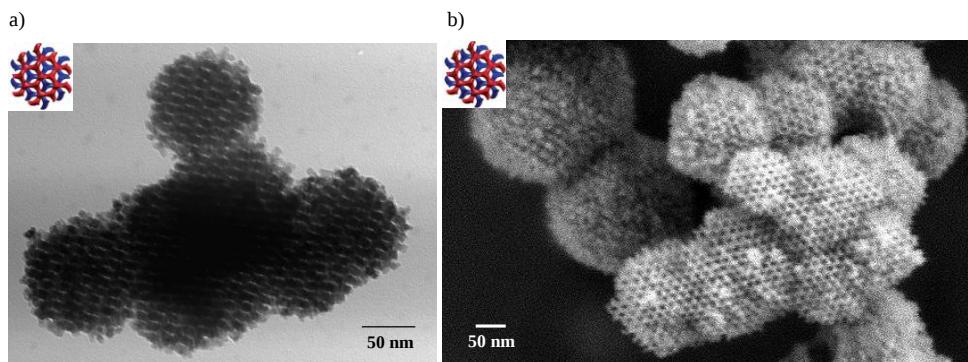
**Figure 5.2a** shows the XRD pattern of the as-synthesized CGO mesoporous structure. The indexed peaks correspond to a cubic fluorite structure of  $\text{Ce}_{0.8}\text{Gd}_{0.2}\text{O}_{1.9}$ . Furthermore, as depicted in **Figure 5.2b**, low-angle XRD, i.e. from  $0.5^\circ$  to  $3.5^\circ$ , corroborates the ordered mesoporous structure. The pattern shows the typical reflections of a double gyroid structure like the KIT-6 silica template, consisting of a sharp peak at  $0.94\text{-}0.98^\circ$  and a weak reflection at  $1.08\text{-}1.1^\circ$ . Therefore, the original matrix of KIT-6 was well transferred to the CGO mesoporous replica.



**Figure 5.2:** (a) XRD and (b) low angle XRD patterns of as synthesized CGO-mesoporous.

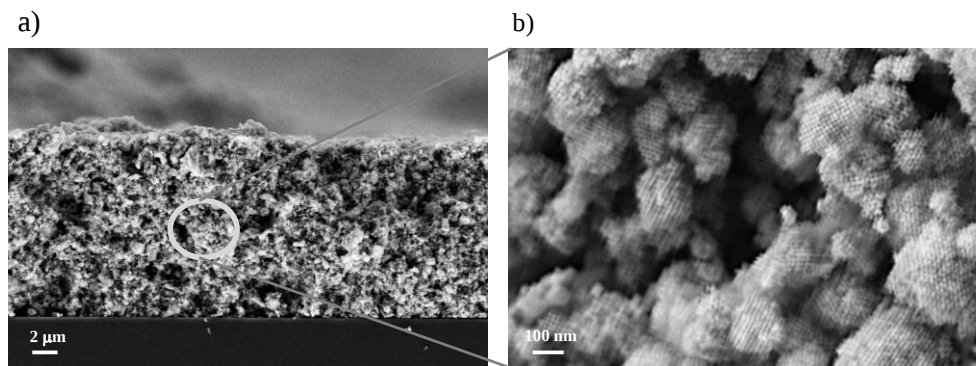


As illustrated in **Figure 5.3**, the mesostructure of the CGO was corroborated by TEM and SEM images. As expected from XRD, highly ordered porous matrices with cross-linked walls were observed, forming periodically distributed porous of *ca.* 10 nm in diameter. The images clearly show the double gyroid structure (detailed in the insets) confirming again that the KIT-6 template was well-transferred.



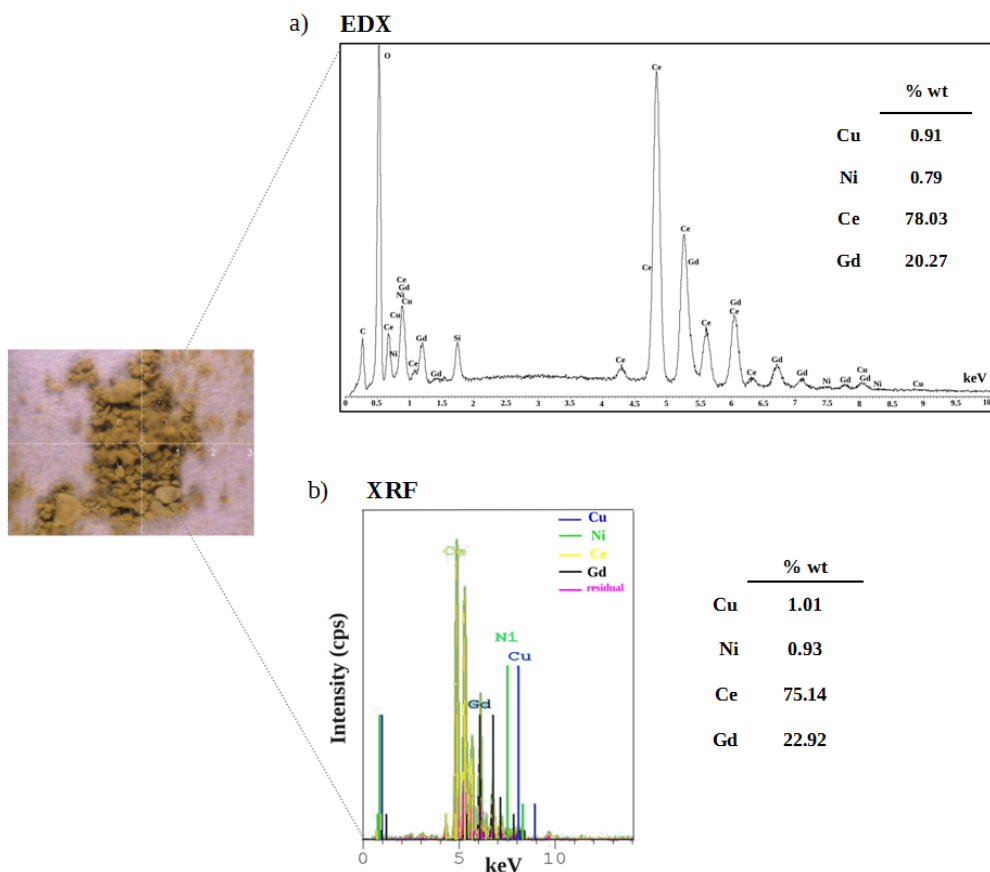
**Figure 5.3:** (a) TEM and (b) SEM images of the as-synthesized CGO-mesoporous support.

After being synthesized, the mesoporous scaffold was impregnated with the metal oxides as described in *Section 2.4.2* of **Chapter II**. The microstructure of the CuO-NiO/CGO catalyst, as observed by cross-section SEM, is depicted in **Figure 5.4**. A general view of the catalyst material deposited on a silicon chip is presented in Figure 5.4a. An ordered porous matrix resulting from the KIT-6 template replica can be also distinguished by image magnification after placing the powder on the silicon substrate and annealing at 350 °C for 2 h (see Figure 5.4b).



**Figure 5.4:** SEM images of the mesoporous CuO-NiO/CGO catalyst (a) deposited on a silicon chip and (b) detail of the porous matrix obtained.

Additional composition analyses were carried out by EDX and XRF to confirm the presence of CuO and NiO within the CGO mesoporous scaffold. EDX and XRF elemental analyses of different elements are represented in weight percentage in **Figure 5.5a** and **Figure 5.5b**, respectively. Both techniques detect similar contents of Cu and Ni (close to the theoretically expected values).



**Figure 5.5:** EDX (a) and XRF (b) spectra of the CGO-mesoporous structure impregnated with CuO and NiO. The semi-quantitative elemental composition analyses are presented in both cases in weight percentage of metals (% wt).

### 5.3. Synergic effect of multi-component metal oxides

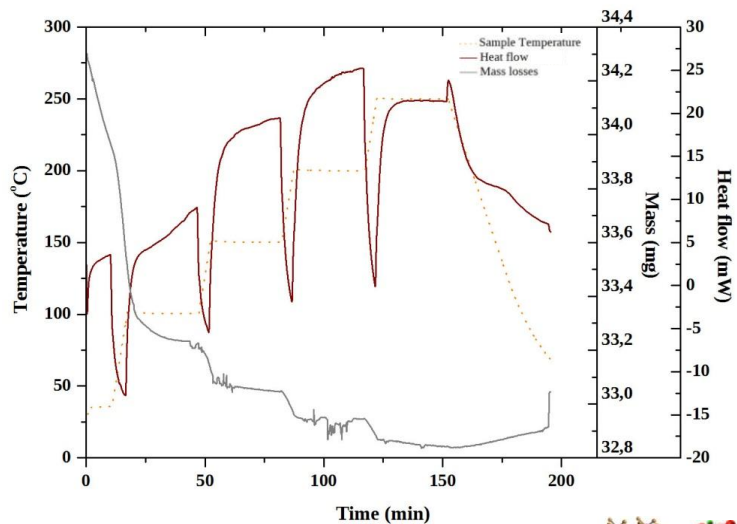
The catalytic activity of NiO/CGO, CuO/CGO and CuO-NiO/CGO was studied for the H<sub>2</sub> oxidation at low temperatures by monitoring the heat flux and the mass losses as a function of temperature, as illustrated in **Figure 5.6**. The temperature analysed ranged from 100 to 250 °C in order to compare to reference [13] (considered in **Chapter III** to compute the start-up simulations).

For all catalysts, the most important mass loss occurred during the first heating ramp up to 100 °C, likely resulting from degassing the mesoporous structure (*ca.* 3% of mass loss). Mass losses observed in the following ramps were also due to degasification, mainly of water produced in the reaction and trapped within the mesoporous material according to mass spectroscopy analysis (not depicted in the figure for sake of clarity). Once the target temperature for testing the reaction was reached and kept constant, a slight loss of mass was observed due to the partial reduction of the metal oxides and/or due to the OSC of the CGO-mesoporous support. The fluctuations of mass detected during the H<sub>2</sub> combustion (more remarkable at 200 °C) could be attributed to the reversible adsorption of the hydroxyl group (of the resulting water vapour) on the catalyst surface.

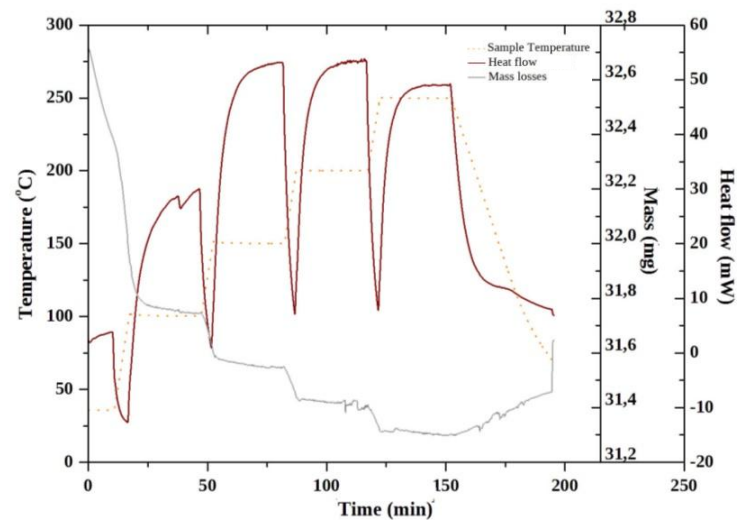
The three catalysts were active in the whole temperature range studied, since a heat flow was released in all the cases due to the exothermic reaction of H<sub>2</sub> oxidation. The NiO/CGO activity increased almost linearly with temperature. The maximum heat released was at 200 °C (see Figure 5.6a). Conversely, the CuO/CGO activity exhibits a remarkable improvement from 100 to 150 °C that was maintained also at 200 °C (see Figure 5.6b). As illustrated in Figure 5.6c, CuO-NiO/CGO catalyst showed a higher heat flow at low temperature (100 °C) compared with the other two configurations. The activity of the binary-component catalyst also improved significantly at 150 °C, as in the CuO-CGO catalyst case, but slightly decreased at 200 °C. After two hours of operation, the activity at the maximum temperature (250 °C) diminished for all catalysts, probably due to a dynamic behaviour of the active sites. Therefore, the progressive metal oxides reduction into metals might change the active site interaction with the reactants (O<sub>2</sub> and H<sub>2</sub>).

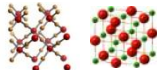
## CHAPTER V. Post combustion unit

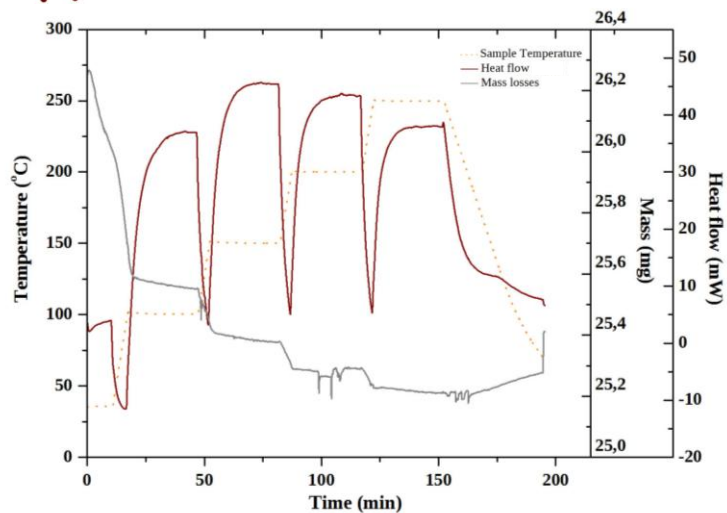
a)  NiO/CGO-mesoporous



b)  CuO/CGO-mesoporous

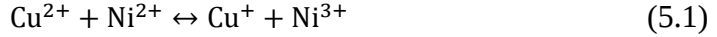


c)  CuO-NiO/CGO mesoporous

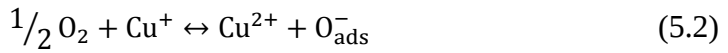


**Figure 5.6:** DSC and TGA for the catalytic systems, (a) NiO/CGO, (b) CuO/CGO and (c) CuO-NiO/CGO.

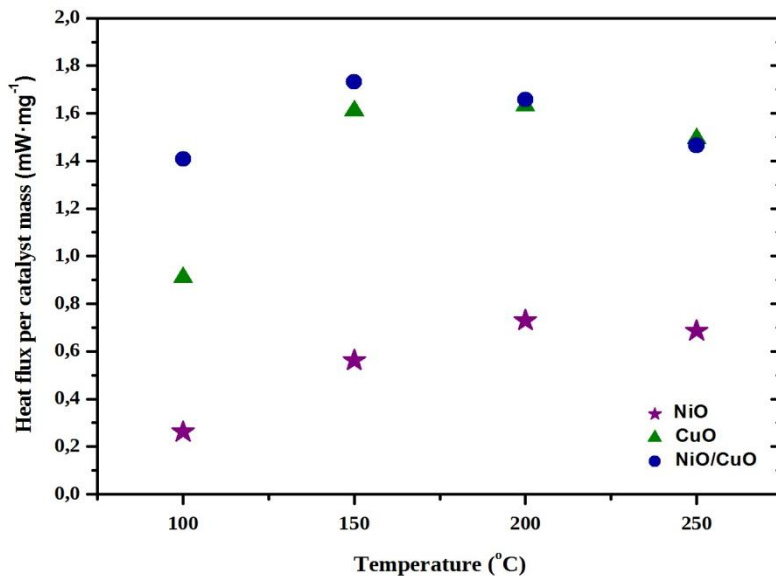
As shown in **Figure 5.7**, the catalytic activity of the single component metal oxide catalysts and the binary mixed composition was compared after normalizing the heat flux with the total mass of catalyst used. A synergistic effect of the catalyst containing the two metal oxides was clearly observed at 100 °C. This higher activity of the multi-component oxide catalyst could be explained by electron transfer between the metallic cations of the oxides (see equation 5.1), as suggested in [30, 31];



which likely allows an oxidation mechanism for H<sub>2</sub> combustion described by equations 5.2-5.4.



The catalytic activity of CuO-NiO/CGO was also higher at 150 °C than their respective mono-component configurations, but it tends to converge towards a similar activity to the CuO/CGO at higher temperatures (200 and 250 °C). Although the activity of NiO /CGO catalyst improved with temperature, this configuration showed the lowest values of heat released in all the temperatures analyzed. Therefore, a synergistic effect was observed at low temperatures for CuO-NiO/CGO catalyst in which copper oxide seems to play a more important role than nickel oxide in the H<sub>2</sub> oxidation reaction. However, a deeper study should be carried out in future to analyse in situ the reaction and investigate the surface mechanisms that take place in each catalyst.



**Figure 5.7:** Comparison between the catalytic activity of the single-component metal oxide catalysts and the binary mixed oxides composition.

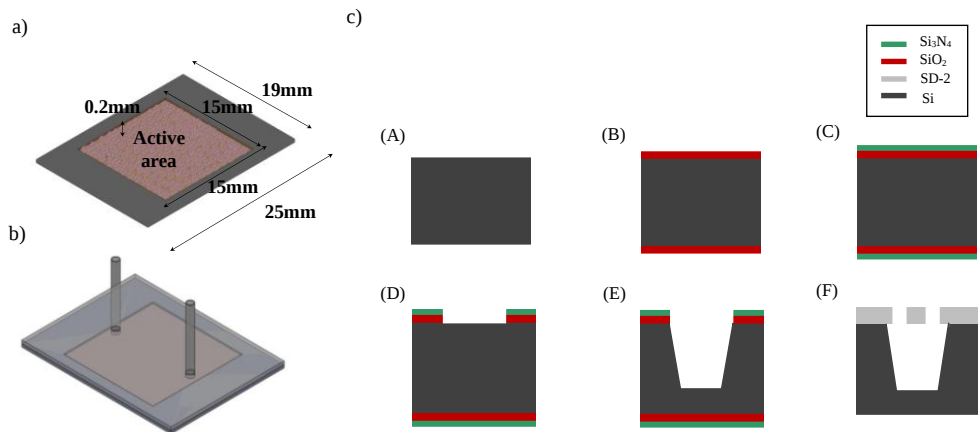
Considering that one of the most important challenges of the  $\mu$ SOFC PG device is to achieve a rapid start-up system, the CuO-NiO/CGO catalyst was selected to be infiltrated in the  $\mu$ combustor since it clearly showed a better catalytic activity at 100 °C.

## 5.4. Post combustor prototype for a $\mu$ SOFC PG

The following sections are focused on the fabrication and test of the silicon  $\mu$ post combustor as a standalone device, based on the CuO-NiO/CGO mesoporous catalyst.

### 5.4.1 Micro-fabrication of the silicon $\mu$ combustor

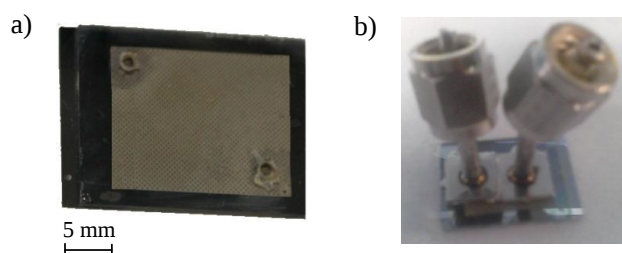
A silicon bed microreactor was designed for an easy impregnation of the catalyst system (see **Figure 5.8a and b**). A scheme of the microfabrication process is depicted in **Figure 5.8c**. The first step started from a single crystal (100)-oriented p-type silicon wafer of 100 mm diameter and 500  $\mu\text{m}$  thick, which was first thermally oxidized at 1100°C to obtain a 100 nm thick  $\text{SiO}_2$  layer (Figure 5.8A-B). Then, a 300 nm thick  $\text{Si}_3\text{N}_4$  layer was deposited of on both sides of the wafer by LPCVD (Figure 5.8C). A photolithographic step was used afterwards to define a squared reaction bed of 15x15  $\text{mm}^2$ . Both dielectrics and 200 microns of silicon were selectively etched by RIE and wet chemical etching (40 wt% KOH solution at 80°C), respectively (Figure 5.8D-E), defining the reaction bed. After removing the protective resist, a second RIE step was carried out to eliminate the remaining dielectric layers from the rest of the silicon chip. Finally, the microreactor was encapsulated with a SD-2 glass cover (with two micro holes, 1 mm in diameter and fabricated as described in **Chapter IV**) by anodic bonding (Figure 5.8F).



**Figure 5.8:** (a), (b) Design of the silicon bed micro-reactor and (c) sketch of the steps required to fabricate the  $\mu$ combustor.

### 5.4.2 Catalyst infiltration

Since the micro bed reactor was encapsulated first (to allow a proper anodic bonding), the two micro holes were used to introduce the catalyst solution in the bed reactor. The encapsulated microfabricated reactor can be observed in **Figure 5.9a**. After the catalyst infiltration, the fluidic connectors were sealed using Nural 30 (see **Figure 5.9b**). The  $\mu$ combustor was filled with 50 mg of CuO-NiO/CGO catalyst, achieving a homogeneous dispersion within the chamber. The total surface area of catalyst was  $5.75 \text{ m}^2$ . This powder bed configuration increases the active area compared with more conventional reactors (based on coating the chamber with lower surface area catalysts) in more than 1200 times [32, 33]. The catalyst did not significantly increase the pressure drop through the reactor.



**Figure 5.9:** (a)  $\mu$ combustor filled with the CuO-NiO/CGO catalyst and (b) image of the reactor including standard fluid connections.

### 5.4.3 Operation conditions

In order to reproduce realistic operating conditions of the  $\mu$ combustor, the experimental tests for the oxidation of  $\text{H}_2$  using the CuO-NiO/CGO catalyst were split in two. In the first set of experiments, the influence of the temperature was studied between 120 and 200 °C (validated in the previous sections for the hydrogen combustion), while the volumetric gas flow rates were fixed at  $12.5 \text{ ml}\cdot\text{min}^{-1}$  for 100 %  $\text{H}_2$  and  $60 \text{ ml}\cdot\text{min}^{-1}$  for synthetic air (in agreement with the thermodynamic calculations presented in **Chapter III**). In the second set of experiments, the influence of the residence time of gas mixture was investigated. The air flow rate was ranging from 60 to  $120 \text{ ml}\cdot\text{min}^{-1}$ , while the  $\text{H}_2$  flow rate was maintained at  $12.5 \text{ ml}\cdot\text{min}^{-1}$  and the operating temperature at 150 °C. The residence times ( $\tau$ ) of the gas mixture inside the bed reactor were ranged between  $1.14\cdot 10^{-2}$  and  $6.20\cdot 10^{-3}$  seconds<sup>1</sup>.

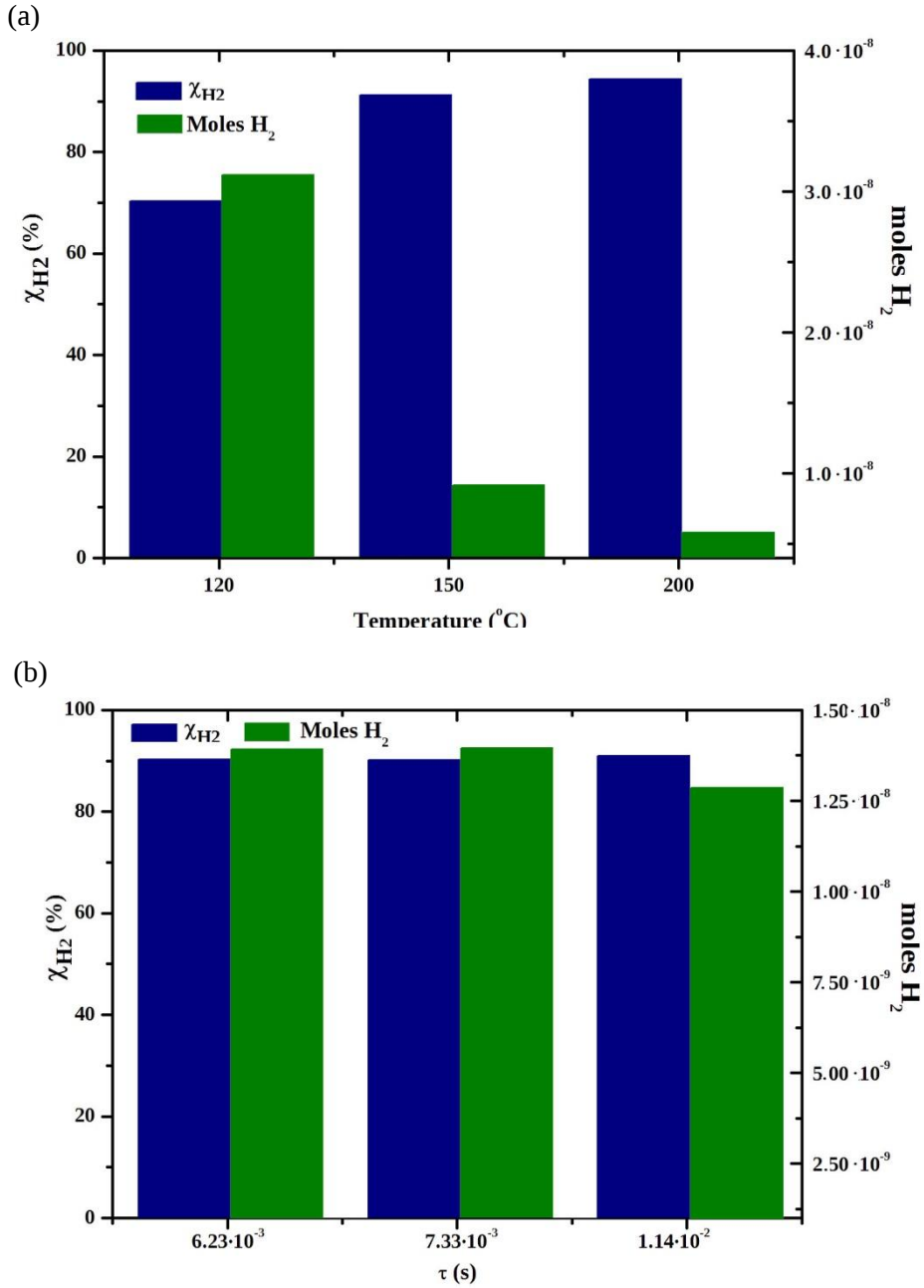
<sup>1</sup>Example of the residence time calculation.

$$\tau = \frac{\text{Volume}_{\text{porous}}}{\text{Flow rate}_{\text{gas mixture}}} = \frac{2.75 \times 10^{-4} \text{ ml} \cdot \text{mg}^{-1}}{72.5 \text{ ml} \cdot \text{min}^{-1}} \times 50 \text{ mg} \times \frac{60 \text{ s}}{\text{min}} = 1.14 \times 10^{-2} \text{ s}$$



#### **5.4.4 Reaction tests**

The influence of the reaction temperature and residence times was studied. The hydrogen conversion and the amount of unreacted hydrogen are depicted in **Figure 5.10** as a function of the operating temperature and residence time. As shown in the Figure 5.10a, the fuel conversion increased from 70 % at 120 °C to 94 % at 200 °C by flowing 72.5 ml·min<sup>-1</sup> of gas mixture. Complementary, the unreacted hydrogen at the outlet decreased with operating temperature. In particular, the molar hydrogen was reduced 81 % from 120 to 200 °C. Moreover, as presented in Figure 5.10b, the hydrogen conversion was almost constant (*ca.* 91 %) for all the residence times tested at 150 °C. This result indicates that the large contact area of the mesoporous catalyst allows high hydrogen conversions independently of the residence time of gas mixture in the  $\mu$ combustor (within the range of study), i.e. the excellent performance is kept under high fuel loads.



**Figure 5.10:** Performance of hydrogen oxidation reaction for (a) different operating temperatures by flowing 72.5 ml·min<sup>-1</sup> of gas mixture and (b) different residence times of gas mixture in the  $\mu$ combustor at 150 °C.

## 5.5. Conclusions

The functionality of a silicon-based  $\mu$ combustor has been presented in this chapter for the catalytic combustion of hydrogen at low temperatures. Inexpensive metal oxides, NiO and CuO, infiltrated in a CGO mesoporous structure were chosen as the catalyst system. Highly ordered double channel gyroid mesostructures with porous of *ca.* 10 nm in diameter were obtained. The CGO mesoporous material was properly infiltrated with the corresponding metal oxides forming thermally stable compact units. The catalytic activity of the CuO-NiO/CGO system was compared to those of the respective single metal oxides. Although all the catalysts proved to be active at temperatures above 100 °C for the hydrogen flameless combustion, a synergic effect was observed for the CuO-NiO/CGO configuration.

A powder bed  $\mu$ combustor was microfabricated and encapsulated by using robust and reproducible mainstream MEMS technology. The 45 mm<sup>3</sup> volume of reactor filled with 50 mg of CuO-NiO/CGO catalyst presents more than 5 m<sup>2</sup> of specific contact area. The catalytic performance of the  $\mu$ combustor for the hydrogen oxidation was proved compatible with the final  $\mu$ SOFC PG under operating conditions. High hydrogen conversions of 70 and 94 % were obtained at operating temperatures of 120 and 200 °C, respectively. It was proven that the residence time had a small influence on the hydrogen conversion (conversions higher than 90 % were attained for all the residence times tested). The promising performance of the  $\mu$ combustor was kept under high fuel loads and low temperatures, so the preliminary results presented demonstrate its suitability as a subunit of the  $\mu$ SOFC PG.

## References

- [1] Kinnunen, N. M., Hirvi, J. T., Venäläinen, T., Suvanto, M. & Pakkanen, T. A. Procedure to tailor activity of methane combustion catalyst: Relation between Pd/PdO<sub>x</sub> active sites and methane oxidation activity. *Appl. Catal. A Gen.* **397**, 54–61 (2011).
- [2] Sano, H. & Toyama, I. Emission of nitrogen oxides from combustion of hydrogen-hydrocarbon mixture, *Nenryo Kyokaishi (J. Japan Fuel Assoc.)* **56**, 686 (1975)
- [3] Pfefferle, W. C. The catalytic combustor - An approach to cleaner combustion (by reaction control in gas turbine engines). *J. Energy* **2**, 142–146 (1978).
- [4] Greeley J, Rossmeisl J, Hellmann A & Norskov J K. Theoretical Trends in Particle Size Effects for the Oxygen Reduction Reaction. *Zeitschrift für Phys. Chemie* **221**, 1209 (2007).
- [5] Hellsing, B., Kasemo, B. & Zhdanov, V. P. Kinetics of the hydrogen-oxygen reaction on platinum. *J. Catal.* **132**, 210–228 (1991).
- [6] Fogelberg, J. & Petersson, L.G. Kinetic modelling of the H<sub>2</sub>-O<sub>2</sub> reaction on Pd and of its influence on the hydrogen response of a hydrogen sensitive Pd metal-oxide-semiconductor device. *Surf. Sci.* **350**, 91–102 (1996).
- [7] Deshpande, P. A. & Madras, G. Catalytic hydrogen combustion for treatment of combustible gases from fuel cell processors. *Appl. Catal. B Environ.* **100**, 481–490 (2010).
- [8] Deshpande, P. A., Poliseti, S., Madras, G., Jyothi, D. & Chandrasekaran, S. Dispersed ZrO<sub>2</sub> nanoparticles in MCM-48 with high adsorption activity. *AIChE J.* **58**, 2987–2996 (2012).
- [9] Kipnis, M. & Volnina, E. H<sub>2</sub> oxidation and preferential CO oxidation over Au: New approaches. *Appl. Catal. B Environ.* **103**, 39–47 (2011).
- [10] Borchert, H. *et al.* Pd nanoparticles with highly defined structure on MgO as model catalysts: An FTIR study of the interaction with CO, O<sub>2</sub>, and H<sub>2</sub> under ambient conditions. *J. Catal.* **247**, 145–154 (2007).
- [11] Pease, R.N. & Taylor H.S. Catalytic formation of water vapor from hydrogen and oxygen in the presence of copper and copper oxide. *J. Am. Chem. Soc.* **44**, 1637–1647 (1922).
- [12] Benton, A.F. & Emmett, P.H. Catalytic Synthesis of Water Vapor in Contact with Metallic Nickel. *J. Am. Chem. Soc.* **48**, 632-640 (1926).
- [13] Haruta, M. & Sano, H. Catalytic combustion of hydrogen I—Its role in hydrogen utilization system and screening of catalyst materials. *Int. J. Hydrogen Energy* **6**, 601–608 (1981).

- [14] Blank, J. H., Beckers, J., Collignon, P. F. & Rothenberg, G. Redox Kinetics of Ceria-Based Mixed Oxides in Selective Hydrogen Combustion. *ChemPhysChem* **8**, 2490–2497 (2007).
- [15] R. S., Bond, G. C. & Webb, G. *Catalysis* (Royal Society of Chemistry, 1989).
- [16] Zhou, Z.Y., Tian, N., Li, J. T., Broadwell, I. & Sun, S.-G. Nanomaterials of high surface energy with exceptional properties in catalysis and energy storage. *Chem. Soc. Rev.* **40**, 4167–4185 (2011).
- [17] Almar, L. *et al.* High-temperature long-term stable ordered mesoporous Ni-CGO as an anode for solid oxide fuel cells. *J. Mater. Chem. A* **1**, 4531–4538 (2013).
- [18] Almar, L. *et al.* High-surface-area ordered mesoporous oxides for continuous operation in high temperature energy applications. *J. Mater. Chem. A* **2**, 3134–3141 (2014).
- [19] Otroshchenko, T. P. *et al.* NiO and ZrO<sub>2</sub>-based catalysts in the reaction of complete methane oxidation. *Russ. J. Phys. Chem. A* **87**, 1804–1808 (2013).
- [20] Pakulska, M. M., Grgicak, C. M. & Giorgi, J. B. The effect of metal and support particle size on NiO/CeO<sub>2</sub> and NiO/ZrO<sub>2</sub> catalyst activity in complete methane oxidation. *Appl. Catal. A Gen.* **332**, 124–129 (2007).
- [21] Marbán, G. & Fuertes, A. B. Highly active and selective CuO<sub>x</sub>/CeO<sub>2</sub> catalyst prepared by a single-step citrate method for preferential oxidation of carbon monoxide. *Appl. Catal. B Environ.* **57**, 43–53 (2005).
- [22] Shinde, V. M. & Madras, G. Nanostructured Pd modified Ni/CeO<sub>2</sub> catalyst for water gas shift and catalytic hydrogen combustion reaction. *Appl. Catal. B Environ.* **132–133**, 28–38 (2013).
- [23] Kaisare, N. S., Deshmukh, S. R. & Vlachos, D. G. Stability and performance of catalytic microreactors: Simulations of propane catalytic combustion on Pt. *Chem. Eng. Sci.* **63**, 1098–1116 (2008).
- [24] Kaisare, N. S., Stefanidis, G. D. & Vlachos, D. G. Comparison of ignition strategies for catalytic microburners. *Proc. Combust. Inst.* **32**, 3027–3034 (2009).
- [25] Specchia, S., Vella, L. D., Burelli, S., Saracco, G. & Specchia, V. Combustion of CH<sub>4</sub>/H<sub>2</sub>/Air Mixtures in Catalytic Microreactors. *ChemPhysChem* **10**, 783–786 (2009).
- [26] Mehra, A. Ph.D. Thesis, Massachusetts Institute Technology (2000).
- [27] Peck, J. Ph.D. Thesis, Massachusetts Institute Technology (2003).
- [28] Almar, L. Ph.D. Thesis, Catalonia Institute for Energy Research (2014).

- [29] Gu, D. & Schuth, F. Synthesis of non-siliceous mesoporous oxides. *Chem. Soc. Rev.* **43**, 313–344 (2014).
- [30] S. Veprek, D.L. Cocke, S. Kehl & H.R. Oswald. Mechanism of the deactivation of Hopcalite catalysts Studied by XPS, ISS, and other techniques. *J. Catal.* **100**, 250 (1986).
- [31] Buciuman, F. C., Patcas, F. & Hahn, T. A spillover approach to oxidation catalysis over copper and manganese mixed oxides. *Chem. Eng. Process. Process Intensif.* **38**, 563–569 (1999).
- [32] Leu, C.H. *et al.* Investigation of the packed bed and the micro-channel bed for methanol catalytic combustion over Pt/Al<sub>2</sub>O<sub>3</sub> catalysts. *Appl. Catal. A Gen.* **382**, 43–48 (2010).
- [33] Leu, C.H. *et al.* Visible images of the catalytic combustion of methanol in a micro-channel reactor. *Chem. Eng. J.* **226**, 201–208 (2013).



# **VI. FULL CERAMIC-BASED MICRO SOLID OXIDE FUEL CELL**



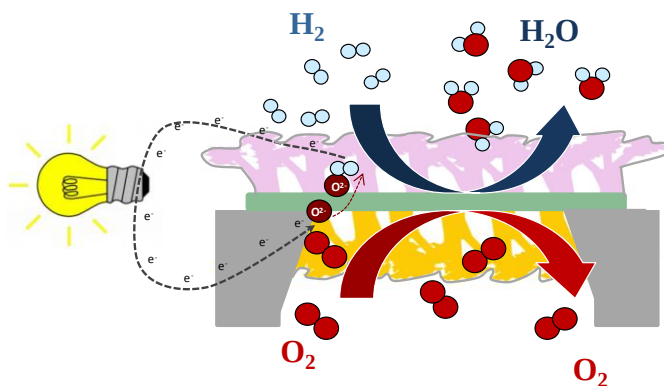


<b>6.1. Introduction.....</b>	<b>175</b>
<b>6.2. Self-supported electrolyte.....</b>	<b>179</b>
6.2.1. Low thermal mass architecture.....	179
6.2.2. Structural and microstructural characterization.....	180
6.2.3. YSZ cross-plane conductivity.....	181
<b>6.3. Ceramic cathodes for <math>\mu</math>SOFC.....</b>	<b>183</b>
6.3.1. Thin film $\text{La}_{0.6}\text{Sr}_{0.4}\text{CoO}_{3-\delta}$ .....	183
6.3.1.1. Structural and microstructural characterization.....	183
6.3.1.2. Integration in self-suspended membranes of YSZ.....	185
6.3.1.3. Electrochemical characterization.....	186
6.3.2. Thin film $\text{La}_{0.8}\text{Sr}_{0.2}\text{MnO}_{3+\delta}$ .....	189
6.3.2.1. Structural and microstructural characterization.....	189
6.3.2.2. Oxygen mass transport properties of the dense LSM layer.....	191
6.3.2.3. Electrochemical characterization.....	195
<b>6.4. Ceramic anodes for <math>\mu</math>SOFC.....</b>	<b>197</b>
6.4.1. Thin film $\text{Ce}_{0.8}\text{Gd}_{0.2}\text{O}_{1.9-\delta}$ .....	197
6.4.1.1. Structural and microstructural characterization.....	197
6.4.1.2. Integration in self-suspended membranes of YSZ.....	199
6.4.1.3. Electrochemical characterization.....	200
6.4.2. Thin film $\text{Sr}_2\text{Fe}_{1.5}\text{Mn}_{0.5}\text{O}_{6-\delta}$ .....	202
6.4.2.1. Structural and microstructural characterization.....	202
6.4.2.2. Oxygen mass transport properties of the dense LSM layer.....	203
6.4.2.3. Electrochemical characterization.....	204
<b>6.5. Full ceramic-based <math>\mu</math>SOFC.....</b>	<b>206</b>
6.5.1. Structural and microstructural characterization.....	206
6.5.2. Electrochemical performance of the $\mu$ SOFC.....	207
<b>6.6. Conclusions.....</b>	<b>210</b>



## 6.1. Introduction

The development of  $\mu$ SOFCs is mainly based on thin-film functional layers supported on low thermal mass structures [1-7]. This configuration keeps the major benefits of SOFC technology, namely, high specific energy per unit mass and volume, efficiency and fuel flexibility, while overcoming its major drawbacks, i.e. *long and high energy consumption start-up processes* and *unnecessarily high operating temperatures*. **Figure 6.1** shows a scheme of a planar  $\mu$ SOFC, consisting of a dense electrolyte covered by two porous electrodes (an anode and a cathode) supported on a microfabricated silicon platform.



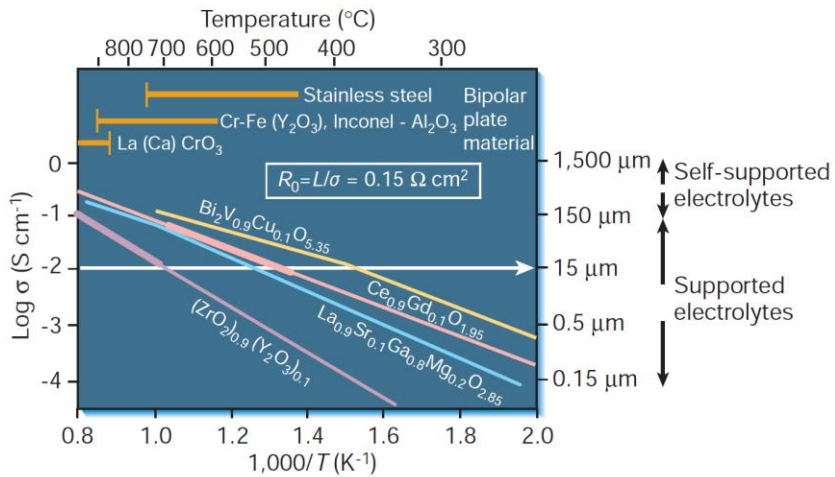
**Figure 6.1:** Scheme of a planar miniaturized SOFC based on thin-film layers.

This scheme allows overcoming the two major drawbacks previously mentioned:

- A. Low thermal mass architectures** reduce the thermal response and the energy consumption of the fuel cell start-up.

Different designs have been reported in the literature, most of them based on free-standing electrolyte membranes supported on silicon-based substrates [2-6]. Thin film electrolytes allow maintaining low thermal masses, since oxygen ion conducting materials reduce their Area Specific Resistance (ASR) to the targeted values ( $0.15 \Omega \cdot \text{cm}^2$ ) at intermediate operating temperatures ( $T=400\text{-}800 \text{ }^\circ\text{C}$ ) [8, 9]. Oxygen ion conducting materials are often doped fluorite-type oxides (e.g.  $\text{ZrO}_2$  and  $\text{CeO}_2$ ). Apart from stabilizing the cubic ceramic phase (which has better ionic conductivity), reasonably high ionic conductivities are achieved through substitution with dopants that increase the oxygen vacancy concentration and mobility. Common dopants are di- or trivalent rare-earth or

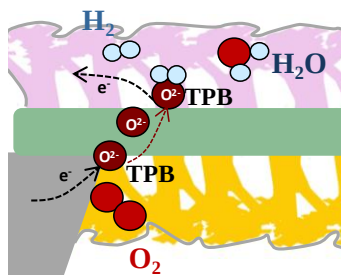
alkaline-earth cations (e.g.,  $\text{Ca}^{+2}$ ,  $\text{Mg}^{+2}$ ,  $\text{Y}^{+3}$ ,  $\text{Nd}^{+3}$ ,  $\text{Sm}^{+3}$ ,  $\text{Yb}^{+3}$  and  $\text{Sc}^{+3}$ ). **Figure 6.2** summarizes the ionic conductivity versus reciprocal temperature relationship of a selection of solid electrolytes [10]. By taking the typical value of  $0.15 \text{ } \Omega \cdot \text{cm}^2$  for the electrolyte ASR, it is possible to see the maximum allowable thickness (right-hand ordinate) for a given material and temperature. Furthermore, the ceramic electrolyte should be dense, insulating for electron conduction and gas-tight, i.e. pinhole- and crack-free. The electrolyte should have also good mechanical properties and be compatible with the support from chemical and thermo-mechanical point of view. Stabilized zirconia, in particular Yttria Stabilized Zirconia (YSZ) has become the prevalent electrolyte in  $\mu\text{SOFCs}$  [11-16]. In addition to its good ionic conductivity, YSZ is also characterized for showing high strength and toughness [17, 18].



**Figure 6.2:** Specific conductivity versus reciprocal temperature for selected solid oxide electrolytes. The axis on the right refers to the thickness layer to achieve the desired contribution of the electrolyte to the whole device ASR. From reference [10].

In addition to the electrolyte, electrodes in thin film form are required to ensure good mechanical stability (dominated by the electrolyte) and maintain the low thermal mass structure [19]. Moreover, electrodes must be porous to enhance gas access and with similar thermo-mechanical properties as the electrolyte to avoid stresses due to the thermal cycles [20]. The electrode should exhibit high electro-catalytic activity at the operating temperature, i.e. towards oxygen reduction in the cathode and fuel oxidation in the anode, through increasing the Triple Phase Boundary (TPB) area. The TPB, as represented in **Figure 6.3**, corresponds to the area where the gas, electrode and

electrolyte interface are in contact and the electrochemical reactions take place. So, the electrode should present enough electronic conductivity and high chemical stability in oxidizing and/or reducing atmospheres without forming highly resistive parasite phases with the electrolyte and current collectors [21].



**Figure 6.3:** Scheme of electrode-electrolyte interfaces and TPB.

**B. State of the art electrodes** (noble metals like Pt) allow  $\mu$ SOFC operation at low temperatures ( $300\text{ }^{\circ}\text{C} < T < 500\text{ }^{\circ}\text{C}$ ). However, operation temperatures smaller than  $600\text{ }^{\circ}\text{C}$  are not compatible with hydrocarbons and reforming processes. This becomes an important issue for future commercialization of real systems.

The temperature required for a high conversion and selectivity in hydrocarbons reforming reactions (either internal or using an external  $\mu$ reformer) is typically above  $600\text{ }^{\circ}\text{C}$  [22, 23]. However, the  $\mu$ SOFC development up to now has been focused on electrodes based on noble metals to operate at temperatures below  $600\text{ }^{\circ}\text{C}$  [24]. Platinum (Pt) is the most common choice, at least for one of the  $\mu$ SOFC electrodes [25], because of its excellent catalytic activity at low temperatures [26]. But Pt thin films show a quick degradation above  $400\text{ }^{\circ}\text{C}$ , associated to dewetting processes, leading to a rapid drop on the power density of the final device [24]. Therefore, more reliable electrodes are required as alternative to metals in order to allow operation at temperatures higher than  $600\text{ }^{\circ}\text{C}$ . By direct analogy with bulk SOFCs, porous ceramic-based electrodes would be a suitable choice with a number of advantages over metals such as redox and thermal stability, and fine microstructure. Recently, Mixed Ionic Electronic Conductors (MIECs) were presented as promising electrodes because of their dual conduction capacity that increases the TPB active region by extending it beyond the surface [27].

The development of thin film based full ceramic  $\mu$ SOFCs is the next goal. Indeed, although several works have been recently published devoted to

the development of pure oxide based thin film electrodes [28-31], only few have focused on their implementation in  $\mu$ SOFC configurations (i.e. in free-standing membrane configurations) [24-25, 32-33]. In particular, there is a lack of studies devoted to the development of thin film anodes. The state of the art anodes on bulk SOFC are based on cermet materials, i.e. composition of an oxide ionic conductor (ceramic) and an electronic conductor (metal) [34]. However cermet transferability to thin films has been shown to be difficult. Metals are still the most common material used as anode in  $\mu$ SOFCs, especially Pt [25]. Only a few works are based on the transferability of functional doped-ceria to thin films for  $\mu$ SOFC applications [35-37]. Doped-ceria thin films could act as pure ceramic anodes or as optimum ceramic component on cermets [38]. Moreover, perovskites are commonly chosen as thin film cathodes, e.g.  $\text{La}_{0.8}\text{Sr}_{0.2}\text{MnO}_{3+\delta}$  (LSM) [39] and  $\text{La}_{0.6}\text{Sr}_{0.4}\text{CoO}_{3-\delta}$  (LSC) [40], and novel materials like  $\text{Sr}_2\text{Fe}_{1.5}\text{Mo}_{0.5}\text{O}_{6-\delta}$  (SFM) [41] can be also extended to thin film technology.

**This chapter** is focused on the development of a full ceramic  $\mu$ SOFC. *Section 6.2* describes an overview of the electrochemical and thermo-mechanical properties of large-area free standing YSZ membranes fabricated at wafer level by PLD as  $\mu$ SOFC electrolytes. The following sections are devoted to the fabrication and characterization of non-metallic based electrodes implemented in real  $\mu$ SOFC configurations. In particular, *Section 6.3* is focused on  $\text{La}_{0.6}\text{Sr}_{0.4}\text{CoO}_{3-\delta}$  (LSC) porous films and  $\text{La}_{0.8}\text{Sr}_{0.2}\text{MnO}_{3+\delta}$  (LSM) dense films as  $\mu$ SOFC cathodes, while *Section 6.4* depicts a similar study but is focused on ceramic films as  $\mu$ SOFC anodes, i.e. porous  $\text{Ce}_{0.8}\text{Gd}_{0.2}\text{O}_{1.9-\delta}$  (CGO) and  $\text{Sr}_2\text{Fe}_{1.5}\text{Mo}_{0.5}\text{O}_{6-\delta}$  (SFM) films. Finally, *Section 6.5* presents the performance of a large area full-ceramic free standing  $\mu$ SOFC.

It is noteworthy that much of the research carried out in this chapter has been done in close collaboration with colleagues of the Nanoionics Group (I. Garbayo and A.M. Saranya) at IREC, the Imperial College (M. Burriel, A. Cavallaro and J.A. Kilner) and the University of Castilla-La Mancha (J. Canales-Vázquez); as it appears reflected in the resulting publications.

## 6.2. Self-supported electrolyte

This section describes the background of the group on self-supported electrolytes implemented in low thermal mass silicon platforms. Therefore, it is intentionally brief and has been included mainly for the sake of completeness. Further details on the structural, thermo-mechanical and electrochemical properties of YSZ electrolytes can be found in refs. [4, 44-47].

Yttria Stabilized Zirconia (YSZ) is the material of choice for the electrolyte. Cubic 8YSZ and tetragonal 3YSZ are taken into consideration because of their respective advantages. On the one hand, the maximum oxygen ion bulk conductivity in YSZ occurs at a concentration of around 8 mol% of yttria (8YSZ) and is higher than that of tetragonal 3YSZ [42]. On the other hand, tetragonal 3YSZ has better thermo-mechanical properties, i.e. high flexural strength ( $\sim 1$  GPa) and good fracture toughness ( $\sim 10$  MPa m<sup>1/2</sup>) that enable processing of much thinner electrolyte layers [43], and, more importantly, reduce the number of ejected particulates (origin of pinholes) during the PLD deposition.

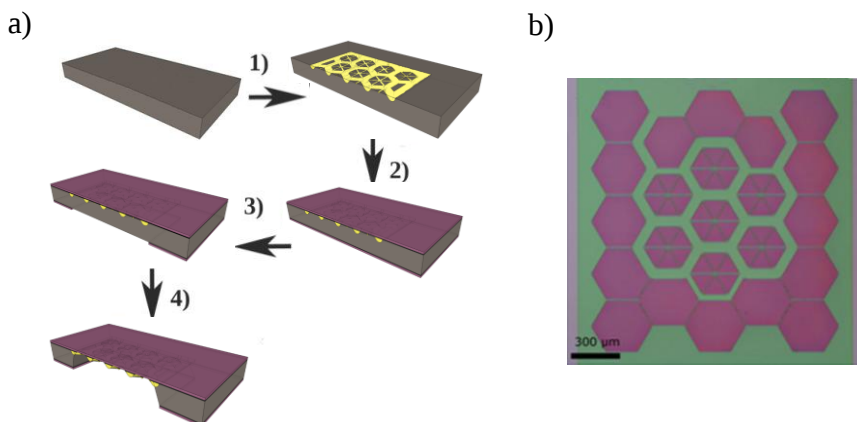
### 6.2.1. Low thermal mass architecture

The  $\mu$ SOFC design adopted in this thesis had been developed previously by I. Garbayo *et al.* [44, 45]. It consists of a large area free-standing membrane supported on a grid of doped-silicon slabs [45, 46]. This configuration allows to enlarge the active area per single device, i.e. the total power, as well as to improve the temperature homogenization along the membrane (see results presented in **Chapter III**).

**Figure 6.4a** shows the main steps of the fabrication process of the micro device by using MEMS technology. (1) A first photolithographic step was carried out to expose the silicon substrate to boron doping. Doped silicon regions yielded the membrane supporting slabs at the end of the microfabrication process. (2) In a second step, the silicon substrate with doped silicon slabs was passivated with a stress-free combination of SiO<sub>2</sub> (100 nm thick) and Si<sub>3</sub>N<sub>4</sub> (300 nm thick). (3) Then, a photolithographic step defined square windows on the back side (from 2x2 mm<sup>2</sup> to 4x4 mm<sup>2</sup>, depending on the  $\mu$ SOFC design) where the dielectric layers were removed by RIE. (4) Finally, the silicon substrate was etched from the back side by KOH wet etching. Doped silicon zones were not etched by anisotropic etchants like KOH



since the Si etch reaction needs free electrons to proceed and the presence of electrons is scarce in the doped material.

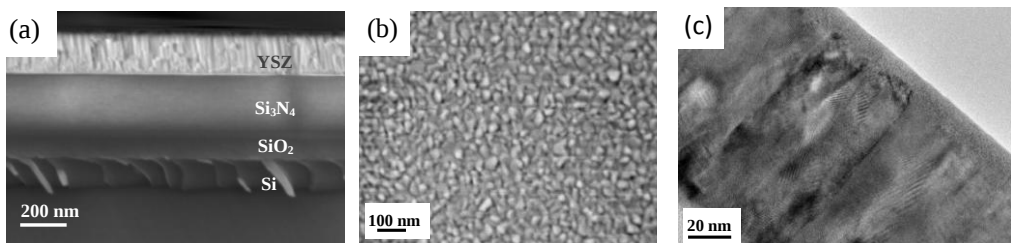


**Figure 6.4:** (a) Scheme of the fabrication process. (1) A photolithographic step defined the doped-silicon slabs of 5  $\mu\text{m}$  in thickness; (2) a  $\text{SiO}_2/\text{Si}_3\text{N}_4$  dielectric bi-layer was deposited on both sides of the Si substrate; (3) a second photolithographic step from the back side defined the  $\text{Si}_3\text{N}_4$  zone to be etched that it was selectively eliminated by dry etching in the following step; (4)  $\text{SiO}_2$  and Si were wet etched from the back side, obtaining large-area  $\text{Si}_3\text{N}_4$  membranes on the top side. (b) Detail of a fabricated large area self-supported  $\text{Si}_3\text{N}_4$  membrane.

Once the self-supported free-standing  $\text{Si}_3\text{N}_4$  membranes were successfully fabricated by silicon micromachining, PLD depositions of 3YSZ and 8YSZ at wafer level were optimized minimizing the particle ejection. The set of conditions used are detailed in *Section 2.3* of **Chapter II**. The growth rate of both thin film electrolytes were known from a previous work [4, 47]. Reflectometry was used to measure YSZ film thicknesses ( $\sim \pm 200$  nm). Then, a RIE process was carried out to eliminate the  $\text{Si}_3\text{N}_4$  layer and release the YSZ films. A high percentage of crack and pinhole free membranes ( $> 75\%$ ) were obtained.

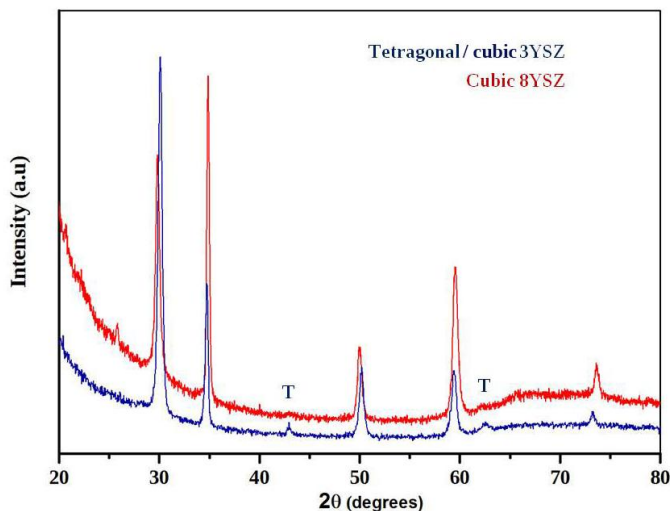
### 6.2.2. Structural and microstructural characterization

Dense electrolyte films were obtained for both 8YSZ and 3YSZ. SEM images confirmed the dense and well ordered columnar-like grain growth for the YSZ (see **Figure 6.5**)



**Figure 6.5:** (a) Cross-sectional and (b) top-view SEM images, and (c) cross-section TEM image of an YSZ large-area free standing membrane.

The XRD pattern of dense 3YSZ and 8YSZ films deposited on  $\text{Si}_3\text{N}_4/\text{SiO}_2/\text{Si}$  substrates at 600 °C is depicted in **Figure 6.6**. The red line corresponds to a cubic structure of 8YSZ, whereas the blue line corresponds to a partially tetragonal/cubic structure of 3YSZ.

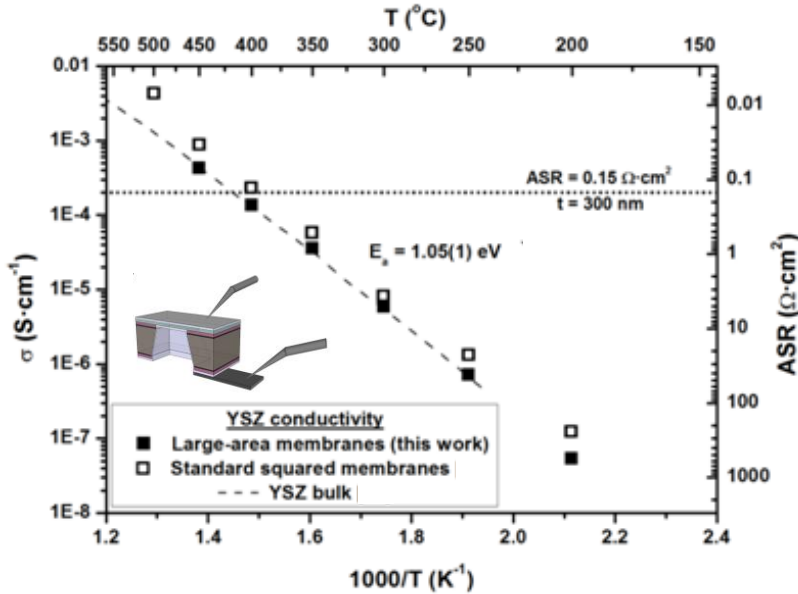


**Figure 6.6:** XRD pattern of dense 3YSZ and 8YSZ layers deposited on a  $\text{Si}_3\text{N}_4/\text{SiO}_2/\text{Si}$  substrate at 600 °C. The red line corresponds to 8YSZ cubic structure, while the blue line represents the tetragonal/cubic 3YSZ structure where “T” symbol shows tetragonal peaks.

### 6.2.3. YSZ cross-plane conductivity

The dense and columnar microstructure (see SEM and TEM images on previous section) leads to a minimum and aligned number of grain boundaries, reducing the total electrolyte resistance. The conductivity across the 8YSZ thin films is presented in **Figure 6.7** (3YSZ thin films show similar conductivity, as detailed in [47]). Large area membranes exhibited values of

conductivity similar to those previously reported [4] and also for bulk 8YSZ [48], confirming the reproducibility of their fabrication. The reference target value for the  $ASR_{\text{electrolyte}}$  was reached at temperatures as low as 450°C (for <300 nm thick YSZ films), proving the YSZ membranes as an excellent electrolyte on the whole IT range (400 °C < T < 800 °C).



**Figure 6.7:** Arrhenius plot of cross-plane electrical conductivity of large-area YSZ membranes. Previously reported values for YSZ conductivity measured on standard squared membranes [4] and also bulk YSZ conductivity [48] are included for comparison. Values of ASR plotted on right Y axis were calculated for 300 nm thick YSZ films.

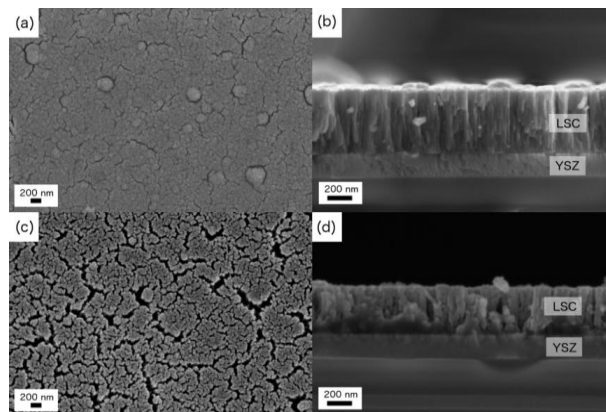
### 6.3. Ceramic cathodes for $\mu$ SOFC

#### 6.3.1. Thin film $\text{La}_{0.6}\text{Sr}_{0.4}\text{CoO}_{3-\delta}$

Lanthanum strontium cobaltite ( $\text{La}_{0.6}\text{Sr}_{0.4}\text{CoO}_{3-\delta}$ , LSC) is amongst the most studied MIEC material for SOFC cathodes, especially at IT range. However, the possible reaction between LSC and YSZ at high temperatures (forming insulating phases at  $T > 700$  °C in the cathode/YSZ interface, like  $\text{La}_2\text{Zr}_2\text{O}_7$  or  $\text{SrZrO}_3$  [24, 52]), and the large mismatch in their thermal expansion coefficients ( $\text{TEC}_{\text{LSC}} = 23 \text{ ppm}\cdot\text{K}^{-1}$  [53];  $\text{TEC}_{\text{YSZ}} = 10 \text{ ppm}\cdot\text{K}^{-1}$  [49]) limit its applicability. Therefore, alternative electrolytes or diffusion barrier layers are sometimes introduced between the electrolyte and the cathode for reducing these effects [23, 54-55]. The implementation of porous LSC thin films deposited at low temperature ( $T < 700$  °C) has been recently proposed as a good solution to overcome these issues and promising results have been reported in the IT operation range [24, 31, 57]. This section is devoted to the fabrication of LSC porous thin films by PLD and their microstructural and electrical characterization in symmetrical cells LSC/8YSZ/LSC.

##### 6.3.1.1. Structural and microstructural characterization

Firstly, LSC thin film layers were fabricated over dense 8YSZ film; both deposited by PLD on (100) silicon substrates passivated with a stress-free combination of amorphous  $\text{SiO}_2$  and  $\text{SiN}_x$  layers. Deposition conditions to obtain porous LSC and dense YSZ layers are detailed on **Chapter II** (*Section 2.3*). **Figure 6.9** shows top view and cross section SEM images of as-deposited (a, b) and post-annealed at 700 °C (c, d) LSC porous layers (350 nm thick). The typical columnar growth of PLD-deposited complex oxides [54] is observed for both the YSZ and LSC layers. However, while the YSZ film presents ordered and well-defined compact grains, LSC was intentionally prepared to have disordered columnar clusters with open porosity along the whole film thickness. The origin of these differentiated microstructures is on the temperature and pressure PLD deposition conditions used for each material. According to Infortuna and co-workers [54], a high background pressure promotes the mobility of species allowing the formation of single clusters on the film, while the substrate temperature is the responsible of re-crystallization and grain growth during the deposition (see **Chapter II** for more details). Thus, low temperature and high pressure conditions employed for LSC provide disordered films formed by separated clusters with a high percentage of amorphous phase and porosity.

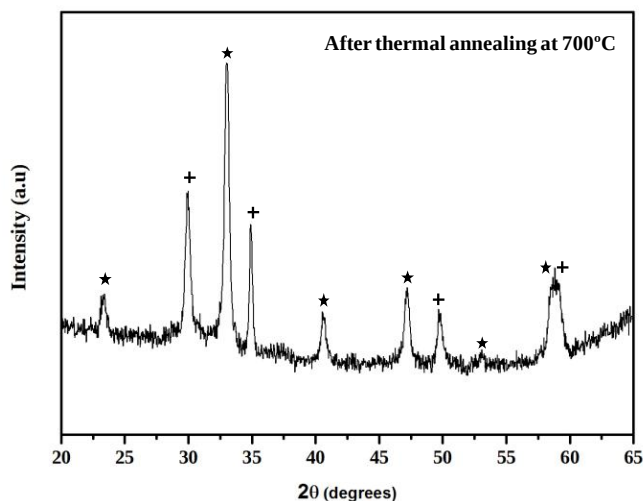


**Figure 6.9:** Top view and cross-section SEM images of as-deposited (a, b) and post-annealing (c, d) 350 nm thick porous LSC layers over previously deposited dense 8YSZ.

The comparison of the **Figure 6.9** shows the evolution of the microstructure with a thermal treatment at 700 °C. While the microstructure of the YSZ layer remains essentially the same, showing a great stability against temperature [4], the microstructure of the LSC layers evolves towards an inhomogeneous porosity. Indeed, cracks are apparently observed in the top view image of the layer (**Figure 6.9c**). These cracks are only affecting the upper part of the layer (see **Figure 6.9d**), but they are not affecting the quality of the attachment between the film and the substrate. An excellent adhesion between YSZ and LSC is observed by SEM, i.e. no loss of percolation is expected after crystallization. This microstructural evolution is likely associated to the combined effect of the crystallization of the film from its initial amorphous nature and the partial sintering and densification of the original clusters into bundles. No cracking or delamination was observed on the fabricated films. By simple image processing of the SEM images, the in plane porosity was found to be of *ca.* 30% ensuring good percolation, large TPB lengths and reasonable diffusion of gas species. Presumably, the observed porosity helps to balance the big difference in thermal expansion coefficient (TEC) reported for both materials, avoiding strontium segregation [53, 57] and limiting the presence of significant stresses in the final multilayer.

The XRD pattern of the LSC/YSZ bilayer deposited on  $\text{Si}_3\text{N}_4/\text{SiO}_2/\text{Si}$  substrates after a thermal annealing at 700 °C is depicted in **Figure 6.10**. The indexed peaks marked with a cross correspond to a cubic  $Fm\bar{3}m$  structure of 8YSZ, whereas the indexed peaks marked with a star correspond to a cubic  $Pm\bar{3}m$  structure of LSC. It is important to notice that no reactivity between

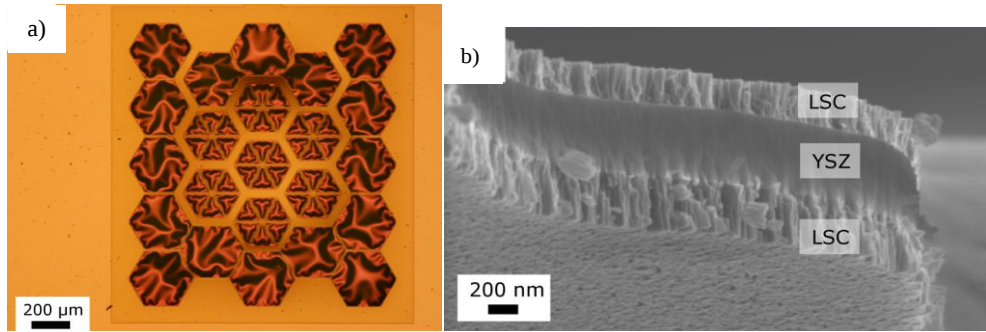
LSC and YSZ was observed, showing the applicability of LSC in the IT range ascribed to the  $\mu$ SOFC.



**Figure 6.10:** XRD pattern of a porous LSC film deposited over dense YSZ on a  $\text{Si}_3\text{N}_4/\text{SiO}_2/\text{Si}$  substrate after a thermal annealing at 700 °C. The crosses correspond to YSZ diffraction peaks, while the stars point out the main peaks of a crystalline LSC pattern.

### 6.3.1.2. Integration into self-suspended membranes of YSZ

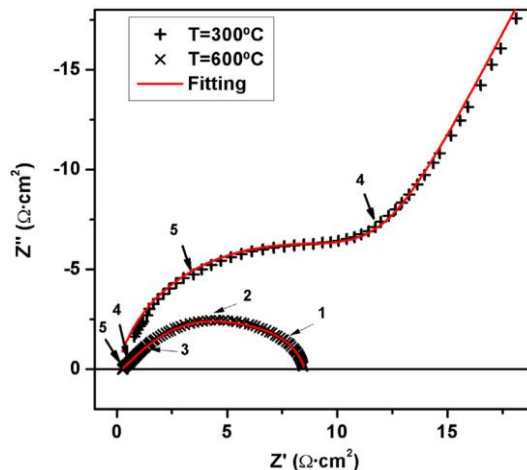
Once characterized the porous LSC thin film, it was implemented on a large-area  $\mu$ SOFC, i.e. free-standing membrane. **Figure 6.11** shows top view and cross section images (optical and SEM, respectively) of the LSC/YSZ/LSC symmetrical membranes. The area of the membranes is 2.8 mm<sup>2</sup> for a total active area of 2 mm<sup>2</sup>, which represents an enhancement of *ca.* 20x over previously reported basic free-standing membrane configurations [1]. The buckling patterns observed in the membranes (see Figure 6.11a) correspond to a compressive strain mainly associated to the YSZ layer (see references [4, 23, 51] for further details). The LSC double deposition did not affect the buckling pattern suggesting a minimal contribution from the electrode layer to the total strain (as expected being LSC a porous layer able to easily release stress). The total thickness of the LSC/YSZ/LSC membranes was *ca.* 1.2  $\mu\text{m}$ , with 500 nm of dense YSZ electrolyte and 350 nm of porous LSC at both sides (Figure 6.9b).



**Figure 6.11:** Top view optical image of a large area YSZ free-standing membrane supported on doped-silicon slabs (a) and SEM cross sectional view of a free-standing LSC/YSZ/LSC trilayer (b).

### 6.3.1.3. Electrochemical characterization

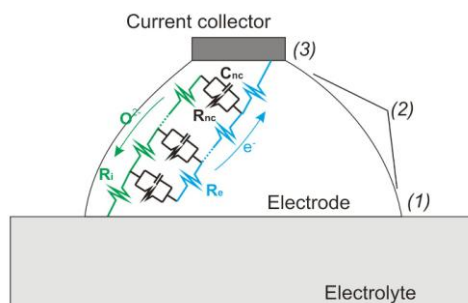
The LSC/YSZ/LSC membranes were characterized by EIS in order to evaluate their electrochemical performance in the final  $\mu$ SOFC device. Before measuring, high electronic conducting layers were implemented on top of the electrodes as current collectors. Although part of the active area was lost (zones covered by the dense current collectors become inactive), the percolating distance was significantly reduced and the associated resistance was lowered. Platinum films of 150 nm thickness were deposited by sputtering on both sides of the membrane. **Figure 6.12** depicts two Nyquist plots corresponding to the impedance spectra obtained at different temperatures.



**Figure 6.12:** Impedance spectra of a symmetrical LSC/YSZ/LSC free-standing membrane, measured at 300 °C and 600 °C. Solid red lines represent the fitting for the two spectra. The numbers refer to the frequency decades covered by the EIS analysis.

Two arcs are clearly observed at 300 °C. A small arc appears at high frequencies due to the resistance associated to the ionic conduction through the bulk electrolyte, while a big arc at lower frequencies is presumably associated to poor performance at the electrodes. No grain boundary contribution to the resistance was observed for the electrolyte due to the typical columnar growth of PLD (see reference [4] for further details). At higher temperatures (600 °C), the arc corresponding to the electrolyte becomes a pure serial resistance while the low-frequency arc associated to the symmetrical electrodes shows a great reduction in resistance. The continuous line represents the fitted ALS<sup>1</sup> continuum model [55] useful for describing porous MIEC like LSC. The agreement between model and experimental data suggests that the non-charge transfer phenomena (solid-state oxygen diffusion and O<sub>2</sub> surface exchange) and the gas-phase diffusion dominate the electrochemical behaviour of the system.

<sup>1</sup> The ALS model is commonly used for describing MIEC in base of a transmission line model. The figure below shows a scheme of an electrode/electrolyte system, with the associated equivalent circuit. The electrode behaviour is described as two coupled transmission lines, i.e. an ionic pathway ( $R_i$ ) and an electronic pathway ( $R_e$ ). A series of coupling elements connect the two channels, representing the non-charge transfer phenomena occurred on the electrode ( $R_{nc}$   $C_{nc}$ ). Then, three opposed scenarios can be found depending on the electrode properties. First, if the electrode presents high resistances associated to the ionic conduction (high  $R_i$ ), the reactions (non-charge transfer phenomena,  $R_{nc}$   $C_{nc}$ ) would be limited to the zone (1), close to the electrolyte. Second, if the electrode presents very low electronic conductivity but good ionic conduction (high  $R_e$ ), the active area would be limited to the zone (3) (problems with gas diffusion could be an extra cause of this second behaviour). Finally, the ideal situation would be having both good electronic and ionic conductivity on the electrode with perfect gas diffusion and thus the whole electrode area (zones (1), (2) and (3)) would be catalytically active. This last scenario corresponds to a MIEC behaviour and can be explained by the ALS model. On the contrary, the two first scenarios mean that only a part of the electrode is actively used, while the rest of it remains catalytically inactive.

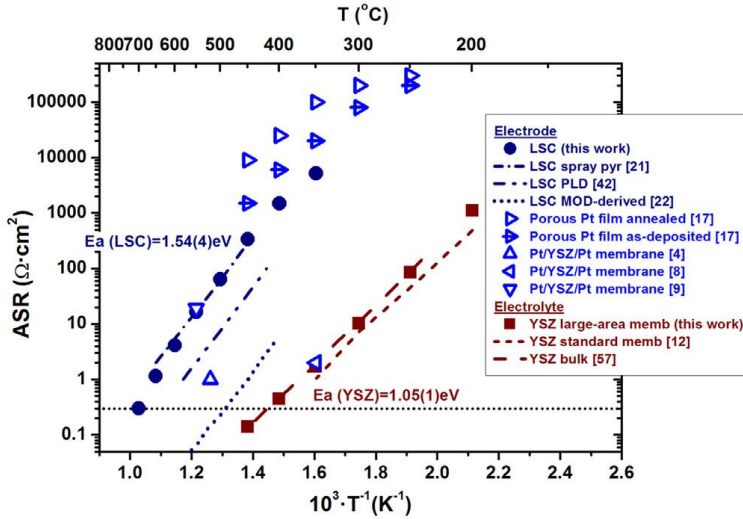


Further information and a complete description of the model can be found in [55].



**Figure 6.13** shows Arrhenius plots of the electrolyte ( $ASR_{YSZ}$ ) and the electrolyte-cathode interface ( $ASR_{LSC}$ ) as a function of the temperature, compared to previously reported values for both materials as well as state of the art Pt electrodes. ASR values were obtained from the equivalent circuit fitting of the set of impedance spectra. Only the active area of the membrane was used for the calculations. The ASR dependence on temperature follows an Arrhenius-type law for both the YSZ and the LSC, with activation energies of 1.05 eV and 1.54 eV, respectively. These values are in agreement with previously reported values for the corresponding bulk materials (see references [48, 54, 56, 58] for YSZ and [24, 27, 28, 59] for LSC). The YSZ electrolyte presents similar  $ASR_{YSZ}$  values than those previously reported for bulk [48] and YSZ free-standing membranes measured in cross-plane [4]. LSC resistivity values were slightly higher than other previously reported (some of them also plotted on the figure for direct comparison [27, 28, 59]). This discrepancy can be attributed to the well-known dependency of the oxygen surface exchange properties and electrolyte-electrode polarization resistances on the fabrication routes [27, 28, 59]. Figure 6.13 also includes ASR values for two different porous Pt/YSZ interfaces: (i) based on Pt/YSZ/Pt membranes under real  $\mu$ SOFC operating conditions from three different research groups [2, 7, 60]; (ii) based on porous Pt films deposited on YSZ single crystal as reported by Ryll et al. [61]. The wide variability of reported values is probably due to the instability of these metallic-based electrodes at  $\mu$ SOFC operating temperatures and does not allow clear comparison with the results on LSC's performance.

An absolute value targeted for electrodes/electrolyte polarization resistances is  $ASR=0.3 \Omega \cdot \text{cm}^2$  [62]. The results suggest the need of temperatures higher than 650 °C for having a good performance of both LSC/YSZ interfaces (black dotted line in Figure 6.13). Although this fact forces  $\mu$ SOFCs to work at higher temperatures than those previously published for  $\mu$ SOFCs based on Pt (350-550 °C, [1, 6]), the proven stability of the LSC films at such temperatures makes the system more reliable considering the fast degradation observed for pure metallic-based devices. Moreover, working at such high temperatures allows substantially increasing the electrolyte thickness to several hundreds of nm. Thicker electrolytes make the membrane more robust reducing the probability of pinhole formation, i.e. minimizing one of the most frequent reasons of failure for free-standing electrolyte membranes [47].



**Figure 6.13:** Evolution of the ASR of both LSC electrodes and YSZ electrolyte with temperature, measured on symmetrical LSC/YSZ/LSC free-standing membranes. Reference values from previously published works are also plotted for comparison. Black dot line marks the  $0.3 \Omega \cdot \text{cm}^2$  target value for both electrode/electrolyte polarization resistance.

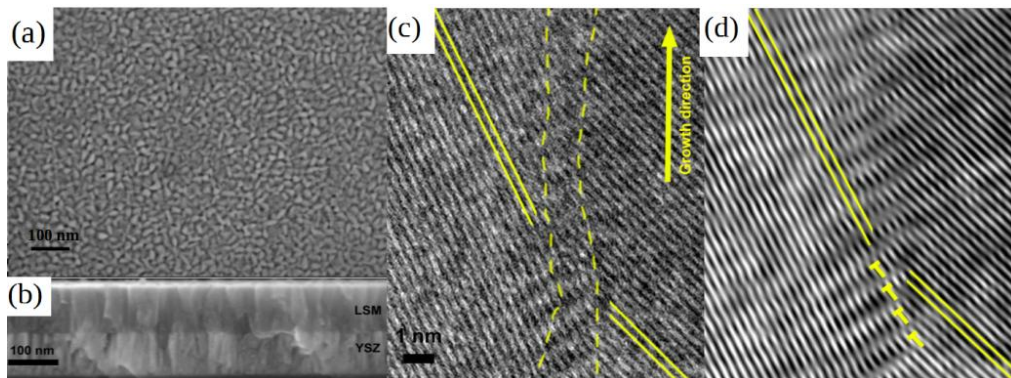
### 6.3.2. Thin film $\text{La}_{0.8}\text{Sr}_{0.2}\text{MnO}_{3+\delta}$

This section is focused on the study of the oxygen mass transport properties of  $\text{La}_{0.8}\text{Sr}_{0.2}\text{MnO}_{3+\delta}$  (LSM) nanostructures in thin film form. In bulk, this material shows oxygen hyperstoichiometry with a very low concentration of oxygen vacancies (metal vacancies and electron holes are the predominant defects), making this material a pure electronic conductor (instead of a targeted MIEC) [63]. However, in this section, it is described how this essentially pure electronic conductor material was converted into a good MIEC by synthesizing a nanostructure with high density of vertically aligned grain boundaries (GB) with high concentration of strain-induced defects where the oxide-ion mass transport is significantly enhanced.

#### 6.3.2.1. Structural and microstructural characterization

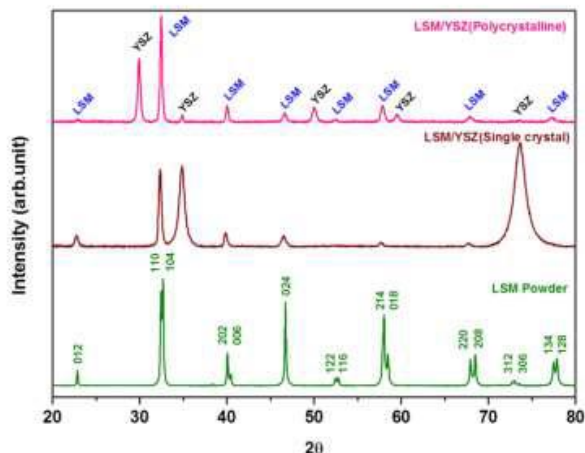
A LSM dense thin film was fabricated over a dense 8YSZ thin film; both deposited by PLD on (100) silicon substrates passivated with a stress-free combination of amorphous  $\text{SiO}_2$  and  $\text{SiN}_x$  layers. An oxygen partial pressure of 0.026 mbar and a substrate temperature of  $700 \text{ }^\circ\text{C}$  were used in the PLD deposition chamber to grow fully dense polycrystalline layers [53]. The heterostructure was characterized by using SEM, TEM and XRD. **Figure 6.14**

shows top view and cross-section SEM pictures (Figure 6.12a and Figure 6.14b, respectively). Full density of the LSM layers and a columnar-type microstructure with grain sizes in the nanoscale ( $d = 16 \pm 7$  nm) were observed. High Resolution TEM (HRTEM) studies reveal well-defined and vertical grain boundaries with a thickness *ca.* 1nm, but a non-homogeneous nature of the LSM columnar grains (Figure 6.14c). Indeed, strain causes distortion at the grain boundaries, which results in the creation of a high density of dislocations in the regions close to the boundaries (Figure 6.14d).



**Figure 6.14:** Microstructural characterization of the LSM films. SEM top view image of the LSM dense film (a); SEM cross section image of the 100 nm LSM/100 nm YSZ bilayer (b); and HRTEM and FFT images of the same area and magnification showing a detail of a typical boundary between two LSM grains, (c) and (d) respectively. Solid lines indicate two families of planes for each grain while the dashed lines represent a guide for the eyes indicating the GB influence region. A high density of dislocations is observed in the GB region, some of them are marked with yellow “T” labels.

XRD diffraction patterns of LSM deposited on polycrystalline YSZ (employed for Isotope Exchange Depth Profiling-Secondary Ion Mass Spectroscopy, IEDP-SIMS, experiments) and on YSZ single crystals (employed for EIS experiments) are represented in **Figure 6.15**. The patterns show single phase deposition of polycrystalline YSZ and LSM layers. The indexed peaks for LSM correspond to a rhombohedral  $R\bar{3}c$  space group. The diffraction pattern of LSM powder is included for comparison. Crystalline and single phase LSM is observed in all cases.

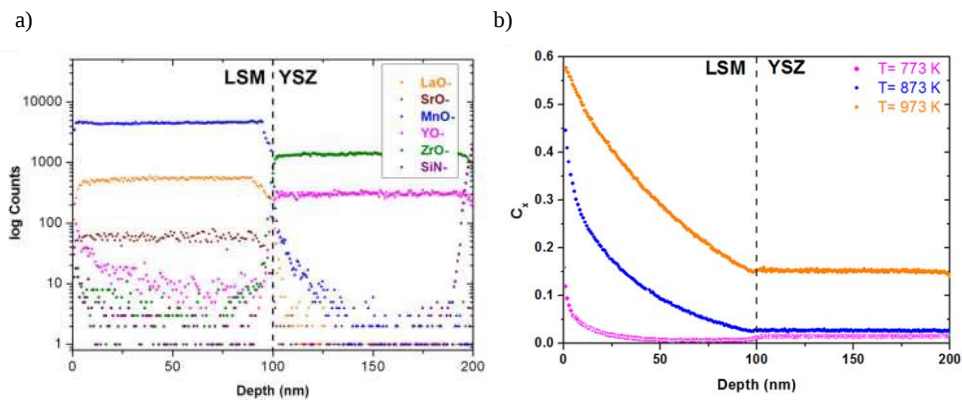


**Figure 6.15:** XRD patterns of LSM thin film deposited on polycrystalline YSZ (employed for IEDP-SIMS experiments) and on YSZ single crystals (used for EIS experiments).

### 6.3.2.2. Oxygen mass transport properties of the dense LSM layer

Amongst the electrochemical techniques that allow measuring mass transport properties,  $^{18}\text{O}$  IEDP-SIMS is the most direct method to measure oxygen diffusion, in particular when applied to dense MIEC in bulk or thin film form [64, 65]. Therefore, to fully understand the oxygen mass transport properties and calculate the oxygen diffusivity ( $D^*$ ) and surface exchange ( $k^*$ ) coefficients of the dense LSM film, IEDP-SIMS at different temperatures between 500 °C and 700 °C were carried out. To avoid oxygen diffusion intake from the backside during the exchange process, a silicon wafer substrate was employed; therefore, limiting the incorporation of oxygen to the top surface area. The proper combination of the measured depth profiles of the  $^{18}\text{O}$  and  $^{16}\text{O}$  ions allowed calculating the normalized  $^{18}\text{O}$  isotopic fraction ( $C_x$ ) as a function of the distance to the top surface [64]. The high quality of the multilayer is confirmed by SIMS depth profiling of the different species (see **Figure 6.16a**). Sharp interfaces and negligible interdiffusion are observed between the LSM and YSZ layers. Moreover, this analysis corroborates that dense YSZ layers represent highly efficient diffusion barriers for silicon coming from the substrate resulting in silicon-free LSM layers. As illustrated in **Figure 6.16b**, a set of isotopic fraction profiles for the whole range of temperature under study were obtained. Three regions can be easily distinguished in all profiles (particularly at low temperatures), namely, a near-surface abrupt decay, a deep-penetrating tail and an unanticipated step at the LSM/YSZ interface that results in a higher isotopic concentration in the YSZ layer. This indicates that LSM is

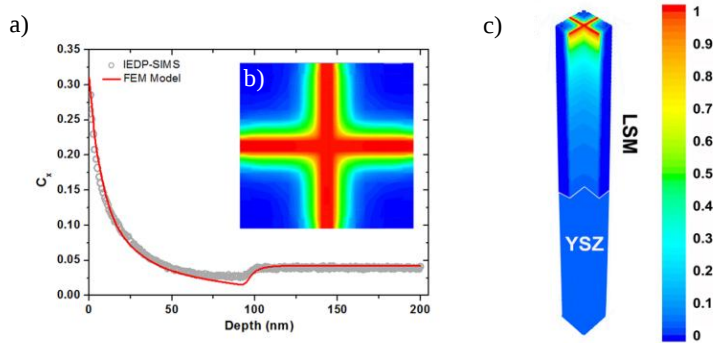
not a homogeneous medium since it combines a slow diffusion process limited to a small region close to the surface and a fast diffusion process extended to the YSZ layer. A higher isotopic concentration in the YSZ layer without accumulation in the LSM layer points toward the existence of *narrow* fast oxygen diffusion pathways across the LSM film. This is consistent with the columnar-like microstructure obtained by PLD if we consider slow diffusion through the bulk and fast diffusion in the grain boundaries (fast diffusion through nanoporous is discarded according to the discussion presented later). This model is in agreement with higher oxygen diffusivities for LSM grain boundaries reported by De Souza *et al.* [63].



**Figure 6.16:** (a) SIMS depth profiles of the different species contained in the LSM/YSZ bilayer and (b) the normalized  $O_{18}$  isotopic fraction exchanged at 500-700 °C for LSM/YSZ bilayers.

Since analytical solutions are not available for diffusion in such an inhomogeneous material with finite geometry, the response of an equivalent bilayer was studied by numerical methods using Finite Element Analysis (FEM) to extract quantitative information of the oxygen transport properties of the bulk and grain boundaries of LSM. Isotope concentration profiles corresponding to the IEDP-SIMS experimental conditions were simulated by FEM for a bilayer consisting of (i) a 100 nm thick film exposed to the atmosphere with vertically aligned squared grains of 16 nm each side and a typically observed 1 nm thick grain boundary [66] (equivalent to the LSM layer) and (ii) a 100 nm thick bulk material (corresponding to our YSZ layer). Since YSZ can be considered an oxygen sink in the range of temperatures under study, the oxygen mass transport properties of the LSM layer, i.e. the diffusion and surface exchange coefficients for the bulk ( $D_b^*$  and  $k_b^*$ ) and grain boundaries ( $D_{gb}^*$  and  $k_{gb}^*$ ), were the only parameters to adjust for fitting the

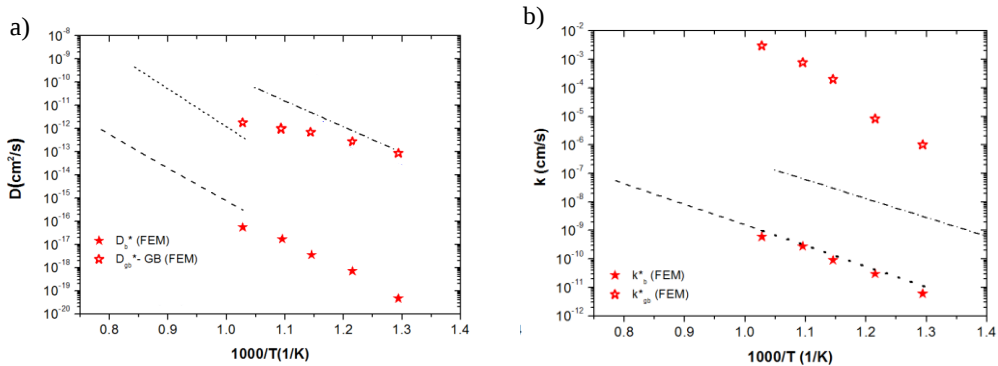
experimental and simulated profiles. Previously reported values of the bulk coefficients [63] were used as a starting point for the fitting. However, the shape of the simulated profiles was very sensitive to all the parameters involved and it was necessary to slightly modify these bulk coefficients to achieve optimum fittings. A very good match between experiments and simulations were obtained for the whole range of temperatures (as illustrated in **Figure 6.17a** for  $T= 550\text{ }^{\circ}\text{C}$ ) yielding a collection of oxygen tracer diffusivities and surface exchange coefficients for bulk and grain boundaries of the nanostructured LSM (see Figure 6.18). The 3D isotopic concentration maps generated by simulation after fitting the mass transport parameters clearly support the existence of an oxygen diffusion “highway” from the surface to the YSZ through the grain boundaries simply explaining the unexpected step present at the YSZ layer in the IEDP-SIMS concentration profiles (see **Figure 6.17b** and **c** for  $T= 550\text{ }^{\circ}\text{C}$ ).



**Figure 6.17:** (a) Normalized  $^{18}\text{O}$  isotopic fraction and fitted solution to the diffusion equation calculated by FEM for the LSM/YSZ bilayer exchanged at  $550\text{ }^{\circ}\text{C}$ , (b) top view and (c) cross section of the isotopic fraction map for the intersection of four quarters of grain as generated by FEM simulation of the LSM/YSZ bilayer exchanged at  $550\text{ }^{\circ}\text{C}$ . The scale bar refers to the normalized isotopic fraction).

**Figure 6.18** shows a representation of the set of oxygen mass transport coefficients obtained by FEM analysis as a function of the reciprocal temperature. The observed linear trends indicate that all the parameters follow an Arrhenius-type behaviour. While the values obtained for the bulk coefficients ( $D_b^*$  and  $k_b^*$ ) are consistent with the literature [63] (included in **Figure 6.18** for comparison), grain boundary properties are orders of magnitude greater. Contrary to the significantly higher activation energy of the GB diffusivity compared to the bulk observed by De Souza *et al.* in micron-sized grain polycrystalline samples [63], the activation enthalpy for  $D_{gb}^*$  is

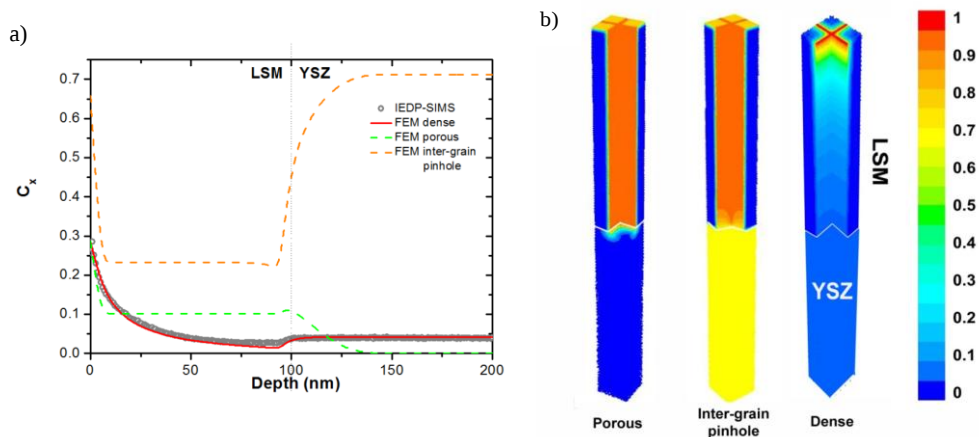
smaller than that for  $D_b^*$  in our nanostructure. As a consequence, the diffusion through the GBs of the PLD-deposited LSM becomes noticeably higher than that previously published, especially at lower temperatures where an astonishing improvement of up to six orders of magnitude is observed ( $T= 500\text{ }^\circ\text{C}$ ). This high diffusion rate means that, unlike the essentially pure electronic conduction of the bulk, the grain boundaries of LSM possess reasonable oxide ion diffusivity, with values close to those of  $\text{La}_{0.8}\text{Sr}_{0.2}\text{CoO}_{3-\delta}$  (see Figure 6.18a). More interestingly, a superior behaviour of the oxygen surface exchange yielded values of  $k_{gb}^*$  among the best ever reported and within the criteria for good cathodes proposed by Steele ( $k^* > 10^{-4} - 10^{-5}\text{ cm/s}$ ) [68] at temperatures as low as  $T= 550\text{ }^\circ\text{C}$ . This effective GB oxygen exchange is thought to be enhanced due to the coupling of the oxygen adsorption and dissociation steps, which could occur along the entire LSM surface, with the oxygen incorporation step, mainly occurring in or close to the grain boundaries (with high oxygen vacancy content). As depicted in Figure 6.18b, the combination of  $D^*$  and  $k^*$  values places this nanostructure of LSM, with a high density of GBs, among the MIEC materials typically employed as electrodes for  $\mu\text{SOFCs}$ .



**Figure 6.18:** Arrhenius plot of (a)  $D^*$  and (b)  $k^*$  coefficients of bulk and grain boundary LSM (filled and unfilled stars, respectively). Tracer diffusion coefficients reported in ref. [63] for bulk (dashed line) and GB LSM (short dashed line) were included together with bulk values of  $\text{La}_{0.8}\text{Sr}_{0.2}\text{CoO}_{3-\delta}$  (dashed dotted line) for comparison. The dotted lines correspond to extrapolated values.

Although pores are not observed by SEM or TEM in the LSM layers, it is important to discard fast diffusion through nanopores. The main difference between fast diffusion through grain boundaries and pores would be that the first occurs via the solid state phase while the other takes place through the gas

phase. The higher diffusivity of molecules in a gas (compared to atomic diffusion in solids) will clearly lead to strong differences in the concentration profiles. FEM simulations were employed to determine the expected isotope diffusion profiles for the same exchange conditions employed in our measurements but considering the existence of: (i) nanoporosity in place of GB; (ii)  $1 \text{ nm}^2$  squared inter-grain pinholes inside GBs. **Figure 6.19** shows the different 3D and linear isotope concentration profiles for these two scenarios compared to the fully dense material. From the simulations, it is clear that both types of porosities would introduce remarkable differences in the concentration profiles making them incompatible with the one experimentally measured. Porosity produces extremely flat tails inside the LSM layer (due to the direct access of the isotopes to the whole surface of the LSM grains) and a different concentration step in the YSZ layer. According to these simulations, it has been demonstrated that the presence of porosity would significantly affect the concentration profiles. Since these profiles are not occurring in the measurements, it is possible to discard a substantial presence of porosity in the samples confirming the full density of the layers already observed by microstructural characterization.



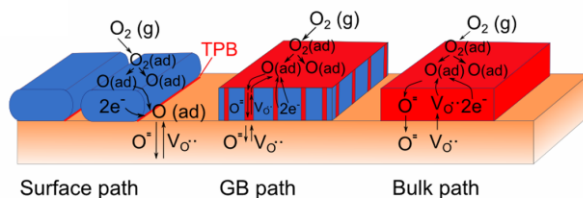
**Figure 6.19:** (a) Normalized  $^{18}\text{O}$  isotope concentration and (b) simulated results to the diffusion equation calculated by FEM for the LSM/YSZ bilayer exchanged at  $550 \text{ }^\circ\text{C}$ . The scale bar refers to the normalized isotope concentration.

### 6.3.2.3. Electrochemical characterization of the LSM layer onto single crystal of YSZ

Finally, the functionality of the vertically nanostructured thin films was also investigated in conventional two-electrode supported electrolyte



electrochemical cells. Symmetrical cells with 40 and 180 nm thick LSM electrodes deposited by PLD on both sides of YSZ single crystal were fabricated. PLD deposition conditions were tuned to obtain cells with porous and fully dense LSM electrodes to clearly show the transition from a pure electronic to a MIEC. It is usually assumed that for porous LSM electrodes with pure electronic conductivity a direct incorporation of oxygen at the triple phase boundary takes place [67] (**Figure 6.20**, surface path). However, employing dense electrodes is only possible for materials which operate as MIECs, since the oxygen reduction reaction is limited to the surface and oxide-ion transport to the electrolyte through the electrode is required (**Figure 6.20**, bulk/grain boundary path). The prepared porous and dense LSM/YSZ/LSM symmetrical cells were characterized by using EIS in the temperature range of 500-700 °C and applying AC voltage of 50 mV under synthetic air.

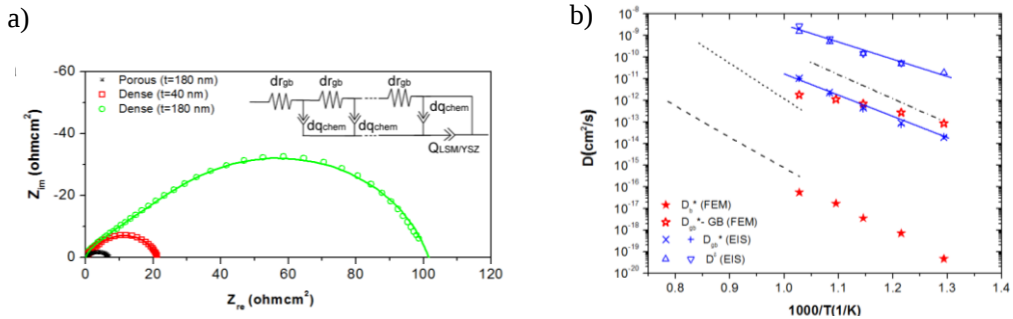


**Figure 6.20:** Sketches of the three paths of the oxygen reduction and incorporation reactions. The surface path is only available for porous samples while bulk and grain boundary paths are the only option for dense films. The red color indicates the active regions for oxygen adsorption and ionic conduction.

The Nyquist plots in **Figure 6.21a** show the contribution of the electrode polarization to the total impedance for porous and dense electrodes of different thickness (from 40 to 180 nm) at 700 °C. While porous electrodes yielded lower polarization resistances and a better performance with thickness, dense electrodes present higher resistance with values increasing almost proportionally to the thickness. This indicates that the reactions at the TPB are dominating for the porous samples whereas the oxygen diffusion through the electrode limits the performance of the cells with dense electrodes, i.e. LSM shows a MIEC behaviour.

By adjusting the EIS spectra of the LSM cells with an equivalent circuit recently proposed by Jamnik *et al.* [69] for MIECs, it was possible to calculate the electrical and chemical diffusion coefficients for the films,  $D^Q$  and  $D^\delta$ ,

respectively. Moreover, since it is well known that the electrical diffusion coefficient is nearly equal to  $D^*$  [70], the tracer diffusion was also easily obtained ( $D^Q = D^*/f$ , where  $f$  is the tracer correlation factor and equal to 0.69 [71]).  $D^*$  and  $D^\delta$  obtained from EIS were plotted in **Figure 6.21b**. The agreement between  $D^*$  obtained by EIS and the grain boundary diffusion coefficients obtained from the FEM fitting of the IEDP-SIMS experiments, confirms that the electrochemical behaviour is clearly dominated by the rapid oxide-ion diffusion along the grain boundaries, i.e.  $D_{gb}^*$ . This diffusivity is characterized by an activation energy of  $E_{gb}^D = 1.9(1)$  eV. This value is remarkably below the one reported by De Souza *et al.* [63] for the bulk,  $E_b^D = 2.9$  eV, and, more interestingly, for the GBs,  $E_{gb}^D = 3.3$  eV. This difference in the activation enthalpy of the GB is associated to the lower degree of order and high dislocation density observed in the shared interface of our columnar grains. Finally, it is worth mentioning that the chemical diffusion coefficients resulting from EIS are in the same range as the values reported for bulk LSM [72], which indicates that the oxygen stoichiometry changes induced by oxygen diffusivity along GBs take place within the grains.



**Figure 6.21:** (a) Nyquist plot for the electrochemical response of the LSM/YSZ/LSM cells with dense and porous LSM layers with different thickness (from 40 to 180 nm) in air at  $T = 700$  °C; the continuous line presents the fitting of the equivalent circuit sketched in the inset. For clarity, the only contribution shown in the figure is that associated with the electrode polarization (the inductance and series resistance was subtracted by deconvolution). (b) Arrhenius plot of  $D^*$  coefficients of bulk and grain boundary LSM calculated by FEM simulations (filled and unfilled stars, respectively) and by EIS measurements (crosses). Chemical diffusion coefficients (triangles) obtained by EIS measurements are also included.

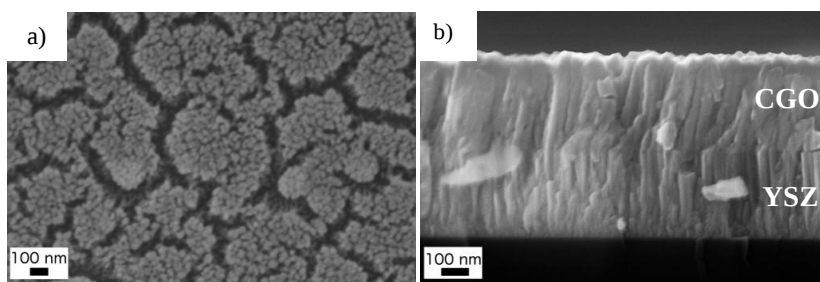
## 6.4. Ceramic anodes for $\mu$ SOFC

### 6.4.1. Thin film $\text{Ce}_{0.8}\text{Gd}_{0.2}\text{O}_{1.9-\delta}$

The  $\text{CeO}_2$  fluorite structure is very tolerant to dissolution of low-valent metal oxides, like Gd, Sm or Pr [73]. Furthermore, under reducing conditions, a portion of the  $\text{Ce}^{4+}$  converts to  $\text{Ce}^{3+}$ , and the resulting electrons are charge balanced by oxygen vacancies, where  $\delta$  in the stoichiometry of ceria compounds represents the vacancy concentration. Therefore, high oxygen vacancy mobility combined with MIEC behaviour under reducing conditions make ceria compounds a suitable material for electro-catalytic applications, such as  $\mu$ SOFC anode [74].  $\text{Ce}_{0.8}\text{Gd}_{0.2}\text{O}_{1.9-\delta}$  (CGO) thin film was the choice for this work.

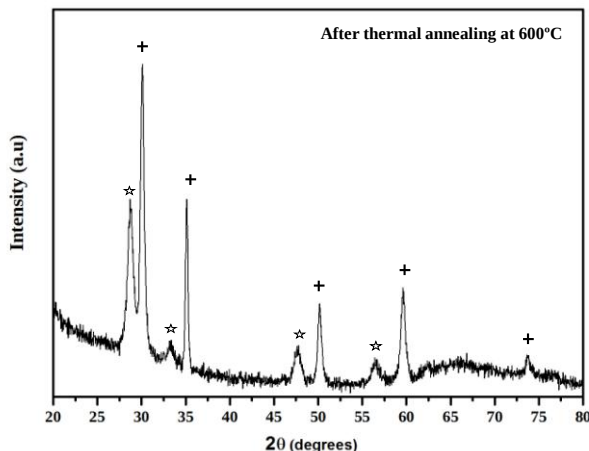
#### 6.4.1.1. Structural and microstructural characterization

CGO porous thin films were fabricated by PLD. Deposition conditions and post-annealing treatment were optimized in order to ensure good crystallinity and enough porosity. **Figure 6.22** shows top view and cross-section SEM images of the porous CGO layers (250 nm thick) deposited over dense 8YSZ films on a  $\text{Si}_3\text{N}_4/\text{SiO}_2/\text{Si}$  substrate. A columnar and well-ordered grain growth was observed for YSZ film, while CGO layer showed porous and disordered clusters. As previously mentioned, the formation of this type of microstructure was driven by a high background pressure during the PLD deposition that increases the mobility of species on the ablation plume and allows the formation of separated clusters that generates a porous network [54].



**Figure 6.22:** (a) Top view and (b) cross-section SEM images 250 nm thick porous CGO layers over previously deposited dense 8YSZ.

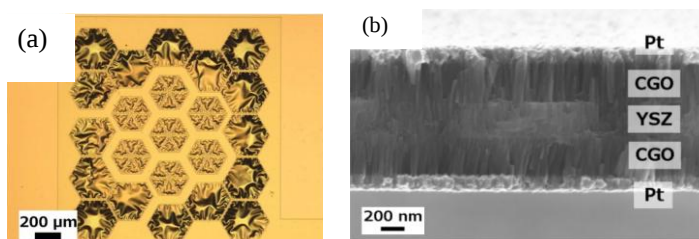
The XRD pattern of the CGO/YSZ bilayer is depicted in **Figure 6.23**. Diffraction peaks from both crystalline YSZ and CGO diffraction patterns are pointed out corresponding to a cubic  $Fm\bar{3}m$  structure.



**Figure 6.23:** XRD pattern of a porous CGO film deposited over dense YSZ. The crosses correspond to YSZ diffraction peaks, while the stars point out the main peaks of a crystalline CGO pattern.

#### 6.4.1.2. Integration into self-suspended membranes of YSZ

The CGO thin film anodes were then implemented on free-standing membranes and tested under real  $\mu$ SOFC conditions. **Figure 6.24a** shows the as fabricated CGO/YSZ/CGO symmetrical free-standing membranes. Cross-sectional SEM image of the same membrane including patterned dense Pt current collectors is presented in the **Figure 6.24b**. A similar microstructure to the one obtained on bulk substrates was observed (i.e. porous and columnar CGO films and highly dense and columnar YSZ film). Film homogeneity was excellent along the whole free-standing membrane. YSZ and CGO films of 300 nm were complemented with dense patterned 150 nm thick Pt films on both sides of the membrane for a total thickness of 1.2  $\mu\text{m}$ . The obtained membranes showed the typical buckling pattern observed on the YSZ membranes [4] indicating a negligible strain contribution of the porous anode films. Therefore, the overall mechanical behaviour was controlled by the electrolyte.



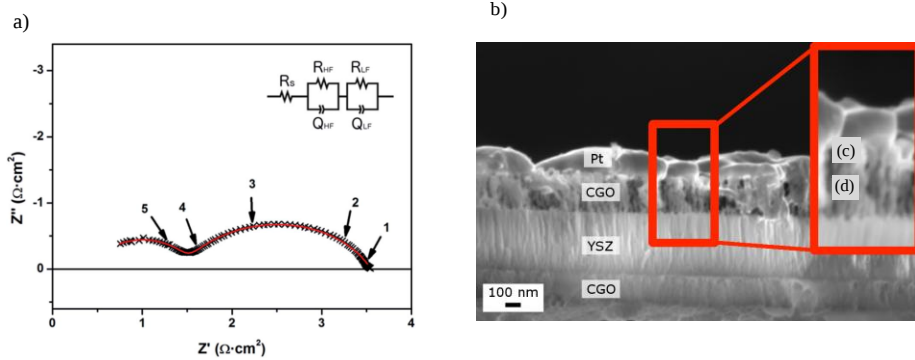
**Figure 6.24:** (a) Top view optical image of a CGO symmetrical cell and (b) SEM cross sectional view of the cell with the current collectors.

### 6.4.1.3. Electrochemical characterization

**Figure 6.25** depicts a Nyquist plot corresponding to the EIS spectrum obtained for a Pt/CGO/YSZ/CGO/Pt symmetrical cell at 650°C under a reducing atmosphere (5% H<sub>2</sub> - 95% Ar), and a cross-sectional SEM image of the cell after the EIS measurements. Two separated arcs were observed in **Figure 6.25a** with resistance values of the same order of magnitude, but separated due to the difference on their associated capacitance, i.e. time constant. The data were fitted according to the equivalent circuit depicted in the inset. It is noteworthy that the contribution from the dense YSZ electrolyte is expected to be negligible at such temperatures as detailed in ref. [4]. So, the series resistance was associated to the current collection and cable resistances, and the two arcs were related to:

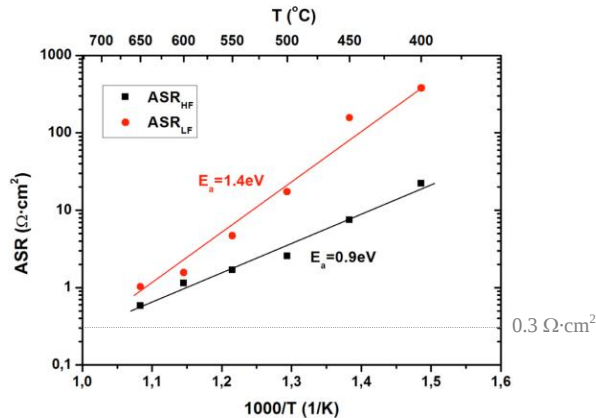
- the oxygen transport in the CGO electrode or through the electrode-electrolyte interface, corresponding to a HF-arc with  $Q_{HF} = 10^{-9} \text{ F}\cdot\text{cm}^{-2}$ ;
- the electrochemical oxidation of hydrogen at the ceria surface, corresponding to a LF-arc with  $Q_{LF} = 10^{-7} \text{ F}\cdot\text{cm}^{-2}$ .

For a better understanding of impedance spectrum, **Figure 6.25b** shows a cross-sectional SEM image of the measured CGO-Pt electrodes. The relatively closed porosity of the CGO film limited the penetration of the Pt metal into the porous network, thus restricting the cermet formation only to the contact surface of the electrodes (marked as (c) in the magnification). Meanwhile, the rest of the CGO film remains unfilled (zone (d) in the magnification). These observations were in agreement with the electrochemical behaviour. On one side, the small porosity and the subsequent gas diffusion problems make improbable the ceria reduction, what would explain the low CGO electronic conductivity measured (see next **Figure 6.26**) and the low MIEC behaviour (HF-arc). On the other side, the catalytically active area of the electrode would be delimited to the CGO-Pt surface where the cermet is formed (LF-arc), while the rest of the CGO film would act as an extra electrolyte.



**Figure 6.25:** (a) Impedance spectrum of a CGO symmetrical cell, measured at 650 °C. The solid red line represents the fitting using the equivalent circuit depicted and the numbers refer to the frequency decades covered by the EIS analysis. (b) Cross-sectional SEM image of the cell after EIS measurements.

Finally, **Figure 6.26** shows an Arrhenius plot of the ASR corresponding to the high frequency ( $ASR_{HF}$ ) and low frequency ( $ASR_{LF}$ ) arcs as a function of the temperature. The activation energies achieved were  $E_a = 0.9$  eV and  $E_a = 1.4$  eV, respectively. These values are in agreement with the previously proposed explanation. Activation energies around 0.8 – 1.0 eV were reported for oxide-ion conduction on CGO films [74], while other reported thin film cermetes were found to have an activation energy of 1.4 – 1.5 eV [76, 77]. Furthermore, the reference  $ASR_{electrodes/electrolyte} = 0.3 \Omega \cdot cm^2$  was attained approximately at 700 °C. This temperature is similar to the one obtained for the LSC/YSZ [24], indicating the possibility of integrating the CGO as anode in a full ceramic  $\mu$ SOFC device.



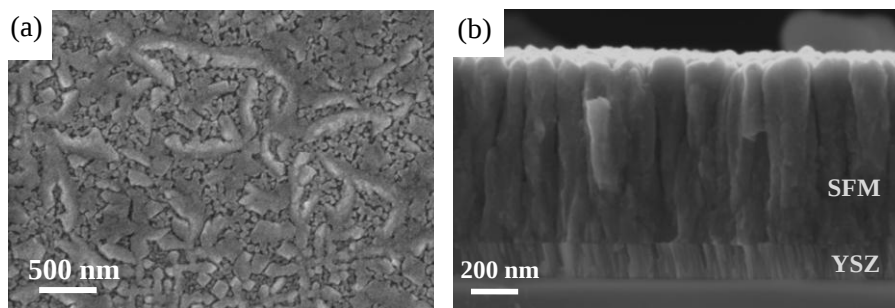
**Figure 6.26:** Temperature evolution of the ASR of the two arcs appearing on the EIS analysis of the CGO symmetrical cells, i.e. HF-arc and LF-arc.

### 6.4.2. Thin film $\text{Sr}_2\text{Fe}_{1.5}\text{Mo}_{0.5}\text{O}_{6-\delta}$

Molybdenum-based double perovskites, i.e.  $\text{Sr}_2\text{M}_x\text{Mo}_{2-x}\text{O}_{6-\delta}$  ( $\text{M} = \text{Mg}, \text{Fe}, \text{Co}$ , and  $\text{Ni}$ ), have been mainly investigated as anode material in SOFCs due to their MIEC behavior and their higher catalytic activity for fuel oxidation than doped ceria anodes [78]. Recently, a novel double perovskite  $\text{Sr}_2\text{Fe}_{1.5}\text{Mo}_{0.5}\text{O}_{6-\delta}$  (SFM) has been reported as a promising material for symmetrical SOFCs architectures [79], because it presents a high electrical conductivity in both air and hydrogen atmospheres, excellent redox stability and a high electrochemical performance for oxygen reduction and hydrogen oxidation reactions [34]. The iron and molybdenum atoms are found partially ordered in the double perovskite structure ( $\text{A}_2\text{BB}'\text{O}_6$ ) due to the size and charge difference; however, for the Fe/Mo ratio of 3:1, the iron-molybdenum ordering ceases and both atoms are randomly distributed over the B and B' sites [80]. This disorder promotes that the Fe/Mo redox couple ( $\text{Fe}^{2+} + \text{Mo}^{6+} \leftrightarrow \text{Fe}^{3+} + \text{Mo}^{5+}$ ) in air atmosphere introduces oxygen vacancies into the lattice leading to a high ionic conductivity; while in hydrogen atmosphere remains mixed-valent generating electronic carriers [81, 82].

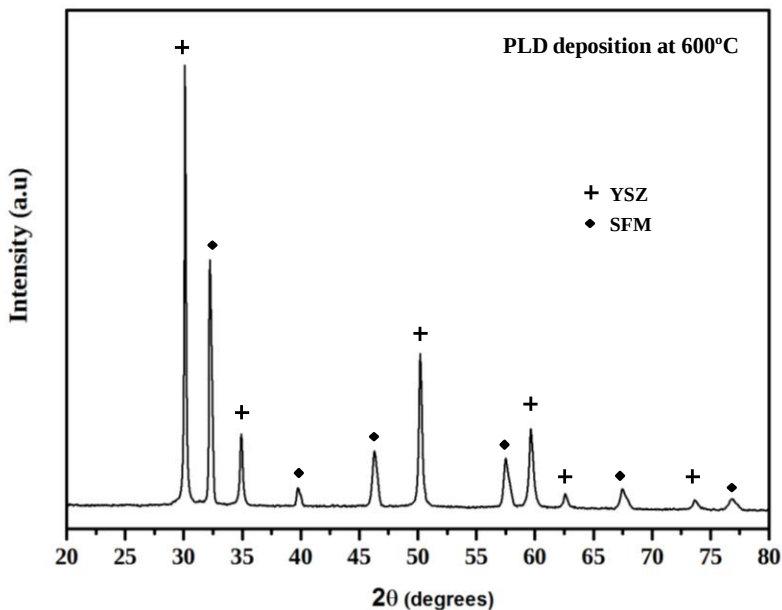
#### 6.4.2.1. Structural and microstructural characterization

SFM thin films were fabricated over dense 8YSZ films; both deposited by PLD on (100) silicon substrates passivated with amorphous  $\text{SiO}_2$  and  $\text{SiN}_x$  layers (Section 2.3 in Chapter II). Deposition conditions for ensuring enough SFM porosity and crystallinity are based on a high background pressure and a high temperature during PLD deposition [54]. **Figure 6.27** shows top view and cross section SEM images of the porous SFM layer. Disordered columnar clusters with open porosity were observed for SFM thin film while a well-ordered columnar grain growth was distinguished for YSZ.



**Figure 6.27:** (a) Top view and (b) cross-section SEM images of porous SFM layer over previously deposited dense YSZ.

The XRD pattern of the SFM/YSZ bilayer is depicted in **Figure 6.28**. The indexed peaks from both crystalline YSZ and SFM correspond to cubic  $Fm\bar{3}m$  structures. The patterns exhibit single phase deposition of polycrystalline YSZ and SFM layers, showing a good chemical compatibility between them in the IT range preferred for the  $\mu$ SOFC.

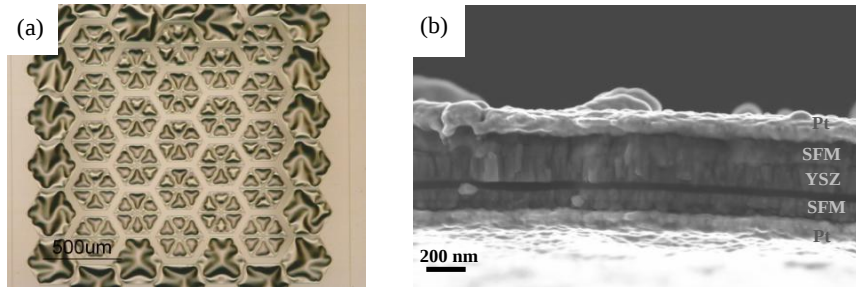


**Figure 6.28:** XRD pattern of a porous SFM film deposited over dense YSZ. The crosses correspond to YSZ diffraction peaks, while the rhombus point out the peaks of a crystalline SFM pattern.

#### 6.4.2.2. Integration into self-suspended membranes of YSZ

The SFM thin films were then implemented on large free-standing membranes ( $\sim 3 \text{ mm}^2$ ) and tested under real  $\mu$ SOFC conditions. **Figure 6.29a** shows a top view optical image of SFM/3YSZ/SFM symmetrical free-standing membranes including the current collectors. Cross-sectional SEM image of the membrane is presented in the **Figure 6.29b**. Porous and columnar SFM films were observed similar to the LSC and CGO layers presented in *Section 6.3.1.1* and *6.4.1.1*, respectively. The YSZ membrane presented 150 nm in thickness and the SFM films 125 nm. Over this trilayer dense patterned 150 nm thick Pt films were deposited on both sides of the membrane for a total thickness of 0.85  $\mu\text{m}$ . As previously mentioned for the LSC and CGO films, the obtained membranes showed the same buckling pattern observed on the YSZ membranes [4] indicating that the mechanical behaviour was mainly controlled by the electrolyte membrane.

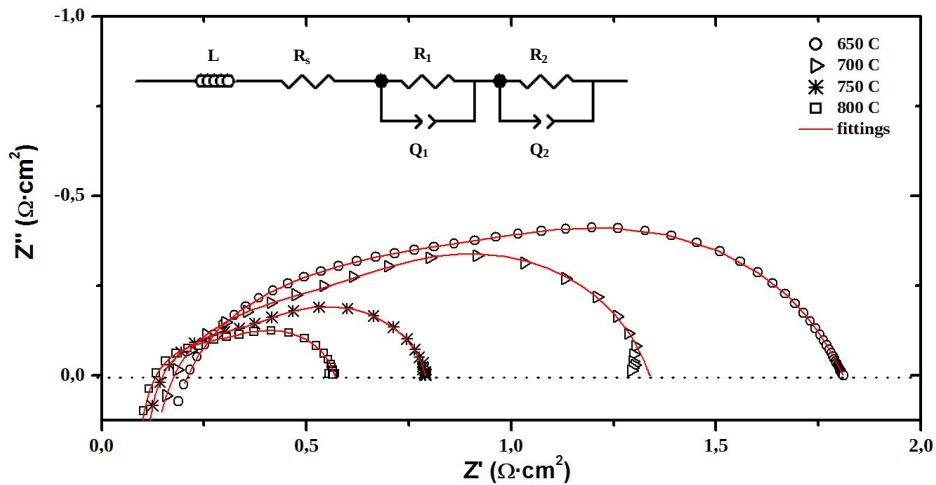




**Figure 6.29:** (a) Top view optical image of a SFM symmetrical cell and (b) SEM cross sectional view of the cell with the current collectors.

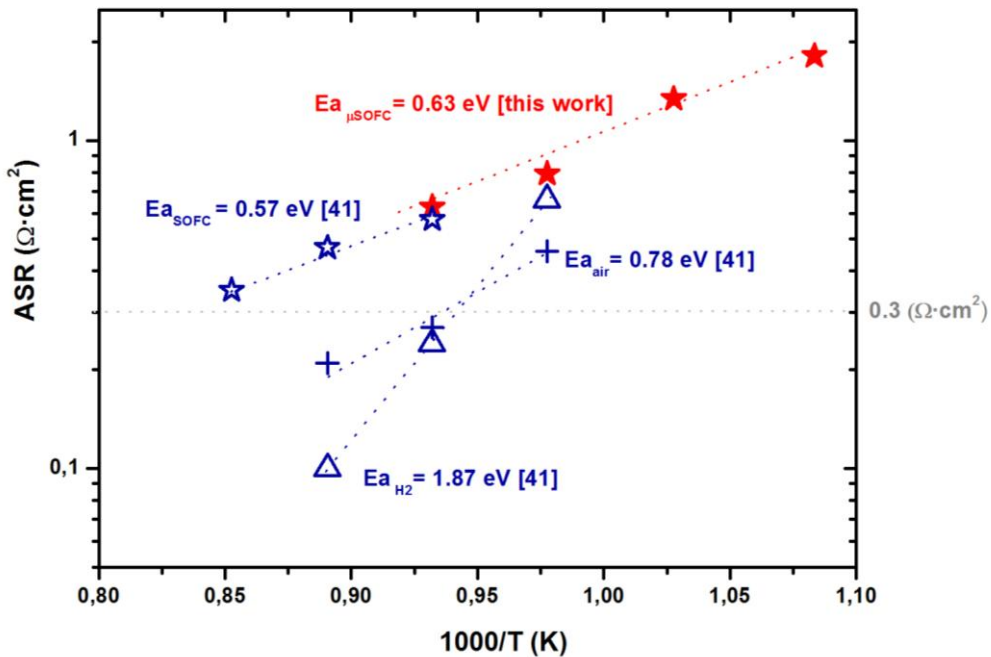
### 6.4.2.3. Electrochemical characterization

**Figure 6.30** depicts the Nyquist plots corresponding to the EIS spectra obtained for a Pt / SFM / YSZ / SFM / Pt symmetrical cell between 650 °C and 800 °C under a reducing atmosphere (5% H<sub>2</sub> - 95% Ar) in the anode side and an oxidizing atmosphere (synthetic air) in the cathode side. The data were fitted according to the equivalent circuit depicted in the inset. The convolution of two arcs with similar capacitance values were observed in the spectra. The arcs were related to the polarization resistance of the electrodes.



**Figure 6.30:** Impedance spectra of a SFM symmetrical cell, measured between 650 °C and 800 °C under 5% H<sub>2</sub> - 95% Ar in the anode and synthetic air in the cathode. The solid red lines represent the fitting using the equivalent circuit depicted and the numbers refer to the frequency decades covered by the EIS analysis.

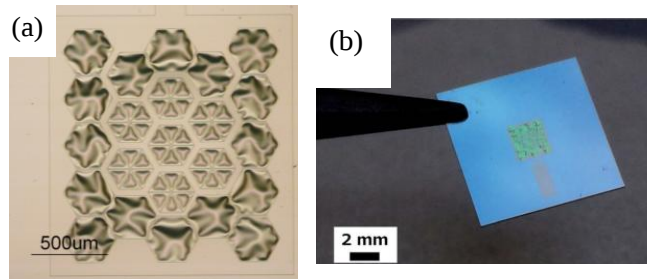
**Figure 6.31** shows an Arrhenius plot of the ASR corresponding to the symmetric SFM thin film cell as a function of the temperature. The activation energy obtained was  $E_a = 0.63$  eV. This value was in agreement with the value previously reported for a SFM / LSGM / SFM cell [41]. Moreover, the activation energies reported for this SFM / LSGM / SFM cell in air and hydrogen (around 0.8 and 1.9 eV, respectively) suggests that the porous thin film SFM had better performance as cathode than as anode. The target ASR =  $0.3 \Omega \cdot \text{cm}^2$  was attained approximately at 900 °C. This temperature is higher than the ones obtained for the LSC/YSZ [24] and CGO/YSZ [25], indicating the need of a SFM microstructure optimization to further reduce the polarization resistance of the electrodes. However, the possibility of using thin film SFM as a cathode and anode in  $\mu$ SOFCs was proven. Further work is ongoing to measure the symmetrical system operating as a  $\mu$ SOFC. Since the measured values of ASR correspond to the ones reported in the literature a good SOFC performance would be expected.



**Figure 6.31:** Evolution of the ASR of the symmetric SFM  $\mu$ SOFC with temperature. Reference values from previously published work [41] are also plotted for comparison.

## 6.5. Full ceramic-based $\mu$ SOFC

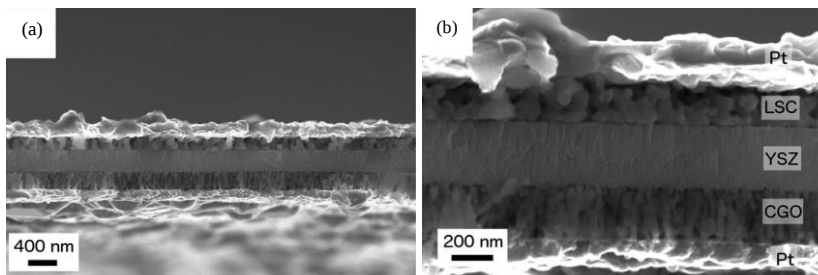
Large-area ( $2 \text{ mm}^2$ ) free-standing ceramic-based  $\mu$ SOFCs were fabricated using a porous LSC thin film as the cathode, a dense membrane of 8YSZ as the electrolyte and a porous CGO thin film as the anode. Highly buckled membranes were obtained after the electrodes deposition (see **Figure 6.32**) due to the clearly dominating compressive strain of the YSZ membranes [51]. No change in the buckling pattern was observed suggesting a negligible stress contribution of the two porous electrodes.



**Figure 6.32:** (a) Top view optical image of a ceramic-based  $\mu$ SOFC (already including the electrodes and current collectors) and (b) real image of the  $\mu$ SOFC device.

### 6.5.1. Structural and microstructural characterization

**Figure 6.33** shows cross-sectional view images of the ceramic-based  $\mu$ SOFC, where the different microstructure of each layer can be distinguished. High porosity was observed on both LSC (top) and CGO (bottom) electrodes with *ca.* 300 nm each, while high density and packed columnar grain arrangements were observed for a 300 nm thick YSZ electrolyte. Pt current collectors of 150 nm thickness were deposited at both sides of the functional trilayer.

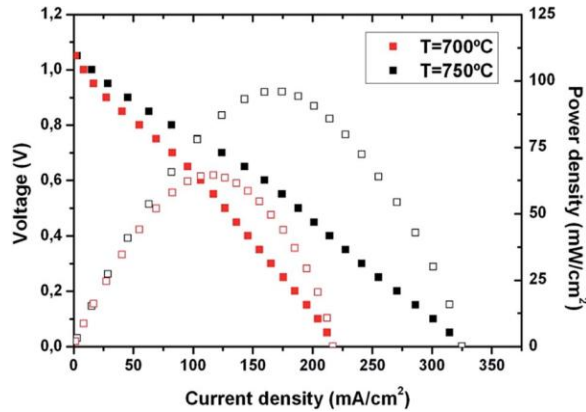


**Figure 6.33:** Different magnification cross-sectional SEM images of a Pt/LSC/YSZ/CGO/Pt free-standing membrane, after measuring at  $750 \text{ }^\circ\text{C}$ .

Despite the fact that thinner electrolyte layers were commonly employed [61], the thickness of the 8YSZ layer implemented here was increased. An electrolyte thickness of several hundreds of nanometers enhances its reliability without affecting the electrochemical performance. Thicker electrolyte layers (deposited in two stages with a cleaning step in between) reduce the formation of through pinholes and increase the thermo-mechanical stability of the membrane while keeping a negligible associated resistance at the operation temperature. For an electrolyte of 300 nm, like in this case, the ASR can be as low as  $0.15 \Omega \cdot \text{cm}^2$  at temperatures below 450 °C (see **Figure 6.7** from previous *Section 6.2*). Considering that the electrodes operated at 700 °C, even thicker electrolyte layers than the one used here will not limit the  $\mu$ SOFC performance.

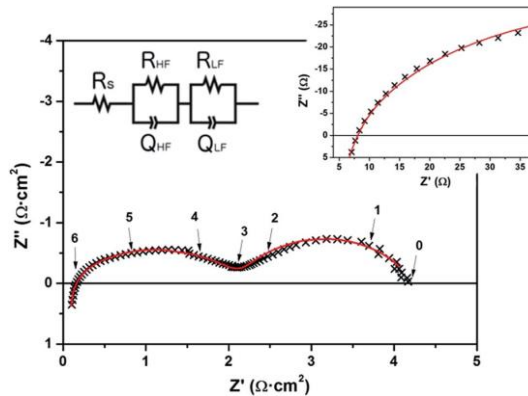
### **6.5.2. Electrochemical performance of the $\mu$ SOFC**

**Figure 6.34** shows I–V curves obtained for one of the measured Pt/LSC/YSZ/CGO/Pt free-standing membranes at different temperatures, up to 800 °C. It is noteworthy that measurements below 650 °C showed insufficient performance (no electrode activation) and tests at higher temperatures ( $T > 800$  °C) resulted in membrane failure (similar thermo-mechanical limits were previously reported in ref. [61]). An OCV close to the theoretical value was obtained once sealed (OCV = 1.05 V), using synthetic air as the oxidizing atmosphere (cathode side) and pure H<sub>2</sub> as the reducing atmosphere (anode side). These values of OCV and stable power densities were maintained for more than 5 h at the operating temperatures ( $T = 700$ – $750$  °C), thus ensuring the reliability of the membranes from an electrochemical point of view, i.e. no pinholes or cracks appeared on the membranes during heating up, sealing and measuring. The power density output was calculated as a function of the current density, showing a maximum value of  $100 \text{ mW} \cdot \text{cm}^{-2}$  at 750 °C and  $65 \text{ mW} \cdot \text{cm}^{-2}$  at 700 °C. The total power output extracted from a single cell was *ca.* 2 mW at 750 °C. This power output value was in the upper range of power per cell previously reported for  $\mu$ SOFCs [21], being a clear proof of concept of the feasibility of a full-ceramic  $\mu$ SOFC operating at the required high temperatures.



**Figure 6.34:** I–V curve (solid symbols) and power density output (unfilled symbols) obtained from a Pt/LSC/YSZ/CGO/Pt free-standing membrane at 700 °C and 750 °C.

As shown in **Figure 6.35**, two separated arcs can be identified in a Nyquist plot corresponding to a Pt/LSC/YSZ/ CGO/Pt  $\mu$ SOFC at 750 °C and operating voltage of 0.7 V. A equivalent circuit  $R_s(R_{HF}Q_{HF})(R_{LF}Q_{LF})$  was proposed. The series resistance ( $R_s$ ) includes the resistances associated with the YSZ electrolyte, the Pt current collectors and the cables and contacts. Values of  $R_s$  of several ohms were measured (see details of the high frequency range in the inset of **Figure 6.35**) mainly corresponding to the current collector and cable resistances (as commented before the YSZ resistance is expected to be negligible at  $T > 700$  °C). Therefore, the thin film ceramic electrodes were the main source of resistance losses in the cell



**Figure 6.35:** Nyquist plot of the ceramic-based  $\mu$ SOFC (2 mm<sup>2</sup> active area) at 750 °C and operating voltage of 0.7 V. The inset shows a zoom of the high frequency part of the plot. The solid red line represents the fitting using the equivalent circuit depicted. The numbers refer to the frequency decades covered by the EIS analysis.

The arcs observed in the plot can be associated with the two electrodes of the  $\mu$ SOFC. High frequency and low frequency arcs present resistance values of the same order of magnitude, i.e. 1.5 and 2.5  $\Omega\cdot\text{cm}^2$  respectively. These values of ASR are one order of magnitude higher than those expected from the symmetrical cell measurements (either for CGO or LSC films) and far from the target value of electrode ASR, indicating that the integration of both ceramic electrodes in the  $\mu$ SOFC requires further optimization. Moreover, the associated capacitances of the two arcs were  $Q_{\text{HF}}=10^{-6}$   $\text{F}\cdot\text{cm}^{-2}$  and  $Q_{\text{LF}}=10^{-3}$   $\text{F}\cdot\text{cm}^{-2}$ . These values of capacitance suggest a double contribution from the different phenomena involved in both electrodes. On the one hand, the  $Q_{\text{HF}}$  is in concordance with the previously measured capacitance on CGO symmetrical cells (see *Section 6.4.1.3*), thus this first arc was associated to the catalytically active area of the Pt-CGO cermet. On the other hand, the high capacitance observed on the low frequency arc was consistent with the chemical capacitance reported for MIEC [69], like LSC that presented such behavior on symmetrical cells (see *Section 6.3.1.3*).

## **6.6. Conclusions**

In this chapter, ceramic thin film electrodes fabricated by PLD have been presented as a suitable alternative to noble metal electrodes in large-area free-standing membranes. For proving this, low-thermal mass platforms and self-supported thin film electrolytes of YSZ belonging to the background of the group were used.

### **❖ For the cathode side:**

Highly porous LSC thin films (up to 33% of in-plane porosity) were well-deposited by PLD over dense YSZ electrolytic layers. No degradation was observed neither with temperature nor time up to 700 °C and for more than 60 h. The implementation and the thermo-mechanical stability of LSC porous layers in large-area symmetrical LSC/YSZ/LSC free-standing membranes were proved. Target values of ASR ( $0.3 \Omega \cdot \text{cm}^2$ ) required for SOFC cathode/electrolyte bilayers were achieved in the IT range.

An artificial mixed ionic electronic conducting oxide of LSM was fabricated by grain boundary engineering thin films. This essentially pure electronic conductor material was converted into a good mixed ionic electronic conductor by synthesizing a nanostructure with high density of vertically aligned grain boundaries with high concentration of strain-induced defects. The grain boundaries presented a remarkable enhancement of their oxide-ion mass transport properties (of up to six orders of magnitude at 500 °C). These results lead to fundamental insights into oxygen diffusion along grain boundaries and to the application of these engineered nanomaterials in new advanced solid state ionic devices such as  $\mu$ SOFCs.

### **❖ For the anode side:**

Porous CGO and SFM thin films were deposited by PLD over dense YSZ layers. In the case of CGO, its electrochemical performance and thermo-mechanical stability were validated in large-area symmetrical CGO/YSZ/CGO free-standing membranes. Moreover, the SFM layers were applied as an anode and a cathode in the membranes. The novel material showed redox stability and electrical conductivity in both oxidizing and reducing environments. In both cases, CGO and SFM, target values of ASR required for SOFC electrodes/electrolyte were achieved in the IT range.

❖ **Full-ceramic  $\mu$ SOFC:**

A full ceramic-based  $\mu$ SOFC was fabricated using a porous LSC thin film as a cathode, a dense membrane of YSZ as an electrolyte and a porous CGO thin film as an anode. The thermo-mechanical stability of the  $\mu$ SOFC membrane was proved up to 750 °C, thus extending the up to now reported operating temperatures of  $\mu$ SOFC (< 550 °C). Measurements of the fuel cell performance of the device were carried out at 700 – 750 °C. A maximum power density of 100 mW·cm<sup>-2</sup> was measured at 750 °C, under pure H<sub>2</sub> as a fuel and synthetic air as an oxidant, for a total power per cell of 2 mW.

A new generation of more reliable  $\mu$ SOFCs, based on ceramics, is demonstrated for a real implementation in portable devices. However, further work should be focused on reducing the ASR of the electrodes by fabricating thinner films and/or increasing the porosity. Finally, all-ceramic-based  $\mu$ SOFCs should be validated by extending the punctual measurements to specific long-term tests.



## References

- [1] Evans, A., Bieberle-Hütter, A., Rupp, J. L. M. & Gauckler, L. J. Review on microfabricated micro-solid oxide fuel cell membranes. *J. Power Sources* **194**, 119–129 (2009).
- [2] Tsuchiya, M., Lai, B.K. & Ramanathan, S. Scalable nanostructured membranes for solid-oxide fuel cells. *Nat Nano* **6**, 282–286 (2011).
- [3] Baertsch, C. D. *et al.* Fabrication and structural characterization of self-supporting electrolyte membranes for a micro solid-oxide fuel cell. *J. Mater. Res.* **19**, 2604–2615 (2004).
- [4] Garbayo, I. *et al.* Electrical characterization of thermo-mechanically stable YSZ membranes for micro solid oxide fuel cells applications. *Solid State Ionics* **181**, 322–331 (2010).
- [5] Su, P.C., Chao, C.C., Shim, J. H., Fasching, R. & Prinz, F. B. Solid oxide fuel cell with corrugated thin film electrolyte. *Nano Lett.* **8**, 2289–2292 (2008).
- [6] Kerman, K., Lai, B.K. & Ramanathan, S. Nanoscale Compositionally Graded Thin-Film Electrolyte Membranes for Low-Temperature Solid Oxide Fuel Cells. *Adv. Energy Mater.* **2**, 655 (2012).
- [7] Muecke, U. P. *et al.* Micro Solid Oxide Fuel Cells on Glass Ceramic Substrates. *Adv. Funct. Mater.* **18**, 3158–3168 (2008).
- [8] Brandon, N. P., Skinner, S. & Steele, B. C. H. Recent Advances in Materials for Fuel Cells. *Annu. Rev. Mater. Res.* **33**, 183–213 (2003).
- [9] Fleig, J., Tuller, H. L. & Maier, J. Electrodes and electrolytes in micro-SOFCs: a discussion of geometrical constraints. *Solid State Ionics* **174**, 261–270 (2004).
- [10] Steele, B. C. H. & Heinzl, A. Materials for fuel-cell technologies. *Nature* **414**, 345–352 (2001).
- [11] De Souza, S., Visco, S. J. & De Jonghe, L. C. Thin-film solid oxide fuel cell with high performance at low-temperature. *Solid State Ionics* **98**, 57–61 (1997).
- [12] Bohac, P. & Gauckler, L. Chemical spray deposition of YSZ and GCO solid electrolyte films. *Solid State Ionics* **119**, 317–321 (1999).
- [13] Nomura, K., Mizutani, Y., Kawai, M., Nakamura, Y. & Yamamoto, O. Aging and Raman scattering study of scandia and yttria doped zirconia. *Solid State Ionics* **132**, 235–239 (2000).
- [14] Sasaki, K. & Maier, J. Re-analysis of defect equilibria and transport parameters in  $Y_2O_3$ -stabilized  $ZrO_2$  using EPR and optical relaxation. *Solid State Ionics* **134**, 303–321 (2000).

- [15] Wanzenberg, E., Tietz, F., Kek, D., Panjan, P. & Stöver, D. Influence of electrode contacts on conductivity measurements of thin YSZ electrolyte films and the impact on solid oxide fuel cells. *Solid State Ionics* **164**, 121–129 (2003).
- [16] Butz, B. *et al.* Correlation between microstructure and degradation in conductivity for cubic  $Y_2O_3$ -doped  $ZrO_2$ . *Solid State Ionics* **177**, 3275–3284 (2006).
- [17] Ji, Z., Haynes, J. A., Voelkl, E. & Rigsbee, J. M. Phase Formation and Stability in Reactively Sputter Deposited Ytria-Stabilized Zirconia Coatings. *J. Am. Ceram. Soc.* **84**, 929–936 (2001).
- [18] Subbarao, E. C. & Maiti, H. S. Solid electrolytes with oxygen ion conduction. *Solid State Ionics* **11**, 317–338 (1984).
- [19] Tarancón, A. Strategies for Lowering Solid Oxide Fuel Cells Operating Temperature. *Energies* **2**, 1130–1150 (2009).
- [20] Ullmann, H., Trofimenko, N., Tietz, F., Stöver, D. & Ahmad-Khanlou, A. Correlation between thermal expansion and oxide ion transport in mixed conducting perovskite-type oxides for SOFC cathodes. *Solid State Ionics* **138**, 79–90 (2000).
- [21] Mitterdorfer, A. & Gauckler, L. J.  $La_2Zr_2O_7$  formation and oxygen reduction kinetics of the  $La_{0.85}Sr_{0.15}Mn_yO_3$ ,  $O_2(g)|YSZ$  system. *Solid State Ionics* **111**, 185–218 (1998).
- [22] Schaevitz, S.B. Powering the wireless world with MEMS. 824802 (2012).
- [23] Pla, D. *et al.* in: 38th International Conference and Exposition on Advanced Ceramics and Composites (ICACC), Daytona Beach (2014).
- [24] Garbayo, I. *et al.* Porous  $La_{0.6}Sr_{0.4}CoO_{3-\delta}$  thin film cathodes for large area micro solid oxide fuel cell power generators. *J. Power Sources* **248**, 1042–1049 (2014).
- [25] Garbayo, I., Pla, D., Morata, A., Fonseca, L., Sabaté, N. & Tarancón, A. Full ceramic micro solid oxide fuel cells: Towards more reliable MEMS power generators operating at high temperatures. *Energy Environ. Sci.* **7**, 3617-3629 (2014).
- [26] Gödickemeier, M., Sasaki, K., Gauckler, L. J. & Riess, I. Electrochemical Characteristics of Cathodes in Solid Oxide Fuel Cells Based on Ceria Electrolytes. *J. Electrochem. Soc.* **144**, 1635–1646 (1997).
- [27] Riess, I., Gödickemeier, M. & Gauckler, L. J. Characterization of solid oxide fuel cells based on solid electrolytes or mixed ionic electronic conductors. *Solid State Ionic* **90**, 91–104 (1996).

- [28] Plonczak, P. *et al.* Tailoring of  $\text{La}_x\text{Sr}_{1-x}\text{Co}_y\text{Fe}_{1-y}\text{O}_{3-\delta}$  Nanostructure by Pulsed Laser Deposition. *Adv. Funct. Mater.* **21**, 2764–2775 (2011).
- [29] Benel, C. *et al.* Synthesis and characterization of nanoparticulate  $\text{La}_{0.6}\text{Sr}_{0.4}\text{CoO}_{3-\delta}$  cathodes for thin-film solid oxide fuel cells. *J. Power Sources* **229**, 258–264 (2013).
- [30] Hayd, J., Yokokawa, H. & Ivers-Tiffée, E. Hetero-Interfaces at Nanoscaled  $(\text{La},\text{Sr})\text{CoO}_{3-\delta}$  Thin-Film Cathodes Enhancing Oxygen Surface-Exchange Properties. *J. Electrochem. Soc.* **160**, F351–F359 (2013).
- [31] Baumann, F. S., Maier, J. & Fleig, J. The polarization resistance of mixed conducting SOFC cathodes: A comparative study using thin film model electrodes. *Solid State Ionics* **179**, 1198–1204 (2008).
- [32] Kerman, K., Lai, B.K. & Ramanathan, S. Free standing oxide alloy electrolytes for low temperature thin film solid oxide fuel cells. *J. Power Sources* **202**, 120–125 (2012).
- [33] Evans, A. *et al.* Integration of Spin-Coated Nanoparticulate-Based  $\text{La}_{0.6}\text{Sr}_{0.4}\text{CoO}_{3-\delta}$  Cathodes into Micro-Solid Oxide Fuel Cell Membranes. *Fuel Cells* **13**, 441–444 (2013).
- [34] Singhal, S., Singhal, S. C. & Kendall, K. *High-temperature Solid Oxide Fuel Cells: Fundamentals, Design and Applications: Fundamentals, Design and Applications.* (Elsevier Science, 2003).
- [35] Rupp, J. L. M., Infortuna, A. & Gauckler, L. J. Thermodynamic Stability of Gadolinia-Doped Ceria Thin Film Electrolytes for Micro-Solid Oxide Fuel Cells. *J. Am. Ceram. Soc.* **90**, 1792–1797 (2007).
- [36] Joo, J. H. & Choi, G. M. Electrical conductivity of thin film ceria grown by pulsed laser deposition. *J. Eur. Ceram. Soc.* **27**, 4273–4277 (2007).
- [37] Scherrer, B. *et al.* Microstructures of YSZ and CGO Thin Films Deposited by Spray Pyrolysis: Influence of Processing Parameters on the Porosity. *Adv. Funct. Mater.* **22**, 3509–3518 (2012).
- [38] Kudo, T. & Obayashi, H. Mixed Electrical Conduction in the Fluorite-Type  $\text{Ce}_{1-x}\text{Gd}_x\text{O}_{2-x/2}$ . *J. Electrochem. Soc.* **123**, 415–419 (1976).
- [39] Jiang, S. Development of lanthanum strontium manganite perovskite cathode materials of solid oxide fuel cells: a review. *J. Mater. Sci.* **43**, 6799–6833 (2008).
- [40] Adler, S. B. Mechanism and kinetics of oxygen reduction on porous  $\text{La}_{1-x}\text{Sr}_x\text{CoO}_{3-\delta}$  electrodes. *Solid State Ionics* **111**, 125–134 (1998).
- [41] Liu, Q., Dong, X., Xiao, G., Zhao, F. & Chen, F. A Novel Electrode Material for Symmetrical SOFCs. *Adv. Mater.* **22**, 5478–5482 (2010).

- [42] Badwal, S. P. S. Grain boundary resistivity in zirconia-based materials: effect of sintering temperatures and impurities. *Solid State Ionics* **76**, 67–80 (1995).
- [43] Rühle, M., Claussen, N. & Heuer, A. H. Microstructure Studies of Y<sub>2</sub>O<sub>3</sub>-Containing Tetragonal ZrO<sub>2</sub> Polycrystals (Y-TZP). *Advances in Ceramics* **12**, 352 (1984).
- [44] Garbayo, I. Ph.D. Thesis, University of Barcelona (2013).
- [45] Garbayo, I. *et al.* in: 10th European SOFC Forum, Luzern, A07 - 38-44 (2012).
- [46] Garbayo, I., Sabaté, N., Salleras, M., Tarancón, A. & Morata, A. in: O.E.P.M. Madrid (Ed.), P201230973, ES (2012).
- [47] Garbayo, I. *et al.* Pinhole-free YSZ self-supported membranes for micro solid oxide fuel cell applications. *Solid State Ionics* **216**, 64–68 (2012).
- [48] Goodenough, J. B. Oxide-Ion Electrolytes. *Annu. Rev. Mater. Res.* **33**, 91–128 (2003).
- [49] Tarancón, A. Ph.D. Thesis, University of Barcelona (2007).
- [50] Okada, Y. & Tokumaru, Y. Precise determination of lattice parameter and thermal expansion coefficient of silicon between 300 and 1500 K. *J. Appl. Phys.* **56**, (1984).
- [51] Tarancón, A. *et al.* Residual Stress of Free-Standing Membranes of Ytria-Stabilized Zirconia for Micro Solid Oxide Fuel Cell Applications. *J. Nanosci. Nanotechnol.* **10**, 1327–1337 (2010).
- [52] Kubicek, M., Limbeck, A., Frömling, T., Hutter, H. & Fleig, J. Relationship between Cation Segregation and the Electrochemical Oxygen Reduction Kinetics of La<sub>0.6</sub>Sr<sub>0.4</sub>CoO<sub>3-δ</sub> Thin Film Electrodes. *J. Electrochem. Soc.* **158**, B727–B734 (2011).
- [53] Petric, A., Huang, P. & Tietz, F. Evaluation of La–Sr–Co–Fe–O perovskites for solid oxide fuel cells and gas separation membranes. *Solid State Ionics* **135**, 719–725 (2000).
- [54] Infortuna, A., Harvey, A. S. & Gauckler, L. J. Microstructures of CGO and YSZ Thin Films by Pulsed Laser Deposition. *Adv. Funct. Mater.* **18**, 127–135 (2008).
- [55] Adler, S. B., Lane, J. A. & Steele, B. C. H. Electrode Kinetics of Porous Mixed-Conducting Oxygen Electrodes. *J. Electrochem. Soc.* **143**, 3554–3564 (1996).
- [56] Johnson, A. C., Lai, B.-K., Xiong, H. & Ramanathan, S. An experimental investigation into micro-fabricated solid oxide fuel cells with ultra-thin

La<sub>0.6</sub>Sr<sub>0.4</sub>Co<sub>0.8</sub>Fe<sub>0.2</sub>O<sub>3</sub> cathodes and yttria-doped zirconia electrolyte films. *J. Power Sources* **186**, 252–260 (2009).

[57] Zhao, F., Peng, R. & Xia, C. LSC-based electrode with high durability for IT-SOFCs. *Fuel Cells Bull.* **2008**, 12–16 (2008).

[58] Heiroth, S. *et al.* Yttria-stabilized zirconia thin films by pulsed laser deposition: Microstructural and compositional control. *J. Eur. Ceram. Soc.* **30**, 489–495 (2010).

[59] Januschewsky, J., Ahrens, M., Opitz, A., Kubel, F. & Fleig, J. Optimized La<sub>0.6</sub>Sr<sub>0.4</sub>CoO<sub>3-δ</sub> Thin-Film Electrodes with Extremely Fast Oxygen-Reduction Kinetics. *Adv. Funct. Mater.* **19**, 3151–3156 (2009).

[60] Huang, H. *et al.* High-performance ultrathin solid oxide fuel cells for low-temperature operation. *J. Electrochem. Soc.* **154**, B20–B24 (2007).

[61] Ryll, T. *et al.* Microscopic and Nanoscopic Three-Phase-Boundaries of Platinum Thin-Film Electrodes on YSZ Electrolyte. *Adv. Funct. Mater.* **21**, 565–572 (2011).

[62] Brett, D. J. L., Atkinson, A., Brandon, N. P. & Skinner, S. J. Intermediate temperature solid oxide fuel cells. *Chem. Soc. Rev.* **37**, 1568–1578 (2008).

[63] De Souza, R. A., Kilner, J. A. & Walker, J. F. A SIMS study of oxygen tracer diffusion and surface exchange in La<sub>0.8</sub>Sr<sub>0.2</sub>MnO<sub>3+δ</sub>. *Mater. Lett.* **43**, 43–52 (2000).

[64] Kilner, J., Skinner, S. & Brongersma, H. The isotope exchange depth profiling (IEDP) technique using SIMS and LEIS. *J. Solid State Electrochem.* **15**, 861–876 (2011).

[65] Burriel, M. *et al.* Anisotropic oxygen diffusion properties in epitaxial thin films of La<sub>2</sub>NiO<sub>4+δ</sub>. *J. Mater. Chem.* **18**, 416–422 (2008).

[66] Peterson, N. L. Grain-boundary diffusion in metals. *Int. Met. Rev.* **28**, 65–91 (1983).

[67] Fleig, J. Solid Oxide Fuel Cell Cathodes: Polarization Mechanisms and Modeling of the Electrochemical Performance. *Annu. Rev. Mater. Res.* **33**, 361–382 (2003).

[68] Steele, B. C. H. Oxygen ion conductors and their technological applications. *Mater. Sci. Eng. B* **13**, 79–87 (1992).

[69] Jamnik, J. & Maier, J. Generalised equivalent circuits for mass and charge transport: chemical capacitance and its implications. *Phys. Chem. Chem. Phys.* **3**, 1668–1678 (2001).

[70] Maier, J. On the correlation of macroscopic and microscopic rate constants in solid state chemistry. *Solid State Ionics* **112**, 197–228 (1998).

- [71] Ishigaki, T., Yamauchi, S., Kishio, K., Mizusaki, J. & Fueki, K. Diffusion of oxide ion vacancies in perovskite-type oxides. *J. Solid State Chem.* **73**, 179–187 (1988).
- [72] Badwal, S. P. S. *et al.* A manometric method for the determination of chemical diffusion in perovskite-type cathode materials of the solid oxide fuel cell. *Ceram. Int.* **27**, 431–441 (2001).
- [73] Mogensen, M., Sammes, N. M. & Tompsett, G. A. Physical, chemical and electrochemical properties of pure and doped ceria. *Solid State Ionics* **129**, 63–94 (2000).
- [74] Steele, B.C.H. & Takahashi, T. (Ed.) *High Conductivity Solid Ionic Conductors, Recent Trends and Applications*. World Scientific, London (1989).
- [75] Inaba, H. & Tagawa, H. Ceria-based solid electrolytes. *Solid State Ionics* **83**, 1–16 (1996).
- [76] Muecke, U. P. *et al.* Electrochemical performance of nanocrystalline nickel/gadolinia-doped ceria thin film anodes for solid oxide fuel cells. *Solid State Ionics* **178**, 1762–1768 (2008).
- [77] Hertz, J. L. & Tuller, H. L. Nanocomposite Platinum–Yttria Stabilized Zirconia Electrode and Implications for Micro-SOFC Operation. *J. Electrochem. Soc.* **154**, B413–B418 (2007).
- [78] Goodenough, J. B. & Huang, Y.-H. Alternative anode materials for solid oxide fuel cells. *J. Power Sources* **173**, 1–10 (2007).
- [79] Xiao, G. *et al.* Sr<sub>2</sub>Fe<sub>1.5</sub>Mo<sub>0.5</sub>O<sub>6</sub> as Cathodes for Intermediate-Temperature Solid Oxide Fuel Cells with La<sub>0.8</sub>Sr<sub>0.2</sub>Ga<sub>0.87</sub>Mg<sub>0.13</sub>O<sub>3</sub> Electrolyte. *J. Electrochem. Soc.* **158**, B455–B460 (2011).
- [80] Bugaris, D. E. *et al.* Investigation of the high-temperature redox chemistry of Sr<sub>2</sub>Fe<sub>1.5</sub>Mo<sub>0.5</sub>O<sub>6-δ</sub> via in situ neutron diffraction. *J. Mater. Chem. A* **2**, 4045–4054 (2014).
- [81] Hou, S. *et al.* Defective Ni Perovskites as Cathode Materials in Intermediate-Temperature Solid-Oxide Fuel Cells: A Structure–Properties Correlation. *Chem. Mater.* **22**, 1071–1079 (2010).
- [82] Shao, Z. & Haile, S. M. A high-performance cathode for the next generation of solid-oxide fuel cells. *Nature* **431**, 170–173 (2004).



## **VII. CONCLUSIONS**





## 7. Conclusions

The main contribution from this thesis work was to design, fabricate and test the basic components of a novel miniaturized fuel cell power generator. The system approach is based on using high energy density hydrocarbons as fuel and  $\mu$ SOFCs as power generators, all fabricated with silicon MEMS technology. One of the most important challenges of this  $\mu$ SOFC PG is the need of operating at high temperatures to ensure high system efficiencies and allow using alternative fuels. Four key aspects were addressed for the system optimization; (i.) an overall design and validation by simulations to cover a complex thermal management, (ii.) the development of a fuel processing unit to produce hydrogen on-board through high temperature hydrocarbon reforming reactions, (iii.) the fabrication of a post combustion unit for catalytic hydrogen oxidation at low temperatures and (iv.) the implementation of functional thin film layers to develop a full ceramic  $\mu$ SOFC.

### ❖ Overall $\mu$ SOFC PG design.

The feasibility of a one-watt  $\mu$ SOFC PG fully integrated in silicon and fuelled with ethanol was proven by FVM simulations. An innovative system design consisting of a vertical stack of a  $\mu$ vaporizer, a double  $\mu$ reformer, a  $\mu$ SOFC stack and a post combustion unit was proposed. The system showed a self-sustained regime of operation at 950 K for an insulation configuration based on materials with a thermal conductivity of  $5 \text{ mW}\cdot\text{m}^{-1}\cdot\text{K}^{-1}$  and a thickness of 10 mm. Observed inhomogeneities of the temperature distribution inside the  $\mu$ SOFC cells were solved by proposing a membrane supported on a grid of silicon slabs. A quick transient regime from room temperature was proven by employing a hybrid electrical-chemical start-up. Start-up times fairly below 1 minute with energy consumptions of 500 J were obtained.

### ❖ Fuel processing unit for efficiently produce hydrogen on-board through high-temperature hydrocarbon reforming reactions.

A novel bulk  $\mu$ reformer was developed based on a microstructure with more than 20000 through-silicon vertically aligned micro-channels per  $\text{cm}^2$ , leading to a total active surface per projected area of  $16 \text{ cm}^2/\text{cm}^2$  and per total volume of  $320 \text{ cm}^2/\text{cm}^3$ . An embedded metal micro-heater (30 nm of TiW, 250 nm of W and 20 nm of Au) was integrated for locally heating the active area of the bulk  $\mu$ reformer. The maximum temperature reached in the active area was  $670 \text{ }^\circ\text{C}$  in 62 s, leading to an energy consumption of 310 J. A catalytic system

based on Pd-Rh/CeO<sub>2</sub> was homogeneously deposited over the walls of the microchannels. The suitability of the catalytic device for methane dry reforming and ethanol steam reforming was proved under operation conditions compatible with the  $\mu$ SOFC PG. Hydrogen yields of 0.36 and 0.28 and hydrogen selectivities of 58% and 64% were obtained for ESR (T=750 °C) and MDR (T=800 °C), respectively.

A thermally optimized  $\mu$ reformer based on a low-thermal mass architecture, i.e. a suspended mass on a silicon nitride membrane, was fabricated in order to achieve a rapid start-up, while keeping the catalytic activity as in the bulk  $\mu$ reformer. The active area, based on a highly dense array of microchannels as in the bulky case, was suspended in a Si<sub>3</sub>N<sub>4</sub> membrane and isolated from the rest of the microreactor by a trench of 50  $\mu$ m without mechanical failure. Using the same heater configuration, a start-up was achieved after 9 s reaching a maximum temperature of 870 °C and consuming 44 J. Thus, this thermally optimized suspended  $\mu$ reformer allowed reducing the start-up time and the energy consumption in *ca.* 86 %. The suspended  $\mu$ reformer was encapsulated by anodic bonding and the Pd-Rh/CeO<sub>2</sub> catalyst was successfully infiltrated. The reactor was proved as a standalone device for ethanol steam reforming under operating conditions compatible with the  $\mu$ SOFC PG.

### ❖ Post combustion unit for the hydrogen oxidation at low temperatures.

The functionality of a silicon-based  $\mu$ combustor has been presented for the catalytic combustion of hydrogen at low temperatures. Inexpensive metal oxides, such as NiO and CuO, infiltrated in a CGO mesoporous structure were synthesized forming thermally stable catalysts. Highly ordered double channel gyroid mesostructures with porous of *ca.* 10 nm in diameter were obtained. The catalytic activity of the CuO-NiO/CGO system was compared to those of the respective single metal oxides. Although all the catalysts proved to be active at temperatures above 100 °C, a synergic effect was observed for the CuO-NiO/CGO configuration.

A volume of the 45 mm<sup>3</sup> was filled with 50 mg of CuO-NiO/CGO catalyst, leading to more than 5 m<sup>2</sup> of specific contact area. The catalytic performance at low temperatures was proven under operating conditions compatible with the  $\mu$ SOFC PG. High hydrogen conversions of 70 and 94 % were obtained at operating temperatures of 120 and 200 °C, respectively,

whereas the air flow rate only showed a small influence on the hydrogen conversion (conversions higher than 90 % were attained for all the residence times tested).

❖ **Thin film-based full ceramic  $\mu$ SOFCs.**

Low-thermal mass platforms and self-supported thin film electrolytes of YSZ were employed. Ceramic thin film electrodes fabricated by PLD have been presented as a suitable alternative to noble metal electrodes in large-area free-standing membranes.

○ **For the cathode side:**

Porous LSC and dense LSM thin films were studied as  $\mu$ SOFC cathodes. Highly porous LSC thin films (up to 33% of in-plane porosity) were well-deposited by PLD over dense YSZ electrolytic layers. Non-degradation was observed neither with temperature nor time up to 700°C and for more than 60 h. The implementation and the thermo-mechanical stability of LSC porous layers in large-area symmetrical LSC/YSZ/LSC free-standing membranes were proved. Target values of ASR ( $0.3 \Omega\cdot\text{cm}^2$ ) required for SOFC cathode / electrolyte bilayers were achieved in the IT range.

An artificial mixed ionic electronic conducting oxide of LSM was fabricated by grain boundary engineering thin films. This essentially pure electronic conductor material was converted into a good MIEC by synthesizing a nanostructure with high density of vertically aligned grain boundaries with high concentration of strain induced defects. The oxygen mass transport properties were analyzed by IEDP-SIMS and EIS measurements at different temperatures (between 773 K and 973 K). The oxygen tracer diffusivities and surface exchange coefficients for bulk and grain boundaries were obtained from the experimental isotope concentration profiles by FVM simulations and from EIS measurements by adjusting the Nyquist plots. The results showed that grain boundaries presented a remarkable enhancement of their oxide-ion mass transport properties (of up to six orders of magnitude at 773 K).

○ **For the anode side:**

Porous CGO and SFM thin films were deposited by PLD over dense YSZ layers. In the case of CGO, its electrochemical performance and thermo-mechanical stability were validated in large-area symmetrical CGO/YSZ/CGO free-standing membranes. Moreover, the SFM layers were applied as an anode and a cathode in the membranes. The novel material showed redox stability

and electrical conductivity in both oxidizing and reducing environments. In both cases, CGO and SFM, target values of ASR required for SOFC electrodes/electrolyte were achieved in the IT range.

- **Full-ceramic  $\mu$ SOFC:**

A full ceramic-based  $\mu$ SOFC was fabricated using a porous LSC thin film as a cathode, a dense membrane of YSZ as a electrolyte and a porous CGO thin film as an anode. The thermo-mechanical stability of the  $\mu$ SOFC membrane was proved up to 750 °C, thus extending the up to now reported operating temperatures of  $\mu$ SOFC (< 550 °C). Measurements of the fuel cell performance of the device were carried out at 700 – 750 °C. A maximum power density of 100 mW·cm<sup>-2</sup> was measured at 750 °C, under pure H<sub>2</sub> as a fuel and synthetic air as an oxidant, for a total power per cell of 2 mW.

# **APPENDICES**



**A. Heat transfer analysis..... 229**

**B. Design and fabrication of a  $\mu$ vaporizer..... 233**

**C. Porous metal current collectors by dealloying..... 237**





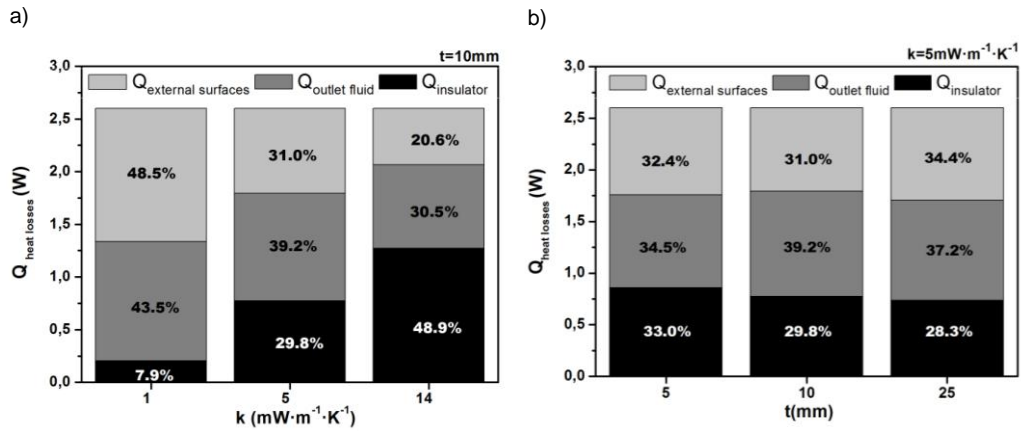
This appendix presents the heat transfer analysis in the  $\mu$ SOFC PG resulting of the thermo-fluidic simulations presented in **Chapter III**.

### A.1. Analysis of thermal losses through the different elements

In order to complete the thermal management study, the percentage of heat losses through the  $\mu$ SOFC PG without nerves was presented in **Figure A.1** for each insulation configuration described in *Section 3.5.1* of **Chapter III**.

Figure A1a shows the variation of the heat losses when changing the thermal conductivity of the insulating material while the thickness is fixed at 10mm. An enhanced heat transfer through the insulation led to more losses across it (see the evolution of  $Q_{\text{insulation}}$ ); whereas the heat contained in the outlet fluid ( $Q_{\text{outlet fluid}}$ ) and the heat released through the external surfaces ( $Q_{\text{external surfaces}}$ ) decreased. This trend was consequence of the higher temperature attained in the HM when the thermal conductivity was lower. So, the higher temperature of the external surfaces and the outlet fluid led to larger heat losses through these two pathways.

In parallel, Figure A.1b shows the variation of heat losses through the  $\mu$ SOFC PG for a variable thickness and a constant thermal conductivity ( $\kappa=5 \text{ mW}\cdot\text{m}^{-1}\cdot\text{K}^{-1}$ ). In all the cases the heat losses through insulation represented approximately one third of the total losses; thus, it can be concluded that (a) there was no dominant part in the heat losses and (b) the effect of the insulation thickness was second order compared to the effect of the variation of the material thermal conductivity. The thinnest insulation ( $t=5 \text{ mm}$ ) led to the lowest temperature in the HM (893 K) due to major losses through the insulation. In contrast, the configuration with 10 mm thickness reached higher temperatures in the HM (951 K), therefore reducing the heat losses through the insulation but by increasing it through the outlet fluid. Finally, the thickest insulating configuration ( $t=25 \text{ mm}$ ) followed a similar trend to the configuration with 10 mm thickness. Despite presenting similar temperatures on the outlet fluid ( $\sim 2 \text{ K}$  of difference) for both cases, in this one the outlet fluid was not the main source of heat losses because of the longer residence time of the fluid inside the system (a thicker insulation means a longer route of the outlet fluid), so the temperature of the outlet fluid was lowered. These results suggest the need of a careful redesigning of the output path for minimizing the heat losses.



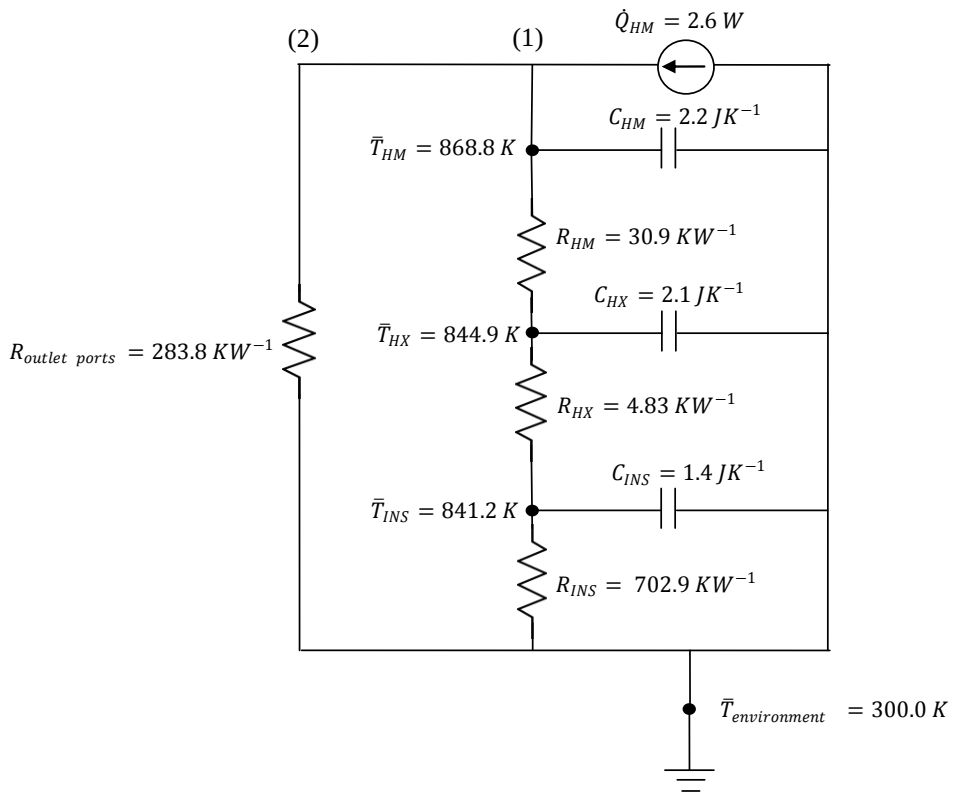
**Figure A.1:** Total heat losses through the  $\mu\text{SOFC}$  PG operating in a steady-state for a thermal insulation configuration with (a) variable conductivity and constant thickness and (b) variable thickness and constant thermal conductivity. Different cases correspond to the configurations described in Section 3.5.1 of Chapter III.

## A.2. Thermal equivalent circuit from FVM simulations

The equivalent thermal circuit of  $\kappa=5 \text{ mW}\cdot\text{m}^{-1}\cdot\text{K}^{-1}$  and  $t=10 \text{ mm}$  insulation configuration is depicted in Figure A.2. The analogy between current flow and heat flow was used here, according to [1]. The heat flow through the different units due to temperature differences between them was associated with a thermal resistance ( $R, \Omega$ ). At the same time, heat sources were elements that supply energy, whereas thermal capacitances were capable of holding a certain amount of energy.

The heat source generated within the  $\mu\text{SOFC}$  PG was 2.6 W, i.e. 1.5 W from the fuel cell membranes and 1.1 W from the catalytic post combustion unit (see energy balance in Section 3.4.3 of **Chapter III**). As described previously, part of this energy was transferred to the different units of the system (0.77 W), whereas the rest flowed through the outlet ports (1.83 W).

In path (1), the heat flowed from the HM to the HX by conduction as consequence of a temperature difference of 23.85 K. The thermal resistance related was  $30.97 \text{ K}\cdot\text{W}^{-1}$ . Then, the heat continued flowing towards the HX with a thermal resistance of  $4.83 \text{ K}\cdot\text{W}^{-1}$ . This lower resistance of the HX led to a better exchange capacity. Finally, the heat flowed through the INS by conduction, natural convection and radiation towards the surroundings with a high thermal resistance ( $R= 702.86 \text{ K}\cdot\text{W}^{-1}$ ). The thermal capacitances associated to the system were  $2.2 \text{ J}\cdot\text{K}^{-1}$  for the HM,  $2.1 \text{ J}\cdot\text{K}^{-1}$  for the HX and  $1.4 \text{ J}\cdot\text{K}^{-1}$  for the INS. In parallel, the heat flowed in path (2) through the outlet ports with a resistance of  $283.77 \text{ K}\cdot\text{W}^{-1}$ .



**Figure A.2:** Thermal equivalent circuit derived from FVM simulations of the  $\mu$ SOFC PG.

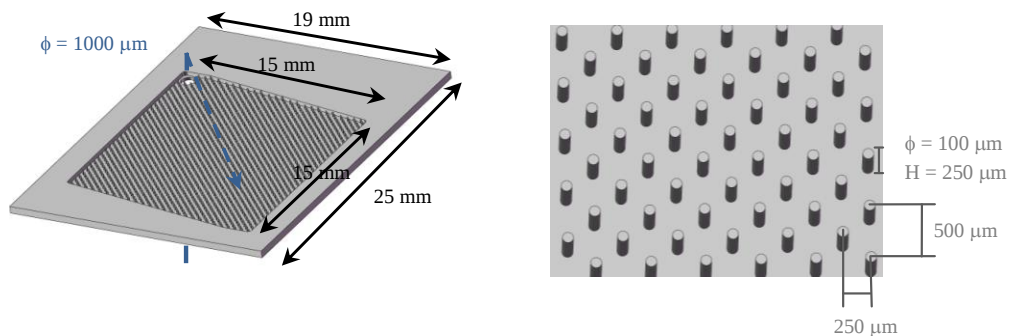
**References**

[1] Sergent, J. & Krum, A. *Thermal Management Handbook for Electronic Assemblies*. (McGraw-Hill Education, 1998).

This appendix gives an overview of the design and fabrication process of a  $\mu$ vaporizer.

### B.1. Design outline and concept

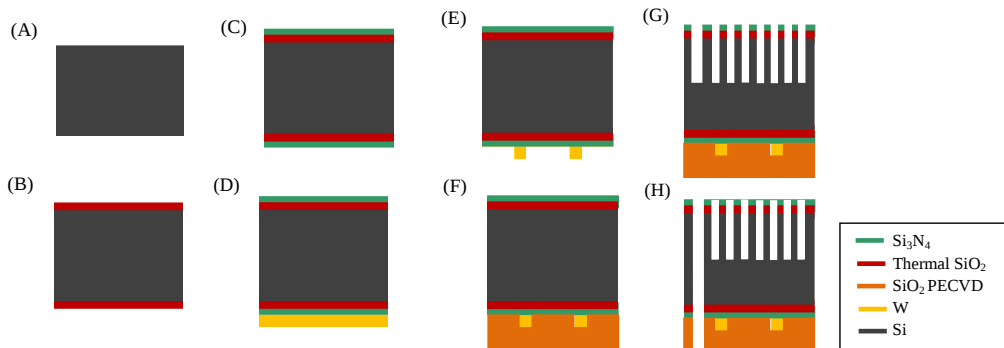
A schematic view of the proposed design is shown in **Figure B.1**. The  $\mu$ vaporizer consisted of a silicon chip of 500  $\mu\text{m}$  in thickness with dimensions of 19x25  $\text{mm}^2$ . The 15x15  $\text{mm}^2$  active area has on a set of micro pillars, with 100  $\mu\text{m}$  in diameter and 250  $\mu\text{m}$  in height, distributed periodically along a 250  $\mu\text{m}$  depth bed defined on the silicon substrate (center-to-center distance of 250  $\mu\text{m}$ ). The micro pillars were chosen because these microstructures enhance the heat transfer by maximizing the contact area between solid and fluid, and avoid bubble formation in the fluid during the evaporation of the liquid fuel [1, 2]. A through-silicon hole of 1000  $\mu\text{m}$  in diameter was defined for the fuel inlet in the  $\mu$ vaporizer. An integrated heater with dimensions of 150  $\mu\text{m}$  long and 100  $\mu\text{m}$  wide was designed on the back side of the silicon chip for locally heating up the active area. The metal multilayer consisted of 30 nm of TiW + 250 nm of W + 20 nm thick of Au.



**Figure B.1:** (a) 3D representation of the  $\mu$ vaporizer design and (b) detail of the micro pillars with geometric parameters.

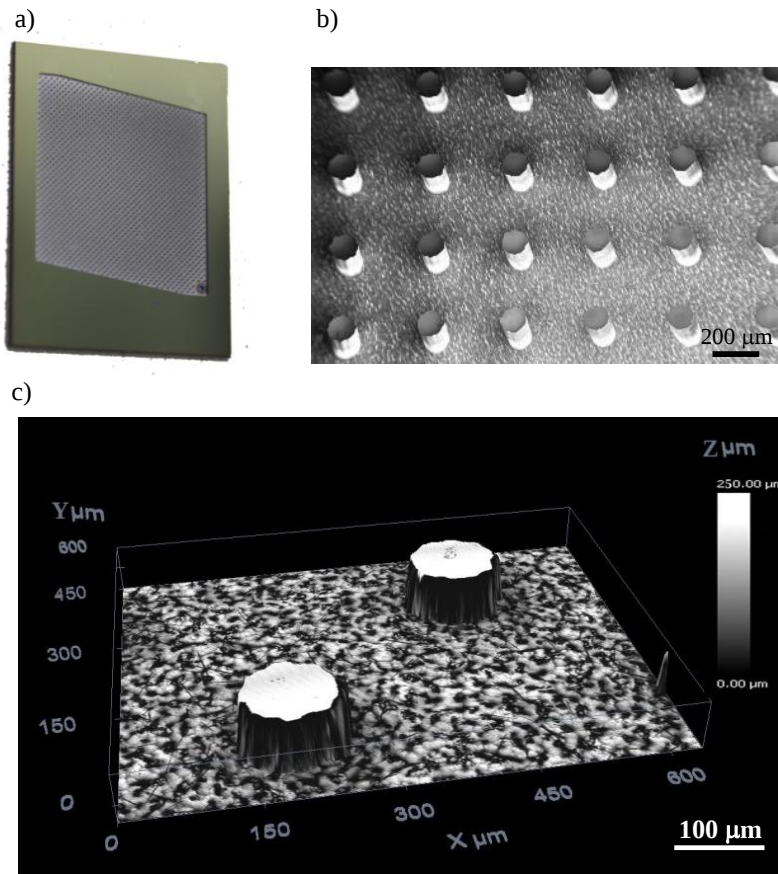
**B.2. Microfabrication process**

**Figure B.2** illustrates the major steps involved in the fabrication of the  $\mu$ vaporizer chips. Single crystal (100)-oriented p-type silicon wafers of 100 mm diameter and 500  $\mu$ m thick were thermally oxidized at 1100  $^{\circ}$ C to obtain a 100 nm thick  $\text{SiO}_2$  layer (Figure B.2A-B). Then, a LPCVD process was used to deposit a 300 nm thick layer of  $\text{Si}_3\text{N}_4$  on both sides (Figure B.2C). A metallic multilayer was deposited by sputtering on the back side of the wafer: 30 nm of TiW as an adhesion layer, 250 nm of W and, finally, 20 nm of Au to avoid W oxidation (Figure B.2D). After that, a photolithographic step was used to define the heater shape and pads. The exposed areas were removed by wet etching in 40 %wt  $\text{H}_2\text{O}_2$  (Figure B.2E). Then, the active area was passivated with a 1 $\mu$ m thick  $\text{SiO}_2$  PECVD layer (FigureB.2F). A second photolithographic step was used to define the active area with the micro pillars and a micro hole of 1000  $\mu$ m in diameter on the top side of the wafer. At that point, a DRIE process was carried out to eliminate the dielectric layers and 250  $\mu$ m of silicon substrate. A double-sided alignment photolithographic step defined the micro hole on the back of the wafer. Finally, another DRIE process was used to form a through-silicon hole (Figure B.2H).



**Figure B.2:** Fabrication flow of the  $\mu$ vaporizer. Silicon wafers were passivated with  $\text{SiO}_2$  and  $\text{SiN}_3$  layers (Figure B.2A-C). A metallic multilayer was deposited by sputtering on the back side of the wafer (Figure B.2D). After that, a photolithographic step defined the heater. The exposed areas were removed by wet etching (Figure B.2E). The active area was passivated with a 1  $\mu$ m thick  $\text{SiO}_2$  PECVD layer (FigureB.2F). Then, the active area with the micro pillars and a micro hole were defined on the top side by a photolithographic and DRIE steps (FigureB.2G). A double-sided alignment photolithographic step defined the micro hole on the back of the wafer. Finally, another DRIE process was used to form a through-silicon hole (Figure B.2H).

**Figure B.3a** shows the fabricated  $\mu$ vaporizer. The total active area achieved by an array of more than 1500 micro pillars was  $\sim 3.8 \text{ cm}^2$ . This value corresponded to a total surface per projected area of  $1.7 \text{ cm}^2/\text{cm}^2$  and per volume of  $34 \text{ cm}^2/\text{cm}^3$ . A SEM image of the micro pillar array is presented in **Figure B.3b**. Well-defined microstructures with smooth surfaces were obtained. A detail of two micro pillars is depicted in **Figure B.3c**. The geometric parameters of the micro pillars were confirmed, i.e. a height of  $250 \text{ }\mu\text{m}$ , a center-to-center spacing of  $250 \text{ }\mu\text{m}$  and a diameter of  $100 \text{ }\mu\text{m}$ . Further work is ongoing to study the evaporation process of the fuel mixture in the  $\mu$ vaporizer.



**Figure B.3:** (a) Image of the fabricated  $\mu$ vaporizer, (b) SEM image of the micro pillar array and (c) CONFOCAL image of details of the micro pillar structure.

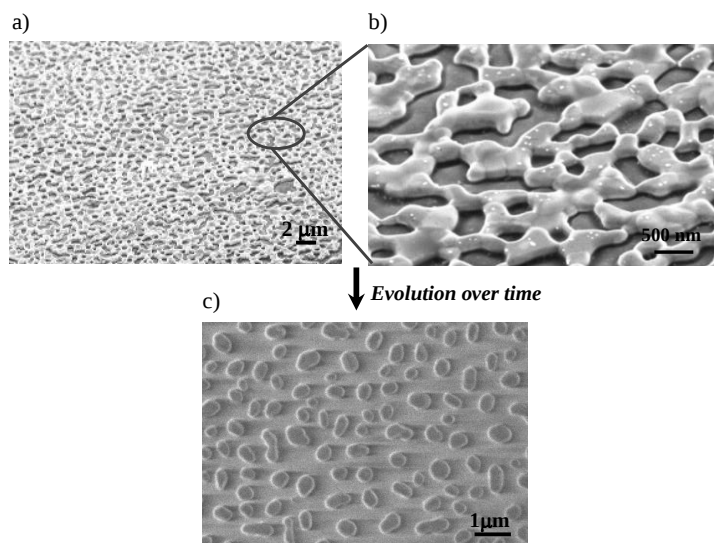


## **References**

- [1] Mihailovic, M., Rops, C., Creemer, J. F. & Sarro, P. M. MEMS silicon-based micro-evaporator with diamond-shaped fins. *Procedia Eng.* **5**, 969–972 (2010).
- [2] Kuang-Han, C. M.Sc. Thesis, Massachusetts Institute of Technology (2013).

### C.1. State of the art current collectors for $\mu$ SOFCs

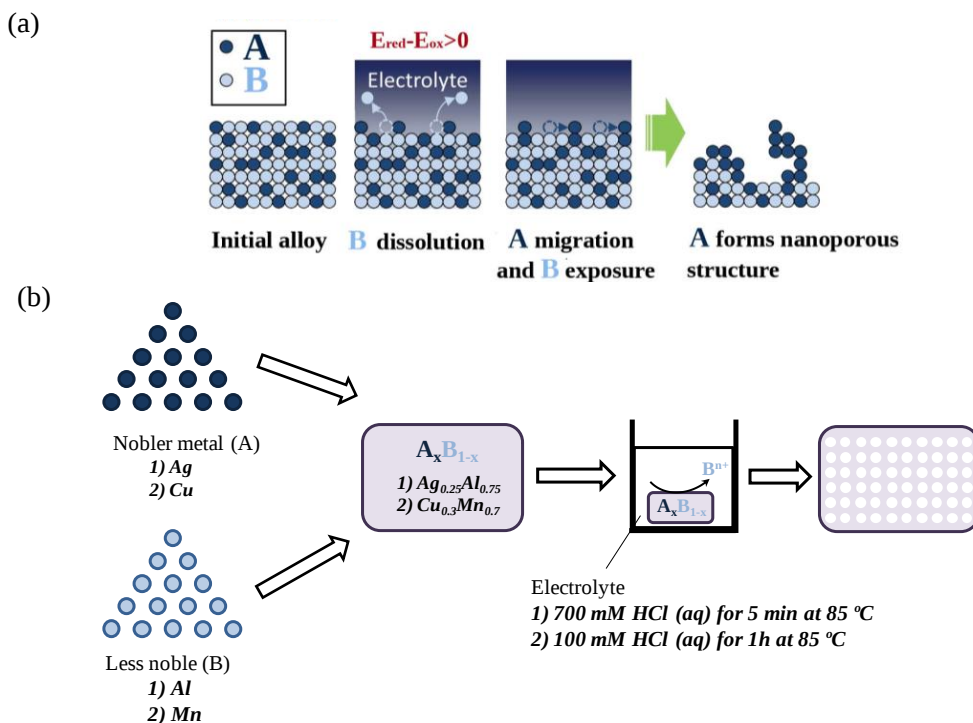
Micro SOFCs usually require the implementation of current collectors for reducing the in-plane resistance of thin film electrodes and ensuring a good current collection. Current collectors are generally based on dense metal films deposited over the electrodes in both sides of the free-standing membrane. Platinum is commonly used because is more thermally stable than other metals (its melting point is 1768 °C, while for silver and nickel are 961 °C and 1455 °C, respectively) and has higher stability in both reducing and oxidizing atmospheres. By thermal dewetting, Pt dense films can be microstructurally tuned in order to balance the losses of active area (the higher the porosity, the larger the active area) and a sufficiently low pore size for maintaining good interconnectivity and conductivity. This process is driven by reducing the surface energy of the film with temperature, and occurs by diffusion even well below the melting point of the film. **Figures C.1a-b** show SEM images of the porosity obtained in this work for the platinum current collectors. Films with 150 nm in thickness were deposited by sputtering and then, a thermal treatment under synthetic air was carried out at 750 °C for 3h. However, the operation conditions of the  $\mu$ SOFCs in the IT range (400 °C < T < 800 °C) provokes that the dewetting process evolves over time (under reducing and oxidizing atmospheres) causing the Pt degradation, i.e. agglomeration into isolated particles (see **Figure C.1c**). A partial metal agglomeration hinders the in-plane percolation and adds an extra resistance, but a complete agglomeration provokes the unusability of the fuel cell.



**Figure C.1:** (a), (b) SEM images of the Pt porosity obtained by dewetting and (c) evolution over time (3h) into isolated particles.

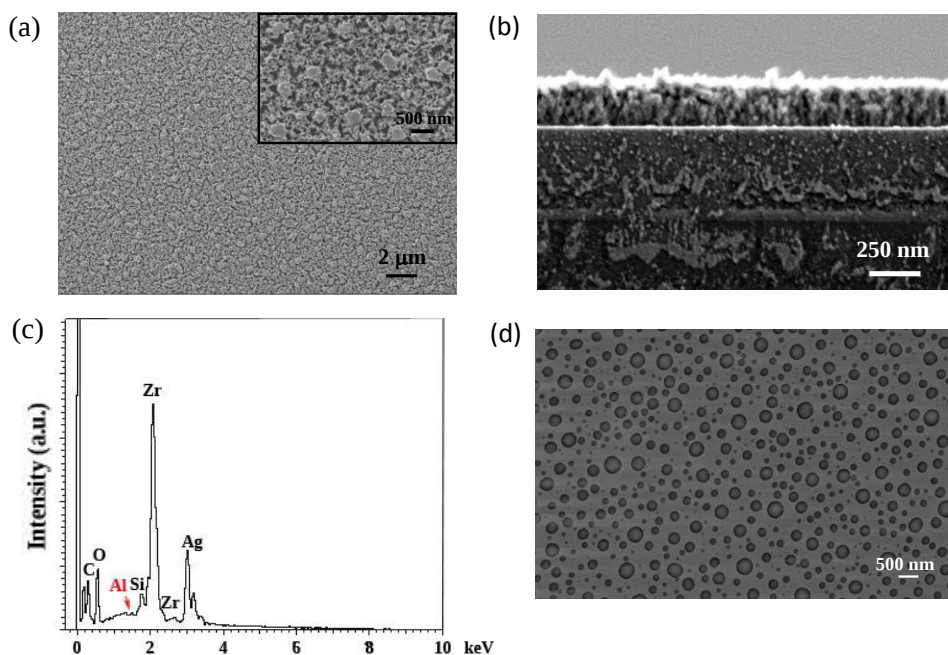
### C.2. Chemical dealloying for nanostructured current collectors

A chemical dealloying technique is proposed here to obtain nanostructured porous current collectors as an alternative to the metal film dewetting process. This technique consists of selectively etching one or more metals from an alloy leading to three-dimensional nanostructures interconnected. **Figure C.2a** shows the mechanism related to the process, adapted from [1]. Preliminary studies were carried out with silver and copper as current collectors for anode and cathode, respectively. The alloys chosen were copper-manganese (Cu-Mn) and silver-aluminum (Ag-Al). **Figure C.2b** shows a schematic illustration of the experimental method used to fabricate nanoporous metals [2, 3]. The alloy film was deposited by sputtering on a dense YSZ film, previously deposited by PLD on a (100) silicon substrate passivated with SiO<sub>2</sub> and SiN<sub>x</sub> layers. A nanoporous Ag layer was produced by chemically dealloying the Ag<sub>0.25</sub>Al<sub>0.75</sub> film (~100 nm thick) for 5 minutes at 85 °C in 700 mM HCl solution that was first bubbled by N<sub>2</sub> gas for 30 min [4]. Similarly, the nanoporous Cu layer was obtained by chemically dealloying a Cu<sub>0.3</sub>Mn<sub>0.7</sub> film (~400 nm thick) for 1 hour at 85 °C in 100 mM HCl solution. In both cases, the residual acid in nanoporous films was removed by N<sub>2</sub> bubbled water rinsing.



**Figure C.2:** (a) Mechanism related to the dealloying process and (b) experimental method used to fabricate Ag and Cu nanoporous films.

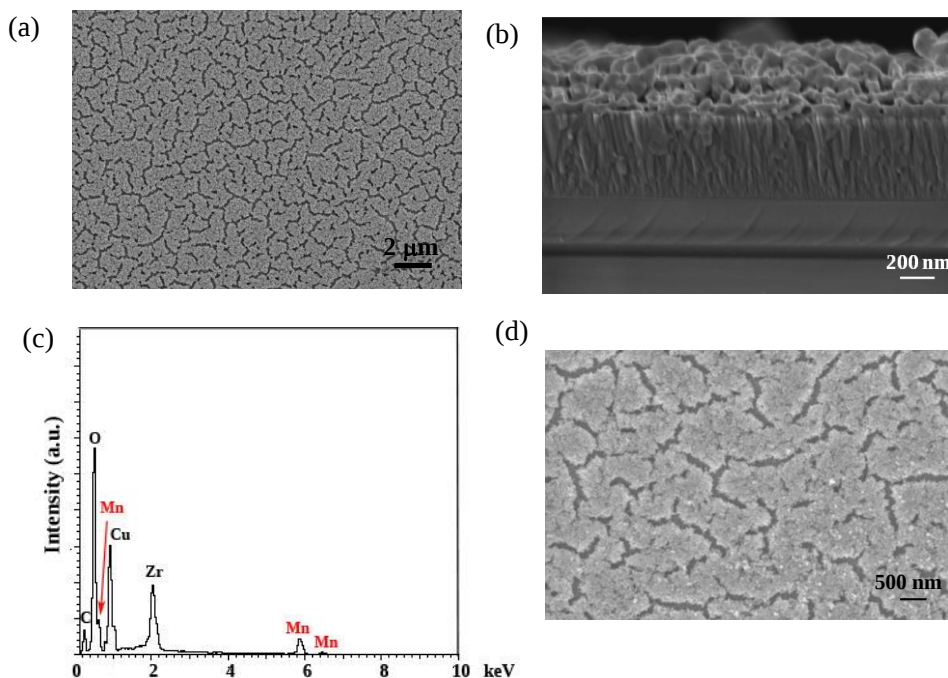
**Figure C.3** presents the Ag porous films obtained as-deposited and after a thermal treatment at 750 °C for 5h under reducing atmosphere (5% H<sub>2</sub> in Ar), i.e. the operating temperature of a ceramic anode  $\mu$ SOFC. As shown in Figure C.3a-b the as-deposited nanostructures obtained had a large surface area due to the three-dimensional interconnections. The electric conductivity was confirmed after the dealloying process. As shown in Figure C.3c, an elemental mapping by EDX in the as-dealloyed nanoporous Ag layer revealed negligible amount of Al (< 0.01 % wt). However, the nanoporous evolved during the thermal annealing to micro droplets by dewetting, leading to a non-electric conductive layer (see Figure C.3d). Thus, the low thermal stability of the nanoporous Ag layer resulted to an unsuitable current collector for a  $\mu$ SOFC system.



**Figure C.3:** (a)-(b) Top view and magnification in the inset, and cross section SEM images of the as-deposited Ag nanoporous layer, (c) elemental mapping by EDX of the as-deposited layer and (d) top view SEM image after thermal annealing.

Analogously, **Figure C.4** compares the Cu porous films obtained as-deposited and after a thermal treatment at 750 °C for 5h under oxidizing atmosphere (air). As depicted in Figure C.4a-b, a homogenous porous layer was obtained after the chemical dealloying. The electric conductivity was

measured after the dealloying process. The microstructure was kept after the thermal annealing (see Figure C.4d), but the conductivity was lost. As shown in Figure C.4c, an elemental mapping by EDX indicated a high concentration of oxygen suggesting the metal oxidation. Moreover, a slight amount of Mn was detected, indicating that the dealloying was incomplete. Although copper was not a good candidate as current collector for the cathode, the stability of its microstructure hints that the dealloying process of other metals like Pt could be an alternative to dense metal thin films.



**Figure C.4:** (a)-(b) Top view and cross section SEM images of the as-deposited Cu porous layer, (c) elemental mapping by EDX and (d) top view SEM image after the thermal annealing.

## **References**

- [1] Hakamada, M. & Mabuchi, M. Fabrication, Microstructure, and Properties of Nanoporous Pd, Ni, and Their Alloys by Dealloying. *Crit. Rev. Solid State Mater. Sci.* **38**, 262–285 (2013).
- [2] Qiu, H., Zhang, Z., Huang, X. & Qu, Y. Dealloying Ag–Al Alloy to Prepare Nanoporous Silver as a Substrate for Surface-Enhanced Raman Scattering: Effects of Structural Evolution and Surface Modification. *ChemPhysChem* **12**, 2118–2123 (2011).
- [3] Hou, C. *et al.* Integrated Solid/Nanoporous Copper/Oxide Hybrid Bulk Electrodes for High-performance Lithium-Ion Batteries. *Sci. Rep.* **3**, (2013).
- [4] Chen, L. Y., Yu, J. S., Fujita, T. & Chen, M. W. Nanoporous copper with tunable nanoporosity for SERS applications. *Adv. Funct. Mater.* **19**, 1221–1226 (2009).



# **SCIENTIFIC CONTRIBUTIONS**





## Publications

1. Is it possible to design a portable power generator based on micro-Solid Oxide Fuel Cells? A finite volume analysis. D. Pla, A. Sánchez, I. Garbayo, M. Salleras, A. Morata, A. Tarancón. *J. Power Sources* **293**, 264–273 (2015).
2. Engineering mixed ionic electronic conduction in  $\text{La}_{0.8}\text{Sr}_{0.2}\text{MnO}_{3+\delta}$  nanostructures through fast grain boundary oxygen diffusivity. A. M. Saranya, D. Pla, A. Morata, A. Cavallaro, J. C. Vázquez, J. A. Kilner, M. Burriel, A. Tarancón. *Adv. Energy Mater.* (2015). doi:10.1002/aenm.201500377
3. Full ceramic micro solid oxide fuel cells: Towards more reliable MEMS power generators operating at high temperatures. I. Garbayo, D. Pla, A. Morata, L. Fonseca, N. Sabaté, A. Tarancón. *Energy Environ. Sci.* **7**, 3617-3629 (2014).
4. Porous  $\text{La}_{0.6}\text{Sr}_{0.4}\text{CoO}_{3-\delta}$  thin film cathodes for large area micro solid oxide fuel cell power generators. I. Garbayo, V. Esposito, S. Sanna, A. Morata, D. Pla, N. Sabaté, A. Tarancón. *J. Power Sources* **248**, 1042–1049 (2014).

## Conference proceedings

5. Fabrication and characterization of a fuel flexible micro-reformer fully integrated in silicon for micro-solid oxide fuel cell applications. D. Pla, M. Salleras, I. Garbayo, A. Morata, N. Sabaté, N. J. Divins, J. Llorca, A. Tarancón. *SPIE Micro Technologies Proceedings* (2015) 9517-102.
6. Fabrication and characterization of a micro-reformer unit fully integrated in silicon for ethanol conversion. D. Pla, M. Salleras, I. Garbayo, A. Morata, N. Sabate, N.J. Divins, J. Llorca, A. Tarancón. *Advances in Solid Oxide Fuel Cells X: Ceramic Engineering and Science Proceedings*, Volume 35 Issue 3 (2014).

7. Fully integrated lambda sensor based on micro machined platforms and Ytria Stabilized Zirconia thin membranes for oxygen measurement. I. Garbayo, A. Morata, D. Pla, M. Salleras, N. Sabaté, A. Tarancón, J. R. Morante. *Procedia Engineering* 87 (2014) 927 – 930.
8. Micro-reformer for hydrogen-rich gas generation from ethanol for a portable micro-SOFC system. D. Pla, M. Salleras, I. Garbayo, A. Morata, N. Sabaté, N. J. Divins, M. Torrell, J. Llorca, A. Tarancón. *European Hydrogen Energy Conference Proceedings* (2014) HPR5-4.
9. Feasibility study of a power generator system based on micro-SOFCs for portable applications. D. Pla, M. Salleras, A. Morata, I. Garbayo, A. Sánchez, A. Tarancón. *Proceedings of the 11th European SOFC and SOEC Forum* (2014) A1220.
10. Fully ceramic-based micro-SOFC integrated in silicon. I. Garbayo, D. Pla, A. Morata, L. Fonseca, N. Sabaté, A. Tarancón. *Proceedings of the 11th European SOFC and SOEC Forum* (2014) A1510.
11. Micro-reformer for hydrogen-rich gas generation for a portable micro-SOFC system. D. Pla, M. Salleras, I. Garbayo, A. Morata, N. Sabaté, N. J. Divins, J. Llorca, A. Tarancón. *Proceedings of the 11th European SOFC and SOEC Forum* (2014) B1504.
12. Catalytic hydrogen micro-combustor for SOFC Portable Applications. D. Pla, L. Almar, G. Gadea, A. Morata, A. Tarancón. *Proceedings of the 11th European SOFC and SOEC Forum* (2014) A1511.
13. Design and manufacture of a micro-reformer for SOFC portable applications. D. Pla, M. Salleras, I. Garbayo, A. Morata, N. Sabaté, N. J. Divins, J. Llorca, A. Tarancón. *Proceedings of the 11th European SOFC Forum* (2012) B1114.

## Contributions in meetings and conferences

1. Grain boundary engineering to improve the performance of microSOFCs. A. Tarancón, A. Morata, D. Pla, A. M. Saranya, I. Garbayo, A. Cavallaro, J. Canales-Vázquez, F. Chiabrera, J. A. Kilner, M. Burriel. *228th ECS Meeting*, Phoenix, USA, Oct 2015. Submitted for oral presentation.
2. Engineering mixed ionic electronic conduction in  $\text{La}_{0.8}\text{Sr}_{0.2}\text{MnO}_{3+\delta}$  nanostructures through fast grain boundary oxygen diffusivity. A.M. Saranya, D. Pla, A. Morata, A. Cavallaro, J. Canales-Vázquez, J. A. Kilner, M. Burriel, A. Tarancón. *20th International Conference on Solid State Ionics*, Colorado, USA, June 2015. Oral presentation.
3. Transforming  $\text{La}_{0.8}\text{Sr}_{0.2}\text{MnO}_3$  into a good mixed ionic-electronic conductor through nanoengineering: grain boundaries as oxygen diffusion highways. A.M. Saranya, D. Pla, A. Morata, A. Cavallaro, J. Canales-Vázquez, J. A. Kilner, M. Burriel, A. Tarancón. *TO-BE Spring Meeting*, Aveiro, Portugal, April 2015. Oral presentation.
4. Fabrication and characterization of a fuel flexible micro-reformer fully integrated in silicon for micro-solid oxide fuel cell applications. D. Pla, M. Salleras, I. Garbayo, A. Morata, N. Sabaté, N. J. Divins, J. Llorca, A. Tarancón. *SPIE Micro Technologies Proceedings*, Barcelona, May 2015. Oral presentation.
5. Combinatorial PLD for mixed conducting oxides: Exploration of entire compositional diagrams in a single experiment. M. Burriel, A.M. Saranya, D. Pla, A. Morata, A. Cavallaro, J. A. Kilner, A. Tarancón. *MRS Fall Meeting*, Boston, USA, Dec 2014. Oral presentation
6. Micro-reformer for hydrogen-rich gas generation for a portable micro-SOFC system. D. Pla, M. Salleras, I. Garbayo, A. Morata, N. Sabaté, N. J. Divins, J. Llorca, A. Tarancón. *Proceedings of the 11th European SOFC and SOEC Forum*, Luzern, Switzerland, July 2014. Oral presentation

7. Micro-reformer for hydrogen-rich gas generation from ethanol for a portable micro-SOFC system. D. Pla, M. Salleras, I. Garbayo, A. Morata, N. Sabaté, N. J. Divins, M. Torrell, J. Llorca, A. Tarancón. *European Hydrogen Energy Conference*, Sevilla, Spain, March 2014. Oral presentation.
8. Integration of nanoionics into functional (micro)systems. A. Tarancón, I. Garbayo, D. Pla, A. M. Saranya, L. Almar, T. Andreu, M. Salleras, N. Sabaté, A. Morata; *7th International Discussion Meeting on Relaxations in Complex Systems*, Barcelona, Spain, Jul 2013. Oral presentation.
9. Integration of nanomaterials in micropower generators. A. Tarancón, A. Morata, I. Garbayo, D. Pla, A. M. Saranya, D. Dávila, M. Salleras, C. Calaza, N. Sabaté, L. Fonseca. *Nanostructured Hybrid Materials for Energy Devices: from experiments to modeling, Summer School ORION*, Granada, Spain, Jun 2013. Oral presentation.
10. A micro solid oxide fuel cell based powering system as energy source for portable devices; I. Garbayo, D. Pla, M. Salleras, A. Morata, N. Sabate, A. Tarancón; *MRS Spring Meeting*, San Francisco, USA, Apr 2013. Oral presentation.
11. Fully integrated lambda sensor based on micro machined platforms and Yttria Stabilized Zirconia thin membranes for oxygen measurement. I. Garbayo, A. Morata, D. Pla, M. Salleras, N. Sabaté, A. Tarancón, J. R. Morante. *EUROSENSORS 2014, XXVIII edition*. Poster presentation.
12. Design and manufacture of a micro-reformer for SOFC portable applications. D. Pla, M. Salleras, I. Garbayo, A. Morata, N. Sabaté, N. J. Divins, J. Llorca, A. Tarancón. *Proceedings of the 11th European SOFC Forum*, Luzern, Switzerland, July 2012. Poster presentation.



